

AB INITIO SIMULATIONS OF IDEALIZED  
SOLID ELECTROLYTES IN LITHIUM ION BATTERIES

BY

AHMAD AL-QAWASMEH

A Dissertation Submitted to the Graduate Faculty of  
WAKE FOREST UNIVERSITY GRADUATE SCHOOL OF ARTS AND SCIENCES

in Partial Fulfillment of the Requirements

for the Degree of

DOCTOR OF PHILOSOPHY

Physics

August 2018

Winston-Salem, North Carolina

Approved By:

Natalie Holzwarth, Ph.D., Advisor

Abdessadek Lachgar, Ph.D., Chair

Samuel S. Cho, Ph.D.

Oana Jurchescu, Ph.D.

Timo Thonhauser, Ph.D.

# Acknowledgements

I am heartily thankful to my advisor Dr. N. A. W. Holzwarth for her unceasing support of my Ph.D study and research. I really appreciate her patience, motivation, enthusiasm, and immense knowledge. Her guidance always helped me to do my research in the right way. In addition to my advisor, I would like to thank the rest of my thesis committee: Dr. Timo Thonhauser, Dr. Samuel Cho, Dr. Oana Jurchescu, and Dr. Abdessadek Lachgar, for their encouragement and insightful comments. In addition, I would like to thank several people for helping to improve my English writing, including Andrew Zeidell and staff members of the Wake Forest University Writing Center. Finally, I would like to express my sincere gratitude to my friend, Dr. Abdullah Shukri, for his encouragement and inspirational guidance throughout this work. His encouragement has been a great motivation to me.

# Contents

<b>Acknowledgements</b>	<b>ii</b>
<b>List of Figures</b>	<b>xi</b>
<b>List of Abbreviations</b>	<b>xii</b>
<b>Abstract</b>	<b>xiii</b>
<b>I Background</b>	<b>1</b>
<b>Chapter 1 Introduction</b>	<b>2</b>
1.1 Thesis Structure . . . . .	2
1.2 Introduction . . . . .	4
<b>Chapter 2 Battery Overview</b>	<b>8</b>
2.1 Components of Batteries . . . . .	8
2.2 Principle of Operation of Batteries . . . . .	9
2.2.1 The Discharge Process . . . . .	11
2.2.2 The Charge Process . . . . .	12
2.3 Properties of Rechargeable Batteries . . . . .	14
2.3.1 Energy Density and Specific Energy . . . . .	14
2.3.2 Charge and Discharge Rate . . . . .	16
2.3.3 Stability and Lifetime . . . . .	18

2.3.4	Safety and Cost . . . . .	20
2.3.5	Summary of Rechargeable Batteries Properties . . . . .	20
2.4	Types of Rechargeable Batteries . . . . .	21
2.5	State of the Art Li-Ion Batteries . . . . .	23
2.5.1	Electrolyte Materials for Li-Ion Batteries . . . . .	25
2.5.2	Promising Research Directions . . . . .	27
2.6	Summary . . . . .	30
<b>Chapter 3 Computational Theory</b>		<b>31</b>
3.1	Quantum Description of Materials . . . . .	31
3.2	Quantum Mechanics . . . . .	32
3.2.1	The Many-Body Schrödinger Equation . . . . .	32
3.3	Why Electronic Structure is an Important Difficult Problem? . . . . .	35
3.4	First-Principles Methods . . . . .	36
3.5	Born-Oppenheimer Approximation . . . . .	37
3.6	Independent Electron Approximation . . . . .	39
3.7	Exclusion Principle . . . . .	41
3.8	Mean-Field Approximation . . . . .	43
3.9	Hartree-Fock Method . . . . .	44
3.10	Ground State Density Functional Theory (DFT) . . . . .	46
3.10.1	Hohenberg-Kohn Theorem . . . . .	48
3.10.2	Kohn-Sham Method . . . . .	49
3.10.3	The Local Density Approximation & The Generalized Gradient Approximation . . . . .	51
3.10.4	Self-Consistent Calculations . . . . .	53
3.10.5	Pseudopotentials . . . . .	55
3.10.6	The Projector Augmented Wave (PAW) Method . . . . .	57
3.10.7	Reasons Behind the Popularity of Density Functional Theory .	62

3.11 Summary . . . . .	63
<b>Chapter 4 Materials Modeling using Density Functional Theory</b>	<b>64</b>
4.1 Crystal Structures . . . . .	64
4.2 Predicting Crystal Structure Using Density Functional Theory . . . . .	65
4.2.1 Calculating Forces Using DFT . . . . .	66
4.2.2 Finding the Equilibrium Nuclear Coordinates Using the Calculated Forces . . . . .	69
4.3 Kinetic Properties of Solid Electrolyte Materials . . . . .	71
4.3.1 Crystal Defects . . . . .	71
4.3.2 Diffusion in Solids . . . . .	74
4.3.3 Transition State Theory . . . . .	76
4.3.4 The Diffusion Coefficient . . . . .	80
4.3.5 Molecular Dynamics Simulation . . . . .	82
4.4 Interfacial Properties of Solid Electrolyte Materials . . . . .	85
4.5 Summary . . . . .	89
<b>II Summary of Research Work</b>	<b>90</b>
<b>Chapter 5 Computational Study of Li Ion Electrolytes Composed of <math>\text{Li}_3\text{AsS}_4</math> Alloyed with <math>\text{Li}_4\text{GeS}_4</math></b>	<b>91</b>
5.1 Overview . . . . .	91
5.2 Main Publication Results . . . . .	92
5.2.1 Conclusions . . . . .	98
5.2.2 My Contribution . . . . .	98
5.3 Published Manuscript . . . . .	98
<b>Chapter 6 <math>\text{Li}_4\text{SnS}_4</math> and <math>\text{Li}_4\text{SnSe}_4</math>: Simulations of Their Structure and Electrolyte Properties</b>	<b>99</b>

6.1	Overview . . . . .	99
6.2	Main Publication Results . . . . .	100
6.3	Conclusions . . . . .	102
6.4	My Contribution . . . . .	102
6.5	Published Manuscript . . . . .	102
<b>Chapter 7</b>	<b>Li<sub>14</sub>P<sub>2</sub>O<sub>3</sub>N<sub>6</sub> and Li<sub>7</sub>PN<sub>4</sub>: Computational study of two nitrogen rich crystalline LiPON electrolyte materials</b>	<b>103</b>
7.1	Overview . . . . .	103
7.2	Main Publication Results . . . . .	104
7.3	Conclusion . . . . .	107
7.4	My contribution . . . . .	108
7.5	Published Manuscript . . . . .	108
<b>Chapter 8</b>	<b>Computational study of the structural and electrolyte properties of Li<sub>4</sub>PS<sub>4</sub>I and related materials</b>	<b>109</b>
8.1	Introduction . . . . .	109
8.2	Crystal structures . . . . .	110
8.3	The Helmholtz Free Energy . . . . .	116
8.4	Models of the disordered phase . . . . .	119
8.5	Li <sub>4</sub> PS <sub>4</sub> I Interface with metallic Li . . . . .	125
8.6	Molecular Dynamics simulation of Li <sub>4</sub> PS <sub>4</sub> I . . . . .	126
<b>Chapter 9</b>	<b>Topological Doping Effects in 2D Chalcogenide Ther- moelectrics</b>	<b>127</b>
9.1	Abstract . . . . .	127
9.2	Calculational Methods . . . . .	128
9.3	My Contribution . . . . .	129

Chapter 10	Summary and Conclusions	132
Appendix A	Computational Study of Li Ion Electrolytes Composed of $\text{Li}_3\text{AsS}_4$ Alloyed with $\text{Li}_4\text{GeS}_4$	135
Appendix B	$\text{Li}_4\text{SnS}_4$ and $\text{Li}_4\text{SnSe}_4$ : Simulations of Their Structure and Electrolyte Properties	146
Appendix C	$\text{Li}_{14}\text{P}_2\text{O}_3\text{N}_6$ and $\text{Li}_7\text{PN}_4$ : Computational study of two nitrogen rich crystalline LiPON electrolyte materials	156
Appendix D	Atomics Units	167
III	Curriculum Vitae	176

# List of Figures

2.1	Artistic illustration of the components of the battery. The anode material is shown on the left of the figure, the cathode material is on the right, and the electrolyte is in the middle of the figure. . . . .	10
2.2	Electrochemical operation of a cell during the discharge process. . . .	12
2.3	Electrochemical operation of a cell during the charge process. . . . .	13
2.4	Schematic open-circuit energy diagram of an electrolyte. $E_g$ is the electrolyte window for thermodynamic stability. $V_{oc}$ is the open circuit voltage. A $\mu_A > \text{LUMO}$ and $\mu_C < \text{HUMO}$ requires a kinetic stability by the formation of an SEI layer. . . . .	19
2.5	Comparison between different types of batteries in term of the specific energy, energy density, size and weight. Adapted from NASA website.	23
2.6	Comparison between different types of batteries in term of lifetime. . .	24
2.7	Comparison between different types of batteries in term of the range of the operation temperature. . . . .	24
2.8	Comparison between different types of batteries in term of cost. . . .	25
2.9	Schematics of Li-Ion battery using $\text{LiCoO}_2$ as cathode and graphite as anode. . . . .	26
2.10	Charge and discharge reactions in Li-ion Battery using $\text{LiCoO}_2$ as cathode and graphite as anode. . . . .	26



2.11	Thermal evolution of ionic conductivity of $\text{Li}_{10}\text{GeP}_2\text{S}_{12}$ , together with those of other lithium solid electrolytes, organic liquid electrolytes, polymer electrolytes, ionic liquids and gel electrolytes. Adapted from Ref. [7] with permission from Nature Publishing group. . . . .	28
3.1	Schematic illustration of all electron (solid lines) and pseudoelectron (dashed lines) and their corresponding wave functions . $r_c$ is the cut-off radius beyond which the wavefunction and the potential are not effected. Adapted from Ref. [31] with permission from the American Physical Society. . . . .	56
3.2	Schematic illustration of the PAW method. The outline represents a region in the crystal , while the filled spheres represent the augmentation spheres around each atom, shaded pink and gray for the PS and AE basis functions, respectively. . . . .	61
4.1	Schematic illustration of finding the equilibrium structure of a material by spanning the energy landscape of the potential energy surface using numerical techniques such as the steepest descent method. . . . .	70
4.2	Example of a jump sequence of two atoms on a lattice. $\Delta R_i, \Delta R_j$ are the mean squared displacement of the atoms $i$ and $j$ respectively. . .	76
4.3	Schematic illustration of the vacancy, interstitial and interstitialcy diffusion mechanisms in the lattice. The vacancy mechanism is shown in black line, The interstitial mechanism with red line and the interstitialcy mechanism with purple line. . . . .	77
4.4	Schematic illustration of an atomic hop in the crystal, where the atom is moving from initial point <b>A</b> to a final point <b>B</b> through a saddle point.	78

4.5	Energy diagram for ideal electrolyte/metal interface. The left panel represents a ball and stick model of Li metal in atomic contact with an electrolyte. The right panel contains three schematic diagrams of the band structures corresponding to the three different regions of space, with increasing energy along the horizontal axis. . . . .	88
8.1	Ball and stick model of optimized structure of $\alpha$ -Li <sub>3</sub> PS <sub>4</sub> with the space group <i>Pbcn</i> . Li, P, and S sites are represented with gray, black, and orange balls, respectively. . . . .	111
8.2	Ball and stick drawing of unit cell for the Sedlmaier structure of Li <sub>4</sub> PS <sub>4</sub> I described in Ref. [58] having the space group <i>P4/nmm</i> . I, P, and S sites are represented by purple, black, and orange balls, respectively. The 5 distinct partially occupied Li sites are represented by partially shaded grey (1), pink (2), blue (3), green (4), and red (5) balls. . . . .	113
8.3	Ball and stick drawing of unit cell for <i>Pmn2</i> <sub>1</sub> structure of Li <sub>4</sub> PS <sub>4</sub> I. I, P, and S sites are represented by purple, black, and orange balls, respectively. The 3 distinct Li sites are represented by small gray (1), pink (2), and blue (3) balls. . . . .	114
8.4	Ball and stick drawing of unit cell for the optimized structure of Li <sub>7</sub> P <sub>2</sub> S <sub>8</sub> I. I, P, and S sites are represented by purple, black, and orange balls, respectively. The small balls representing Li sites are colored in order identify corresponding sites as in Fig. [8.3]. . . . .	114
8.5	Simulated and measured X-ray diffraction patterns for Cu <i>K</i> $\alpha$ radiation. From top to bottom: X-ray pattern for modeled Li <sub>7</sub> P <sub>2</sub> S <sub>8</sub> I unit cell, X-ray data for Li <sub>7</sub> P <sub>2</sub> S <sub>8</sub> I provided by Zachary Hood and consistent with Ref. [59,60], generated X-ray pattern for experimental HT-Li <sub>4</sub> PS <sub>4</sub> I from Ref. [58], and generated X-ray pattern for modeled LT-Li <sub>4</sub> PS <sub>4</sub> I unit cell. . . . .	115

8.6	Plot of the phonon density of states $g(\omega)$ for the LT-Li <sub>4</sub> PS <sub>4</sub> I using the harmonic phonon approximation at the optimize lattice parameters.	118
8.7	Comparison of the Helmholtz free energies per formula unit as a function of temperature for LT-Li <sub>4</sub> PS <sub>4</sub> I (black line) and the sum of contributions of $\gamma$ -Li <sub>3</sub> PS <sub>4</sub> and LiI (red line).	119
8.8	The energy per formula unit for a 100 disordered structures of Li <sub>4</sub> PS <sub>4</sub> I with a SOF similar to experiment. A 9995 eV was added to the energies of these structures.	121
8.9	A histogram for the energy per formula unit of the generated 100 disordered structures of Li <sub>4</sub> PS <sub>4</sub> I.	122
8.10	Comparison of the Helmholtz free energies per formula unit as a function of temperature for the 100 disordered structures of Li <sub>4</sub> PS <sub>4</sub> I and the sum of contributions of $\gamma$ -Li <sub>3</sub> PS <sub>4</sub> and LiI	124
9.1	(a) Structural diagram of supercell for the lateral Ag (111)/Bi <sub>2</sub> Te <sub>3</sub> (1230) interface after relaxation, with Ag, Te and Bi atoms represent by silver, green and purple balls, respectively. (b) The corresponding PDOS plots based on the first principle calculations of the interface and interior region of Ag/Bi <sub>2</sub> Te <sub>3</sub> , bulk Ag, Ag <sub>2</sub> Te and Bi <sub>2</sub> Te <sub>3</sub> . The zero of energy in the plot indicates the Fermi level.	130
9.2	PDOS plots based on the first-principles calculations of Ag/Bi <sub>2</sub> Te <sub>3</sub> interfaces, with different number of Ag atoms. Both (111)/(1230) lateral and (111)/(0001) facial interfaces are shown, together with bulk PDOS of Ag, Ag <sub>2</sub> Te and Bi <sub>2</sub> Te <sub>3</sub> . The zero of energy in the plot indicates the Fermi level.	131

# List of Abbreviations

AE	All Electron
DFT	Density Functional Theory
GGA	Generalized Gradient Approximation
HK	Hohenberg-Kohn theorem
HOMO	Highest Occupied Molecular Orbital
HEG	homogeneous electron gas
LDA	Local Density Approximation
LUMO	Lowest Unoccupied Molecular Orbital
MD	Molecular Dynamics Simulation
PS	Pseudo
PAW	Projector Augmented Wave
SEI	Solid Electrolyte Interphase
TST	Transition State Theory

# Abstract

The general purpose of this work is to develop a detailed understanding of solid state electrolyte materials and to contribute to their development for possible use in Li-Ion batteries using the framework of first-principles computational methods. More specifically, we use different computational methods in the framework of density functional theory to perform an in depth study of the structure, Li ion conductivity, and the stability of recently reported promising inorganic solid electrolyte materials. The structure for some materials was reported from experiment and in some cases was predicted from the simulation and validated to be consistent with the experimental data. Li ion conductivity was studied using the nudged elastic band method and molecular dynamics simulations. The nudged elastic band method was used to analyze the migration barrier of the Li ions. Also, molecular dynamics simulation was used to analyze the migration of the Li ions by visualizing superposed Li positions over the timescale and at various temperatures of the simulation and to calculate the ionic conductivity of the material from the mean square displacement of the Li ions. The stability was studied by analyzing the electronic structure of the interface of the material with metallic Li.

Four classes of solid electrolytes identified as promising electrolytes in the recent experimental literature were investigated in this work. The first class of materials studied was the alloy system  $\text{Li}_{3+x}\text{As}_{1-x}\text{Ge}_x\text{S}_4$  (G. Sahu et al., Journal of Materials Chemistry A, 2, 10396 (2014)) where the simulations were able to model the effects

of Ge in enhancing the conductivity of pure  $\text{Li}_3\text{AsS}_4$ . The second class of materials studied was  $\text{Li}_4\text{SnS}_4$  and  $\text{Li}_4\text{SnSe}_4$  (T. Kaib et al., *Chemistry of Materials*, 24, 2211 (2012), J. A. MacNeil et al., *Journal of Alloys and Compounds*, 586, 736 (2013), T. Kaib et al., *Chemistry of Materials*, 25, 2961 (2013)). Our simulations were able to identify the two different crystal structures of the materials and to investigate differences in their conduction properties. The third set of materials studied were two nitrogen rich crystalline lithium oxonitridophosphate materials,  $\text{Li}_{14}\text{P}_2\text{O}_3\text{N}_6$  (D. Baumann et al., *European Journal of Inorganic Chemistry*, 2015, 617 (2015)) and  $\text{Li}_7\text{PN}_4$  (W. Schnick et al., *Journal of Solid State Chemistry*, 37, 101 (1990)). Our simulations suggest that these materials are promising solid electrolytes due to their ideal interface properties with metallic Li and their promising ionic conductivity. The fourth project is an ongoing study of the newly synthesized electrolyte  $\text{Li}_4\text{PS}_4\text{I}$  (S. Sedlmaier et al., *Chemistry of Materials*, 29, 1830 (2017)). The simulations help in the understanding of the structural and ion mobility properties of this material and to study models of interfaces with Li metal.

# Part I

## Background

# Chapter 1

## Introduction

### 1.1 Thesis Structure

The purpose of this thesis is to explain the role of first-principles (ab initio) methods in resolving some of the current issues of the development of Li-ion batteries. The thesis is organized as follows:

- **Part I** in this thesis is the background. This part gives a detailed description about the background of batteries, first-principles methods, and modeling materials properties using first-principles methods. This part includes 4 chapters, chapter 2, chapter 3, chapter 4 and chapter 5.
- **Chapter 1** in this thesis is an introduction to the thesis main subjects. In the introduction section, I will give an overview about the importance of energy in the modern world, and why we need batteries to solve the energy problem. What is the role of materials research with computations to improve batteries. This introduction section is an overview about what will come in thesis.
- **Chapter 2** in this thesis will explain the basic operating principles of batteries. I will explain the advantages and challenges of Li-ion batteries over other kind



batteries, and what kind of improvements are needed for Li-ion batteries. At the end of this chapter I will motivate the usage of computational research in order to solve the problems I explained earlier and to improve batteries properties.

- **Chapter 3** in this thesis will explain the basics of first-principles methods. In this chapter, I will give a detailed description about the quantum mechanics of materials, explain what we mean by first-principles (ab initio) methods, and explain how we use these methods to calculate the electronic structure and the total energy of materials.
- **Chapter 4** in this thesis will explain how we use first-principles methods to predict and understand materials properties.
- **Part II** in this thesis is the summary of research work. In this part I will summarize the main points in my first author and second author publications, as well as some in progress projects. This part includes 5 chapters, chapter 6, chapter 7, chapter 8, chapter 9 and chapter 10.
- **Chapter 5** in this thesis will include a summary of my first published paper: Computational study of Li Ion electrolytes composed of  $\text{Li}_3\text{AsS}_4$  alloyed with  $\text{Li}_4\text{GeS}_4$ . The actual publication will be included in appendix A.
- **Chapter 6** in this thesis will include a summary of my second published paper:  $\text{Li}_4\text{SnS}_4$  and  $\text{Li}_4\text{SnSe}_4$ : Simulations of Their Structure and Electrolyte Properties. The actual publication will be included in appendix B.
- **Chapter 7** in this thesis will include a summary of my third published paper:  $\text{Li}_{14}\text{P}_2\text{O}_3\text{N}_6$  and  $\text{Li}_7\text{PN}_4$ : Computational study of two nitrogen rich crystalline LiPON electrolyte materials. The actual publication will be included in appendix C.

- **Chapter 8** in this thesis will include my fourth project: Computational study of the structural and electrolyte properties of  $\text{Li}_4\text{PS}_4\text{I}$  and related materials. This work has not been published yet but it is expected to be submitted for publication in the next 2 months. This chapter will include all the results we have so far.
- **Chapter 9** in this thesis will include my fifth project: Topological Doping Effects in 2D Chalcogenide Thermoelectrics. This work was done in collaboration with Chaochao Dun. This work was published in Journal of 2D Materials. I will briefly describe my contribution in this chapter.
- **Chapter 10** in this thesis is the summary and conclusions. This chapter includes the summary and conclusions of the whole thesis.
- **The appendices** this part will mainly include all my first author publications each in a separate chapter.
- **Part III** in this thesis is my curriculum vitae.

## 1.2 Introduction

The world around us has changed significantly over the years. Technology has become one of the main drivers of economic and social development and entertainment. Needless to say, that practically all technologies in the modern world use energy to operate. However, the performance of current energy conversion and storage technologies fall short of their potential for the efficient use of electrical energy in transportation and in commercial and residential applications. The most convenient form of energy storage is portable chemical energy. Chemical energy storage devices (storage devices that use fossil fuel) store the energy in the form of chemical energy, which is relatively easy to store, and deliver this energy in the form of electrical energy, which can be

quickly transported into power lines to power the portable device. No wonder that we are addicted to fossil fuel as a source of chemical energy for heat, propulsion, lighting, and communication.

Fossil fuel has become the dominant chemical energy source because of its ease to storage, access, and transport. However, there are serious environmental risks associated with the usage of fossil fuels. It is a known fact that carbon dioxide, a gas released when fossil fuels are burnt, is one of the primary gases responsible for global warming. The rise in temperature of earth has resulted in melting of polar ice caps, flooding of low lying areas, and an increase in sea levels. If such conditions continue, our planet Earth might face some serious consequences in near future. Another major downside for the usage of fossil fuels is the fact that it is a non-renewable energy source. As of today, fossil fuels are being extracted at an exorbitant rate to meet the gap between demand and supply, and it is estimated that they will be finished in the next 30–40 years. Since they are non-renewable, it is more likely that fuel expenses will face a steep hike in the near future. It would take millions of years to replace coal, and oil, and this means that we will not be able to drive cars anymore unless we switch to electric cars that use energy from renewable energy sources. If we have any hope of solving the energy problems, we need better energy conversion and storage.

Rechargeable batteries are one of the most promising energy storage devices capable of storing energy efficiently from renewable sources. Accordingly, batteries are considered as the key solution for the energy problem, which is a serious threat to our economy, social development and evolution. A rechargeable battery is a collective arrangement of electrical cells that store chemical energy and convert this energy to electrical energy by chemical reactions and vice versa. The rechargeable battery provides the portability of stored chemical energy with the ability to deliver this energy

with high efficiency and no gaseous exhaust. Because of its portability, energy efficiency, and environmental safety, batteries have been widely used to power electronic devices.

Battery research is advancing at a rapid pace, and it is clear that there remains a lot of room for improvement. While today's batteries satisfy most portable applications, improvements are needed if this power source is to become a serious contender for the electric vehicle. Materials have always played a critical role in energy production, conversion and storage, and today there are even greater challenges to overcome if materials are to meet these higher performance demands. Materials used in rechargeable batteries are inherently complex; they are active materials that couple electrical and chemical processes. The state of the field is well-explained in the review article of Ref. [1].

"To design and develop new materials for rechargeable batteries, experimentalists have focused on mapping the synthesis-structure-property relations in different materials families. This approach is time consuming and not very efficient due to the numerous possible chemistries. A longtime goal for scientists is to be able to make materials with ideal properties, something which could be possible if the optimum atomic environment and corresponding processing conditions are known prior to the synthesis. Various experimental techniques, such as X-ray/neutron/electron diffraction (XRD/ND/ED), nuclear magnetic resonance (NMR), and X-ray absorption fine structure spectroscopy (XASF), etc., are capable of probing long-range or short-range atomic arrangement in complex structures, nevertheless, an interpretation on the atomic scale is often based on hypothesis and/or speculation.

With modern computational approaches, one can gain useful insight into the optimal material phase for a specific use for the system under consideration and provide

guidance for the design of the experiment. First-principles (ab initio) modeling refer to the use of quantum mechanics to determine the structure or property of materials. These methods rely only on the basic laws of physics such as quantum mechanics and statistical mechanics, hence they don't require any experimental input beyond the nature of the constituent elements. Ab initio computation methods are best known for precise representation of the structures at the atomic level. It is perhaps the most powerful tool to predict the structure and many ground state properties prior to synthesis. More importantly, the reliability and the accuracy of the computational approach can be significantly improved if experimental information is well integrated to provide a realistic model for computation."

# Chapter 2

## Battery Overview

### **Author's Note:**

The subject of this chapter has been discussed in detail in many textbooks and articles, I found the book given in Ref. [2] to be very useful, in particular for the discussion of Secs. [2.1, 2.2, 2.3]. I found the article given in Ref. [3] to be very useful for the discussion of Secs. [8.1]. I found the thesis given in Ref. [4] to be very useful for the discussion of Secs. [2.5, 2.5.2].

To understand the ways in which batteries can be improved, and the role of computational materials modelling in improving the performance of batteries, it is first necessary to understand the components of batteries, the principle of operation of batteries, what set of properties a battery should exhibit to be practical, what types of batteries are the most practical, and why we need computational materials modelling to improve the battery performance.

### **2.1 Components of Batteries**

Rechargeable batteries are a collection of electrochemical cells connected in series or parallel. The main characteristic of electrochemical cell is the transduction of chem-

ical energy into electrical energy and its reverse, thus enabling rechargeable energy storage. Thus, the battery is a device which converts chemical energy stored in active materials into electrical energy by an electrochemical oxidation-reduction (redox) reaction. Such a reaction involves the transfer of electrons from a material which an electron donor to another material which an electron acceptor. On a fundamental level, the battery cell is composed of:

- The anode, which is oxidized, gives up electrons to the external circuit during the electrochemical reaction.
- The cathode, which is reduced, accepts electrons from the anode during the electrochemical reaction.
- The electrolyte or the ionic conductor, which provides the medium for transfer of charge, as ions, inside the cell between the anode and the cathode. The electrolyte typically has a finite ionic conductivity and negligible electronic conductivity.

The components of the battery are visualized in Fig. [2.1]. Now we have explained the components of batteries, next we will explain in detail the principle of operation of the battery.

## **2.2 Principle of Operation of Batteries**

As shown in Fig. [2.1], a battery is composed of a negative electrode (anode) which is oxidized and a positive electrode (cathode) which is reduced. These electrodes are separated by an electrolyte which has a finite ionic conductivity and negligible electronic conductivity. The electrochemical oxidation-reduction (redox) reaction in the anode and the cathode, transfer chemical energy stored in the electrodes into

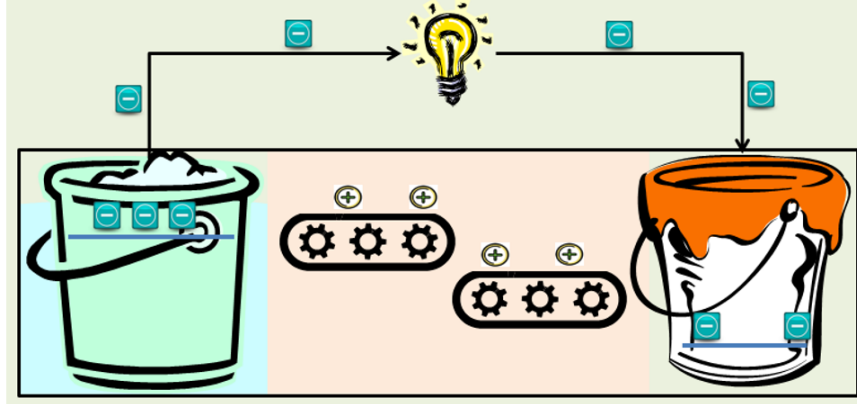


Figure 2.1: Artistic illustration of the components of the battery. The anode material is shown on the left of the figure, the cathode material is on the right, and the electrolyte is in the middle of the figure.

electrical energy, and in rechargeable batteries this transformation is reversible, and obeys the expression:

$$\Delta\mu N \Leftrightarrow Q\Delta V \quad (2.1)$$

Where  $\Delta\mu$  is the chemical potential difference between the anode and the cathode ( $\Delta\mu = \mu_A - \mu_C$ ),  $N$  is the number of charge carriers,  $Q$  is the total charge transferred between the anode and the cathode,  $\Delta V$  is battery voltage. The left hand side of Eq. (2.1) is the chemical energy stored in the electrodes, and righthand side is the electrical energy produced by the chemical energy difference. In the discharge process of the battery, the electrochemical oxidation-reduction (redox) reaction transfer the chemical energy into electrical energy, and this process is reversed during the charge process, where the redox reaction convert back the electrical energy into chemical energy stored in the electrodes. Before we go into the details of the charge/discharge processes, it is convenient to write the battery potential  $\Delta V$  explicitly in term of the chemical potential of the anode and the cathode:



$$\Delta V = \frac{\mu_A - \mu_C}{q} \quad (2.2)$$

where  $\mu_A$  and  $\mu_C$  are the anode and the cathode chemical potentials respectively and  $q$  is  $Q/N$  or the charge per particle.

### 2.2.1 The Discharge Process

The operation of a cell during discharge is shown schematically in Fig. [2.2]. The anode material has a high Fermi level and high chemical potential  $\mu_A$ , and the cathode material has a low Fermi level and low chemical potential  $\mu_C$ . When the anode and the cathode are connected to an external load, the chemical potential difference between the anode and the cathode generate electric potential in the external circuit as shown in Eq. (2.2). The electric potential moves the electrons from the anode, which is oxidized, through the external load to the cathode, where the electrons are accepted and the cathode material is reduced. This process is accompanied by the flow of cations (positive ions) from the anode to the cathode, and the flow of anions (negative ions) from the cathode to the anode.

By assuming that the anode material is a metal ( $Zn$ ) and the cathode material is chlorine ( $Cl_2$ ), the discharge reaction can be written as follows [2]:

- Negative electrode: anodic reaction (oxidation, loss of electrons and release of cations)



- Positive electrode: cathodic reaction (reduction, gain of electrons and release of anions)

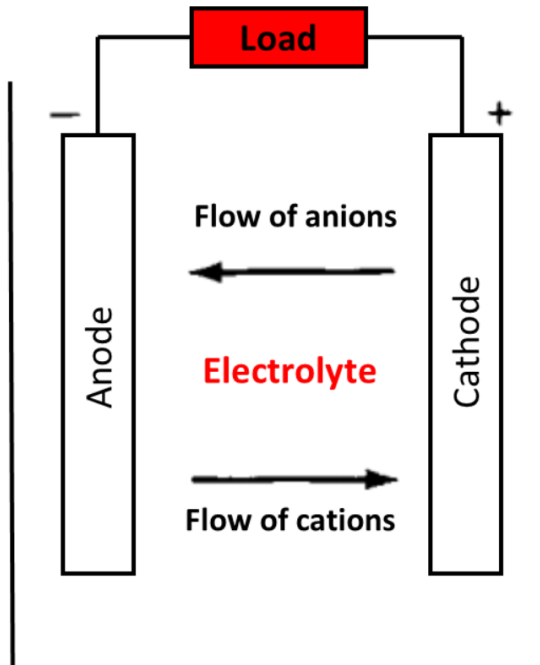
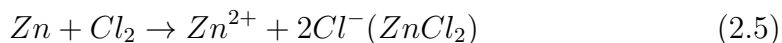


Figure 2.2: Electrochemical operation of a cell during the discharge process.



- Overall reaction (discharge):



### 2.2.2 The Charge Process

The operation of a cell during charge is shown schematically in Fig. [2.3]. The charge process is the reverse of the discharge process, while the energy is provided to battery from the power supply, oxidation takes place at the positive electrode and reduction at the negative electrode. As by definition, the anode is the electrode which is oxidized and the cathode is the electrode which is reduced, the positive electrode is now the anode and the negative electrode is the cathode. The process is accompanied by the

flow of cations from the anode to the cathode, and the flow of anions from the cathode to the anode.

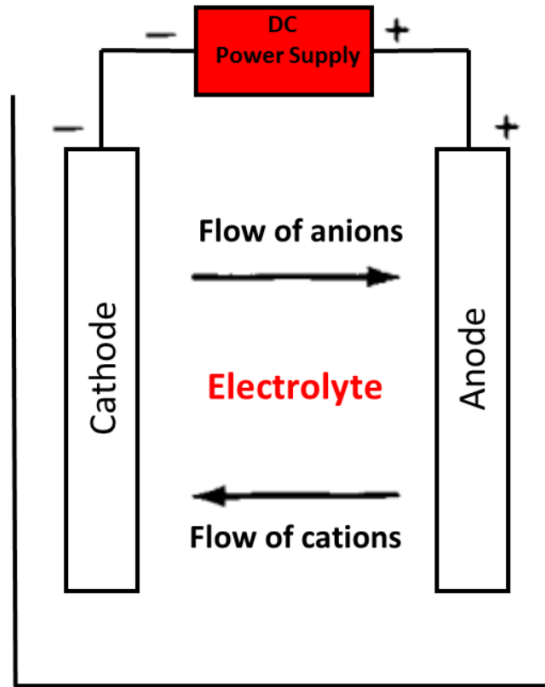


Figure 2.3: Electrochemical operation of a cell during the charge process.

By assuming that the anode material is a metal ( $Zn$ ) and the cathode material is chlorine ( $Cl_2$ ), the charge reaction can be written as follows [2]:

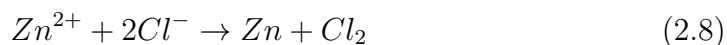
- Negative electrode: cathodic reaction (reduction, gain of electrons)



- Positive electrode: anodic reaction (oxidation, loss of electrons)



- Overall reaction (discharge):



Now we have explained the principle of operation of the battery, next we will explain in detail the set of properties a battery should exhibit to be practical.

## 2.3 Properties of Rechargeable Batteries

For the battery to be practical, it should be able to store a huge amount of energy while maintaining light weight and small volume, it should be able to charge/discharge very rapidly without altering its structure, and it should be able to charge/discharge for thousands of cycles without having any change in its structure. Also, the battery should be made by a safe materials that can operate over wide range of temperatures and intoxicating to the environment. Also, The battery should be affordable for customers, so it should be made of relatively cheap materials. Understanding each of these properties will impose criteria on the components of the batteries (anode, cathode and electrolyte), and will help us to understand which type of batteries is the most practical, and this will open the gates for different research directions to improve the battery performance.

### 2.3.1 Energy Density and Specific Energy

The electrical energy stored in the battery is a very important property of the rechargeable battery, because it determines the amount of energy the battery can deliver. The potential difference between the two electrodes given in Eq. (2.2) not only drives the ions from one electrode to the other but it also has a crucial role in the amount of electrical energy stored in the battery. As shown in Eq. (2.1), the energy stored in the battery can be written as the product of the mobile charge  $Q$  and the potential difference between the two electrodes  $\Delta V$ , given the relation:

$$E = Q\Delta V \quad (2.9)$$

and it can be written as a multiplication of the number of charge carriers  $N$  and the chemical potential difference between the anode and the cathode  $\Delta\mu$ , given the relation:

$$E = N\Delta\mu \quad (2.10)$$

By dividing either expressions by the volume or the mass of the battery gives an expression for the energy density of the battery, though the latter is more accurately termed specific energy. In other words, the specific energy of the battery, is the amount of electrical energy stored in the battery per unit mass and it is typically expressed in the unit of watt $\times$ hour/gram (Whg $^{-1}$ ), and the energy density is the amount of electrical energy stored in the battery per unit volume and it is typically expressed in the unit of watt $\times$ hour/liter (WhL $^{-1}$ ). The battery should have high specific energy/energy density, since a low weight/volume battery is preferred for practical usage in portable electronic devices. Both quantities depend mainly on the magnitude of the charge carrier, the potential difference between the electrodes (the difference between the chemical potential of the electrodes). Thus, in order to increase the energy density/specific energy of the battery it is necessary to increase either the charge carrier density (charge capacity) or the voltage/chemical potential difference between the electrodes.

The theoretical charge density, or theoretical capacity, of an electrode material can be determined by dividing the mobile ion charge per formula unit by the per formula mass, and it is typically expressed in the units of milliampere $\times$ hour/gram (mAhg $^{-1}$ ). The theoretical charge density of metallic lithium from fundamental electrochemistry

is  $3800 \text{ mAhg}^{-1}$  [4], which is very high in comparison to other elements like Mg. This means if we took 1 gram of lithium metal and could effortlessly convert it 100 % into lithium ions, while then sending the electrons released by the lithium through the electrical circuit to do work, that 1 gram of lithium could supply 3800 mA of electron current for 1 hour.

As mentioned above, the energy density/specific energy does not only depend on the charge density of the electrodes, but also on the potential between the electrodes (the chemical potential difference between the electrodes). While the potential difference between the electrodes can be measured experimentally which is the sum of the oxidation energy ( $E_{ox}$ ) at the anode and the reduction energy at the cathode ( $E_{red}$ ), the absolute value of the potential ( $E_{ox}$  or  $E_{red}$ ) at the electrodes cannot be measured experimentally. Since we cannot directly measure the voltage of an individual half reaction, the reduction of hydrogen ions to produce hydrogen gas ( $2\text{H}^+(\text{aq})+2\text{e} \rightarrow \text{H}_2(\text{g})$ ) is, by convention, assigned a reduction potential of 0.00 V. The hydrogen half-cell thus becomes the reference electrode. All the other half cell potentials are measured relative to the hydrogen electrode. The CRC Handbook of chemistry and physics reports these values for different elements. Metallic Li makes an excellent electrode material from a voltage standpoint because it has a voltage of  $-3.04 \text{ V}$  relative to the standard hydrogen electrodes; of the elements reported by The CRC Handbook of chemistry and physics, only Sr and Ca have a lower electrochemical voltages [5].

### 2.3.2 Charge and Discharge Rate

For practical usage in electronic devices, the battery should be able to charge/discharge very rapidly without altering its structure. In other words, the battery should be able

to deliver the energy stored in electrodes to the electronic device very rapidly in the discharge state, also it should be able to restore this energy very rapidly in charge state. As discussed in Sec. [2.2.1] and Sec. [2.2.2], the charge and discharge process of the battery is accompanied by the flow of electrons from the anode to the cathode through the external circuit and the cations and anions through the electrolyte. Accordingly, the charge/discharge rate of the battery is limited mainly by the flow rate of electrons through the external circuit and the cations and anions through the electrolyte.

The flow rate of the electrons and the ions should not differ for the battery cell to remain neutral. The flow rate for the electrons in the external circuit depends mainly on the electrical power of the battery. The electrical power of the battery can be written as the product of the electric current that flows in the external circuit ( $I$ ) times the potential difference between the electrodes ( $\Delta V$ ) described in Eq. (2.2), given the relation:

$$P = I\Delta V \tag{2.11}$$

accordingly, the flow rate of electrons through the external circuit of the battery cell, depends mainly on the potential difference between the electrodes  $\Delta V$ , and therefore on the chemical potential difference between the electrodes. Accordingly, the electrodes should have wide range of electrochemical potential difference to allow rapid charge/discharge in the battery cell. Also, the electrodes should be able to conduct electrons very rapidly through the external circuit.

The other limiting factor for the charge/discharge rate is the flow rate of the ions through the electrolyte which depends mainly on the ionic conductivity of the electrodes and more importantly the ionic conductivity of the electrolyte material.

Accordingly, for rapid charge/discharge rate of the battery cell, electrodes should be fast conducting for ions, and electrolytes should be fast conducting for ions and good insulator for electrons. Generally, electrolytes should have:

- A ionic conductivity  $\sigma > 10^{-4}$  S/cm over the temperature range of the battery operation.
- An electronic conductivity  $\sigma_e < 10^{-10}$  S/cm.

Accordingly, a good ionic conductivity is one of the most important criteria for selecting the electrolyte material for rechargeable battery applications.

### 2.3.3 Stability and Lifetime

Stability is another important property of the battery cell. It is not enough for the battery to be capable of storing huge amount of energy within a small mass and volume and deliver and restore this energy very rapidly in the charge/discharge process, but also for the battery to be practical it should be able to maintain it's structure to be able to operate for thousands of cycles and therefore last for a longtime. In other words, when we refer to a battery cell as stable we mean that it's structure remains unchanged during the charge/discharge process of the battery. During the charge/discharge process, thermodynamics stability requires the chemical stability of the electrodes and the electrolyte. Fig. [2.4] is a schematic of the relative electron energies in the electrodes and the electrolyte of a thermodynamically stable battery cell.

The anode is reductant, the cathode is oxidant. The energy difference between the lowest unoccupied molecular orbital (LUMO) and the highest occupied molecular orbital (HOMO) of the electrolyte is the window of the electrolyte. The two electrodes are electronic conductors with the anode and the cathode electrochemical potentials  $\mu_A$  and  $\mu_C$ . An anode with chemical potential  $\mu_A$  above the electrolyte (LUMO) will



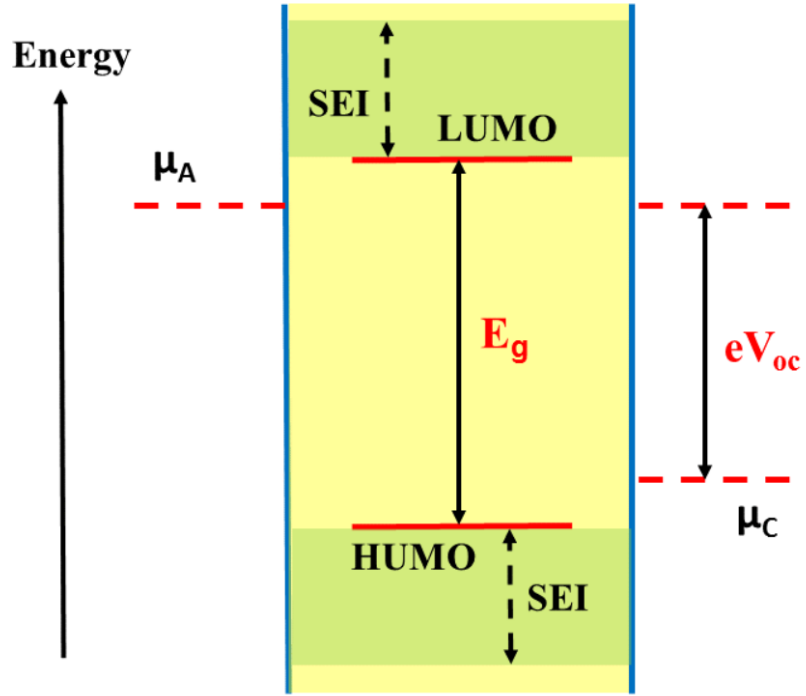


Figure 2.4: Schematic open-circuit energy diagram of an electrolyte.  $E_g$  is the electrolyte window for thermodynamic stability.  $V_{oc}$  is the open circuit voltage. A  $\mu_A > \text{LUMO}$  and  $\mu_C < \text{HUMO}$  requires a kinetic stability by the formation of an SEI layer.

reduce the electrolyte unless a passivation layer blocks the electron transfer from the from the anode to the electrolyte LUMO; and a cathode with  $\mu_C$  below the (HOMO) of the electrolyte will oxidize the electrolyte unless the electrolyte forms a passivation layer blocks the electrons to transfer from the electrolyte (HUMO) to the cathode. Therefore, thermodynamical stability requires locating the electrode electrochemical potentials  $\mu_C$  and  $\mu_A$  within the window of the electrolyte, which constrains the open circuit voltage  $V_{oc}$  of a battery cell to:

$$eV_{oc} = \mu_A - \mu_C \leq E_g \quad (2.12)$$

A passivation solid/electrolyte interface (SEI) layer at the electrode/electrolyte boundary can give extra stability to a large  $V_{oc}$  provided that  $eV_{oc} - E_g$  is not too large.

Accordingly electrolyte materials should have a wide window and should be able to rapidly form a passivation solid/electrolyte interface (SEI) layer at the electrode/electrolyte boundary. Electrode materials should have a chemical potential that aligns well with the electrolyte window.

### **2.3.4 Safety and Cost**

Safety is a key aspect of any energy storage device, including batteries. For instance, thermal stability is the most important property. For a battery to be safe, it should be able to operate over wide range of temperatures without having any damage in its components. Accordingly the battery components (electrodes and electrolyte) are chosen based their thermal stability over wide range of temperatures.

Also for the battery to be practical, it should be made of affordable materials, and it should use electricity efficiently.

### **2.3.5 Summary of Rechargeable Batteries Properties**

For further discussion and analysis, it is convenient to summarize the properties of rechargeable batteries properties. In approximate order of importance, for a battery to be practical, it should:

- Have a high specific energy and energy density.
- Have a fast charge and discharge rate.
- It should be stable in the charge and discharge process.
- It should be made of safe materials that operate over wide range of temperatures.
- It should be affordable for customers and it should use electricity efficiently.

Electrodes should:

- Have a high electrochemical potential difference between the anode and the cathode.
- Should have a high conductivity for ions and electrons.
- Should be able to operate over wide range of temperatures.
- Should be made from affordable materials.

The electrolyte should:

- Have a ionic conductivity  $\sigma > 10^{-4}$  S/cm over the temperature range of the battery operation.
- Have a electronic conductivity  $\sigma_e < 10^{-10}$  S/cm.
- Have a large window, high energy difference between it's LUMO and HUMO.
- It should be able to form rapidly a passivating solid/electrolyte-interface (SEI) layer where kinetic stability is required, if the electrode potential lies outside the electrolyte window.
- It should be made of safe materials that operate over wide range of temperatures.
- Low toxicity and low cost.

## 2.4 Types of Rechargeable Batteries

There are different types of rechargeable batteries and they are usually classified by the type of electrolyte used in their construction. The most known types of rechargeable batteries are (1) Alkaline (2) Lead acid (3) Nickel cadmium (NiCad)

(4) Nickel-metal hybrid (NiMH) (5) Li-ion batteries. More than 50% of the batteries used worldwide are lead-acid. Lead-acid batteries have a number advantages. They are low cost, robust, have high tolerance to over-charging, they also have an established recycling procedure. However, they have some major drawbacks, they are heavy and bulky, unsuitable for fast charging, have a short deep cycle life, have a higher self discharge at higher temperature. They also have a risk of leakage of toxic chemicals. In spite of the overwhelming presence of lead-acid, the requirements for smaller, lighter and deep cycle life rechargeable batteries has grown significantly in the present century. Nickel-cadmium (NiCad) batteries can meet deep cycling needs. They are also lighter and smaller than lead-acid batteries, but they require periodic maintenance and also exhibits a memory effect that results in a reduced usable capacity with time. They were widely adopted for portable electronics and other portable devices, but of late of their use has considerably reduced due to environmental concerns with the use cadmium. Nickel Metal Hydride (NiMH) batteries has emerged as an alternative solution for portable applications. However, large NiMH batteries have not been adopted due to the high cost of nickel and patent limitations. NiMH also exhibits high self discharge rate. Li-ion batteries were first proposed in 1976 [6] and have been widely adopted for portable electronics since the early 1990s. The quick reversibility of lithium ions enables Li-ion batteries to charge and discharge faster than lead-acid and NiMH batteries. In addition, Li-ion batteries produce the same amount of energy as NiMH batteries but they are typically 40% smaller and weight half as much, thus doubling the amount of energy storage. Overall, due to the low electrochemical potential and high charge density of metallic lithium, Li-ion batteries have high energy density/specific energy and they are lighter and smaller than the lead-acid and NiMH batteries as shown in Fig. [2.5]. Li-ion batteries also have longer lifetime in comparison to lead-acid and NiMH batteries [2] as shown in Fig. [2.6]. Li-ion batteries can operate over wide range temperatures in comparison the lead-acid

and NiMH batteries [2] as shown in Fig. [2.7]. However Li-ion batteries have higher cost than the lead-acid and NiMH batteries [2] as shown in Fig. [2.8]. Accordingly, due to its high energy density/specific energy and its long lifetime. Li-ion batteries are considered the best practical batteries for most applications.

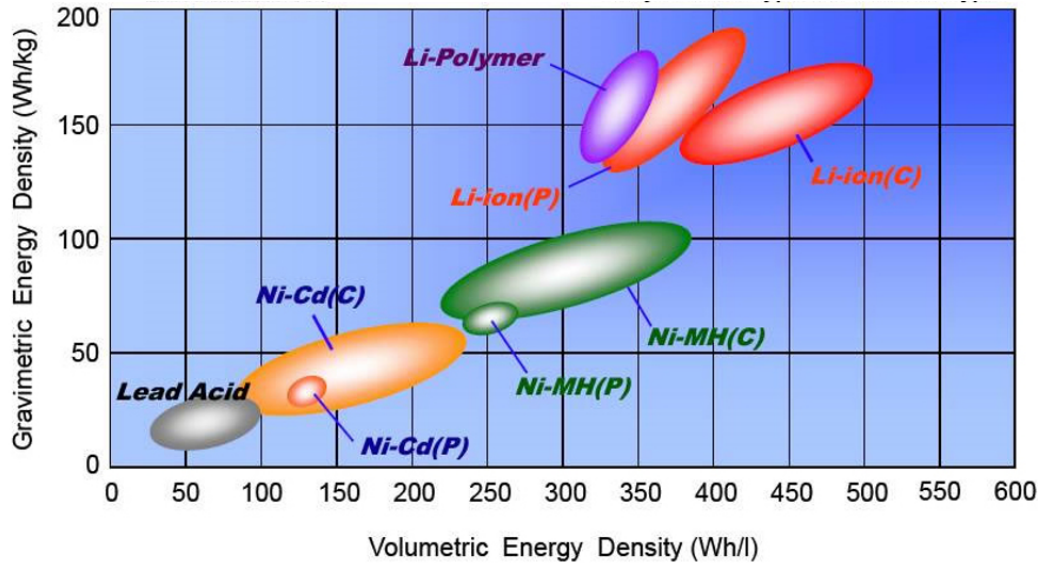


Figure 2.5: Comparison between different types of batteries in terms of the specific energy, energy density, size and weight. Adapted from NASA website.

## 2.5 State of the Art Li-Ion Batteries

Li-ion battery is similar to any battery, it is made of two electrodes separated by an electrolyte. However, the Li-ion battery has a layered electrode materials into which Li is inserted on both sides of the cell. The first models for Li-ion batteries were first proposed in 1976 [6] and have been widely adopted for portable electronics since the early 1990s, this model contains graphite as an anode and  $\text{LiCoO}_2$  as a cathode. This formulation remains one of the most popular Li-ion battery to this date and a model version of it is shown in Fig. [2.9]. Both electrodes allow lithium ion to move in and out of their structure with a process called insertion and extraction. During discharge,

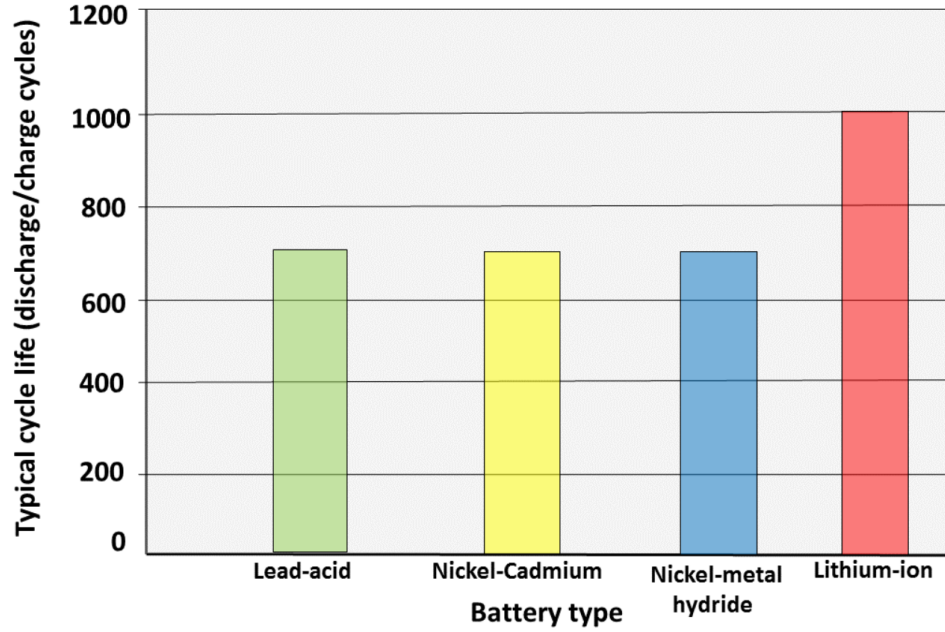


Figure 2.6: Comparison between different types of batteries in term of lifetime.

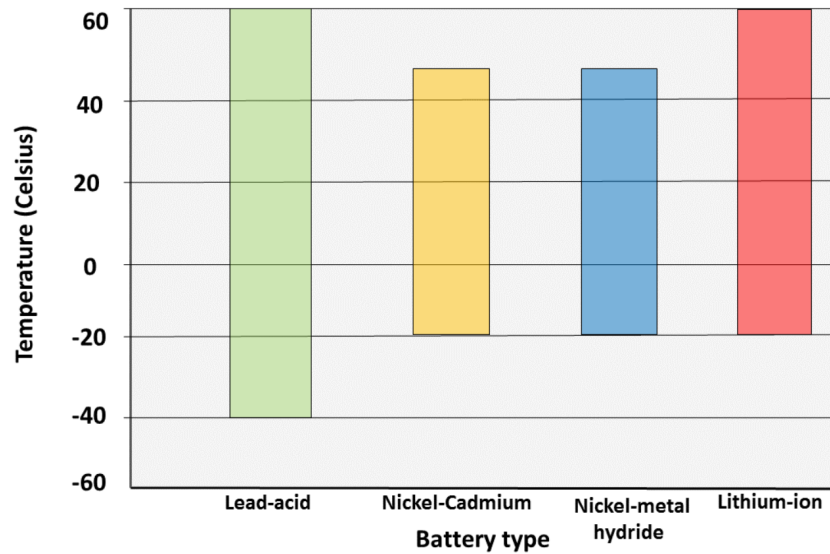


Figure 2.7: Comparison between different types of batteries in term of the range of the operation temperature.

the positive lithium ions move from the negative electrode, which contains graphite, to the positive electrode through the electrolyte while the electrons flow through the external circuit in the same direction. When the cell is charging, the reverse

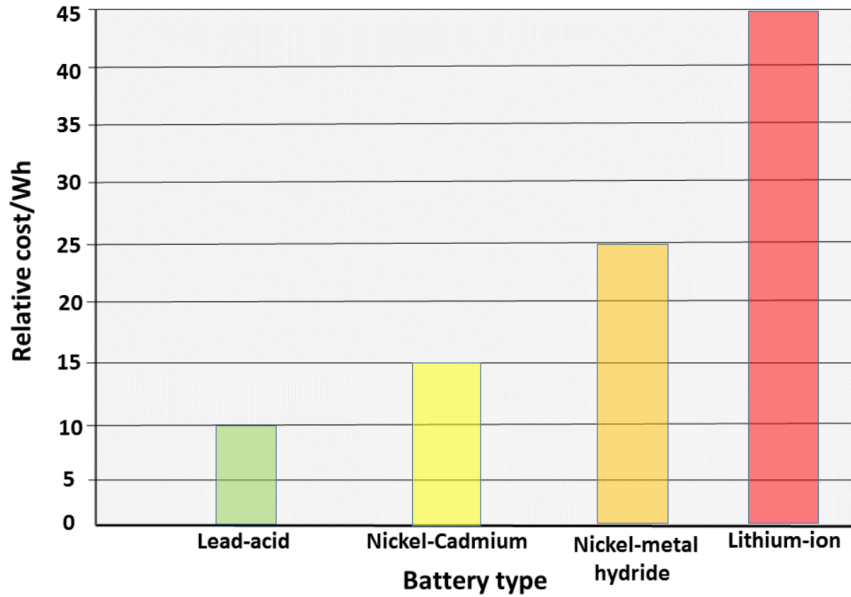


Figure 2.8: Comparison between different types of batteries in term of cost.

occurs with the lithium ions and electrons moved back into the negative electrode in a net higher energy state. The charge/discharge process is shown in Fig. [2.10]. The electrodes materials used in Li-ion battery satisfies most of the requirements we mentioned earlier in Sec. [2.4]. However, for the electrolyte materials the story requires more explanation.

### 2.5.1 Electrolyte Materials for Li-Ion Batteries

In general, the electrolyte is specifically designed for a particular battery application. Different types of electrolytes are used in Li-ion batteries. In this section, we will discuss these types of electrolytes, according to the requirements of the electrolyte materials discussed in Sec. [2.4].

- **Organic liquid electrolytes:** This is the most common type of electrolytes used for Li-ion batteries, due to its high Li conductivity. This type of electrolyte is made of carbonates an organic liquid, and good solvents for Li salts. This type of electrolyte satisfies the electrolytes requirements from 1 to 6, but not 3 and 5.

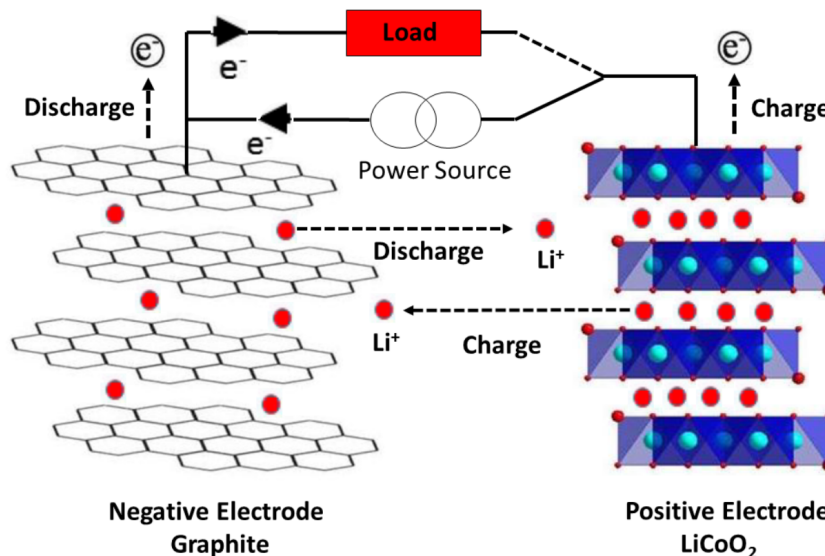


Figure 2.9: Schematics of Li-Ion battery using  $\text{LiCoO}_2$  as cathode and graphite as anode.

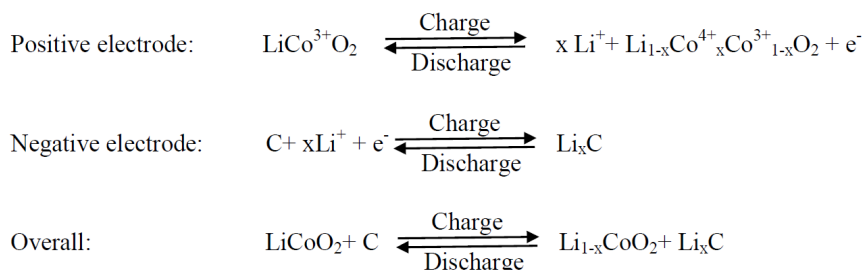


Figure 2.10: Charge and discharge reactions in Li-ion Battery using  $\text{LiCoO}_2$  as cathode and graphite as anode.

Carbonate-based solvent are highly flammable with a flash points below  $30\text{ }^\circ\text{C}$ . Also, the electrolyte window for inorganic solid electrolytes is not wide enough which may cause stability issue during the charge/discharge process.

- Ionic liquids:** Room-temperature ionic liquids have been recently considered as alternative electrolytes for Li-ion batteries, because they have the advantage of thermal stability over carbonate-based electrolytes. This type of electrolyte satisfies the electrolytes requirements from 1 to 6 but not 1. Ionic liquids electrolytes have a high viscosity, which reduces their Li ion conductivity, the Li



ion conductivity of these electrolytes is very poor to be competitive for Li-ion battery applications.

- **Inorganic liquid electrolytes:** The inorganic liquid electrolyte based on  $\text{LiAlCl}_4$  and  $\text{SO}_2$  has a good room temperature Li ion conductivity ( $\sigma_{\text{Li}} = 7 \times 10^{-2} \text{ S/cm}$ ) and is nonflammable, but its electrolyte window is too small to be competitive.
- **Solid polymer electrolytes:** This type of electrolytes satisfies the electrolyte properties from 2 to 6, but not 1. Solid polymer electrolytes have a very poor conductivity of Li ions,  $\sigma_{\text{Li}} < 10^{-5} \text{ S/cm}$ . Accordingly, the Li ion conductivity of these electrolytes is very poor to be competitive for Li-ion battery applications.
- **Inorganic solid electrolytes:** Inorganic solid Li ion conducting materials have been considered for Li-based electrolytes, because they have a wide electrochemical window 0–5 V and additionally meet the electrolyte requirements from 2 to 6, but not 1. In general, the Li ion conductivity inorganic solid electrolytes is not as good as organic liquid electrolytes. For this reason, inorganic solid electrolytes has been excluded from large scale batteries applications. They have only been used in thin film battery applications.

## 2.5.2 Promising Research Directions

As discussed in the previous section. The most common type of electrolytes used in Li-ion batteries, the organic liquid electrolyte, suffers from electrochemical stability issues due to its narrow electrolyte window, and thermal stability issue with a flash point below  $30 \text{ C}^\circ$ . Accordingly, the development of an electrolyte with a wider electrochemical window and improved thermal safety properties has become one of the most promising avenues for improving Li-ion batteries. Inorganic solid electrolytes, look like a good candidates to solve the stability issues of organic liquid electrolytes due to their wide electrochemical window and their thermal stability. However, their

low ionic conductivity prevents them being used in practical applications.

Inorganic solid electrolytes have shown a remarkable improvement in recent years. A large number of novel electrolyte materials have been developed with Li ion conductivity comparable and even beyond organic liquid electrolytes. Fig. [2.11] shows the ionic conductivity of different inorganic solid electrolytes in comparison to organic liquid electrolytes, polymer electrolytes, ionic liquids and gel electrolytes. These materials are crystalline, glassy, polymer and composite systems.

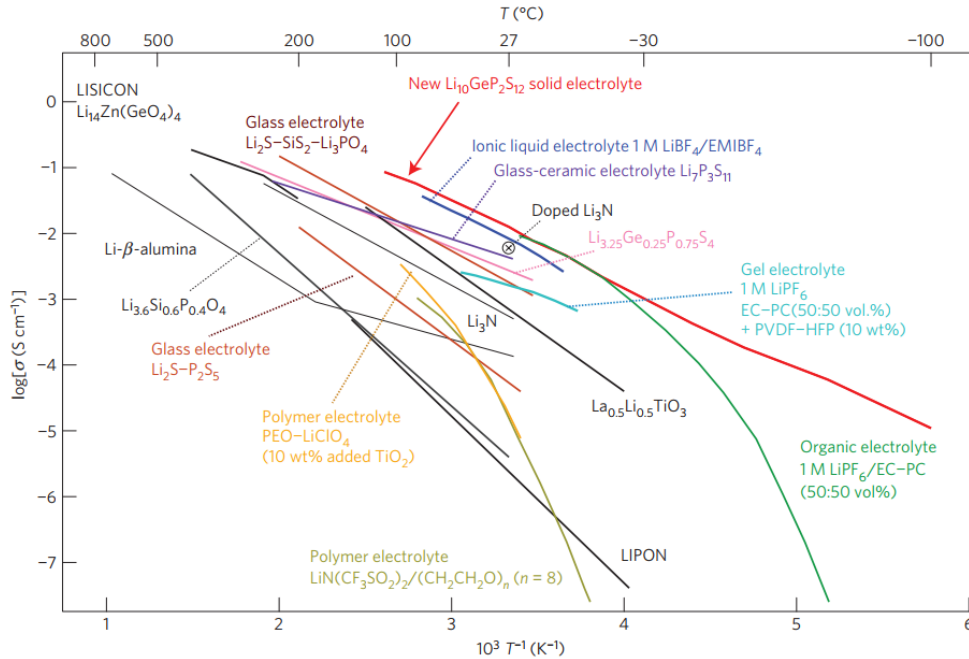


Figure 2.11: Thermal evolution of ionic conductivity of  $\text{Li}_{10}\text{GeP}_2\text{S}_{12}$ , together with those of other lithium solid electrolytes, organic liquid electrolytes, polymer electrolytes, ionic liquids and gel electrolytes. Adapted from Ref. [7] with permission from Nature Publishing group.

The search for solid electrolyte materials with improved conductivity, has been encouraged by the discovery of lithium nitride ( $\text{Li}_3\text{N}$ ), which was discovered in the 1970s, and has a very high conductivity of ( $6 \times 10^{-3} \text{ Scm}^{-1}$ ) at room temperature. The  $\text{Li}_{10}\text{GeP}_2\text{S}_{12}$  material exhibits an extremely high conductivity of over ( $10^{-2} \text{ Scm}^{-1}$ )

at room temperature. Accordingly, it makes excellent electrolyte for Li-ion battery applications. Other systems currently being investigated as battery electrolytes.

The LiPON family of materials [8–16], is very widely used solid electrolyte for thin film batteries and number of other technologies. One of the outstanding attributes of LiPON electrolytes is its long term stability in contact with pure Li anodes. The LiPON electrolytes have the composition of  $\text{Li}_x\text{PO}_y\text{N}_z$ . the LiPON electrolytes have an ionic conductivity of  $10^{-6} \text{ Scm}^{-1}$ . Although, the ionic conductivity of the LiPON material is not competitive with organic liquid electrolytes, the discovery of LiPON materials with enhanced ionic conductivity will solve the stability issue of organic liquid electrolytes, and is an exciting research direction. Meanwhile, the structurally and chemically related Li thiophosphate family of materials have recently received the attention as promising candidates for inorganic solid electrolytes, where ionic conductivity as large as  $10^{-3} \text{ Scm}^{-1}$  have been reported. These materials are characterized by the composition  $\text{Li}_v\text{PS}_w$ . The comparison between the crystalline Li phosphate and the corresponding thiophosphates has provided further insight into solid electrolyte development.

As discussed in chapter 1, the role of computational research is to model the properties of these solid electrolytes at the atomic level, in order to understand and predict the electrochemical stability and the conductivity properties of these solid electrolytes. The most powerful and precise computational methods in modelling the properties of materials are known as first-principles or ab initio methods. These methods use the basic laws of physics, such as quantum mechanics to understand and predict the behaviour of the material.

## 2.6 Summary

In summary, we described the components of batteries and the principle of operation of batteries. We described in detail the set of properties a battery should exhibit to be practical. We discussed the types of batteries, and we explained the advantages of Li-ion batteries. We described in detail the components and principle of operation of Li-ion batteries, we explained the types of electrolytes used within Li-ion batteries, and we explained how solid electrolytes can solve some issues of the inorganic liquid electrolytes. Finally, we explained possible research directions to improve these solid electrolytes and motivated the use of first-principles methods in such a research. In the next chapter, we will explain the details of first-principles methods.

# Chapter 3

## Computational Theory

### Author's Note:

The subject of this chapter has been discussed in detail in many textbooks, I found the book given in Ref. [17] to be very useful, in particular for the discussion of Secs. [3.6, 3.8, 3.10.4, 3.10.7].

### 3.1 Quantum Description of Materials

We know that all materials are made of atoms that are in turn made of electrons and nuclei. In other words, a material is a collection of electrons and nuclei that interact with each other in accordance with Coulomb's law. Classical mechanics fails to describe the behavior of electrons; therefore, only quantum mechanics can give us a correct description of materials. Thus, to understand it, we have to solve a quantum mechanical many-body problem, that is the Schrödinger equation for interacting electrons and nuclei. Although not necessary, but for convenience and simplicity, we shall divide the electrons into valence and core electrons. For example, in sodium, the 3s electron, which is the outermost electron, will be called a valence electron and the remaining will be called core electrons. When a solid is formed, the valence electrons become unbound from atoms and can move in the solid. Since core electrons

do not play much of a role in solid-state properties, we can combine core electrons with their nucleus and call the combined entity an ion. This is called the frozen core approximation. Thus, a condensed matter system can be described as a many-body system of interacting electrons and ions; we are interested in finding a solution of the Schrödinger equation for this system.

## **3.2 Quantum Mechanics**

The best way to describe the behavior of a system of interacting quantum particles, such as those found in materials, is by the laws of quantum mechanics. The quantum mechanical model is based on quantum theory, which says quantum particles also have the shape associated with waves. According to quantum theory, it is impossible to know the exact position and momentum of an electron at the same time. This is known as the uncertainty principle. So, this model is based on probability rather than certainty. Thinking about electrons as probabilistic waves in the quantum mechanical model has major consequences. In order to predict the behavior of the electrons, we should be able to predict the evolution of the wavefunction in space and time. This is a non-trivial problem considering the large number of events varying with space and time. The most reliable equation in quantum mechanics to make such a prediction is known as the Schrödinger equation.

### **3.2.1 The Many-Body Schrödinger Equation**

The Schrödinger equation plays the role of Newton's laws in classical mechanics, it predicts the future behavior of a dynamic system. It is a wave equation in terms of the wavefunction which predicts analytically and precisely probability or outcome. The detailed outcome is not strictly determined, but given a large number of events, the Schrödinger equation will predict the distribution of the results. If we restrict

our discussion to stationary electronic states, then we need to consider the time-independent version of the Schrödinger equation. The time-independent Schrödinger equation takes the following symbolic form:

$$[T + U] \Psi = E\Psi \tag{3.1}$$

Where  $E$  is the energy eigenvalue for the stationary state described by the wave function  $\Psi$ .  $T$  and  $U$  are the kinetic and the potential energies respectively. Similar to classical mechanics, the kinetic and potential energies sum is the Hamiltonian  $H$  which acts upon the wavefunction to generate the evolution of the wavefunction in space, which leads to the well known form of the Schrödinger equation:

$$H\Psi = E\Psi \tag{3.2}$$

The Schrödinger equation together with the normalization conditions give the quantized energies of the system and the form of the wavefunction so that other properties may be calculated. Since we are interested in calculating the properties of materials, we are interested in finding the solution of Eq. (3.2), for the interacting many electrons and nuclei system. When we discuss many electrons and many nuclei together we need to introduce the many-body wavefunction,  $\Psi$ , which depends on the positions of each electron and each nucleus in the system. In the case of  $N$  electrons with coordinates  $\mathbf{r}_1, \mathbf{r}_2, \dots, \mathbf{r}_N$  and  $M$  nuclei with coordinates  $\mathbf{R}_1, \mathbf{R}_2, \dots, \mathbf{R}_M$  we have:

$$\Psi = \Psi(\mathbf{r}_1, \mathbf{r}_2, \dots, \mathbf{r}_N; \mathbf{R}_1, \mathbf{R}_2, \dots, \mathbf{R}_M) \tag{3.3}$$

The many-body wavefunction in Eq. (3.3) is what we need to calculate properties of many electrons and nuclei system. For example, the probability of finding electron number 1 at  $\mathbf{r}$ ,  $P(\mathbf{r}_1=\mathbf{r})$ , while the other electrons can be anywhere, can be calculated from the many-body wavefunction, as follows:

$$P(\mathbf{r}_1 = \mathbf{r}) = \int |\Psi(\mathbf{r}, \mathbf{r}_2, \dots, \mathbf{r}_N; \mathbf{R}_1, \mathbf{R}_2, \mathbf{R}_M)|^2 d\mathbf{r}_2 \dots d\mathbf{r}_N d\mathbf{R}_1 \dots d\mathbf{R}_M \quad (3.4)$$

The electron density  $\rho(\mathbf{r})$  can also be calculated from the many-body wavefunction, as follows:

$$\rho(\mathbf{r}) = N \int |\Psi(\mathbf{r}, \mathbf{r}_2, \dots, \mathbf{r}_N; \mathbf{R}_1, \mathbf{R}_2, \mathbf{R}_M)|^2 d\mathbf{r}_2 \dots d\mathbf{r}_N d\mathbf{R}_1 \dots d\mathbf{R}_M \quad (3.5)$$

Now that the many-body wavefunction has been introduced, we need to define the Hamiltonian in Eq. (3.2). The kinetic energy part of the Hamiltonian, is the sum of the kinetic energies of the electrons and nuclei:

$$T = - \sum_{i=1}^N \frac{\hbar^2}{2m_e} \nabla_i^2 - \sum_{I=1}^M \frac{\hbar^2}{2M_I} \nabla_I^2 \quad (3.6)$$

Where  $m_e$  is the mass of electron and  $M_I$  is the mass of nucleus  $I$ . The potential energy part of the Hamiltonian, is the sum of the Coulomb repulsion between electron pairs and the Coulomb repulsion between nuclei pairs and the Coulomb attraction between electrons and nuclei:

$$U = \frac{1}{2} \sum_{i \neq j} \frac{e^2}{4\pi\epsilon_0} \frac{1}{|\mathbf{r}_i - \mathbf{r}_j|} + \frac{1}{2} \sum_{I \neq J} \frac{e^2}{4\pi\epsilon_0} \frac{Z_I Z_J}{|\mathbf{R}_I - \mathbf{R}_J|} - \sum_{i,I} \frac{e^2}{4\pi\epsilon_0} \frac{Z_I}{|\mathbf{r}_i - \mathbf{R}_I|} \quad (3.7)$$

Here the indices  $I$  and  $J$  run from 1 to  $M$ , while  $i$  and  $j$  from 1 to  $N$ . After defining the wavefunction and the Hamiltonian, we can now write the many-body Schrödinger equation:



$$\begin{aligned}
& \left[ -\sum_i \frac{\hbar^2}{2m_e} \nabla_i^2 - \sum_I \frac{\hbar^2}{2M_I} \nabla_I^2 + \frac{1}{2} \sum_{i \neq j} \frac{e^2}{4\pi\epsilon_0} \frac{1}{|\mathbf{r}_i - \mathbf{r}_j|} \right. \\
& \left. + \frac{1}{2} \sum_{I \neq J} \frac{e^2}{4\pi\epsilon_0} \frac{Z_I Z_J}{|\mathbf{R}_I - \mathbf{R}_J|} - \sum_{i,I} \frac{e^2}{4\pi\epsilon_0} \frac{Z_I}{|\mathbf{r}_i - \mathbf{R}_I|} \right] \psi = E_{\text{tot}} \psi
\end{aligned} \tag{3.8}$$

For simplicity, we will rewrite Eq. (3.8) with atomic units. The definition of atomic units is given in the appendix.

$$\left[ -\sum_i \frac{\nabla_i^2}{2} - \sum_I \frac{\nabla_I^2}{2M_I} - \sum_{i,I} \frac{Z_I}{|\mathbf{r}_i - \mathbf{R}_I|} + \frac{1}{2} \sum_{i \neq j} \frac{1}{|\mathbf{r}_i - \mathbf{r}_j|} + \frac{1}{2} \sum_{I \neq J} \frac{Z_I Z_J}{|\mathbf{R}_I - \mathbf{R}_J|} \right] \Psi = E_{\text{tot}} \Psi \tag{3.9}$$

If we were able to solve Eq. (3.9) and find the eigenstate with the lowest energy, which is called the ground state of the system, then we would be able to calculate many equilibrium properties of materials, from elastic properties to enthalpies of formation, thermal properties, and phase diagrams. The trouble is that the solution of Eq. (3.9) for most systems is very challenging, and in some cases it is practically impossible. Why?

### 3.3 Why Electronic Structure is an Important Difficult Problem?

The electronic structure problem is quite complicated, The most obvious reason is that usually there are many more electrons than nuclei in materials. Nuclei, are massive, so their wavefunctions are strongly localized. Thus, their wavefunctions hardly overlap; they behave much more like classical particles. On the other hand, electronic wavefunctions are widely spread over space. Thus, their wavefunctions strongly overlap. As described in Eq. (3.9), the electronic structure is a quantum mechanical problem.

Now, the electrons interact, via the Coulomb potential, not only with the stationary nuclei but also with each other: each electron repels each other electron via the repulsive Coulomb potential. This makes the electronic structure a many-body problem.

Quantum many-body problems are very difficult to solve, much more difficult than classical ones. The reason is that for  $N$  electrons the many-body wavefunction in Eq. (3.3) is a function of  $3N$  variables where the position vector  $\mathbf{r}_i$  is 3 dimensional vector. Highly accurate numerical representation of such functions is next to impossible for  $N > 1$ . Thus, the electronic structure methods invariably include approximate methods.

### 3.4 First-Principles Methods

As shown in Sec. [3.2.1], quantum mechanical methods, require a solution to the many-body Schrödinger equation. The exact solution of the full many-body Schrödinger equation describing a material is not solvable today, for the reasons mentioned in Sec. [3.3]. Using a series of numerical quantum mechanical approximations without any empirical fitting to experimental data, first-principles methods usually simplify the complicated many-body Schrödinger equation, so that the electronic structure and the total energy of most materials can be calculated quite accurately. Although, all first-principles methods are quantum mechanical, they use different strategies to calculate the electronic structure and the total energy of materials. In the following sections, we will discuss the details of first-principles methods. We will discuss the physics of these approximations, the pros and cons of each approximation, and the accuracy for such approximations in predicting materials properties.

## 3.5 Born-Oppenheimer Approximation

In a solid, we can think of nuclei, having coordinates  $(\mathbf{R}_1, \dots, \mathbf{R}_M)$  as heavy, and therefore modeled as classical particles, which are slowly moving. The electrons are light and they feel the effect of slowly moving nuclei. This known as Born-Oppenheimer approximation [18]. In response to any external parameter the electrons will move very quickly before the nuclei move. In other words, the electrons will adjust their positions for a fixed nuclei positions. Such a treatment, may be used for mathematical simplification of Eq. (3.9), we can rewrite the many-body wavefunction in Eq. (3.3) as multiplication of a wavefunction that depends explicitly on the electrons coordinates and parametrically on the nuclei coordinates  $\psi(\mathbf{r}_1, \dots, \mathbf{r}_N; \mathbf{R}_1, \dots, \mathbf{R}_M)$  multiplied by a wavefunction that depends only on the nuclei coordinates  $\phi(\mathbf{R}_1, \dots, \mathbf{R}_M)$ :

$$\Psi(\mathbf{r}_1, \dots, \mathbf{r}_N; \mathbf{R}_1, \dots, \mathbf{R}_M) = \psi(\mathbf{r}_1, \dots, \mathbf{r}_N; \mathbf{R}_1, \dots, \mathbf{R}_M) \times \phi(\mathbf{R}_1, \dots, \mathbf{R}_M) \quad (3.10)$$

For simplicity we will drop the nuclear coordinate dependence in the electronic portion of the wavefunction, as follows:

$$\psi(\mathbf{r}_1, \dots, \mathbf{r}_N; \mathbf{R}_1, \dots, \mathbf{R}_M) \rightarrow \psi(\mathbf{r}_1, \dots, \mathbf{r}_N) \quad (3.11)$$

Further simplification can be made to Eq. (3.9) by setting  $M_I = \infty$ . This choice implies that we can neglect the kinetic energy of the nuclei because they very heavy, and that the Coulomb repulsion between nuclei is simply a function of the nuclear coordinates only. For convenience we bring this function to the right-hand side of Eq. (3.9) by defining:

$$E = E_{\text{tot}} - \frac{1}{2} \sum_{I \neq J} \frac{Z_I Z_J}{|\mathbf{R}_I - \mathbf{R}_J|} \quad (3.12)$$

This definition allows us to approximate Eq. (3.9) as:

$$\left[ -\sum_i \frac{\nabla_i^2}{2} - \sum_{i,I} \frac{Z_I}{|\mathbf{r}_i - \mathbf{R}_I|} + \frac{1}{2} \sum_{i \neq j} \frac{1}{|\mathbf{r}_i - \mathbf{r}_j|} \right] \psi(\mathbf{r}_1, \dots, \mathbf{r}_N) = E\psi(\mathbf{r}_1, \dots, \mathbf{r}_N) \quad (3.13)$$

It is convenient to regard the nuclear coordinates,  $\mathbf{R}_I$ , as external parameters. This procedure becomes more transparent if we define the Coulomb potential of the nuclei experienced by the electron:

$$v_{\text{ext}}(r) = -\sum_I \frac{Z_I}{|\mathbf{r} - \mathbf{R}_I|} \quad (3.14)$$

Accordingly Eq. (3.13) can be written as:

$$\left[ -\sum_i \frac{\nabla_i^2}{2} + \sum_i v_{\text{ext}}(\mathbf{r}_i) + \frac{1}{2} \sum_{i \neq j} \frac{1}{|\mathbf{r}_i - \mathbf{r}_j|} \right] \psi = E\psi \quad (3.15)$$

This is a fundamental equation in electronic structure theory, in some context it is called the electronic Schrödinger equation. At this point it is clear that this equation looks similar to the single particle Schrödinger equation discussed in quantum mechanics textbooks. The main difference is that we now have several electrons interacting via Coulomb repulsion.

For further discussions and analysis, it is convenient to define the many-electron Hamiltonian and relate it to the single electron Hamiltonian:

$$H(\mathbf{r}_1, \dots, \mathbf{r}_N) = -\sum_i \frac{1}{2} \nabla_i^2 + \sum_i v_{\text{ext}}(\mathbf{r}_i) + \frac{1}{2} \sum_{i \neq j} \frac{1}{|\mathbf{r}_i - \mathbf{r}_j|} \quad (3.16)$$

Where the last term is  $v_{\text{ee}}$ , the electron-electron Coulomb interaction. The single electron Hamiltonian can be written as:

$$H_0(\mathbf{r}) = -\frac{1}{2}\nabla^2 + v_{\text{ext}}(\mathbf{r}) \quad (3.17)$$

So we can write the many-electron Hamiltonian as follows:

$$H(\mathbf{r}_1, \dots, \mathbf{r}_N) = \sum_i H_0(\mathbf{r}_i) + \frac{1}{2} \sum_{i \neq j} \frac{1}{|\mathbf{r}_i - \mathbf{r}_j|} \quad (3.18)$$

## 3.6 Independent Electron Approximation

At this point, it is clear that Eq. (3.15) is very complicated and very hard solve because of the Coulomb interaction between electrons. Researchers have been developing approximation methods since the late 1920s to solve this equation. Let us imagine that we do not have access to any of these theories. What would we do in order to solve this equation?

Similar to many problems in physics, let us consider the simplest case which is not realistic at all, so we can understand what physics we are ignoring, and then we can increase the complexity of this simple case until we reach the most realistic picture. Our first step would be to simplify the problem. We already noted the analogy between Eq. (3.15) and the single electron Schrödinger equation. Let's push this analogy further by imagining that we can ignore the Coulomb interaction between electrons, and therefore we can eliminate the last term on the left hand side of the equation. This dramatic simplification of the problem is called the independent electrons approximation. Accordingly, Eq. (3.15) within the independent electron approximation becomes:

$$\sum_i H_0(\mathbf{r}_i)\psi \approx E\psi \quad (3.19)$$

Where  $H_0$  is the single electron Hamiltonian defined in Eq. (3.17),  $\psi$  is the many-electrons wavefunction. Since electrons are independent, the probability  $|\psi(\mathbf{r}_1, \dots, \mathbf{r}_N)|^2$  of finding electron number 1 at  $\mathbf{r}_1$  and electron number 2 at  $\mathbf{r}_2 \dots$  electron number  $N$  at  $\mathbf{r}_N$  must be given by the product of the individual probabilities of finding the  $i$ -th electron at the position  $\mathbf{r}_i$ . Accordingly the electrons charge density can be approximated in term of the single-electron wave function  $\phi_i(\mathbf{r})$ :

$$\rho(\mathbf{r}) \approx \sum_i |\phi_i(\mathbf{r}_i)|^2 \quad (3.20)$$

Similarly, the many electron wavefunction  $\psi(\mathbf{r}_1, \dots, \mathbf{r}_N)$  can be written as a product of the single-electron wavefunction  $\phi_i(\mathbf{r}_i)$ :

$$\psi(\mathbf{r}_1, \dots, \mathbf{r}_N) \rightarrow \tilde{\psi}(\mathbf{r}_1, \dots, \mathbf{r}_N) = \phi_1(\mathbf{r}_1) \dots \phi_N(\mathbf{r}_N) = \prod_{i=1}^N \phi_i(\mathbf{r}_i) \quad (3.21)$$

Where the wavefunctions,  $\phi_i$ , are obtained as the solution of the single electron Schrödinger equation:

$$H_0(\mathbf{r})\phi_i(\mathbf{r}) \approx \epsilon_i\phi_i(\mathbf{r}) \quad (3.22)$$

Where  $\epsilon_i$  are the energy eigenvalues for the eigenstates  $\phi_i$ . Now, by substituting the many electron wavefunction in Eq. (3.21) in Eq. (3.19), we get:

$$\left[ \sum_i H_0(\mathbf{r}_i) \right] \phi_1(\mathbf{r}_1) \dots \phi_N(\mathbf{r}_N) \approx E\phi_1(\mathbf{r}_1) \dots \phi_N(\mathbf{r}_N) \quad (3.23)$$

Since in this equation the single-electron Hamiltonian,  $H_0(\mathbf{r}_1)$ , acts only on the function  $\phi_1(\mathbf{r}_1)$ , we can rewrite:

$$[H_0(\mathbf{r}_1)]\phi_1(\mathbf{r}_1) \dots \phi_N(\mathbf{r}_N) + \phi_1(\mathbf{r}_1)[H_0(\mathbf{r}_2)]\phi_2(\mathbf{r}_2) \dots \phi_N(\mathbf{r}_N) + \dots \approx E\phi_1(\mathbf{r}_1) \dots \phi_N(\mathbf{r}_N) \quad (3.24)$$

Therefore, using Eq. (3.22), we find:

$$E \approx \epsilon_1 + \epsilon_2 + \dots + \epsilon_N \quad (3.25)$$

This result means that, in the independent electrons approximation, the lowest-energy configuration of the system is obtained when we fill the the lowest-energy eigenstates of the single-electron equation with one electron in each state, starting from the lowest eigenvalue. This beautiful and simple picture drawn in the independent electrons approximation neglects a lot of physics. So, what physics we are ignoring? The independent electrons approximation written in Eq. (3.21) has two important drawbacks. This first relates to the fact the wavefunction,  $\psi$ , should obey Pauli exclusion principle, which requires that the function changes sign whenever we exchange two electrons. The other problem is that the Coulomb term that we neglected is actually of the same magnitude as the other terms, and therefore it cannot be ignored. We will address these two issues in the following sections.

## 3.7 Exclusion Principle

The electronic wavefunctions are functions of  $N$  electronic coordinates  $\psi(\mathbf{r}_1, \dots, \mathbf{r}_N)$ . The Pauli exclusion principle states that this wavefunction must be antisymmetric with respect to interchange of two electrons position or spin :

$$\psi(\mathbf{r}_1, \dots, \mathbf{r}_i, \dots, \mathbf{r}_j, \dots, \mathbf{r}_N) = -\psi(\mathbf{r}_1, \dots, \mathbf{r}_j, \dots, \mathbf{r}_i, \dots, \mathbf{r}_N) \quad (3.26)$$

Where  $\mathbf{r}_i \rightarrow (\mathbf{r}_i, \sigma_i)$ , refer to electron position and spin. This is a condition we should impose while solving any electronic wavefunction. It is obvious that the wave function proposed by the independent electrons approximation in Eq. (3.21) does not satisfy this requirement. In order to develop a way to easily represent antisymmetric functions of all types, let us consider a simple example of two electrons, the wavefunction  $\phi(\mathbf{r}_1)\phi(\mathbf{r}_2)$  does not satisfy this requirement. However, the wavefunction:

$$\psi(\mathbf{r}_1, \mathbf{r}_2) = \frac{1}{\sqrt{2}} [\phi_1(\mathbf{r}_1)\phi_2(\mathbf{r}_2) - \phi_1(\mathbf{r}_2)\phi_2(\mathbf{r}_1)] \quad (3.27)$$

does satisfy the requirement. A general way of writing the wavefunction in Eq. (3.27) is by using the Slater determinant:

$$\psi(\mathbf{r}_1, \mathbf{r}_2) = \frac{1}{\sqrt{2}} \begin{vmatrix} \phi_1(\mathbf{r}_1) & \phi_1(\mathbf{r}_2) \\ \phi_2(\mathbf{r}_1) & \phi_2(\mathbf{r}_2) \end{vmatrix} \quad (3.28)$$

this Slater determinant can be used can be generalized for  $N$  electrons, as follows:

$$\psi(\mathbf{r}_1, \dots, \mathbf{r}_N) = \frac{1}{\sqrt{N!}} \begin{vmatrix} \phi_1(\mathbf{r}_1) & \cdots & \phi_1(\mathbf{r}_N) \\ \vdots & \ddots & \vdots \\ \vdots & \ddots & \vdots \\ \phi_N(\mathbf{r}_1) & \cdots & \phi_N(\mathbf{r}_N) \end{vmatrix} \quad (3.29)$$

The wavefunction in Eq. (3.29), is different from the wavefunction in Eq. (3.21) which represents the simple independent electron approximation. However, the electronic charge density in Eq. (3.20) in the independent electrons approximation, is still valid because electrons are still independent, in the sense that the probability of finding electron  $i$  at point  $\mathbf{r}$  is independent of finding electron  $j$  at point  $\mathbf{r}$ .



## 3.8 Mean-Field Approximation

Now that we have fixed the first drawback of the independent electrons approximation, we have to deal the second drawback, which is the drastic cancellation of the Coulomb interaction between electrons. Thus, the single electron Schrödinger equation in Eq. (3.22) should include the Coulomb interaction with other electrons. Let's but aside quantum mechanics for a moment, and go back to classical electrostatics. From fundamentals of electrostatics, the charge density of electrons, such as the one described in Eq. (3.20) will produce electrostatic potential  $\phi(\mathbf{r})$  through Poisson's equation:

$$\nabla^2\Phi = 4\pi\rho(\mathbf{r}) \quad (3.30)$$

The electrons immersed in this electrostatic potential have, in Hartree units, a potential energy  $v_H(\mathbf{r}) = -\Phi(\mathbf{r})$ , which is called the 'Hartree potential'. By definition also the Hartree potential satisfies Poisson's equation:

$$\nabla^2v_H(\mathbf{r}) = -4\pi\rho(\mathbf{r}) \quad (3.31)$$

The formal solution of this equation for a confined charge density is:

$$v_H(r) = \int d^3r' \frac{\rho(\mathbf{r}')}{|\mathbf{r} - \mathbf{r}'|} \quad (3.32)$$

since each electron experiences the Hartree potential, we can improve Eq. (3.22) by imposing the potential in the equation:

$$\left[ -\frac{\nabla^2}{2} + v_{ext}(\mathbf{r}) + v_H(\mathbf{r}) \right] \phi_i(\mathbf{r}) = \epsilon_i \phi_i(\mathbf{r}) \quad (3.33)$$

where:

$$\rho(\mathbf{r}) = \sum_i |\phi_i(\mathbf{r})|^2 \quad (3.34)$$

and:

$$\nabla^2 v_H(\mathbf{r}) = -4\pi\rho(\mathbf{r}) \quad (3.35)$$

The improvement here over the independent electron approximation, is that we add  $v_H$  which represents the average electrostatic potential experienced by each electron. This approximation is called the mean-field approximation. Eqs. (3.33–3.35) must be solved self consistently.

### 3.9 Hartree-Fock Method

In Sec. [3.5] we introduced the electronic Schrödinger equation, and we explained the difficulties in solving this equation to obtain the ground state energy. In Sec. [3.6] we introduced a very simple way to simplify the complicated electronic Schrödinger equation, by treating electrons as independent particles, and we explained the drawbacks of this simple method. In Sec. [3.7] we fixed the first drawback of independent electrons approximation, by introducing the wavefunction given in Eq. (3.29) which takes into account the antisymmetry with the interchange of two electrons spin and position. we fixed the second drawback of the independent electron approximation, by introducing the  $v_H$  which represents the average electrostatic potential experienced by the single electrons. By adding the  $v_H$  which represents the average electrostatic potential experienced by the single electrons. By adding  $v_H$  we improved the single electron Schrödinger equation in the independent electron approximation to the single electron equation given in Eq. (3.33), which must be solve self consistently with Eq. (3.34) and Eq. (3.35). Hartree-Fock method uses the wavefunction given in Eq.

(3.29) and the mean field approximation, to predict the ground-state energy of the many electron system as follows:

- Starting from the many electron Hamiltonian given Eq. (3.16), which reads:

$$H(\mathbf{r}_1, \dots, \mathbf{r}_N) = - \sum_i \frac{1}{2} \nabla_i^2 + \sum_i v_{\text{ext}}(\mathbf{r}_i) + \frac{1}{2} \sum_{i \neq j} \frac{1}{|\mathbf{r}_i - \mathbf{r}_j|} \quad (3.36)$$

- the total energy of the many electron system is the expectation value of the Hamiltonian in Eq. (3.36)

$$E = \langle \psi | H | \psi \rangle \quad (3.37)$$

- The wave function in Eq. (3.37) should be the wavefunction given in Eq. (3.29), which was imposed by Pauli exclusion principle.
- We minimize the energy E given in Eq. (3.37) with respect to the variations of the functions  $\phi_i(\mathbf{r})$  in the Slater determinant of Eq. (3.29), and require these functions be orthonormal:

$$\frac{\delta E}{\delta \phi_i^*} = 0 \quad (3.38)$$

$$\int d\mathbf{r} \phi_i^*(\mathbf{r}) \phi_j(\mathbf{r}) = \delta_{ij}. \quad (3.39)$$

- Then we obtain the so called Hartree-Fock equations:

$$\left[ -\frac{\nabla^2}{2} + v_{\text{ext}}(\mathbf{r}) + v_H(\mathbf{r}) \right] \phi_i(\mathbf{r}) + \int d\mathbf{r}' v_x(\mathbf{r}, \mathbf{r}') \phi_i(\mathbf{r}'), \quad (3.40)$$

- where:

$$\rho(\mathbf{r}) = \sum_i |\phi_i(\mathbf{r})|^2. \quad (3.41)$$

- and

$$\nabla^2 v_H(\mathbf{r}) = -4\pi\rho(\mathbf{r}) \quad (3.42)$$

- Eqs. (3.40–3.42) must be solved self consistently.

The difference between Eqs. (3.40–3.42) and Eqs. (3.33–3.35) is the additional term,  $v_x(\mathbf{r}, \mathbf{r}')$ , which comes from Pauli exclusion principle:

$$v_x = - \sum_j \frac{\phi_j^*(\mathbf{r})\phi_j(\mathbf{r}')}{|\mathbf{r} - \mathbf{r}'|} \quad (3.43)$$

Where the sum runs over the occupied single-particle states. The  $v_x$  term is called the Fock exchange potential, which represent the exchange interaction between electrons. Although this approximation includes the exchange interaction in  $v_x$ , but it neglects the correlation interaction between electrons. Including the effect of correlation into first-principles simulations, while ensuring that the method is computationally tractable, has led to the development of an entirely different approach.

## 3.10 Ground State Density Functional Theory (DFT)

As discussed in the previous sections, several approaches, such as Hartree-Fock method, have been proposed in order to approximate the ground state energy for the interacting  $N$  electrons system in term of the ground state wavefunction. In general, these methods are not so practical because they neglect the effect of correlation between electrons, and they rely on calculating the ground state wavefunction which is very hard and usually limited to very small systems.

Therefore, one has to develop a more practical technique that uses a more practical quantity than the ground state wavefunction and captures the effect of correlation between electrons. First, Thomas and Fermi (TF) [19,20] introduced the first density functional theory, in which they managed to use the density as a basic variable of the total energy. Based on the uniform electron gas, they completely expressed the total energy of the electrons in terms of the ground state density, as follows:

$$E^{TF}[\rho(\mathbf{r})] = \frac{3}{10}(3\pi^2)^{\frac{2}{3}} \int d\mathbf{r} \rho^{\frac{5}{3}}(\mathbf{r}) + \int d\mathbf{r} \rho(\mathbf{r}) v_{\text{ext}}(\mathbf{r}) + \frac{1}{2} \int \int d\mathbf{r} d\mathbf{r}' \frac{\rho(\mathbf{r})\rho(\mathbf{r}')}{|\mathbf{r} - \mathbf{r}'|} \quad (3.44)$$

where the first term is the Thomas-Fermi kinetic energy  $T^{TF}$  of the non interacting homogeneous electron gas, the second term is the energy due to the electrostatic effect of the external potential  $v_{\text{ext}}$  on electrons, and the last term is the electrostatic electron electron interaction, the Hartree energy  $E_H$ .

Thomas-Fermi model can not be used as it is for real systems because of two main limitations:

- In general, this model does not incorporate the actual orbital structure of electrons.
- The electron-electron interaction is only treated with an electrostatic term and there is no account for exchange or correlation.

For instance, the Thomas-Fermi model manages to use the electron density,  $\rho(\mathbf{r})$ , as the main quantity for calculating the ground state energy of the many electrons system. However, it fails to include the effect exchange and correlation between electrons which makes this model not accurate. Here after, we review the modern DFT introduced by Hohenberg-Kohn with their celebrated theorem.

### 3.10.1 Hohenberg-Kohn Theorem

In 1964, the modern ground state density functional theory or DFT was introduced by Hohenberg and Kohn [21]. DFT derives the ground state energy for a system of  $N$  interacting electrons subject to an external potential,  $v_{\text{ext}}$ , which has the Hamiltonian:

$$H = T + v_{\text{ee}} + v_{\text{ext}} \quad (3.45)$$

the first term is the kinetic energy and second term is the electron-electron interaction and the last term is the external potential acting on the electrons.

For this system of interacting electrons, the Hohenberg-Kohn theorem (HK) states that the electron density depends only on the external potential,  $v_{\text{ext}}$ . In other words, HK theorem states that there is a one-to-one mapping between the electron density and the external potential. This exclusive mapping between the electron density and the external potential has some major consequences:

- Total energy of the many electrons is a functional of electron density only  $\rho(\mathbf{r})$  only.
- According to the variational principle, the total energy functional  $E[\rho(\mathbf{r})]$  has a minimum. The ground state energy  $E_0$ , only if the density is the true ground state density  $\rho_0(\mathbf{r})$ .

According to HK theorem, the total energy functional is defined as:

$$E[\rho] = F[\rho] + \int d\mathbf{r} v_{\text{ext}}(\mathbf{r})\rho(\mathbf{r}). \quad (3.46)$$

$F[\rho]$  is called the universal functional, since its functional form does not depend on the external potential and it depends on the electron density only. For the moment, the exact form of this universal functional is unknown in HK theorem. HK theorem

tells us only about the existence of such a functional, but it does not tell us anything about its form. Accordingly, knowing the exact form of the universal functional,  $F[\rho]$ , is essential for calculating the ground state properties of materials.

Since the total energy of the system is given by the expectation value of the Hamiltonian in Eq. (3.45):

$$E = \langle \psi[\rho] | T + v_{ee} + v_{\text{ext}} | \psi[\rho] \rangle \quad (3.47)$$

by comparing Eq. (3.47) and Eq. (3.46). We can write a general form of the universal function  $F[\rho]$ :

$$F[\rho] = \langle \psi[\rho] | T + v_{ee} | \psi[\rho] \rangle \quad (3.48)$$

Accordingly, we can rewrite Eq. (3.46) as follows:

$$E[\rho] = \int d\mathbf{r} v_{\text{ext}}(\mathbf{r})\rho(\mathbf{r}) + \langle \psi[\rho] | T + v_{ee} | \psi[\rho] \rangle \quad (3.49)$$

### 3.10.2 Kohn-Sham Method

The HK theorem tells us that the total energy of many electrons is a functional of the electron density. However, it does not tell us how to construct such a functional. In Eq. (3.49), we see that the first term is already explicitly dependent on the electron density,  $\rho(\mathbf{r})$ ; however, there are two extra terms for which the dependence on the density is only implicit. The idea of Kohn and Sham [22] was to split these implicit terms into the kinetic and Coulomb energy of independent electrons, plus an extra term which accounts for the difference:

$$E = \int d\mathbf{r} \rho(\mathbf{r}) v_{\text{ext}}(\mathbf{r}) - \sum_i \int d\mathbf{r} \phi_i^*(\mathbf{r}) \frac{\nabla^2}{2} \phi_i(\mathbf{r}) + \frac{1}{2} \int \int d\mathbf{r} d\mathbf{r}' \frac{\rho(\mathbf{r}) \rho(\mathbf{r}')}{|\mathbf{r} - \mathbf{r}'|} + E_{\text{xc}}[\rho] \quad (3.50)$$

The third term is the Hartree energy,  $E_H$ . The extra term,  $E_{\text{xc}}$ , contains every thing that is left out and is called the exchange and correlation energy. Eq. (3.50) simply breaks down the unknown functional of the density,  $F[\rho]$ , into sum of known contributions taken from the independent electrons approximation, and an unknown contribution, the exchange and correlation energy. If we knew the exchange and correlation energy,  $E_{\text{xc}}[\rho]$ , then we could calculate the total energy of the system. The remaining question is how to determine the electron density.

It turns out that the ground state density,  $\rho_0$ , is precisely the function that minimizes the total energy in Eq. (3.50). Minimizing the total energy with respect to the density indeed corresponds to solving an effective Hamiltonian eigenvalue problem, the so-called KS equation:

$$H_{KS} \phi_i(\mathbf{r}) = \left[ -\frac{1}{2} \nabla^2 + v_{KS}(\mathbf{r}) \right] \phi_i(\mathbf{r}) = \epsilon_i^{KS} \phi_i(\mathbf{r}), \quad (3.51)$$

Where  $\phi_i(\mathbf{r})$  are the single particle orbitals obtained from the diagonalization of  $H_{KS}$ , and  $v_{KS}$  is the functional derivative of the first term and the last two terms in the total energy equation:

$$v_{KS}(\mathbf{r}) = v_{\text{ext}}(\mathbf{r}) + v_H[\rho](\mathbf{r}) + v_{\text{xc}}[\rho](\mathbf{r}) \quad (3.52)$$

and the exchange-correlation potential reads

$$v_{\text{xc}}[\rho](\mathbf{r}) = \frac{\delta E_{\text{xc}}(\mathbf{r})}{\delta \rho(\mathbf{r})}. \quad (3.53)$$



In order to find the ground-state density  $\rho_0(\mathbf{r})$ , Eq. (3.51) needs to be solved self-consistently with the electron density:

$$\rho(\mathbf{r}) = \sum_i^N |\phi_i(\mathbf{r})|^2 \quad (3.54)$$

In practice, from the solution of the Kohn-Sham equation, we can evaluate the energy via the eigenvalues as:

$$E[\rho(\mathbf{r})] = \sum_i^N \epsilon_i - E_H[\rho(\mathbf{r})] - \int d\mathbf{r} v_{xc}(\mathbf{r})\rho(\mathbf{r}) + E_{xc}[\rho(\mathbf{r})] \quad (3.55)$$

So far the only unknown part in the last equation is  $E_{xc}[\rho(\mathbf{r})]$ . So that the total energy of the  $N$  electron system can be evaluated. Although, the unknown term,  $E_{xc}$ , can not be determined exactly, there are two well known and efficient approximations to approximate this term; the local density approximation (LDA) and the generalized gradient approximation (GGA). In the next section, we will explain these approximations in detail.

### 3.10.3 The Local Density Approximation & The Generalized Gradient Approximation

The local density approximation or LDA [23] is the simplest and the most popular approximation for calculating exchange and correlation energy function. The LDA approximation deals with homogeneous system by assuming that the electron density varies very slowly in space. Accordingly, in this approximation the exchange and correlation energy is approximated by the exchange and correlation energy of the homogeneous electron gas (HEG) in each point in space. This leads to approximate the exchange correlation energy function as:

$$E_{xc}^{LDA}[\rho] = \int d\mathbf{r} \rho(\mathbf{r}) \epsilon_{xc}^{heg}[\rho(\mathbf{r})] \quad (3.56)$$

where  $\epsilon_{xc}^{heg}[\rho(\mathbf{r})]$  is the exchange-correlation energy per electron of a electron gas of density  $\rho(\mathbf{r})$

Generally, the LDA works the best with homogeneous systems because it was derived on this basis, and it leads to a reasonable results even with inhomogeneous systems where density fluctuates noticeably. Accordingly, LDA can be regarded as an accurate approximation, whereas it gives reasonable molecular structures. However, LDA has the drawback of overestimating the binding energy, which can lead to underestimating atomic distances. Thus, the lattice parameters of solids are generally underestimated [24] within the LDA.

The Generalized Gradient Approximation or GGA tries to improve the LDA by dealing with inhomogeneous systems where density fluctuates noticeably, by introducing the exchange and correlation terms which further depends on the density gradient  $\nabla\rho$ . Accordingly, in the GGA the exchange and correlation energy term,  $E_{xc}$ , is a function of the electron density and its gradient as follows [25]:

$$E_{xc}[\rho] = \int d\mathbf{r} \rho(\mathbf{r}) f_{xc}[\rho(\mathbf{r}), \nabla\rho(\mathbf{r})] \quad (3.57)$$

where  $f_{xc}[\rho(\mathbf{r}), \nabla\rho(\mathbf{r})]$  is a function of the local density and the local density gradient. In general, the GGA improves the LDA results concerning the binding energies of molecules. However, the GGA has the drawback of overestimating lattice constants of solids [26,27]. Also, the LDA generally better represents the vibrational frequencies of atoms in solids [28,29] than GGA.

As discussed above, each of the LDA and GGA has its pros and cons in modeling materials properties. Accordingly, deciding which of these approximations best represent the exchange and correlation energy depend mainly on the properties of interest

for the simulation.

### 3.10.4 Self-Consistent Calculations

Now, we have introduced the basic concept of density functional theory in Sec. [3.10.1], and in Sec. [3.10.2] we have introduced Kohn-Sham method to determine the form of the DFT functional, Eq. (3.51) and Eq. (3.55) determine the total energy of the system using Kohn-Sham formalism. In Sec. [3.10.3], we introduced the methods to approximate the  $E_{xc}$  term of the DFT functional. The question that remains to be answered now is: how do we actually solve Kohn-Sham equation. To answer such a question, it is convenient to rewrite Kohn-Sham equation and each term appearing in it:

$$H_{KS}\phi_i(\mathbf{r}) = \left[ -\frac{1}{2}\nabla^2 + v_{KS}(\mathbf{r}) \right] \phi_i(\mathbf{r}) = \epsilon_i^{KS} \phi_i(\mathbf{r}), \quad (3.58)$$

$$v_{KS}(\mathbf{r}) = v_{\text{ext}}(\mathbf{r}) + v_H[\rho](\mathbf{r}) + v_{xc}[\rho](\mathbf{r}) \quad (3.59)$$

$$v_{\text{ext}}(r) = - \sum_I \frac{Z_I}{|\mathbf{r} - \mathbf{R}_I|} \quad (3.60)$$

$$\nabla^2 v_H(\mathbf{r}) = -4\pi\rho(\mathbf{r}) \quad (3.61)$$

$$v_{xc}[\rho](\mathbf{r}) = \frac{\delta E_{xc}(\mathbf{r})}{\delta \rho(\mathbf{r})} \quad (3.62)$$

$$\rho(\mathbf{r}) = \sum_i^N |\phi_i(\mathbf{r})|^2 \quad (3.63)$$

It is obvious that Eq. (3.58) looks similar to the single electron Schrödinger equation, and can be solved as a standard eigenvalue problem. However, in order to determine the eigenfunctions,  $\phi_i(\mathbf{r})$ , and the eigenvalues,  $\epsilon_i$ , we need to determine the Kohn-Sham potential  $v_{KS}(\mathbf{r}) = v_{\text{ext}}(\mathbf{r}) + v_H[\rho](\mathbf{r}) + v_{\text{xc}}[\rho](\mathbf{r})$ . The complication here is the  $v_H$  and  $v_{\text{xc}}$  depends on the density,  $\rho(\mathbf{r})$ , through Eq. (3.61) and Eq. (3.62), and the density depends on the unknown eigenfunction,  $\phi_i(\mathbf{r})$ , through Eq. (3.63). In other words, each solution  $\phi_i$  depends implicitly on all other solutions,  $\phi_j$ , describing the occupied electronic states. The fact that all solutions  $\phi_i$  are linked with each other in Eqs. (3.58–3.63) implies that they must be determined self-consistently. ‘Self-consistency’ means that, if we inserted the solutions  $\phi_i$  inside Eq. (3.63) to calculate the density, determine the corresponding Kohn-Sham  $v_{KS}$  using Eq. (3.59), and solve the Schrödinger equation [Eq. (3.58)] again, then we find as a solution the same function  $\phi_i$  from which we started.

The practical procedure for solving Kohn-Sham equation, Eqs. (3.58–3.63), is the following:

- We start by specifying the nuclear coordinates, in such a way that we can calculate the nuclear potential,  $v_{\text{ext}}$ , from Eq. (3.60). Typically this information is available from crystallography data.
- We guess a possible electron density,  $\rho(\mathbf{r})$ , in order to determine a preliminary approximation to the Hartree and exchange and correlation potentials using Eq. (3.61) and Eq. (3.62) respectively. A simple but very useful approximation is to construct the first guess for the electron density by adding up the densities corresponding to completely isolated atoms, but arranged in the atomic positions corresponding to the material under consideration.
- Using the density we obtain the initial estimates of the Hartree and the exchange

and correlation potentials,  $v_H + v_{xc}$ .

- We calculate the Kohn-Sham potential using Eq. (3.59).
- We obtain a numerical solution for the the Schrödinger equation, Eq. (3.58), to calculate the eigenvalues,  $\epsilon_i$ , and the eigenfunctions,  $\phi_i$ . This can be done by discretizing the space into a mesh of points and representing the Laplace operator using finite difference formulas.
- Using the wavefunction obtained in the previous step, we calculate the new density using Eq. (3.63).
- We repeat the previous steps until we achieve self-consistency.

Now that we have determined the steps for solving Kohn-Sham equations, the next question is: how can we improve these steps in order to obtain accurate and computationally efficient numerical solution? For the computational efficiency, the first concern is the shape of the nuclei potential  $v_{\text{ext}}$  in Eq. (3.60). The nuclei potential  $v_{\text{ext}}$  in Eq. (3.60), has an infinite value near the nucleus as  $r \rightarrow 0$ , accordingly obtaining accurate numerical solution for Kohn-Sham equations in the presence of this potential is difficult and computationally expensive. Approximate methods should be used to replace the nuclei potential near the nuclei (core region) while maintaining the numerical accuracy for solving Kohn-Sham equations.

### 3.10.5 Pseudopotentials

In order to solve Kohn-Sham equations [3.58 - 3.63] efficiently, we need a systematic method to replace the nuclear potential  $v_{\text{ext}}$  in the core region of the atom, by a computationally more effective potential. In solids it is reasonable to separate the electron density described in Eq. (3.63) into core and valence part, as follows:

$$\rho(\mathbf{r}) = \rho_{\text{core}}(\mathbf{r}) + \rho_{\text{valence}}(\mathbf{r}) \quad (3.64)$$

where,  $\rho_{\text{core}}(\mathbf{r})$  is the electron density for core electrons,  $\rho_{\text{valence}}(\mathbf{r})$  is the electron density for valence electrons. For the core electrons is largely unaffected by the valence states. Accordingly we can treat core electrons as fixed and develop a smoother (computationally more effective) nuclei potential in the core region, while maintaining the shape of the nuclei potential  $v_{\text{ext}}$  in the valence region. This approach is known as the 'pseudopotential method' [30]. This procedure is illustrated in Fig. [3.1].

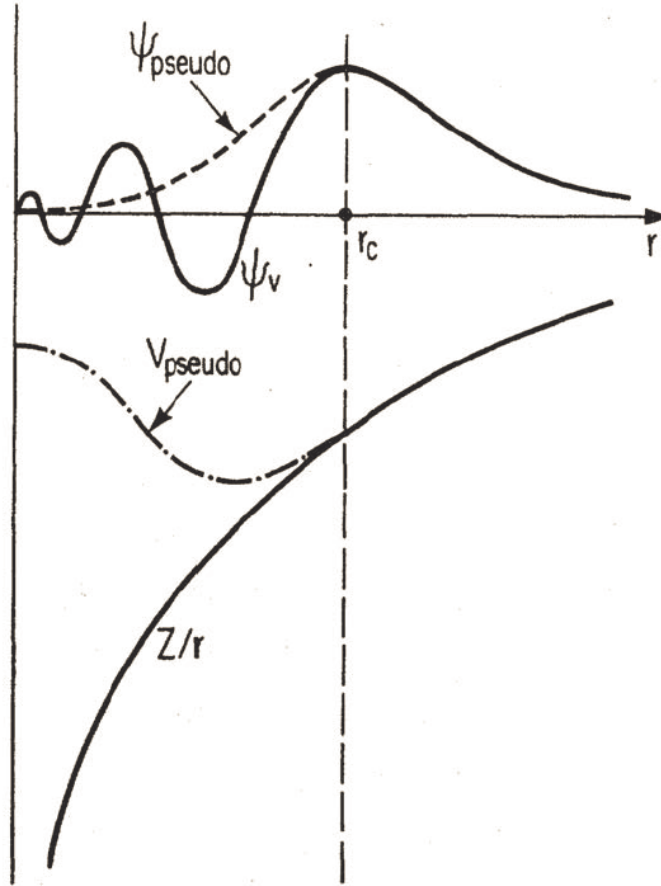


Figure 3.1: Schematic illustration of all electron (solid lines) and pseudoelectron (dashed lines) and their corresponding wave functions .  $r_c$  is the cutoff radius beyond which the wavefunction and the potential are not effected. Adapted from Ref. [31] with permission from the American Physical Society.

As shown in Fig. [3.1], the nuclear potential  $v_{\text{ext}}$  is replaced by a smoother potential (pseudopotential)  $v_{\text{pseudo}}$  in the core region ( $r < r_c$ ), which has a finite value near the origin ( $r \rightarrow 0$ ). Also, the all-electron (AE) wavefunction in Kohn-Sham equations [3.58 - 3.63] which oscillate very rapidly in the core region ( $r < r_c$ ) is replaced by a smoother wavefunction, the pseudo-wavefunction  $\psi_{\text{pseudo}}$ . Such a replacement will reduce the number of plane waves needed to obtain a numerical solution for Kohn-Sham equations and thus will reduce the computational cost for solving these equations.

### 3.10.6 The Projector Augmented Wave (PAW) Method

As shown in Sec. [3.10.5], the pseudopotential method reduces the computational cost for solving Kohn-Sham equations (3.58 - 3.63), by replacing the nuclear potential by smoother potential,  $v_{\text{pseudo}}$ , and the AE wavefunction by smoother wavefunction,  $\psi_{\text{pseudo}}$ , in the core region of the atom. Although, this method is very simple and computationally very efficient but the drawback here, is that in some cases the shape of the wavefunction in the core region ( $r < r_c$ ) near the atomic site carries a lot of physics and therefore cannot be fully replaced. Thus, a more accurate treatment should be able to capture some of the properties of the AE wavefunction in the core region ( $r < r_c$ ), to capture the lost physics of the pseudopotential method. The PAW method [32] tries to correct the shape of the PS wavefunction, so it captures some of the properties of the AE wavefunction at the atomic site. Generally, the strategy of the PAW method is as follows:

- We will use the Dirac notation for the wavefunctions,  $|\psi\rangle$  is the AE wavefunction,  $|\tilde{\psi}\rangle$  is the PS wavefunction.
- We divide the Hilbert space  $\Omega$  into Augmented region  $\Omega_R$  ( $r < r_c$ ) surrounding the atomic sites and interstitial region ( $r > r_c$ ).
- We need to find a transformation  $\tau$ , which transform the PS wavefunction into

the AE wavefunction in the augmentation region  $\Omega_R$ . As follows:

$$|\psi\rangle = \tau|\tilde{\psi}\rangle \quad \Omega \in \Omega_R \quad (3.65)$$

- Since we need the transformation operator  $\tau$  to keep the PS wavefunction the same outside the augmentation region and probe it in the augmentation region. Thus, we need  $\tau$  to be linear and it should be unitary outside the augmentation region and have a localized term ( $S_R$ ) in the augmentation region. As follows:

$$\tau = 1 + \sum_R S_R \quad (3.66)$$

- In the augmentation region  $\Omega_R$ , we expand the PS wavefunction  $|\tilde{\psi}\rangle$  in term of a complete set of basis functions  $\{\tilde{\phi}_i\}$ , where  $\{\tilde{\phi}_i\}$  are called PS partial waves. As follows:

$$|\tilde{\psi}\rangle = \sum_i c_i |\tilde{\phi}_i\rangle \quad \Omega \in \Omega_R \quad (3.67)$$

- In the augmentation region  $\Omega_R$ , we expand the AE wavefunction  $|\psi\rangle$  in term of a complete set of basis functions  $\{\phi_i\}$ , where  $\{\phi_i\}$  are called AE partial waves. As follows:

$$|\psi\rangle = \sum_i c_i |\phi_i\rangle \quad \Omega \in \Omega_R \quad (3.68)$$

- When we act by the transformation operator in Eq. (3.66) on the PS partial waves, we should get the AE partial waves:

$$|\phi_i\rangle = (1 + S_R)|\tilde{\phi}_i\rangle \quad (3.69)$$



- Accordingly, we can write the local function  $S_R$  in term of the AE partial waves and the PS partial waves

$$S_R|\tilde{\phi}_i\rangle = |\phi_i\rangle - |\tilde{\phi}_i\rangle = \sum_j (|\phi_i\rangle - |\tilde{\phi}_i\rangle)\delta_{ij} \quad (3.70)$$

- By substituting Eq. (3.70) in Eq. (3.66), we can write the transformation operator  $\tau$  in term of AE and PS partial waves:

$$\tau = 1 + \sum_j (|\phi_i\rangle - |\tilde{\phi}_i\rangle)\delta_{ij} \quad (3.71)$$

- We define a complete set of projector functions  $\{\tilde{p}_j\}$  orthonormal to the PS partial waves and localized in augmentation region, as follows:

$$\langle \tilde{p}_j | \tilde{\phi}_i \rangle = \delta_{ij} \quad (3.72)$$

- By substituting Eq. (3.72) in Eq. (3.71), we can write the transformation operator in term AE and PS partial waves and the projector functions:

$$\tau = 1 + \sum_j (|\phi_j\rangle - |\tilde{\phi}_j\rangle)\langle \tilde{p}_j | \tilde{\phi}_j \rangle \quad (3.73)$$

- Now since we know the form of the transformation operator  $\tau$ , we act on the PS wavefunction in Eq. (3.65) to correct its shape in the augmentation region:

$$|\psi\rangle = |\tilde{\psi}\rangle + \sum_j (|\phi_j\rangle - |\tilde{\phi}_j\rangle)\langle \tilde{p}_j | \tilde{\psi}\rangle \quad (3.74)$$

- Accordingly, the wave function within the PAW formalism can be written as follows:

$$|\psi\rangle = |\tilde{\psi}\rangle + |\psi^1\rangle - |\tilde{\psi}^1\rangle \quad (3.75)$$

$$|\tilde{\psi}^1\rangle = \sum_j |\tilde{\phi}_j\rangle \langle \tilde{p}_j | \tilde{\psi}\rangle \quad (3.76)$$

$$|\psi^1\rangle = \sum_j |\phi_j\rangle \langle \tilde{p}_j | \tilde{\psi}\rangle \quad (3.77)$$

- The wavefunction in Eq. (3.75), is the sum of the PS wavefunction  $|\tilde{\psi}\rangle$  plus an onsite correction  $|\psi^1\rangle$  minus onsite error  $|\tilde{\psi}^1\rangle$ , as shown in Fig. [3.2]. In other words, the PAW method replace the wrong character by the right character in the augmentation region of the atom.
- The only thing left, is the generation of the PS partial waves  $\{\tilde{\phi}_i\}$  and the projector functions  $\{\tilde{p}_j\}$ , there are two schemes to generate the PS partial waves and the projector functions. The Vanderbilt [33] and Bloch [32] schemes. In this context we will explain the Vanderbilt scheme only.
- **The Vanderbilt method:** In this scheme, the shape of PS partial waves  $\{\tilde{\phi}_i\}$  are directly controlled, while the projector functions  $\{\tilde{p}_j\}$  are derived. Each PS partial wave is chosen to have the form:

$$\tilde{\phi}_{n_i l_i}(r) = \begin{cases} r^{l_i+1} \sum_{m=0}^4 C_m r^{2m} & r < r_i \\ \phi_{n_i l_i}(r) & r \geq r_i \end{cases} \quad (3.78)$$

- The matching radii  $r_i \leq r_c$  are used to control the shapes. The 5 coefficients  $C_m$  are chosen so that  $\tilde{\phi}_{n_i l_i}(r) = \phi_{n_i l_i}(r)$  at 5 points in the neighborhood of  $r_i$  which is roughly equivalent to ensuring that the function and its first 4 derivatives match at  $r_i$ . For each PS partial wave, we can form a localized auxiliary function

$$\chi_{n_i l_i}(r) = \left[ \epsilon_i + \frac{1}{2} \left( \frac{d^2}{dr^2} - \frac{l_i(l_i + 1)}{r^2} \right) - v_{pseudo}(r) \right] \tilde{\phi}_{n_i l_i}(r) \quad (3.79)$$

- Which, by design vanishes for  $r > r_c$ . The projector functions are then formed from a linear combination of these auxiliary functions of the same angular momentum:

$$\tilde{p}_{n_i l_i}(r) = \sum_{n_j} \chi_{n_j l_i} (B^{-1})_{n_j n_i} \quad (3.80)$$

$$B_{n_i n_j} = \int_0^{r_c} dr \tilde{\phi}_{n_i l_i}(r) \chi_{n_j l_i}(r) \quad (3.81)$$

- This construction ensures the orthonormality between the PS partial waves and the projector functions given in Eq. (3.72).
- After we generate the PS partial waves and the projector functions using Vanderbilt or Blochl schemes, we use these functions in Eq. (3.74) to correct the shape of the PS wavefunction in the augmentation region.

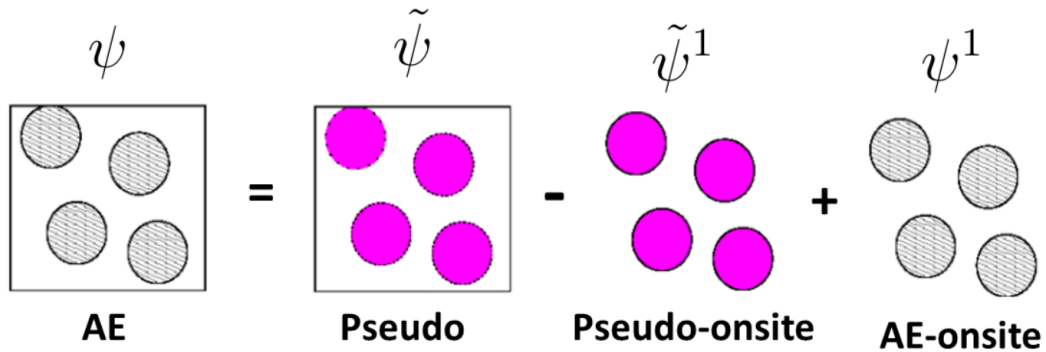


Figure 3.2: Schematic illustration of the PAW method. The outline represents a region in the crystal, while the filled spheres represent the augmentation spheres around each atom, shaded pink and gray for the PS and AE basis functions, respectively.

### 3.10.7 Reasons Behind the Popularity of Density Functional Theory

- **Transferability:** The first advantage of using density functional theory modelling is its transferability. Over the years, density functional theory has become a truly universal method. This means that we do not need to use or develop different techniques for each physical problem or for different classes of materials. On the contrary, the same technique can be used to describe a wide class of physical problems and materials. The transferability of density functional theory allows for the fast development of techniques that use this method, where a wide class of scientists uses and develops the same technique. Also, the transferability of DFT saves us a substantial time and effort in comparison to methods such as classical force field methods, where a new model is required for each new class of materials considered.
- **Simplicity:** Density functional theory can be regarded as a very simple method, in comparison to other modelling methods and techniques. The reason behind this simplicity is that DFT relies on the solution of Kohn-Sham equations [3.58 - 3.63] which describes electrons as independent particles. Accordingly, we have to solve the Schrödinger equation for a single electron, such a treatment is far more simple than dealing with a complicated many-body problem, where one has to take into account the physical forces between particles and develop different schemes to describe each system.
- **Reliability:** Although density functional theory can be regarded as very simple, it is very accurate in calculating material properties. Density functional theory has been tested thousands of times in comparison with experiment, and it was shown that it yields results in a very good agreement with experimental results within a few percent. Accordingly, DFT can be regarded as the most accurate

method in calculating materials properties. Because of its accuracy and reliability, nowadays DFT is being used to predict materials properties before even carrying on the experiment.

- Software sharing: Because of its transferability, simplicity and reliability, density functional theory has become very popular among the scientific community, DFT has been implemented in a very well known codes such as Quantum Espresso [34] and Abinit [35], and many softwares are being developed, such as XCrySDen [36] to work in parallel with these codes. Because of its popularity, DFT is being tested and developed by global community.

### 3.11 Summary

In summary, we have presented a detailed description of the quantum mechanics of materials. We have explained the difficulties in solving Schrödinger equation for materials. We have explained several first-principles approximations to simplify the complicated many-body Schrödinger equation. We have introduced Hartree-Fock method for calculating the ground state energy for the many electrons system and we explained the drawbacks of this method. Finally, we have introduced and explained the static Density Functional Theory and we explained the approximation we use within this theory, and we have explained the importance of DFT in predicting materials properties and the popularity of DFT among the scientific community. In the next chapter, we will explain how we use DFT to calculate properties of solid electrolyte materials.

# Chapter 4

## Materials Modeling using Density Functional Theory

The purpose of this chapter is to explain how we use first-principles (ab initio) methods to understand solid electrolytes materials properties. In particular, I will focus on explaining the most important properties like the crystal structures, kinetic properties and the interfaces properties.

### 4.1 Crystal Structures

The crystal structure is a description of the ordered arrangement of atoms in crystalline materials. Ordered structures occur as a result of the symmetry arrangement of the atoms along the three dimensional axes in space.

The unit cell of the crystal is defined as the smallest arrangement of atoms that exhibit the symmetry of the crystal, and which constitutes the crystal by consecutive symmetry operations. In general, there are seven shapes of the unit cell of materials; cubic, hexagonal, tetragonal, orthorhombic, rhombohedral, monoclinic and triclinic. These shapes are the possible building blocks for any crystal structure.

The concept of space groups is a mathematical description of all the symmetry properties in the unit cell. All the properties of the atoms in the unit cell can be described by 230 space groups. These space groups are the results of a combination of translational symmetry of the unit cell and point symmetry operations, like reflection and rotation.

Understanding the crystal structure and the symmetry is essential for understanding many physical properties of the material, like electronic band structures, thermodynamics properties and kinetic properties.

Accordingly, predicting the crystal structure using first-principles methods is the first step in modelling materials properties.

## 4.2 Predicting Crystal Structure Using Density Functional Theory

From a theoretical prospective, the crystal structure of a material refers to the most stable structure or the equilibrium structure. The equilibrium structure is defined as the configuration of atoms at which the total force acting on the nucleus of each atom vanishes. Accordingly, to predict the crystal structure of materials, we should:

- Calculate the total forces acting on the nucleus of each atom using DFT.
- Find the nuclear coordinates of atoms for which the total forces vanish.

In the following sections, I will explain these points in detail.

### 4.2.1 Calculating Forces Using DFT

In this section, I will explain how we use DFT to calculate forces on the atom nuclei. In order to do so, it is necessary to review the Born-Oppenheimer approximation which was discussed in Sec. [3.5]. In Sec. [3.5], we showed that within the Born-Oppenheimer approximation the total wavefunction,  $\Psi$ , can be written as a multiplication of a wavefunction that depends explicitly on the electrons coordinates and parametrically on the nuclei coordinates  $\psi(\mathbf{r}_1, \dots, \mathbf{r}_N; \mathbf{R}_1, \dots, \mathbf{R}_M)$  multiplied by a wavefunction that depends only on the nuclei coordinates  $\phi(\mathbf{R}_1, \dots, \mathbf{R}_M)$ :

$$\Psi(\mathbf{r}_1, \dots, \mathbf{r}_N; \mathbf{R}_1, \dots, \mathbf{R}_M) = \psi(\mathbf{r}_1, \dots, \mathbf{r}_N; \mathbf{R}_1, \dots, \mathbf{R}_M) \times \phi(\mathbf{R}_1, \dots, \mathbf{R}_M) \quad (4.1)$$

After that, we neglected the total energy of nuclei because they are very heavy particles and we defined the total energy within Born-Oppenheimer approximation in Eq. [3.12], as follows:

$$E = E_{tot} - \frac{1}{2} \sum_{I \neq J} \frac{Z_I Z_J}{|\mathbf{R}_I - \mathbf{R}_J|} \quad (4.2)$$

For clarity, the energy defined in Eq. (4.2) is a function of the nuclear coordinates. Accordingly, we will show this dependence explicitly, by writing  $E \rightarrow E(\mathbf{R}_1, \dots, \mathbf{R}_M)$ . After that, we defined the Coulomb potential of the nuclei experienced by the electron,  $v_{\text{ext}}(r)$ , in Eq. (3.14). Using these approximations, we reduced the complicated many-body Schrödinger equation described in Eq. (3.9) into the electronic Schrödinger equation, described in Eq. (3.15), which reads:

$$\left[ - \sum_i \frac{\nabla_i^2}{2} + \sum_i v_{\text{ext}}(\mathbf{r}_i) + \frac{1}{2} \sum_{i \neq j} \frac{1}{|\mathbf{r}_i - \mathbf{r}_j|} \right] \psi = E(\mathbf{R}_1, \dots, \mathbf{R}_M) \psi \quad (4.3)$$



By substituting Eq. (4.3) and Eq. (4.1) in the many-body Schrödinger equation described in Eq. (3.9), we get:

$$E\psi\phi + \left[ -\sum_I \frac{\nabla_I^2}{2M_I} + \frac{1}{2} \sum_{I \neq J} \frac{Z_I Z_J}{|\mathbf{R}_I - \mathbf{R}_J|} \right] \psi\phi = E_{\text{tot}}\psi\phi \quad (4.4)$$

Now, by multiplying both sides by  $\psi^*$  and integrating over the electronic variables, we obtain:

$$\left[ -\sum_I \frac{\nabla_I^2}{2M_I} + \frac{1}{2} \sum_{I \neq J} \frac{Z_I Z_J}{|\mathbf{R}_I - \mathbf{R}_J|} + E(\mathbf{R}_1, \dots, \mathbf{R}_M) \right] \phi(\mathbf{R}_1, \dots, \mathbf{R}_M) = E_{\text{tot}}\phi(\mathbf{R}_1, \dots, \mathbf{R}_M) \quad (4.5)$$

Eq. (4.5) is the many-body Schrödinger equation for nuclei alone. The effect of electrons on nuclei is contained in the electronic energy,  $E(\mathbf{R}_1, \dots, \mathbf{R}_M)$ , which acts as an effective potential for a fixed nuclear position. For further discussion and analysis it is convenient to define the nuclear Hamiltonian used in Eq. (4.5):

$$H_R = -\sum_I \frac{\nabla_I^2}{2M_I} + U(\mathbf{R}_1, \dots, \mathbf{R}_M) \quad (4.6)$$

$U(\mathbf{R}_1, \dots, \mathbf{R}_M)$  is the effective potential experienced by the nuclei, which is the sum of the Coulomb interaction between nuclei and the electronic energy at a fixed nuclear position.

$$U(\mathbf{R}_1, \dots, \mathbf{R}_M) = \frac{1}{2} \sum_{I \neq J} \frac{Z_I Z_J}{|\mathbf{R}_I - \mathbf{R}_J|} + E(\mathbf{R}_1, \dots, \mathbf{R}_M) \quad (4.7)$$

The effective potential in Eq. (4.7) is all we need to calculate the total force acting on the nuclei. This effective potential  $U(\mathbf{R}_1, \dots, \mathbf{R}_M)$  is a function with  $3M$  dimensions, due to the  $3M$  degrees of freedom of the nuclei, and can be regarded as a potential energy surface.

Let's put aside quantum mechanics and move to classical description, which tells us that the total force acting on the nucleus is the derivative of effective potential in Eq. (4.7) with respect to the nuclear position.

$$F_I = -\frac{\partial U(\mathbf{R}_1, \dots, \mathbf{R}_M)}{\partial \mathbf{R}_I} \quad (4.8)$$

This is a very important equation, and it shows explicitly the link between the equilibrium structure of the material and the the total force acting on the nucleus. The most stable structure is defined by the nuclei coordinates  $(\mathbf{R}_1, \dots, \mathbf{R}_M)$ , where the nuclei have zero acceleration and the total forces vanish.

At this point, it is clear that the only thing left to calculate the total forces acting on the nuclei as an explicit function of the nuclear coordinates is to calculate the right hand side of Eq. (4.8), which is the partial derivative of the potential energy surface  $U(\mathbf{R}_1, \dots, \mathbf{R}_M)$  with respect to the nuclear positions.

$$\frac{\partial U(\mathbf{R}_1, \dots, \mathbf{R}_M)}{\partial \mathbf{R}_I} = \frac{1}{2} \frac{\partial}{\partial \mathbf{R}_I} \frac{Z_I Z_J}{|\mathbf{R}_I - \mathbf{R}_J|} + \frac{\partial}{\partial \mathbf{R}_I} E(\mathbf{R}_1, \dots, \mathbf{R}_M) \quad (4.9)$$

The evaluation of the first term in Eq. (4.9) is straightforward. The evaluation of the second term for each nuclear configuration can be very time-consuming.

This drawback of calculating forces can be fixed by the Hellmann-Feynman theorem. The Hellmann-Feynman theorem [37] states that: a non-degenerate eigenvalue of a hermitian operator in a parameter dependent eigensystem varies with respect to the parameter according to the formula:

$$\frac{\partial E}{\partial \nu} = \langle \psi | \frac{\partial H}{\partial \nu} | \psi \rangle = \int d\mathbf{r} \psi^* \frac{\partial H}{\partial \nu} \psi \quad (4.10)$$

provided that the associated normalized eigenfunction,  $\psi$ , is continuous with respect

to the parameter,  $\nu$ . The only assumption behind Eq. (4.10) is the,  $\psi$ , is an eigenstate of  $H$ . Accordingly, Eq. (4.10) is very general and does not depend on the system under consideration. By substituting the eigenvalue  $E$  by the electronic energy  $E \rightarrow E(\mathbf{R}_1, \dots, \mathbf{R}_M)$  and the parameter  $\nu$  by the nuclear coordinates  $\mathbf{R}_I$ , we get:

$$\frac{\partial E(\mathbf{R}_1, \dots, \mathbf{R}_M)}{\partial \mathbf{R}_I} = \int d\mathbf{r} \psi^* \frac{\partial H}{\partial \mathbf{R}_I} \psi \quad (4.11)$$

By combining Eq. (4.11) with Eq. (3.49) and Eq. (3.14) with some mathematics we get:

$$\frac{\partial E(\mathbf{R}_1, \dots, \mathbf{R}_M)}{\partial \mathbf{R}_I} = -Z_I \int d\mathbf{r} \rho(\mathbf{r}) \frac{\mathbf{r} - \mathbf{R}_I}{|\mathbf{r} - \mathbf{R}_I|^3} \quad (4.12)$$

By substituting Eq. (4.12) in Eq. (4.9) and substituting the result in Eq. (4.8), we get:

$$F_I = Z_I \left[ \int d\mathbf{r} \rho(\mathbf{r}) \frac{\mathbf{r} - \mathbf{R}_I}{|\mathbf{r} - \mathbf{R}_I|^3} - \sum_{I \neq J} Z_J \frac{\mathbf{R}_I - \mathbf{R}_J}{|\mathbf{R}_I - \mathbf{R}_J|^3} \right] \quad (4.13)$$

Eq. (4.13) states that all we need to calculate the forces acting on nuclei of atoms in the system is electron density,  $\rho(\mathbf{r})$ , instead of performing  $3M$  energy calculation in Eq. (4.9).

## 4.2.2 Finding the Equilibrium Nuclear Coordinates Using the Calculated Forces

We have explained the first point in finding the equilibrium structure of the material, which is calculating the total forces acting on the nucleus of each atom using DFT. Now, we have to find the configuration of nuclear coordinates of atoms for which these total forces vanish. This configuration of atoms refers to the equilibrium structure of the material.

This problem of finding the configuration of atoms for which the total forces vanish, is equivalent to finding the lowest point or the global minimum of the potential energy surface given in Eq. (4.7) with respect to the  $3M$  nuclear coordinates. There are plenty of powerful numerical techniques such as steepest descent and conjugate gradient which are designed to find the local minimum of the potential energy surface. The details about how these methods work is beyond the scope of this thesis. In general, these methods span the energy landscape of the potential energy surface with nuclear coordinates using the knowledge of  $U(\mathbf{R}_1, \dots, \mathbf{R}_M)$  and its slope (which represents the forces) to find the global minimum of the potential energy surface. Additional numerical techniques are needed to determine the global minimum as shown in Fig. [4.1].

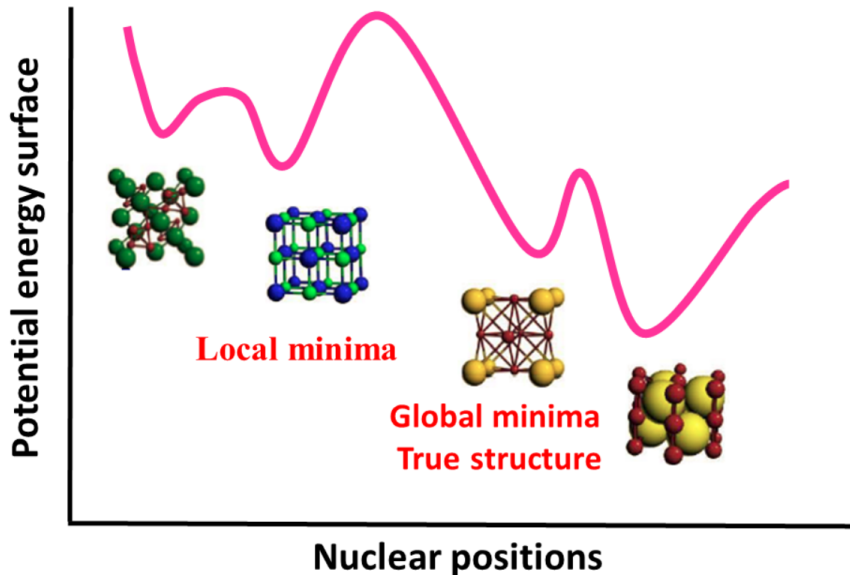


Figure 4.1: Schematic illustration of finding the equilibrium structure of a material by spanning the energy landscape of the potential energy surface using numerical techniques such as the steepest descent method.

Exploring the possible crystal structure of materials is necessary in order to model their properties, such as their electronic band structures, thermodynamics proper-

ties, kinetic properties, vibrational properties, and interfacial properties. All of these properties are very important but for solid electrolyte materials, the most important properties are the kinetic and the interfacial. In the following sections I will explain these properties in detail.

## 4.3 Kinetic Properties of Solid Electrolyte Materials

Kinetic properties of solid electrolyte materials are very important because diffusion determines the rate for charging/discharging of the battery. Diffusion in solids occurs due to thermally-activated random motion of the atoms. As the temperature of a solid increases, atoms become displaced from their lattice sites thus generating defects in the crystal. These defects play an important role in the diffusion process, as they are the vehicles that allow atoms to move in the diffusion process. Accordingly, before we go into the details of the diffusion processes, it is essential to understand the formation processes and the properties of these defects.

### 4.3.1 Crystal Defects

As the temperature of the crystal increases, atoms displace from their lattice sites, generating vacant lattice sites. The presence of these vacancies may cause a distortion in the crystal structure. After these vacancies are formed, they may cause two types of defects depending on the final positions of the displaced atoms, as follows:

- **Frenkel defect:** The displaced atom moves to an interstitial site within the lattice.
- **Schottky defect:** The displaced atom moves to the surface of the crystal.

These defects are intrinsic defects, which means that, starting from an ideal lattice, they are the result of thermal activation and their concentration increases with temperature. As the temperature of the crystal increases, the concentration of these defects increases and they become more mobile causing more diffusion in the material. Accordingly, it is essential to understand the functional dependence of the defect concentration with temperature.

In order to derive the functional dependence of the defect concentration with temperature, we will consider the Frenkel defect type. As the temperature of the crystal increases, more atoms will displace from their lattice sites forming more vacancies and interstitial pairs. Accordingly, the number of vacancies and the number of interstitials,  $n$ , will increase. The increase in the number of vacancies and interstitials will lead to more disorder in the crystal. Because of the increase in the number of these defects, the number of configurations for the arrangements of these defects increases, resulting in the increase of the configurational entropy of the crystal. This increase of the configurational entropy will decrease the overall energy of the system as shown in Eq. (4.14):

$$\Delta G = \Delta U - T\Delta S \quad (4.14)$$

where  $\Delta G$  is the change of the Gibb's free energy for a constant pressure and temperature system.  $\Delta U$  is the change of the internal energy of the system and  $\Delta S$  is the change of the configurational entropy of the system. The change in the internal energy can be given as the product of the number of vacancy-interstitial pairs,  $n$ , multiplied by the energy required to form one pair of vacancies and interstitials,  $E_f$ .

$$\Delta U = nE_f \quad (4.15)$$

The change in the configurational entropy of the system can be given as:

$$\Delta S = k_B \ln w \quad (4.16)$$

where  $k_B$  is the Boltzmann constant and  $w$  is the number of arrangements for the defects, which equals the number of ways for arranging  $n$  vacancies on  $N$  lattice sites multiplied by the number of ways for arranging  $n$  interstitials in the lattice. A rough approximation can be given by the following equation.

$$w = \frac{N!}{n!(N-n)!} \times \frac{N!}{n!(N-n)!} = \left[ \frac{N!}{n!(N-n)!} \right]^2 \quad (4.17)$$

By substituting Eq. (4.17) in Eq. (4.16) we get:

$$\Delta S = 2k_B [\ln N! - \ln n! - \ln (N-n)!] \quad (4.18)$$

By assuming that these numbers are large, we can use Stirling's approximation to approximate Eq. (4.18), as follows:

$$\Delta S = 2k_B [N \ln N - n \ln n - (N-n) \ln (N-n)] \quad (4.19)$$

By substituting Eq. (4.19) and Eq. (4.15) in Eq. (4.14) we get:

$$\Delta G = nE_f - 2k_B T [N \ln N - n \ln n - (N-n) \ln (N-n)] \quad (4.20)$$

By considering thermodynamics equilibrium, the total energy of the system is minimum and thus the first derivative of the Gibbs free energy given in Eq. (4.20) with respect to  $n$  will vanish:

$$\frac{\partial G}{\partial n} = E_f - 2k_B T \ln \left( \frac{N-n}{n} \right) = 0 \quad (4.21)$$

By rearranging the terms in Eq. (4.21), we obtain the expression:

$$\frac{n}{N} = \exp \left[ -\frac{E_f}{2k_B T} \right] \quad (4.22)$$

The left hand side of Eq. (4.22) is the number of vacancies-interstitials pairs formed,  $n$ , divided by the number of lattice sites,  $N$ , which represent the concentration of the defects formed in the crystal at temperature,  $T$ . As shown in Eq. (4.22) the concentration depends proportionally on the temperature,  $T$ , and inversely on the formation energy for vacancy-interstitial pair,  $E_f$ , which can be estimated using first-principles as follows:

$$E_f = E^{crystal} - E^{defect} \quad (4.23)$$

Where  $E^{crystal}$  is the energy of the perfect crystal, and  $E^{defect}$  is the energy of the crystal with a vacancy-interstitial pair.

### 4.3.2 Diffusion in Solids

In general, diffusion can be defined as the transport of matter from one point to another by the thermal motion of atoms. The most common driving force for such a transport process is the concentration gradient, where the atoms flow from a point of high concentration to a point of low concentration. The flux of the particles can be described by Fick's first law:

$$J = -D\nabla C \quad (4.24)$$

where  $J$  is the flux of particles and  $C$  is their number density or concentration, and the factor of proportionality,  $D$ , is known as the diffusion constant of the flowing atoms.



While Fick's first law describes the the diffusion process from a macroscopic point of view, using macroscopic parameters such as the flux of the particles and the diffusion constant, it is essential to understand the diffusion process from microscopic point of view as well. This is a more exciting point of view, since it gives more insight about the actual motion of the atoms in the diffusion process.

From a microscopic point of view, diffusion can be thought of as a random walk or fluctuations of the atoms. In 1905, Albert Einstein was the first to describe such a motion in his published theory for the chaotic motion of small particles in a liquid, where he argued the the motion of particles is a result of their presence in the fluid. Also, he argued that the Boltzmann distribution of energy of atoms are always subject to thermal movements of a statistical nature. These statistical fluctuations are the cause for the stochastic random motions occurring in matter. Einstein also was the first to relate the macroscopic diffusion constant,  $D$ , to the the microscopic mean squared displacement of atoms.

This random walk of atoms has different characteristics in gases, liquids and solids. Unlike gases and liquids where diffusion occur as free flights of atoms, in crystalline solids, diffusion occurs by consecutive atomic hops in the lattice as shown in Fig. [4.2].

There is a separation of time scales between the elementary jumps between neighboring lattice sites and the large succession of the steps, which leads to macroscopic diffusion. The most important point here is that this diffusion process of consecutive atomic hops occurs in conjunction with (or with the help of) intrinsic defects discussed in Sec. [4.3.1]. These intrinsic defects are the mediator for the atoms in the diffusion process, and for each type of defect there is a unique mechanism of diffusion, and in some cases a combination of these mechanisms leads to a more complicated

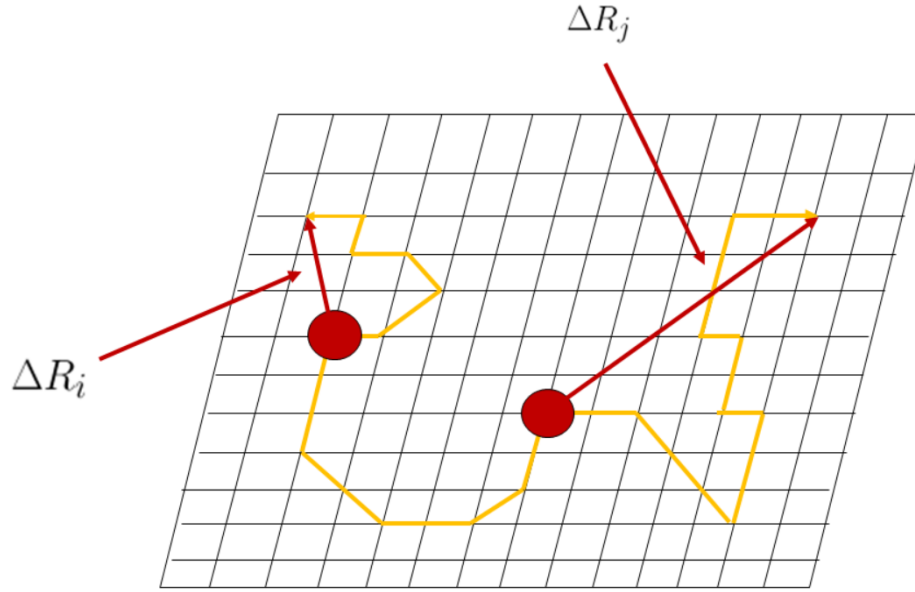


Figure 4.2: Example of a jump sequence of two atoms on a lattice.  $\Delta R_i$ ,  $\Delta R_j$  are the mean squared displacement of the atoms  $i$  and  $j$  respectively.

diffusion mechanism, as follows:

- **Vacancy mechanism:** In this diffusion process, the atom migrates from a lattice site to a neighbouring vacant site, as shown in Fig. [4.3].
- **Interstitial mechanism:** In this diffusion process, the atom migrates from a interstitial site to another neighbouring interstitial site, as shown in Fig [4.3].
- **Interstitialcy mechanism:** In this diffusion process, an interstitial atom kicks a lattice atom to another interstitial site, as shown in Fig [4.3].

### 4.3.3 Transition State Theory

In the preceding section, we have explained the atomic hops mechanisms during the diffusion in crystalline solids. Now, we have to explain the rates or the probability of these consecutive atomic jumps. Let us examine these hops closely by considering one

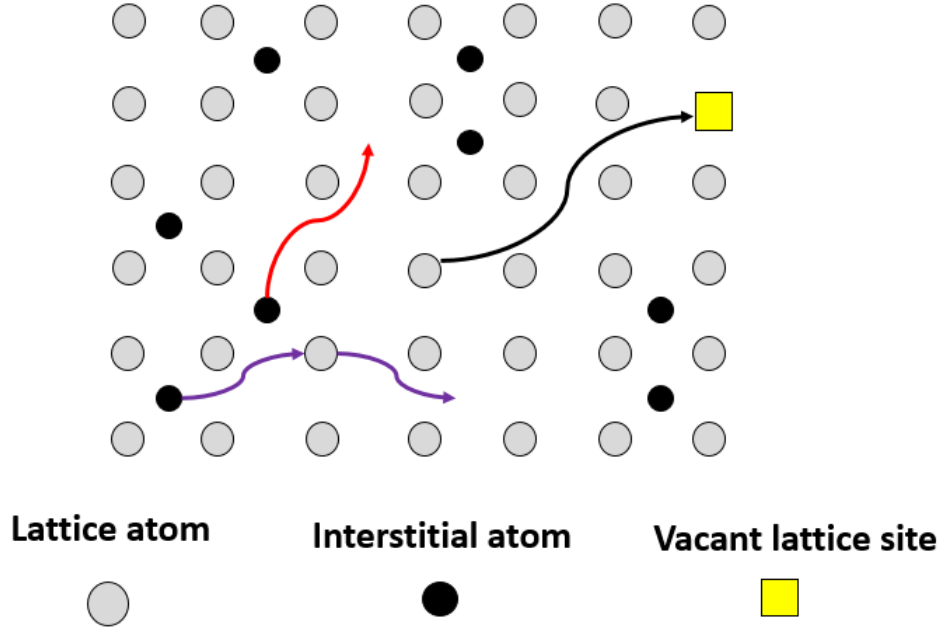


Figure 4.3: Schematic illustration of the vacancy, interstitial and interstitialcy diffusion mechanisms in the lattice. The vacancy mechanism is shown in black line, The interstitial mechanism with red line and the interstitialcy mechanism with purple line.

hop event as shown in Fig. [4.4], as the atom is moving from point **A** to point **B** in the crystal by the vacancy mechanism or by the interstitial or interstitialcy mechanisms. The moving atom has to pass through a saddle point where it passes through two or more neighbouring atoms, in this state which we refer to as the transitional state, the moving atom will experience physical forces like the electrostatic Coulombs force from neighbouring atoms and therefore it will require energy to migrate. Transition State Theory (TST) [38, 39] describes the rate (the number of jumps per unit time) for these individual hops. TST assumes that the hop event from point **A** to point **B** in the crystal is happening at a constant rate by neglecting the correlated events during the atomic motion. Accordingly, in energy landscape, TST describes the hop event as a difference in the Gibbs free energy between the stationary points **A** and **B** and the saddle point,  $G_m$ , where  $G_m$  stands for the Gibbs free energy for migration between **A** and **B**. According to TST, the rate of migration between point **A** and

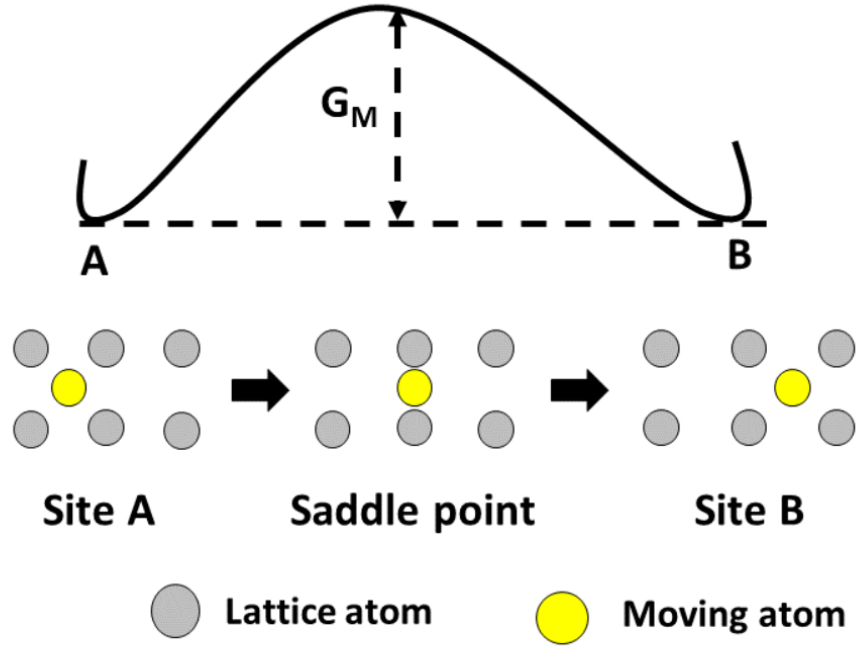


Figure 4.4: Schematic illustration of an atomic hop in the crystal, where the atom is moving from initial point **A** to a final point **B** through a saddle point.

point **B** in the crystal,  $\Gamma$ , is a simple Arrhenius, as follows:

$$\Gamma = \omega_0 \exp\left(-\frac{G_m}{k_B T}\right) \quad (4.25)$$

where  $\omega_0$  is called the attempt frequency, which is vibration frequency around the equilibrium site in the direction of the migration path,  $G_m$  is the Gibbs free energy for migration,  $k_B$  is the Boltzmann constant and  $T$  is the temperature of the crystal.

The Gibbs free energy for migration,  $G_m$ , can be written as follows:

$$G_m = E_m - TS_m \quad (4.26)$$

where  $E_m$  is the migration enthalpy, and  $S_m$  is the entropy of migration. By substituting Eq. (4.26) in Eq. (4.25) we get:

$$\Gamma = \omega_0 \exp\left(\frac{S_m}{k_B T}\right) \exp\left(-\frac{E_m}{k_B T}\right) \quad (4.27)$$

Now, we can define the Vineyard term [39],  $\nu_0$ , as the product of attempt frequency,  $\omega_0$ , multiplied by  $\exp\left(\frac{S_m}{k_B T}\right)$ , as follows:

$$\nu_0 = \omega_0 \exp\left(\frac{S_m}{k_B T}\right) \quad (4.28)$$

by substituting Eq. (4.28) in Eq. (4.27), we get:

$$\Gamma = \nu_0 \exp\left(-\frac{E_m}{k_B T}\right) \quad (4.29)$$

The TST presented in Eq. (4.29) clearly states that the migration rate depends inversely on the enthalpy of migration,  $E_m$ , which is the energy required for the atom to escape from point **A** to point **B** in the crystal and it can be calculated using first-principles methods. Such a dependence is very useful for analysing the diffusion mechanisms and for analysing the local environment of the migration as well. Eq. (4.29) can be used for analysing the diffusion mechanisms (vacancy mechanism, interstitial, interstitialcy mechanism) by comparing their migration enthalpy, the most likely diffusion should have the highest migration rate,  $\Gamma$ , and accordingly it should have the lowest migration enthalpy. Similarly Eq. (4.29) can be used for analysing the local environment of the migration, by comparing the migration enthalpy for different environment in the crystal and the most conductive environment should have the lowest migration enthalpy, for example let us suppose that we have a LiPON material with oxygen and nitrogen layers, if we find the migration enthalpy to be lower near the nitrogen plane than the oxygen plane, this tells us that the nitrogen concentration increase the conductivity of the material and therefore we can suggest increasing the nitrogen concentration to enhance the conduction properties of similar materials.

### 4.3.4 The Diffusion Coefficient

As described in Eq. (4.24), the diffusion constant,  $D$ , is a macroscopic function proportional to the flux of the diffusion atoms,  $J$ , in the crystal. The larger the diffusion constant is, the higher the mobility for the diffusing atoms and therefore the higher the conductivity for the material and vice versa. Accordingly, calculating the diffusion constant using first-principles methods provides information about conductivity of the material. As we explained earlier in this chapter, diffusion in the crystal can occur using different mechanisms (vacancy, interstitial, and interstitialcy mechanisms), where the vacancies and interstitial defects provide the sites and/or sources for the diffusing ions. Accordingly, the diffusion constant,  $D$ , is the sum of the diffusion constant of the vacancies,  $D_{\text{Vacancy}}$ , to the diffusion constant of the interstitials,  $D_{\text{Interstitial}}$ , as follows:

$$D = D_{\text{Vacancy}} + D_{\text{Interstitial}} \quad (4.30)$$

In other words, Eq. (4.30) states that the diffusion in the crystal is the sum of the contribution of the two modes of diffusion. The diffusion constant for any defect species,  $x$ , can be related to its concentration described in Eq. (4.22), as follows:

$$D_x = \frac{n_x}{N} d_x \quad (4.31)$$

Where  $\frac{n_x}{N}$  is the concentration of defect  $x$  which could be vacancies or interstitials,  $d_x$  is known as the diffusivity function, which is a function that describes the ease of which the mechanism of defect,  $x$ , can provide diffusion. The formula of  $d_x$  is given in Eq. (4.32).

$$d_x = \frac{1}{6} f z a^2 \Gamma \quad (4.32)$$

Where  $f$  is a correlation factor, which describes the correlation between atoms in the diffusion process, which is beyond the scope of this thesis.  $z$  is the number of equivalent pathways for the diffusion process,  $a$  is the jump distance for an individual hop in the diffusion process and  $\Gamma$  is the rate for the individual hop in the diffusion process as described in Eq. (4.29). By combining Eq. (4.29) and Eq. (4.32) and Eq. (4.31) and Eq. (4.22) and Eq. (4.30) together, we can obtain a new formula for the diffusion constant as follows:

$$D = \frac{1}{3} f z a^2 \nu_0 \exp\left(-\frac{E_m + \frac{E_f}{2}}{k_B T}\right) \quad (4.33)$$

Now we can define the prefactor of the exponential function in Eq. (4.33), as follows:

$$D_0 = \frac{1}{3} f z a^2 \nu_0 \quad (4.34)$$

And we can define the total activation energy for the diffusion process,  $E_a$ , as follows:

$$E_a = E_m + \frac{E_f}{2} \quad (4.35)$$

By substituting Eq. (4.34) and Eq. (4.35) in Eq. (4.33) we get:

$$D = D_0 \exp\left(-\frac{E_a}{k_B T}\right) \quad (4.36)$$

Eq. (4.36) states that the diffusion constant depends inversely on the total activation energy. Accordingly, the total activation energy for the diffusion process is a very precise quantitative value for the mobility of atoms and the conductivity of the material. In most experimental findings of materials, a plot of  $1000/T$  against  $\log(D)$  is a straight line and the value of  $E_a$  is obtained from the slope of the line according to Eq. (4.36). From a simulation stand point, the activation energy is the minimum energy required to activate the diffusion process, which according to Eq. (4.35) can

be obtained from the minimum migration energy for the possible diffusion processes, and from the minimum formation energy for vacancies-interstitials pairs described in Eq. (4.23).

Although we can calculate the activation energy using first-principles methods using Eq. (4.35), calculating the diffusion constant using first-principles methods will help us to make a direct comparison to the experimental  $1000/T$  against  $\log(D)$  plot. Einstein was the first to derive such an equation for calculating the diffusion constant [40]. where he related the macroscopic diffusion constant,  $D$ , to the microscopic mean squared displacement of the diffusing atoms visualized in Fig. [4.2], as follows:

$$D = \frac{1}{6} \lim_{t \rightarrow \infty} \sum_{i=1}^N \frac{\Delta R_i}{t - t_0} \quad (4.37)$$

Where  $t$  is the time,  $N$  is the number of diffusing atoms,  $\Delta R_i$  is the mean squared displacement of the atom  $i$  and it is given in Eq. (4.38)

$$\Delta R_i = \frac{1}{N} |\mathbf{r}_i(t) - \mathbf{r}_i(t_0)|^2 \quad (4.38)$$

$\mathbf{r}_i(t)$  is the position vector of the atom  $i$  at the time  $t$ . Accordingly, in order to calculate the diffusion constant in Eq. (4.37) using first-principles methods, we should be able to calculate the evolution of the position vector,  $\mathbf{r}_i(t)$ , with time, which we can do using molecular dynamics simulation.

### 4.3.5 Molecular Dynamics Simulation

In the previous section, we learned that predicting the evolution of atoms in the crystal is necessary to calculate macroscopic quantities such as the diffusion constant, which gives an estimate about the conductivity of the material. Such a prediction can be made with a molecular dynamics simulation (MD). Molecular dynamics consists of



the numerical, step-by-step, solution of Newton's equations of motion. In molecular dynamics, each atom in the crystal will be assigned initial position,  $\mathbf{r}_0$ , and initial random velocity,  $\mathbf{u}$ , which on average represents the temperature of the simulation. At these initial conditions, each atom in the crystal will experience a force from its neighbouring atoms,  $\mathbf{F}$ , and therefore it will gain acceleration proportional to the force acting on it, according to Newton's second law:

$$\mathbf{a} = \frac{\mathbf{F}}{m} \quad (4.39)$$

where  $m$  is the mass of the atom. The force,  $\mathbf{F}$ , which describes that interaction between the atoms can be either classical force which maps into classical molecular dynamics, or it can be determined using first-principles methods as shown in Eq. (4.13) which maps to first-principles molecular dynamics. In this work, we use only first-principles molecular dynamics. Due to the acceleration caused by the force,  $F$ , the velocity of the atom,  $\mathbf{v}$ , can be given at anytime,  $t$ , as follows:

$$\mathbf{v}(t) = \mathbf{u} + \int_0^t \frac{\mathbf{F}}{m} dt \quad (4.40)$$

now assuming that the force rate is unchanged with time, we will discuss the consequences of this assumption later. Accordingly, we can write Eq. (4.40) as follows:

$$\mathbf{v}(t) = \mathbf{u} + \frac{\mathbf{F}}{m}t \quad (4.41)$$

The position of the atom at any time,  $\mathbf{r}(t)$ , can be obtained from the integration of the velocity function in Eq. (4.41) with time, as follows:

$$\mathbf{r}(t) = \mathbf{r}_0 + \int_0^t dt \left[ \mathbf{u} + \frac{\mathbf{F}}{m}t \right] = \mathbf{r}_0 + \mathbf{u}t + \frac{1}{2} \frac{\mathbf{F}}{m}t^2 \quad (4.42)$$

The position function in Eq. (4.42) includes the force acting on the atom, which is the second order derivative of the position with time. For more numerical accuracy we can expand Eq. (4.42) to the order derivative of the position with time,  $\ddot{\mathbf{r}}(t)$  as follows:

$$\mathbf{r}(t) = \mathbf{r}_0 + \mathbf{u}t + \frac{1}{2} \frac{\mathbf{F}}{m} t^2 + \frac{\ddot{\mathbf{r}}(t)}{m} t^3 \quad (4.43)$$

Using the Verlet algorithm [41], we can find the position in the neighbour of  $t$ , as follows:

$$\mathbf{r}(t + \tau) = \mathbf{r}(t) + \mathbf{u}(t)\tau + \frac{1}{2} \frac{\mathbf{F}(t)}{m} \tau^2 + \frac{\ddot{\mathbf{r}}(t)}{m} \tau^3 \quad (4.44)$$

$$\mathbf{r}(t - \tau) = \mathbf{r}(t) - \mathbf{u}(t)\tau + \frac{1}{2} \frac{\mathbf{F}(t)}{m} \tau^2 - \frac{\ddot{\mathbf{r}}(t)}{m} \tau^3 \quad (4.45)$$

where  $\tau$  is a very small time period. By adding Eq. (4.44) to Eq. (4.45) we get the following:

$$\mathbf{r}(t + \tau) = 2\mathbf{r}(t) - \mathbf{r}(t - \tau) + \frac{\mathbf{F}(t)}{m} \tau^2 \quad (4.46)$$

Eq. (4.46) tells us that we can predict the future position of the atom by knowing its past position and the force acting on it. In order to perform MD simulation, the total time of the simulation should be divided into very small time intervals,  $\tau$ , and we can find the position of the atom at each time step using numerical methods such as the Verlet algorithm in Eq. (4.46). Calculating the position of the atoms for each step of the simulation time is not only helpful for calculating macroscopic quantities such as the diffusion constant in Eq. (4.37) but it can also give insight about the random walk of atoms visualized in Fig. [4.2]. By visualizing the positions of atoms through the time of the simulation, we can have a good understanding about the diffusion

mechanisms of the atoms in the crystal. Now, let us recall the assumption made in Eq. (4.40) that the force rate is unchanged with time; this is obviously incorrect and will lead to error in the MD simulation. In order to reduce such an error, we should make sure that the time step,  $\tau$ , is as small as possible, usually in the order of  $10^{-15}$  s, so that the variation of the force in the time step will be very small.

Finally, MD simulation can be performed in many statistical ensembles; the most common and simple ensemble is known as microcanonical ensemble. In this ensemble the total number of particles,  $N$ , and the volume of the ensemble,  $V$ , and the total energy of the system,  $E$ , are preserved which represents a thermodynamically isolated system. This ensemble is called the  $(N, V, E)$  ensemble. If the system is connected to a heat path that keeps the temperature of the system,  $T$ , fixed, then the ensemble is canonical ensemble and it is called  $(N, V, T)$ . If the system is connected to a diathermic that gives a constant pressure,  $P$ , and constant temperature to the system, the ensemble is canonical and it's called  $(N, P, T)$ . All of these ensembles are being used for different cases in MD simulations, but the  $(N, V, E)$  ensemble remains the most popular.

## 4.4 Interfacial Properties of Solid Electrolyte Materials

The purpose of this section is to characterize the interface between solid electrolyte materials and metallic Li using first-principles methods. Before we explain how we characterize the interface between crystalline materials, it is necessary to explain the general concept of the interface. In general, the interface between two crystalline materials  $a$  and  $b$  can be defined by the configuration of atoms,  $\Omega$ , that make up the interface. In general, there are three possible configurations for the interface accord-

ing to the level of match between the lattice constants of the two materials [42]. In the case of the coherent interface, the lattice constants of the two materials align perfectly across the interface plane. In the case of the semi-coherent interface, which is the most common case for the interface of solid electrolyte materials and metallic Li, the lattice of the two materials are geometrically similar but not equal, which introduces a strain at the interface. In the case of the incoherent interface, the lattice constants of the two materials are completely incompatible. In this work, we deal only with the first two kinds of interfaces.

A quantitative measure of the interface stability between two crystalline materials  $a$  and  $b$  for a given configuration,  $\Omega$ , can be obtained from calculating the quasi-intensive interface energy,  $\gamma_{ab}(\Omega)$ , which is defined as:

$$\gamma_{ab}(\Omega) = \frac{E(\Omega, A, n_a, n_b) - n_a E_a - n_b E_b}{2A} \quad (4.47)$$

Where  $E(\Omega, A, n_a, n_b)$  is the optimized total energy of the supercell containing the interface with  $n_a$  and  $n_b$  formula units of materials  $a$  and  $b$ .  $E_a$  and  $E_b$  denotes the bulk energy per unit cell of materials  $a$  and  $b$ .  $\Omega$  represent the particular configuration of the system.  $A$  denotes the area normal to the surface. The material  $a$  refers to the solid electrolyte and usually it has fixed number  $n_a$  material, and material  $b$  refers to metallic Li which has variable number  $n_b$ . In order to assess the strain due to the lattice mismatch between material  $a$  and  $b$  in the case of semi-coherent interface, we follow the approach of Lepley et al [42], where the quasi-intensive interface energy for a fixed number of formula units of the solid electrolyte is defined as:

$$\gamma_{ab}(\Omega, n_b) = \gamma_{ab}^{lim}(\Omega) + n_b \sigma(\Omega) \quad (4.48)$$

where  $\sigma(\Omega)$  represents the strain of metallic Li in the configuration  $\Omega$  and  $\gamma_{ab}^{lim}(\Omega)$

represent the surface energy extrapolated to zero strain.

A more qualitative measure for the interface stability can be obtained from calculating the partial density of states,  $N^a(E)$ , which has the expression:

$$N^a(E) = \sum_{n\mathbf{k}} W_{n\mathbf{k}} Q_{n\mathbf{k}}^a \delta(E - E_{n\mathbf{k}}) \quad (4.49)$$

In this expression  $a$  denotes an atomic site,  $W_{n\mathbf{k}}$  denotes the Brillouin-zone sampling and degeneracy weight factor for band index  $n$  and wave vector  $\mathbf{k}$ , and  $E_{n\mathbf{k}}$  denotes the corresponding band energy. For each eigenstate  $n\mathbf{k}$  and atomic site  $a$ . The local density of states factor,  $Q_{n\mathbf{k}}^a$ , is given by the charge within the augmentation sphere of radius  $r_c^a$  which can be approximated as follows:

$$Q_{n\mathbf{k}}^a \approx \sum_{ij} \langle \tilde{\psi}_{n\mathbf{k}} | p_{n_i l_i m_i}^a \rangle \langle p_{n_i l_i m_i}^a | \tilde{\psi}_{n\mathbf{k}} \rangle q_{n_i l_i; n_j l_j}^a \delta_{l_i l_j} \quad (4.50)$$

Where

$$q_{n_i l_i; n_j l_j}^a = \int_0^{r_c^a} dr \phi_{n_i l_i}^a \phi_{n_j l_j}^a \quad (4.51)$$

In these expressions,  $|\tilde{\psi}_{n\mathbf{k}}\rangle$  denotes the pseudowave function,  $|p_{n_i l_i m_i}^a\rangle$  is the PAW atomic projector function, which is localized within the augmentation sphere, and  $n_i l_i m_i$  denotes the radial and spherical harmonic indices of the projector function [32,43]. In order to analyse the interface stability, it is convenient to define the energy bands for the atoms involved in the interface as shown in Fig. [4.5].

In the figure there are three schematic diagrams of the band structure. The bottom diagram represents the bulk band structure, the middle diagram represents the atoms at the interface, and the top diagram represents the Li metal. Such a definition of the energy bands is very helpful in analysing the interface stability. In the case of the ideal interface, the metallic Li atoms are physically separated from the bulk of the

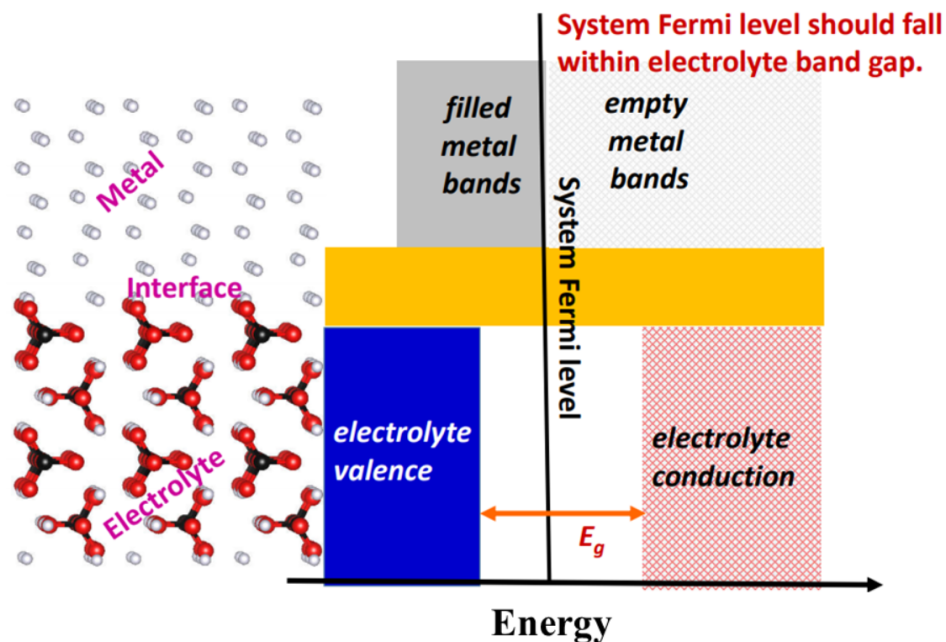


Figure 4.5: Energy diagram for ideal electrolyte/metal interface. The left panel represents a ball and stick model of Li metal in atomic contact with an electrolyte. The right panel contains three schematic diagrams of the band structures corresponding to the three different regions of space, with increasing energy along the horizontal axis.

electrolyte, the physical and chemical nature of the electrolyte remains unchanged. Accordingly, the energy bands of the interior of the electrolyte should be similar to the energy bands of the bulk material; and the system Fermi level should fall within the electrolyte band gap. In the case of a reactive interface, there are two possibilities. For a limited reaction, the material is altered in a small region near the interface and the band structure for the interface region may be complicated. For a fully reactive interface the bulk material is altered and the system can no longer perform as an electrolyte and anode.

## 4.5 Summary

In this chapter, we have explained in detail how we use first-principles methods to model materials properties. In particular, we explained how we predict the structure of the material using first-principles methods. Also we explained how we understand several kinetic properties of materials using first-principles methods, like the defect concentration in the crystal and the diffusion of atoms in the crystal. And finally, we explained how we use first-principles methods to understand the stability of the electrolyte with metallic Li.

## Part II

# Summary of Research Work



# Chapter 5

## Computational Study of Li Ion Electrolytes Composed of $\text{Li}_3\text{AsS}_4$ Alloyed with $\text{Li}_4\text{GeS}_4$

This work was published in the Journal of Electrochemical Society, volume 163, issue 9, pages A2079–A2088, 2016. The full text of the paper may be found in appendix A. The publication is reproduced with a permission from Elsevier.

### 5.1 Overview

The motivation of this work is a recent experimental study by Sahu et al [44] at Oak Ridge National Laboratory. The study explored new electrolyte compositions for Li ion electrolytes and found promising results based on the alloys of  $\text{Li}_3\text{AsS}_4$  with  $\text{Li}_4\text{GeS}_4$ . The alloys system has the compositions  $\text{Li}_{3+x}\text{As}_{1-x}\text{Ge}_x\text{S}_4$  with  $0 < x < 0.5$ ; this alloys system has a significantly higher ionic conductivity compared with the pure materials. The experimental study did not report any structural or Li ion migration data about the pure material  $\text{Li}_3\text{AsS}_4$  and the alloys system, which leaves

these questions opened for computational investigations.

In this work, we use the PAW formalism and the LDA approximation with the framework of density functional theory (DFT) as programmed in Quantum espresso code, to investigate the structures and the Li ion migration of the  $\text{Li}_3\text{AsS}_4$  and the alloy systems. The first task of the simulations is to determine the structure of the  $\text{Li}_3\text{AsS}_4$ . Secondly, based on the structure of the  $\text{Li}_3\text{AsS}_4$  and the likely Ge substitutions, the structure of the alloys system must be determined. Based on the structure of the  $\text{Li}_3\text{AsS}_4$  and the alloys system, we should be able to analyse the Li ion diffusion mechanisms in the pure material and the alloys, and understand the effect of Ge in enhancing the conductivity properties in the alloys materials.

## 5.2 Main Publication Results

The first task of the simulations is to determine the structure of the  $\text{Li}_3\text{AsS}_4$  material. The experimental study by Sahu et al [44] reports the experimental X-ray diffraction pattern for  $\text{Li}_3\text{AsS}_4$  material, no experimental data was provided about the structure of the material. It is reasonable to assume that  $\text{Li}_3\text{AsS}_4$  has structural properties similar to those of  $\text{Li}_3\text{PS}_4$ , which has been the subject of many studies [45–48].  $\text{Li}_3\text{PS}_4$  has a low temperature structure,  $\gamma\text{-Li}_3\text{PS}_4$ , characterized by the space group  $Pmn2_1$  (No. 31). At high temperature between 200–300 degrees C, a transition occurs to  $\beta\text{-Li}_3\text{PS}_4$  which is characterized by the space group Pnma (No. 62) with fractional occupancy of some of the Li sites. In previous work [46], two ordered models of  $\beta\text{-Li}_3\text{PS}_4$  were simulated, the first model,  $\beta\text{-Li}_3\text{PS}_4\text{-b}$ , has 100% occupancy of the b sites. The second model,  $\beta\text{-Li}_3\text{PS}_4\text{-c}$ , has 100% occupancy of the c sites. Four possible models of  $\text{Li}_3\text{AsS}_4$  were simulated by substituting p by As in the three ordered models of  $\text{Li}_3\text{PS}_4$ , and by substituting p by As and O by S in  $\gamma\text{-Li}_3\text{PO}_4$ , which is characterized by the space

group  $Pnma$  (No. 62). The heat of formation ( $\Delta H_f$ ) for the four proposed models in comparison to the heat of formation of  $\text{Li}_3\text{PS}_4$  models, was calculated according to Eq. (1) in the publication and is shown in Table I in the publication. The heat of formation results show that  $\text{Li}_3\text{AsS}_4$  structure based on  $\gamma\text{-Li}_3\text{PS}_4$  has the lowest heat of formations, followed by the  $\text{Li}_3\text{AsS}_4$  based on  $\beta\text{-Li}_3\text{PS}_4\text{-c}$ . Accordingly, these two models look to be the most plausible models. For the  $\text{Li}_3\text{AsS}_4$  structure, in order to validate which one of these two models is more likely, we generated the X-ray diffraction patterns for the two models using Mercury software and compared these patterns to the experimental X-ray diffraction patterns, as shown in Fig. [2] in the publication. Fig. [2] show that X-ray diffraction patterns for the two models agrees well with the experiment, however the X-ray diffraction patterns for  $\gamma\text{-Li}_3\text{PS}_4$  model has a better agreement with the experiment in particular the peaks in the middle. Accordingly, based the calculated heat of formations and the X-ray diffraction patterns the  $\text{Li}_3\text{AsS}_4$  structure based on  $\gamma\text{-Li}_3\text{PS}_4$  looks like the most plausible structure for the  $\text{Li}_3\text{AsS}_4$ . The simulated structure of  $\text{Li}_3\text{AsS}_4$  is shown in Fig. [1] in the publication. The structure of the  $\text{Li}_3\text{AsS}_4$  is characterized by the  $Pmn2_1$  space group similar to  $\gamma\text{-Li}_3\text{PS}_4$ .  $\text{Li}_3\text{AsS}_4$  has two unique Li sites with a and b similar to  $\gamma\text{-Li}_3\text{PS}_4$  as shown in Fig. [1] in the publication. The fractional coordinate of these sites is shown in Table II in comparison to  $\gamma\text{-Li}_3\text{PS}_4$ , the fractional coordinate of the unique Li sites is very close to  $\gamma\text{-Li}_3\text{PS}_4$ . In order to simulate the alloy system, it is essential to understand the structure of  $\text{Li}_4\text{GeS}_4$  which has been the subject of many studies [49, 50]. The crystal structure of  $\text{Li}_4\text{GeS}_4$  has the  $Pnma$  (No. 62) space group. The  $\text{GeS}_4$  tetrahedra are very similar to the  $\text{AsS}_4$  tetrahedra in  $\text{Li}_3\text{AsS}_4$ , consistent with the formation of alloys.

In the search for the optimal alloy structures, we considered two alloy systems with the highest experimental ionic conductivity, with  $x = 1/4$  and  $x = 1/3$  compositions. The search for optimal structure for these alloy systems was based on supercells of the

$\text{Li}_3\text{AsS}_4$  structure; four and six formula units of  $\text{Li}_3\text{AsS}_4$  were used for the  $x = 1/4$  and  $x = 1/3$  respectively. For each supercell, all unique configurations of the Ge substitutions were considered. For each Ge substitution, an additional Li was added on a grid of likely positions. For all the configurations considered, the optimized alloy model was found to have a lower energy by 0.2-0.3 eV per formula unit relative to all the other configurations. In order to validate these models, we sampled more configurations in larger supercells with the help of the symmetry analysis from the Site Occupancy Disorder (SOD) program [51], but we failed to find alloy structures with lower energy. Accordingly, the optimized alloy systems are very plausible models but they are not the only possibilities. The first alloy system modeled in this study is the  $x = 1/4$  alloy which has the composition of  $\text{Li}_{13/4}\text{As}_{3/4}\text{Ge}_{1/4}\text{S}_4$ . This alloy system has the second highest ionic conductivity after the  $x = 1/3$  alloy model. The crystal structure of this alloy was investigated in a  $2 \times 1 \times 1$  supercell of  $\text{Li}_3\text{AsS}_4$  by substituting As by Ge and adding one extra Li for each Ge. The crystal structure of this alloy is characterized by the  $Pm$  (No. 6) space group and is shown in Fig. [3a] of the publication. The fractional coordinates of the unique atoms is shown in Table AII of the publication. This structure has 8 unique Li sites, 7 of which are labelled relative to their equivalent in  $\text{Li}_3\text{AsS}_4$  structure, the extra Li atom is labelled,  $x$ , which is at  $3 \text{ \AA}$  on the vertical axis from the Ge atom. The second alloy system modelled in this study is the  $x = 1/3$  alloy which has the composition  $\text{Li}_{10/3}\text{As}_{2/3}\text{Ge}_{1/3}\text{S}_4$ . This alloy system was reported to have the highest ionic conductivity. The crystal structure of this alloy was investigated in a  $2 \times 1 \times 1$  supercell of  $\text{Li}_3\text{AsS}_4$  by substituting As by Ge and adding one extra Li for each Ge. The optimal structure of this alloy is 0.27 eV lower in energy than the other configurations considered. The crystal structure of this alloy is shown in Fig. [3b]. It has the  $Pmn2_1$  (No. 31) space group similar to  $\text{Li}_3\text{AsS}_4$ , the fractional coordinates of the unique sites are shown in Table AIII. This alloy has 6 unique Li sites, 5 of which are labelled relative to their equivalent

in  $\text{Li}_3\text{AsS}_4$  structure. The extra Li atom is labelled,  $x$ , has the multiplicity of 2, it is located at 3 Å on the vertical axis from the Ge atom. In order to investigate the ordered nature of the structures of the alloys, we adjusted the occupancy of the As and Ge sites randomly, and the X-ray diffraction patterns for the ordered structures is nearly as good as the disordered models, which means there is no evidence for the ordered nature of these alloys.

It is interesting to compare the partial density of states (PDOS) for these alloy systems with the pure materials. Fig. [4] in the publications shows the PDOS for the  $x = 1/4$  and  $x = 1/3$  alloys in comparison with  $\text{Li}_3\text{AsS}_4$  and  $\text{Li}_4\text{GeS}_4$ . The PDOS for these alloys looks very similar. The valence bands of these alloys are primarily composed of the S 3p states, while the conduction bands are composed of the unoccupied As and Ge states, hybridized with S. The band gap of the alloys is very similar to that of  $\text{Li}_3\text{AsS}_4$ . A more quantitative measure of the alloy stability can be determined from the decomposition energy of the alloys into pure materials which can be estimated according to Eq. (2) in the publication. The decomposition energy results are given in Table V in the publication. The decomposition energies for the alloy have very small positive values with the order of magnitude of the expected finite temperature correction [52]. This suggests that the alloys are stable with respect to decomposition into the pure materials.

One of the main tasks of the simulations is to analyze the mechanisms of conductivity of the pure materials and the alloy systems. In order to do so, it is essential to analyse the defects energies in these systems. The  $Pmn2_1$  structure of  $\text{Li}_3\text{AsS}_4$  has two distinct host lattice sites of Li with Wyckoff labels  $a$  and  $b$  as shown in Fig. [1] in the publication. Several metastable interstitials sites were found in this crystal; the lowest energy sites are labelled I (having the multiplicity of 2 in the unit cell)

and II (having the multiplicity of 4). These interstitials are shown in Fig. [1] in the publication. The relative energies of these defects were calculated in 16 formula units supercell, and are given in comparison to their equivalent in  $\gamma$ -Li<sub>3</sub>PS<sub>4</sub>, which are given in Table II in the publication. The fractional coordinates and the relative energies of these defects are very similar to the  $\gamma$ -Li<sub>3</sub>PS<sub>4</sub> analogue. The formation energy to form a vacancy-interstitial pair,  $E_f$ , was calculated for all the possible pairs in this crystal. We found the lowest formation energy to be  $E_f = 0.86$  eV corresponding to a type I interstitial and the nearest vacant site. The  $Pm$  structure of the  $x = 1/4$  alloy has 8 distinct Li sites and 6 distinct interstitial sites as shown in Fig. [3a] in the publication. The corresponding relative energies of vacancies and interstitials are listed in Table III in the publication. The  $x$  Li ion site has the lowest vacancy energy. The nearest neighbour Li vacancy sites are all unstable relative to the  $x$  site. The vacancy energies were found to be lower for sites in proximity to a Ge ion, while vacancies farther from the Ge were found to be 0.5 eV higher in energy. The interstitials  $K$  and  $K'$  correspond to type I interstitial in Li<sub>3</sub>AsS<sub>4</sub> and the interstitials  $J$ ,  $L$ ,  $M$  and  $N$  correspond to type II interstitial in Li<sub>3</sub>AsS<sub>4</sub>. The  $J$  interstitial site which is the closest to the Ge atom was found to have the lowest relative energy. In this alloy, the lowest formation energy for a vacancy-interstitial pair,  $E_f$ , was found to be 0.27 eV, which involves the lowest energy vacancy,  $x$ , and the lowest energy interstitial,  $J$ . The  $Pmn2_1$  structure of the  $x = 1/3$  alloy has 6 distinct Li sites and 4 distinct interstitial sites as shown in Fig. [3b] in the publication. The corresponding relative vacancy and interstitial energies are listed in Table IV in the publication. Similar to the case of the  $x = 1/4$  alloy, the  $x$  Li ion site has the lowest vacancy energy. The nearest neighbour Li vacancy sites are all unstable relative to the  $x$  site. The vacancy energies were found to be lower for sites in proximity to a Ge ion, while vacancies farther from the Ge were found to be 0.5 eV higher in energy. In this alloy, the interstitial  $K$  corresponds to the type I interstitial in Li<sub>3</sub>AsS<sub>4</sub> and the interstitials  $A$ ,  $B$  and  $C$  correspond to

type  $II$  interstitial in the  $\text{Li}_3\text{AsS}_4$ . The  $B$  interstitial site which is the closest the Ge atom was found to have the lowest relative energy. The lowest formation energy for a vacancy-interstitial pair,  $E_f$ , was found to be 0.27 eV, which involves the lowest energy vacancy,  $x$ , and the lowest energy interstitial,  $B$ .

The Li ion migration was analysed using the NEB method in the pure  $\text{Li}_3\text{AsS}_4$  and the two alloys. Table VI in the publication summarizes the migration energies for all the diffusion pathways considered and compares them with the corresponding experimental activation energies. For  $\text{Li}_3\text{AsS}_4$ , several diffusion pathways were considered for the vacancy mechanism. The diffusion pathways are shown in Fig. [5a] and the NEB energy is shown in Fig. [5b] in comparison with  $\gamma\text{-Li}_3\text{PS}_4$ . The minimum migration energy was found to be 0.4 eV, which is larger than the 0.3 eV migration energy for the  $\gamma\text{-Li}_3\text{PS}_4$ . The pure interstitial and the kick-out mechanisms were considered for this material as well. For these mechanisms, several paths were considered as shown in Fig. [6a] and Fig. [6b] and the corresponding NEB energy is shown in Fig. [7a] and Fig. [7b]. The minimum migration barrier was found to be 0.3 eV for the Kick-out path  $II_1 \rightarrow b_1 \rightarrow I_1 \rightarrow a_1 \rightarrow II_2$ , which takes place along the  $y$ -axis, and for the pure interstitial mechanism for the path  $II_1 \rightarrow II_2 \rightarrow II_3$  which is along the  $z$ -axis. The pure interstitial and the Kick-out mechanisms were considered for the  $x = 1/4$  and the  $x = 1/3$  alloys. For the  $x = 1/4$  alloy, several paths were considered as shown in Fig. [8a] and Fig. [8b] and the NEB energy results are shown in Fig. [9a] and Fig. [9b]. The minimum migration energy was found to be 0.3 eV for the kick-out mechanism along the  $y$ -axis and for interstitial mechanism along the  $z$ -axis. For the  $x = 1/3$  alloy, several paths were considered as shown in Fig. [10a] and Fig. [10b] and the NEB energy results are shown in Fig. [11a] and Fig. [11b]. The minimum migration energy was found to be 0.2 eV for the kick-out mechanism along the  $y$ -axis and for interstitial mechanism along the  $z$ -axis.

### 5.2.1 Conclusions

In conclusion, we have performed a detailed computational study of structures and the Li ion migration of the pure  $\text{Li}_3\text{AsS}_4$  and the alloy system  $\text{Li}_{3+x}\text{As}_{1-x}\text{Ge}_x\text{S}_4$  with  $0 < x < 0.5$  reported by Sahu et al [44]. We are very confident in our simulated  $Pmn2_1$  crystal structure of  $\text{Li}_3\text{AsS}_4$ . Also, we believe that our simulated crystal structures of  $Pm$  for the  $x = 1/4$  alloy and  $Pmn2_1$  for the  $x = 1/3$  alloy are very reasonable models, but more extensive search may reveal more possibilities. The Li ion migration analysis in  $\text{Li}_3\text{AsS}_4$  and the two alloy systems, shows that conduction process is dominated by pure interstitial mechanism along the  $\mathbf{c}$  axis and a kick-out mechanism along the  $\mathbf{c}$  axis. For these mechanisms, the lowest migration energy was found for the  $x = 1/3$  alloy followed by  $x = 1/4$  alloy followed by the pure  $\text{Li}_3\text{AsS}_4$ , suggesting that the substitutional Ge incrementally reduces the migration energy and improves the ionic conductivity. Also, the formation energy in the alloy systems was found to be much lower than the pure  $\text{Li}_3\text{AsS}_4$ , which involves the Li site  $x$  introduced by the presence of Ge in the alloys. Overall, we find the effect of Ge is to adjust the position and energy of interstitials in  $\text{Li}_3\text{AsS}_4$  to lower the migration barrier and to reduce the formation for vacancy-interstitial pairs.

### 5.2.2 My Contribution

I performed the majority of the computations and geometry analyses of this study. The paper was written by me in collaboration with N. A. W. Holzwarth.

## 5.3 Published Manuscript

The published manuscript of this projects is shown in appendix A.



## Chapter 6

# $\text{Li}_4\text{SnS}_4$ and $\text{Li}_4\text{SnSe}_4$ : Simulations of Their Structure and Electrolyte Properties

This work was published in the Journal of Electrochemical Society, volume 164, issue 1, pages A6386–A6394, 2017. The full text of the paper may be found in appendix B. The publication is reproduced with a permission from Elsevier.

### 6.1 Overview

The motivation of this project is a recent experimental literature which reports the solid electrolyte properties of  $\text{Li}_4\text{SnS}_4$  and  $\text{Li}_4\text{SnSe}_4$  opening interesting questions for the simulations. In detail, we use the LDA approximation and the PAW method in the framework of density functional theory to study the structure and the Li ion conduction properties for the  $\text{Li}_4\text{SnS}_4$  and  $\text{Li}_4\text{SnSe}_4$  along with the  $\text{Li}_4\text{GeS}_4$ .

## 6.2 Main Publication Results

The crystal structure of the  $\text{Li}_4\text{SnS}_4$  has been reported by two different experiments [50, 53]. While the two groups agree on the  $Pnma$  (No. 62) space group of the material, they differ slightly in the reported lattice constants and fractional coordinates of one of the Li sites. The crystal structure of MacNeil [50] was reported to be ordered and has one Li site at the  $4a$  Wyckoff label; the crystal structure of Kaib [53] was reported to be disordered and has slightly larger lattice constants. With several successive attempts, we were able to simulate ordered structures which agree well with the experimental X-ray results. Our simulations identify the MacNeil [50] to be the ground state structure and the Kaib [53] to be the meta-stable state structure with a 0.02 eV/formula unit energy difference from the ground state structure. Accordingly, we use the notation  $\text{Li}_4\text{SnS}_4^0$  for the MacNeil [50] structure and  $\text{Li}_4\text{SnS}_4^*$  for the Kaib [53] structure. It is interesting to ask the question whether the structurally and chemically similar materials,  $\text{Li}_4\text{GeS}_4$  and  $\text{Li}_4\text{SnSe}_4$  behave in a similar way. To answer such a question we have substituted Sn by Ge and S by Se in the  $\text{Li}_4\text{SnS}_4^0$  and  $\text{Li}_4\text{SnS}_4^*$ . Our simulation suggest that it is likely for the  $\text{Li}_4\text{SnSe}_4$  to behave similarly to the  $\text{Li}_4\text{SnS}_4$ , with a ground state structure  $\text{Li}_4\text{SnSe}_4^0$  and a metastable structure  $\text{Li}_4\text{SnSe}_4^*$  which is 0.07 eV/formula unit higher in energy. While it is unlikely for the  $\text{Li}_4\text{GeS}_4$  to behave in a similar way with the  $\text{Li}_4\text{GeS}_4^*$  having 0.25 eV/formula unit higher energy than the ground state  $\text{Li}_4\text{GeS}_4^0$ .

The NEB method was used to study the Li ions migration properties in the ground state and the meta-stable state structures of  $\text{Li}_4\text{SnS}_4$  and  $\text{Li}_4\text{SnSe}_4$ . For the  $\text{Li}_4\text{SnS}_4^0$  and  $\text{Li}_4\text{SnSe}_4^0$ , the vacancy and interstitialcy mechanisms were considered as shown in Fig. [4] in the manuscript and the corresponding NEB energies is shown in Fig. [6] and Fig. [7] for the vacancy and interstitialcy mechanisms respectively. The interstitialcy mechanism was found to be more favorable in both materials with lower

migration energy which is approximately 0.2 eV in both materials. For the  $\text{Li}_4\text{SnS}_4^*$  and  $\text{Li}_4\text{SnSe}_4^*$ , the interstitialcy mechanism was considered as shown in Fig. [5] in the manuscript and the corresponding NEB energies are shown in Fig. [7] in the manuscript. The migration energy for these materials was found to be approximately 0.07 eV which is much lower than the ground state structures indicating better conduction properties. The formation energies for vacancy-interstitial pairs was found to be much lower in the meta-stable state structures than the ground state structures pointing to a disordered nature of the meta-stable state structures. Table [VI] in the manuscript summarize the simulated formation energies and the migration energies and the total activation energies for these materials in comparison to experiment.

In order to get a better understanding of the properties of the materials, molecular dynamics simulation were performed for the ground state structures and the meta-stable state structures. The scatter plots shown in Fig. [8] in the manuscript for the  $\text{Li}_4\text{SnS}_4^0$  and  $\text{Li}_4\text{SnS}_4^*$  show a 3 dimensional migration pathways in these materials consistent with our NEB results. The fractional occupancy defined in Eq. (3) and Eq. (2) in the manuscript was calculated at each temperatures of the MD simulation, and is shown in Fig. [10] in the manuscript for the ground state and meta-stable state structures. It indicates that the meta-stable structures tend to become disordered at low temperature while the ground state structures remains ordered even at high temperature which is consistent with experimental observation. The calculated ionic conductivity according to Eq. (6) in the manuscript is shown in Fig. [11] in the manuscript for all the materials. The results show that the meta-stable state structures have a higher ionic conductivity than the ground state structures which is consistent with our NEB results.

## 6.3 Conclusions

In conclusions, we have identified a ground state and ideal meta-stable state structures for  $\text{Li}_4\text{SnS}_4$ ,  $\text{Li}_4\text{SnSe}_4$  and  $\text{Li}_4\text{GeS}_4$ . Based on these ideal models, Li ion migration was investigated for  $\text{Li}_4\text{SnS}_4^0$ ,  $\text{Li}_4\text{SnSe}_4^0$ ,  $\text{Li}_4\text{SnS}_4^*$ ,  $\text{Li}_4\text{SnSe}_4^*$  and found to be dominated by the interstitialcy mechanism along the **b** and **c** axes. According to the Li ion migration analysis, the meta-stable state structures was found to have a better conduction properties. The molecular dynamics simulations, show that the meta-stable state structures tend to be disordered at high temperature while the ground state structure remains ordered which is consistent with the experimental observation.

## 6.4 My Contribution

I performed the calculations and analyzed the results of defects, formation energy of vacancy-interstitial pairs, NEB, electronic structure, heat of decomposition for all the materials in this study. Also I performed all the MD simulation for  $\text{Li}_4\text{SnSe}_4^0$  and  $\text{Li}_4\text{SnSe}_4^*$ . I simulated the ground state structure and the metastable state structure for the  $\text{Li}_4\text{SnSe}_4$ . I wrote the manuscript attached to this report with the help of Jason Howard and N. A. W. Holzwarth.

## 6.5 Published Manuscript

The published manuscript of this projects is shown in appendix B.

# Chapter 7

**$\text{Li}_{14}\text{P}_2\text{O}_3\text{N}_6$  and  $\text{Li}_7\text{PN}_4$ :**

## **Computational study of two nitrogen rich crystalline LiPON electrolyte materials**

This work was published in the Journal of Power Sources, volume 364, pages 410–419, 2017. The full text of the paper may be found in appendix C. The publication is reproduced with a permission from Elsevier.

### **7.1 Overview**

In this work, we computationally examine the electrolyte properties of two recently reported nitrogen rich crystalline LiPON inorganic solid electrolyte materials,  $\text{Li}_{14}\text{P}_2\text{O}_3\text{N}_6$  [54] and  $\text{Li}_7\text{PN}_4$  [55, 56]. In particular, we use the LDA approximation and the PAW method in the framework of density functional theory to perform an in depth study

and investigation of the structure, Li ion conductivity and the stability of these materials. Finally, the simulations results of these two materials are compared to the oxygen rich material,  $\gamma$ -Li<sub>3</sub>PO<sub>4</sub>, to analyse the effect of nitrogen on the Li ion conductivity and the stability of these LiPON materials.

## 7.2 Main Publication Results

The simulated crystal structure of the Li<sub>14</sub>P<sub>2</sub>O<sub>3</sub>N<sub>6</sub> was found to have a trigonal structure characterized by the space group  $P\bar{3}$  (No. 147 as listed in the international Table of Crystallography). Fig. [1] in the manuscript shows a ball and stick diagram of this structure from two different perspectives and Table [1] in the manuscript list the calculated lattice constants and fractional coordinates compared with the experimental results. The calculated lattice constants are found to be in a good agreement with experiment and the simulated P, O and N fractional coordinates agree very well with experiment. However, the Li fractional coordinates differ by about 0.06 from experiment. The reason for this difference may be the insensitivity of the X-ray analysis to the Li positions due to their small atomic number. The trigonal symmetry of this structure was found to be stabilized by the isolated O<sup>2-</sup> ions located at the 2c sites. In addition, the crystal structure of this material features an interesting arrangement of the PON<sub>3</sub> tetrahedra, forming alternating O<sup>2-</sup> and N<sup>3-</sup> planes perpendicular to the c-axis. The simulated crystal structure of the Li<sub>7</sub>PN<sub>4</sub> was found to have a cubic structure characterized by the space group  $P\bar{4}3n$  (No. 218) with 8 formula units (96 atoms) in the unit cell. The simulated lattice constants and fractional coordinates of atoms agree well with the experiment. The Li density in these two structures was found to be approximately 0.2Å<sup>-3</sup> which is much higher than the Li density of 0.04Å<sup>-3</sup> of the  $\gamma$ -Li<sub>3</sub>PO<sub>4</sub>.

For these two materials, the partial density of states was calculated and compared to the  $\gamma$ -Li<sub>3</sub>PO<sub>4</sub> and the Li<sub>2</sub>O as shown in Fig. [2] in the manuscript. The decomposition energies for a possible products were calculated for Li<sub>14</sub>P<sub>2</sub>O<sub>3</sub>N<sub>6</sub> and Li<sub>7</sub>PN<sub>4</sub> as shown in Eq. (5) and Eq. (7) respectively. The electronic structure results for the Li<sub>14</sub>P<sub>2</sub>O<sub>3</sub>N<sub>6</sub>, shows that the valence band states are characterized by the 2p states of O with a bonding combinations with P 3s and 3p states while the conduction bands are characterized by the corresponding antibonding states. The partial density of states of the Li<sub>7</sub>PN<sub>4</sub> looks very similar to the  $\gamma$ -Li<sub>3</sub>PO<sub>4</sub>, while the Li<sub>7</sub>PN<sub>4</sub> has a smaller band gap between the valence bands and the conduction bands. The calculated decomposition energies for these materials shows a negative values at the right hand side of Eq. (5) and Eq. (7), which indicates that these materials are stable with respect to the decomposition in the products considered in these equations.

In preparation for the Li ion migration analysis, the energies of point defects were analysed for Li<sub>14</sub>P<sub>2</sub>O<sub>3</sub>N<sub>6</sub> in a  $2 \times 2 \times 1$  supercell and for the Li<sub>7</sub>PN<sub>4</sub> in the unit cell. The relative energies and the fractional coordinates for the distinct vacancies and interstitials are given in Table [2] in the manuscript for the Li<sub>14</sub>P<sub>2</sub>O<sub>3</sub>N<sub>6</sub> and in Table [5] for the Li<sub>7</sub>PN<sub>4</sub>. The Li<sub>14</sub>P<sub>2</sub>O<sub>3</sub>N<sub>6</sub> has 3 distinct vacancies and 2 distinct interstitials; the  $g'$  vacancy was found to have the lowest energy and the other has relative energies greater than 0.41 eV relative to it. The  $I$  interstitial was found to have the lowest energy and the  $II$  has a relative energy of 0.22 eV relative to the  $I$  interstitial. The Li<sub>7</sub>PN<sub>4</sub> has 5 distinct vacancies and 2 distinct interstitials, the  $f$  vacancy was found to have the lowest energy and the vacancies has a relative energy of 0.25 eV or less relative to it. The  $I$  interstitial has the lowest energy and the  $II$  has a relative energy of 0.32 relative to it. The formation energy to form vacancy-interstitial pairs was analysed as well for these materials. For the Li<sub>14</sub>P<sub>2</sub>O<sub>3</sub>N<sub>6</sub>, the lowest formation energy was found to be 0.3 eV which involves the  $I$  and  $g'$  pair, the other pairs has

a formation energy greater than 1 eV; for  $\text{Li}_7\text{PN}_4$ , the formation energy was found to be large with a minimum value of 1.9 eV which involves the  $I$  interstitial and all kind of vacancies. The Li ion migration was analysed in these structures as well. For the  $\text{Li}_{14}\text{P}_2\text{O}_3\text{N}_6$ , the vacancy mechanism was considered as shown in Fig. [3a] in the manuscript and the corresponding NEB energies is shown in Fig. [3b] in the manuscript. The path that takes place near the oxygen plane which involves the  $g'$  vacancies was found to be the most favourable with a migration energy of 0.3 eV. The pure interstitial mechanism and the kick-out mechanism were considered as shown in Fig. [3c] and the corresponding NEB energies is shown in Fig. [3d] in the manuscript. The NEB energy for these mechanism was found to be about 0.6 eV which is much larger than the vacancy mechanism. For the  $\text{Li}_7\text{PN}_4$ , only the vacancy mechanism was considered for diffusion because of geometrical consideration. For this mechanism, diffusion takes place in a 3 dimensions, the NEB energies for path considered are shown in Fig. [6a] in the manuscript. The lowest migration energy was found to be 0.3 eV. For the path  $i \rightarrow e \rightarrow i \rightarrow e \rightarrow i$ . The minimum migration energy is lower than the experimental activation energy  $E_a = 0.48$  eV, which suggest that the experimental materials have a significant source of Li ion vacancies which might be due to the presence of O ions. We explored the presence of O in this material by substituting N by O near the minimum energy path as shown in Fig. [6b] and Fig. [6d] in the manuscript and the corresponding NEB for the minimum energy path after the substitution of O is shown in Fig. [6c] in the manuscript. The migration energy for the minimum energy path was raised to 0.5 eV after the O substitution which agrees better with experiment. The formation and the migration energies for these materials are summarized in Table [6] in the publication.

Interfaces with Li were considered for both of these materials in order analyse their stability. For the  $\text{Li}_{14}\text{P}_2\text{O}_3\text{N}_6$ , the surface along the  $\mathbf{c}$  direction near the nitrogen plane



was found to be more favorable according to the interface with vacuum and the  $\gamma_{ab}$  in Eq. (4.47) converges for one single layer of the bulk material. For this particular surface, we prepared two series of configurations with Li as shown in Fig. [4a] and [4b] in the manuscript. The corresponding plots of the surface energy versus the number  $n_b$  of metallic Li atoms are evaluated according to Eq. (4.48) and plotted in Fig. [4c] in the manuscript. The configuration ( $\Omega_1$ ) has more regularity with the electrolyte and therefore produces less strain on it, the  $\gamma_{ab}^{lim}$  for the two configurations was found to be  $0.05 \text{ eV}/\text{\AA}^2$  which is similar to the value reported by Lepley et al., [42] for the interfaces of  $\gamma$  and  $\beta$   $\text{Li}_3\text{PO}_4$  with Li metal. For configuration 1, the partial density of states was calculated as shown in Fig. [4d] in the manuscript. The partial density of states for the interior of the electrolyte is very similar to the bulk structure. The metallic Li states are separated from the interior of the electrolyte and overlap with the top of the valence band by approximately 1 eV. The partial density of states associated with metallic Li at the interface has more electronic charge than those in the interior of the electrolyte, and the Fermi level of the system falls well within the band gap of the electrolyte. For the  $\text{Li}_7\text{PN}_4$ , the partial density of states was analysed as shown in Fig. [7c] for the interface with metallic Li shown in Fig. [7b]. The partial density of states indicates that the  $\text{Li}_7\text{PN}_4/\text{Li}$  system has the properties of ideal interface. It is actually metastable and the Fermi level falls well within the band gap of the interior of the electrolyte. The partial density of states contribution for metallic Li has the typical shape of free electron metal.

### 7.3 Conclusion

In conclusion, the simulations suggest that both of the nitrogen rich materials -  $\text{Li}_{14}\text{P}_2\text{O}_3\text{N}_6$  and  $\text{Li}_7\text{PN}_4$  - are promising solid electrolyte materials due to their ideal interface with metallic Li and their promising activation energies. The simulated ac-

tivation energies for these materials given in Table [6] in the manuscript, shows that the simulated activation energy for the  $\text{Li}_7\text{PN}_4$  agrees well with experiment, the activation energy for the  $\text{Li}_{14}\text{P}_2\text{O}_3\text{N}_6$  is lower than experimental activation energies of  $\text{Li}_7\text{PN}_4$  and  $\gamma$ - and  $\beta$ -  $\text{Li}_3\text{PO}_4$  which points to a better conduction properties. The dominant diffusion mechanism for the nitrogen rich materials was found to be the vacancy mechanism in comparison to the kick-out mechanism in the  $\gamma$ - $\text{Li}_3\text{PO}_4$ .

## 7.4 My contribution

I performed the majority of the computations and geometry analyses of this study. The paper was written by me in collaboration with N. A. W. Holzwarth.

## 7.5 Published Manuscript

The published manuscript of this project is shown in appendix C.

# Chapter 8

## Computational study of the structural and electrolyte properties of $\text{Li}_4\text{PS}_4\text{I}$ and related materials

### 8.1 Introduction

Several recent experimental [57–60] and computational [61] studies have shown that the incorporation of LiI into lithium thiophosphate electrolytes can improve their stability and ionic conductivity with possible positive implications for battery technology. In the present work, first-principles computer simulations are used to study the structural and stability properties of these materials, as well as to model their mechanisms of ionic conductivity, and to examine properties of idealized interfaces of these electrolytes with Li metal anodes. In general, our results are consistent with the recently reported results of Sicolo *et al.* [61] for  $\text{Li}_4\text{PS}_4\text{I}$ , and provide some additional insights into its structure and its stability issues.

## 8.2 Crystal structures

Rangasamy *et al.* [57] reported a crystalline electrolyte having the composition of  $\text{Li}_7\text{P}_2\text{S}_8\text{I}$ . While the crystal structure was not analyzed, independent researchers were able to form the same material as evidenced by the X-ray diffraction pattern [59,60]. To our knowledge, the crystal structure of this material has not yet been successfully determined [62].

More recently, Sedlmaier *et al.* [58] synthesized and analyzed a crystalline electrolyte having the composition of  $\text{Li}_4\text{PS}_4\text{I}$ . Its room temperature crystal structure was found to be tetragonal having the space group [63]  $P4/nmm$  (No. 129) with disorder (fractional occupancy) on the Li sites. It is reasonable to assume that this Sedlmaier structure represents a high-temperature phase of  $\text{Li}_4\text{PS}_4\text{I}$  and that a lower temperature phase should exist with full occupancy on the Li sites. Such an ordered  $\leftrightarrow$  disordered crystal phase transition has been observed for many ion-conducting system such as AgI [64] and lithium argyrodites [65]. The challenge for the simulations is to first search for an ordered ground state (low temperature) structure of  $\text{Li}_4\text{PS}_4\text{I}$  and to determine possible candidate structures for  $\text{Li}_7\text{P}_2\text{S}_8\text{I}$ .

The structural analysis of Sedlmaier *et al.* [58], is based on the observation that  $\text{Li}_4\text{PS}_4\text{I}$  is derived from  $\alpha\text{-Li}_3\text{PS}_4$  structure, shown in Fig. [8.1] which is distinguished by having its lattice axes aligned along the tetrahedral axes of the  $\text{PS}_4^{3-}$  ions as opposed to the alignment of the crystal axes along one or the P–S bonds in the  $\beta$  and  $\gamma$  structures [48]. The structure shown in Fig. [8.1] represents the analysis by Homma *et al.* [66] of the experimental high temperature ( $T = 906$  K) phase of  $\alpha\text{-Li}_3\text{PS}_4$ , based on the space group  $Pbcn$  (No. 60). Based on this high temperature structure, we are able to optimize a similar structure representing a zero temperature metastable phase of  $\alpha\text{-Li}_3\text{PS}_4$ . The simulated lattice constants and fractional coordinates are compared with experiment in Table 8.1. It is perhaps understandable that there are discrepancies between the simulations and experiments since the experiments were carried out at

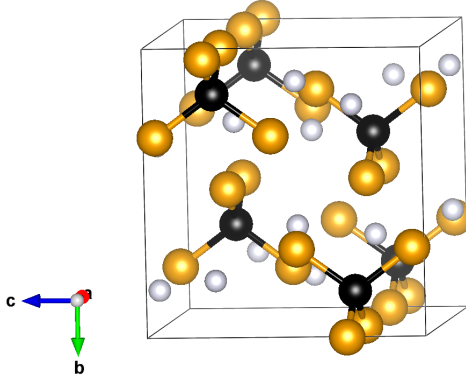


Figure 8.1: Ball and stick model of optimized structure of  $\alpha$ - $\text{Li}_3\text{PS}_4$  with the space group  $Pbcn$ . Li, P, and S sites are represented with gray, black, and orange balls, respectively.

906 K while the simulations assume 0 K. It is not clear that this optimized structure is related to the physical materials, since its static lattice energy is 0.24 eV per formula unit higher than that of the experimentally verified low energy structure of  $\gamma$ - $\text{Li}_3\text{PS}_4$ . On the other hand, it does suggest that the tetrahedrally-oriented  $\text{PS}_4^{-3}$  components can exist in thiophosphate materials.

Sedlmaier *et al.* [58], reasoned that that  $\text{Li}_4\text{PS}_4\text{I}$  is derived from  $\alpha$ - $\text{Li}_3\text{PS}_4$  by replacing two  $\text{Li}_3\text{PS}_4$  units with two  $\text{LiI}$  units. This is consistent with the structural analysis of their synthesized crystals as illustrated in Fig. [8.2]. In order to search for a low temperature structure, we started with this  $P4/nmm$  structure which is disordered on the Li sites and we optimized a series of structures with different Li configurations. We found an ordered metastable structure as a candidate for the low temperature phase of this material. It has an orthorhombic lattice with the space group  $Pmn2_1$  (space group No. 31) [63]. In order to compare this candidate ground state structure with the analysis of Sedlmaier *et al.* [58], it is first convenient to shift the original results to its equivalent “choice 1” coordinates and to rotate the conventional setting of the  $Pmn2_1$  space group by 90 degrees about the  $x$ -axis. In this setting, the four symmetry elements expressed in terms of the fraction coordinates

Table 8.1: Lattice parameters of  $\alpha$ -Li<sub>3</sub>PS<sub>4</sub> in the *Pbcn* structure. The “Calc.” results were determined from optimized static lattice calculations in this work with lattice constants scaled by 1.02. The “Exp.” results report measurements at 906 K reported in Ref. [66].

		Calc.			Exp.		
$a$ (Å)		8.87			8.61		
$b$ (Å)		8.40			9.02		
$c$ (Å)		8.16			8.42		
At.	Wyck.	$x$	$y$	$z$	$x$	$y$	$z$
P	4 $c$	0.000	0.842	0.250	0.000	0.827	0.250
S	8 $d$	0.306	0.482	0.248	0.307	0.453	0.250
S	8 $d$	0.018	0.306	0.545	0.004	0.294	0.550
Li	8 $d$	0.750	0.640	0.010	0.708	0.631	0.069
Li	4 $c$	0.000	0.200	0.250	–	–	–

are  $(x, y, z)$ ,  $(\bar{x}, y, z)$ ,  $(x + \frac{1}{2}, y + \frac{1}{2}, \bar{z})$ , and  $(\bar{x} + \frac{1}{2}, y + \frac{1}{2}, \bar{z})$ . The corresponding comparison is given in Table. [8.2]. Even though the ground state structure deviates from tetragonal, the similarity of the fractional coordinates of the two structures is apparent. The comparison is also clear from the ball and stick visualizations of the structures shown in Fig. [8.3] and Fig. [8.2].

At this point, we can ask the question of whether this structure can exist with one of LiI groups removed as a model of the ground state structure of Li<sub>7</sub>P<sub>2</sub>S<sub>8</sub>I. Optimizing several configurations of this structure, the lowest energy structure is shown in Fig. [8.4]. The optimized and measured lattice constants for these materials are listed in Table [8.3].

A measure of the consistency of these results with experiment is the comparison of simulated and measured X-ray diffraction patterns. The X-ray pattern for Li<sub>7</sub>P<sub>2</sub>S<sub>8</sub>I was reported in Ref. [57] and is reproduced in Fig. [8.5]. The X-ray pattern for Li<sub>4</sub>PS<sub>4</sub>I was reported in Ref. [58] for Mo  $K\alpha$  radiation. However, using the refinement parameters of their analysis, it is possible to visualize the equivalent pattern for Cu  $K\alpha$  radiation. This is also shown in Fig. [8.5]. From the comparison of the X-ray patterns of the experimental Li<sub>7</sub>P<sub>2</sub>S<sub>8</sub>I and Li<sub>4</sub>PS<sub>4</sub>I crystals, it is apparent that

Table 8.2: Optimized structure for  $\text{Li}_4\text{PS}_4\text{I}$ , comparing the fractional coordinates for the ground state structure  $Pmn2_1$  (No. 31) rotated from conventional setting as explained in the text with the Sedlmaier [58] structure  $P4/nmm$  (No. 129, choice 1). The columns labeled “Wyck.” give the multiplicity and Wyckoff label. for the corresponding group. In some cases, multiple fractional coordinates are listed for the higher symmetry structure. In the  $Pmn2_1$  structure all Li sites are fully occupied, while in the  $P4/nmm$  structure the X-ray data were analyzed with fractional Li occupancies of 0.58 for  $2a$ , 0.68 for  $2c$ , 0.53 for  $4d$ , and 0.38 for  $8j$  sites.

At.	$Pmn2_1$				$P4/nmm$			
	Wyck.	$x$	$y$	$z$	Wyck.	$x$	$y$	$z$
I	2 $a$	0.000	0.529	0.839	2 $c$	0.000	0.500	0.847
P	2 $a$	0.000	0.000	0.500	2 $b$	0.000	0.000	0.500
S	2 $a$	0.000	0.190	0.280	8 $i_1, i_2$	0.000	0.194	0.297
S	2 $a$	0.000	0.802	0.302	8 $i_3, i_4$	0.000	0.806	0.297
S	4 $b$	0.302	0.506	0.291	8 $i_5..i_8$	0.306	0.500	0.297
Li	2 $a$	0.000	-0.012	0.000	2 $a$	0.000	0.000	0.000
Li	2 $a$	0.000	0.476	0.383	2 $c$	0.000	0.500	0.406
Li					4 $d$	0.250	0.250	0.000
Li	4 $b$	0.216	0.723	0.583	8 $j_1..j_4$	0.204	0.704	0.585
Li					8 $j_5..j_8$	0.204	0.296	0.585

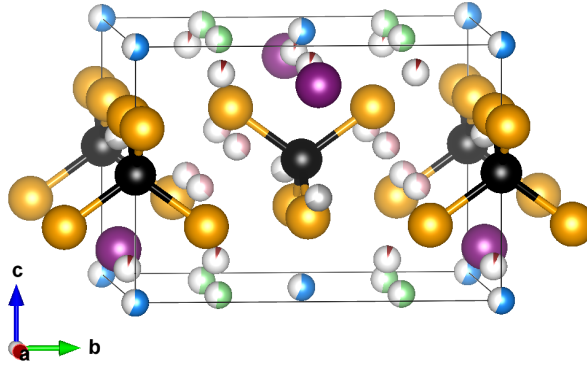


Figure 8.2: Ball and stick drawing of unit cell for the Sedlmaier structure of  $\text{Li}_4\text{PS}_4\text{I}$  described in Ref. [58] having the space group  $P4/nmm$ . I, P, and S sites are represented by purple, black, and orange balls, respectively. The 5 distinct partially occupied Li sites are represented by partially shaded grey (1), pink (2), blue (3), green (4), and red (5) balls.

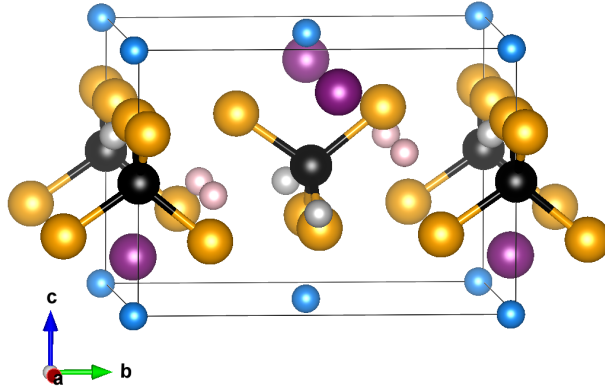


Figure 8.3: Ball and stick drawing of unit cell for  $Pmn2_1$  structure of  $\text{Li}_4\text{PS}_4\text{I}$ . I, P, and S sites are represented by purple, black, and orange balls, respectively. The 3 distinct Li sites are represented by small gray (1), pink (2), and blue (3) balls.

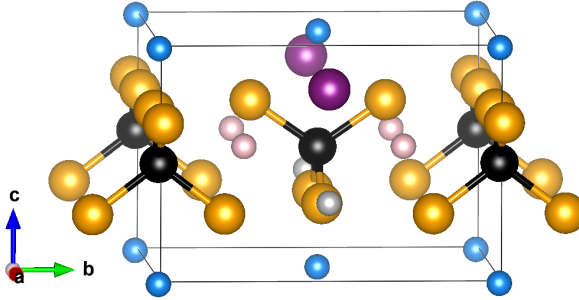


Figure 8.4: Ball and stick drawing of unit cell for the optimized structure of  $\text{Li}_7\text{P}_2\text{S}_8\text{I}$ . I, P, and S sites are represented by purple, black, and orange balls, respectively. The small balls representing Li sites are colored in order identify corresponding sites as in Fig. [8.3].

Table 8.3: Comparison of lattice constants in  $\text{\AA}$  units; all simulation results were scaled by 1.02 to correct for the LDA error. The “LT- $\text{Li}_4\text{PS}_4\text{I}$ ” column lists the simulated ordered model results illustrated in Fig. 8.3. The “HT- $\text{Li}_4\text{PS}_4\text{I}$ ” column lists the experimental result reported in Ref. [58]. The “ $\text{Li}_7\text{P}_2\text{S}_8\text{I}$ ” column lists the simulated ordered model results illustrated in Fig. 8.4.

	LT- $\text{Li}_4\text{PS}_4\text{I}$	HT- $\text{Li}_4\text{PS}_4\text{I}$	$\text{Li}_7\text{P}_2\text{S}_8\text{I}$
$a$	8.40	8.48	8.57
$b$	8.56	8.48	8.58
$c$	6.02	5.93	5.95



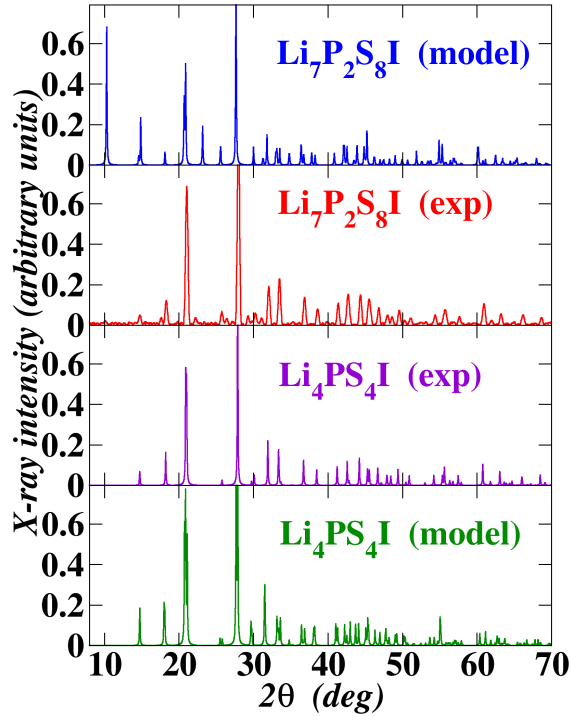


Figure 8.5: Simulated and measured X-ray diffraction patterns for Cu  $K\alpha$  radiation. From top to bottom: X-ray pattern for modeled  $\text{Li}_7\text{P}_2\text{S}_8\text{I}$  unit cell, X-ray data for  $\text{Li}_7\text{P}_2\text{S}_8\text{I}$  provided by Zachary Hood and consistent with Ref. [59,60], generated X-ray pattern for experimental HT- $\text{Li}_4\text{PS}_4\text{I}$  from Ref. [58], and generated X-ray pattern for modeled LT- $\text{Li}_4\text{PS}_4\text{I}$  unit cell.

the two structures are closely related. The two simulated structures also show similar X-ray patterns. Some of the discrepancies are apparently due to the fact that we are simulating the lower symmetry ordered structures while the experimental structures are disordered higher symmetry structures. One expects the lower symmetry ordered structures to exhibit extra reflections and detailed peak splitting. On the other hand, the main reflections of the patterns are clearly related.

From the simulations of the optimized structures, we determine the internal energies of the ground state materials in the static lattice approximation. Differences of this internal energies estimate the relative stabilities of these systems at zero temperature in the form:

Table 8.4: Static lattice contributions to various energy differences defined by Eq. (8.1).

$\Delta E$ (eV)	Reactants	Products
0.24	$\alpha$ -Li <sub>3</sub> PS <sub>4</sub>	$\gamma$ -Li <sub>3</sub> PS <sub>4</sub>
-0.02	LT-Li <sub>4</sub> PS <sub>4</sub> I	$\alpha$ -Li <sub>3</sub> PS <sub>4</sub> + LiI
0.25	Li <sub>7</sub> P <sub>2</sub> S <sub>8</sub> I	2 $\alpha$ -Li <sub>3</sub> PS <sub>4</sub> + LiI
0.22	LT-Li <sub>4</sub> PS <sub>4</sub> I	$\gamma$ -Li <sub>3</sub> PS <sub>4</sub> + LiI
0.49	Li <sub>7</sub> P <sub>2</sub> S <sub>8</sub> I	2 $\gamma$ -Li <sub>3</sub> PS <sub>4</sub> + LiI

$$\Delta E = \sum_i U_{SL}(R_i) - \sum_j U_{SL}(P_j), \quad (8.1)$$

where  $R_i$  and  $P_j$  represent the reactant and product materials, respectively. A positive value for  $\Delta E$  indicates that the reactants are unstable relative to the products. A table of these energy differences is given in Table 8.4. These results show that the static lattice contributions to the stability of the low temperature form of Li<sub>4</sub>PS<sub>4</sub>I is unstable with respect to decomposition into its constituents in their ground states –  $\gamma$ -Li<sub>3</sub>PS<sub>4</sub> and LiI. The Li<sub>7</sub>P<sub>2</sub>S<sub>8</sub>I material is even less stable.

### 8.3 The Helmholtz Free Energy

In order to obtain an accurate understanding for the stability of Li<sub>4</sub>PS<sub>4</sub>I, we considered calculating the Helmholtz free energy for the decomposition energies calculations. The static lattice energies used in Eq. [8.1] for the decomposition energies calculation neglect the effect of the quantum mechanical lattice vibrations. A more accurate quantity can be used for these decomposition energies is the Helmholtz free energy. In general, the Helmholtz free energy,  $F$ , is a function of the system temperature and it can be written for any system as:

$$F = U_{SL} + F_{vib}(T) - TS_{\Omega}, \quad (8.2)$$

where  $T$  is the temperature of the material,  $U_{SL}$  is the static lattice energy,  $F_{vib}(T)$  is the vibrational Helmholtz free energy,  $S_{\Omega}$  is the configuration entropy and is given by the expression:

$$S_{\Omega} = k_B \ln(\Omega), \quad (8.3)$$

where  $k_B$  is the Boltzmann constant and  $\Omega$  is the number of possible configurations for the atoms in the crystal. The vibrational free energy,  $F_{vib}(T)$ , is given by the expression:

$$F_{vib}(T) = k_B T \int_0^{\infty} \ln \left[ 2 \sinh \left( \frac{\hbar \omega}{2k_B T} \right) \right] g(\omega) d\omega, \quad (8.4)$$

Where  $g(\omega)$  is the phonon density of states, which is calculated using the harmonic approximation at fixed lattice constants, as follows:

$$g(\omega) = \frac{V}{(2\pi)^3} \int d^3q \sum_{v=1}^{3N} \delta(\omega - \omega_v(\mathbf{q})), \quad (8.5)$$

where,  $V$  is the volume of the unit cell,  $N$  is the number of atoms in the unit cell,  $\mathbf{q}$  is the phonon wave vector. The integral was carried out over the whole Brillouin zone. For each  $\mathbf{q}$  point there are  $3N$  normal modes of vibration  $\omega_v$ , which are determined from the diagonalization of the dynamical matrix.

When considering the Helmholtz free energy for the what we called LT-Li<sub>4</sub>PS<sub>4</sub>I and its decomposition products,  $\gamma$ -Li<sub>3</sub>PS<sub>4</sub> and LiI, the configurational entropy given in Eq. [8.3] can be ignored since these materials are fully ordered. In order to calculate the vibrational Helmholtz free energy for these materials, their phonon spectra was generated using the harmonic approximation. Fig. [8.6] shows the phonon density

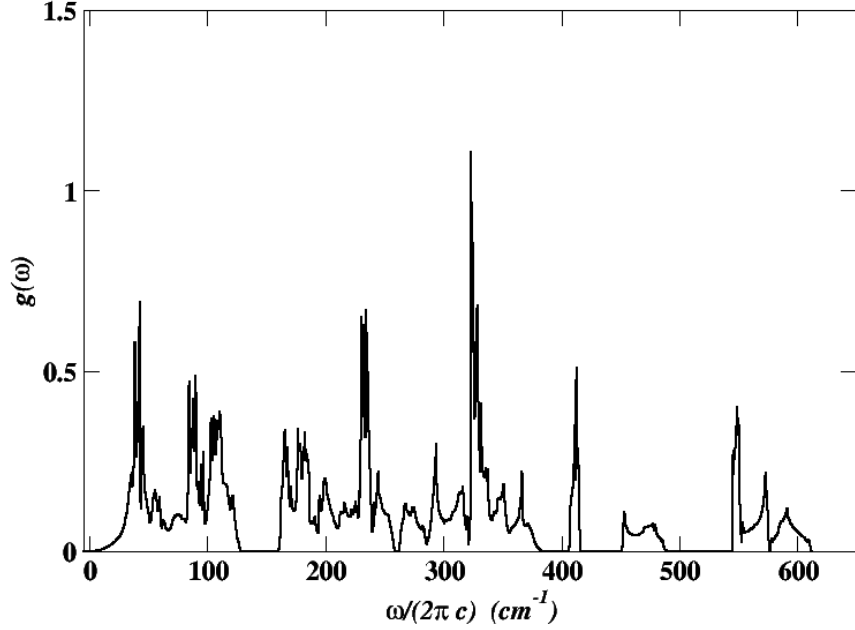


Figure 8.6: Plot of the phonon density of states  $g(\omega)$  for the LT-Li<sub>4</sub>PS<sub>4</sub>I using the harmonic phonon approximation at the optimize lattice parameters.

of states for the LT-Li<sub>4</sub>PS<sub>4</sub>I. As shown in Fig. [8.6], the normal modes of vibrations for the LT-Li<sub>4</sub>PS<sub>4</sub>I are all real corresponding to the real forces acting on the atoms, which ensure that the LT-Li<sub>4</sub>PS<sub>4</sub>I is a real structure from a dynamical prospective and not just an error of the calculations.

The calculated Helmholtz free energy per formula unit for the LT-Li<sub>4</sub>PS<sub>4</sub>I and the sum of it is decomposition products, the  $\gamma$ -Li<sub>3</sub>PS<sub>4</sub> and LiI, over a temperature range form 0 K to 800 K is shown in Fig. [8.7]. The figure shows that the free energy for the LT-Li<sub>4</sub>PS<sub>4</sub>I remains greater than the free energy for the decomposition products, it only becomes lower than the free energy of the decomposition products at high temperature near 800 K. The difference in free energy between the LT-Li<sub>4</sub>PS<sub>4</sub>I and the free energy of the decomposition products near room temperature is about 0.1 (eV/formula unit), which is lower than the static lattice difference 0.22 eV shown in Table. [8.4] due to the vibrational contribution to the free energy. This suggests that

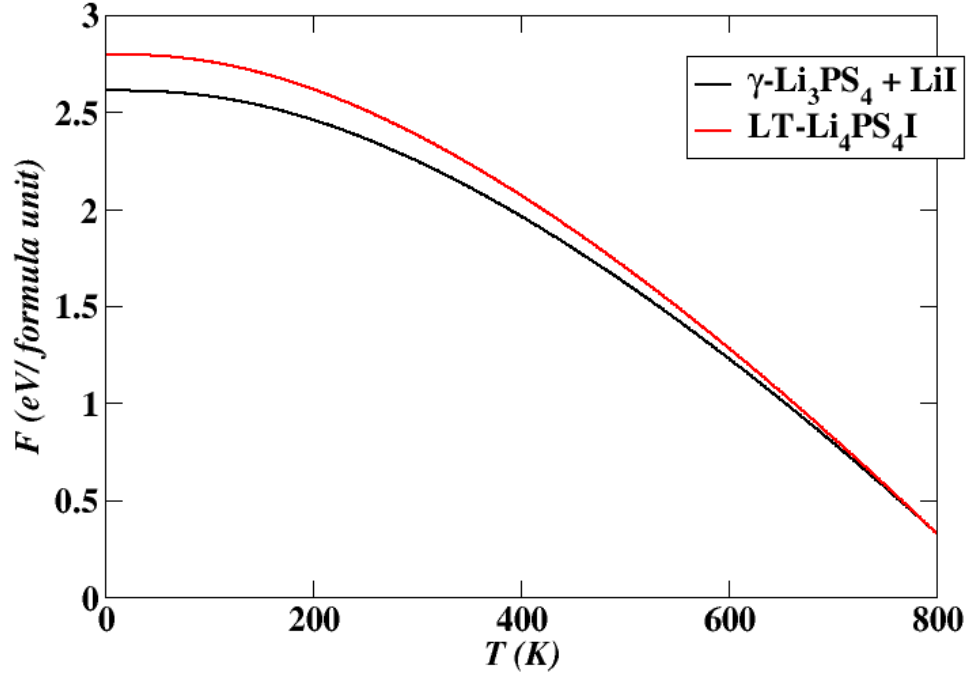


Figure 8.7: Comparison of the Helmholtz free energies per formula unit as a function of temperature for  $\text{LT-Li}_4\text{PS}_4\text{I}$  (black line) and the sum of contributions of  $\gamma\text{-Li}_3\text{PS}_4$  and  $\text{LiI}$  (red line).

$\text{LT-Li}_4\text{PS}_4\text{I}$  is meta-stable with respect to decomposition into  $\gamma\text{-Li}_3\text{PS}_4$  and  $\text{LiI}$  in this temperature range.

## 8.4 Models of the disordered phase

The second task of the simulations is to analyse the high temperature structure of  $\text{Li}_4\text{PS}_4\text{I}$ ,  $\text{HT-Li}_4\text{PS}_4\text{I}$ , which was observed experimentally to have a tetragonal crystal structure with disorder (fractional occupancy) on the Li sites. In order to do so, we have implemented the following strategy:

- (1) The experimental lattice constants shown in Table. [8.3] were scaled by 0.98 to take into account the known LDA underestimation of lattice constants.

(2) Starting from the scaled lattice constants a  $2 \times 2 \times 2$  supercell was created for the tetragonal HT-Li<sub>4</sub>PS<sub>4</sub>I. The supercell contains 16 unique *a* Li sites, 16 unique *c* Li sites, 32 unique *d* Li sites, 64 unique *j* Li sites, 64 unique *i* Li sites.

(3) The experimental fractional occupancy for the Li sites was approximated in this supercell by removing some of the occupied Li sites while ensuring the charge neutrality of the material. For the *a* site 7 out of the 16 occupied Li sites were removed which corresponds the fractional occupancy of 0.5625, for the *c* site 5 out the 16 occupied Li sites were removed which corresponds the fractional occupancy of 0.6875, for the *d* site 16 out the 32 occupied Li sites were removed which corresponds the fractional occupancy of 0.50, for the *j* site 40 out the 64 occupied Li sites were removed which corresponds the fractional occupancy of 0.375, for the *i* site 60 out the 64 occupied Li sites were removed which corresponds the fractional occupancy of 0.0625.

(4) For each of these sites 5 different configurations were generated by randomly choosing the atoms to remove for each site, resulting to a total of  $5^5$  possible combinations of these configurations. Finally, we have randomly selected 100 structures out of the  $5^5$  possible combinations.

(5) We relaxed the atomic positions in these 100 structures at fixed lattice constants. The reason we chose to fix the lattice constants is that each of these structures experience different stress due to the different arrangement in the Li sites, which will lead to a different shape of unit cell, and from our experience the final shape for most structures will no longer remain tetragonal and therefore it will represent the HT-Li<sub>4</sub>PS<sub>4</sub>I.

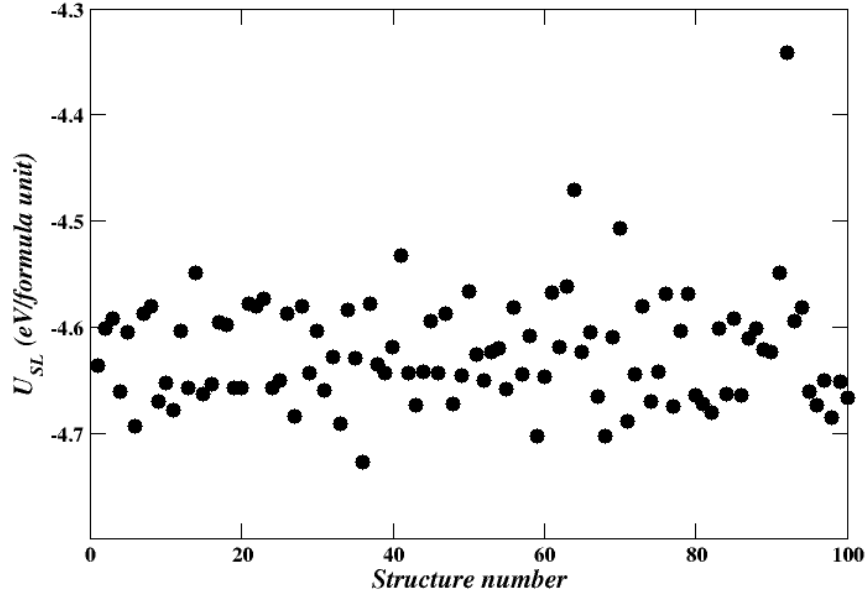


Figure 8.8: The energy per formula unit for a 100 disordered structures of  $\text{Li}_4\text{PS}_4\text{I}$  with a SOF similar to experiment. A 9995 eV was added to the energies of these structures.

The relaxed static lattice energies of these 100 disordered structures are shown in Fig. [8.8], and the energies distribution is shown in Fig. [8.9]. The energies shown in Fig. [8.8] shows that several disordered structures have a comparable and even lower energies relative to the LT- $\text{Li}_4\text{PS}_4\text{I}$ . In particular, structure # 36 was found to have the lowest energy among the configurations and its energy is 0.03 eV/formula lower than the LT- $\text{Li}_4\text{PS}_4\text{I}$ , structures # 68 and # 59 were found to have an energy lower than the LT- $\text{Li}_4\text{PS}_4\text{I}$  by 0.003 eV/formula, structure # 33 was found to have a similar energy to the LT- $\text{Li}_4\text{PS}_4\text{I}$ . The presence of several disordered configurations with energies lower than our optimized LT- $\text{Li}_4\text{PS}_4\text{I}$ , shown in Fig. [8.3], suggest that this structure is just one of many meta-stable structures and it does not represent a fully ordered low temperature phase of  $\text{Li}_4\text{PS}_4\text{I}$ .

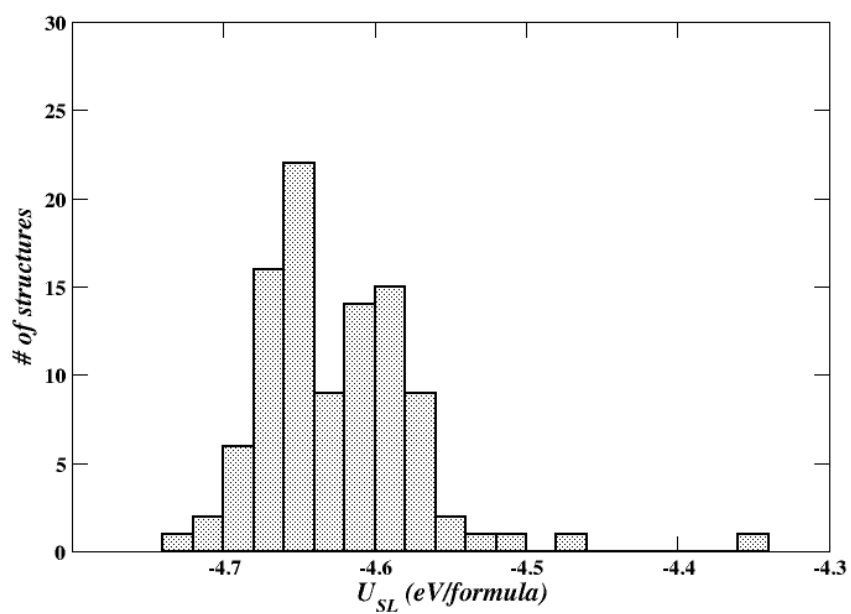


Figure 8.9: A histogram for the energy per formula unit of the generated 100 disordered structures of  $\text{Li}_4\text{PS}_4\text{I}$ .



We have also calculated the Helmholtz free energy for 100 disordered configurations of  $\text{Li}_4\text{PS}_4\text{I}$ , with the static lattice energy and energy distribution shown in Fig. [8.8] and Fig. [8.9] respectively, and its decomposition products, the  $\gamma\text{-Li}_3\text{PS}_4$  and  $\text{LiI}$ . For these configurations, we approximated  $F_{vib}(T)$  in Eq. [8.3] from the result of  $\text{LT-Li}_4\text{PS}_4\text{I}$ . The configurational entropy in Eq. [8.3] was calculated considering the experimental SOF, the total number of configurations of the atoms in the crystal in Eq. [8.3] was calculated, as follows:

$$\Omega = \Omega_a \times \Omega_c \times \Omega_d \times \Omega_j \times \Omega_i \quad (8.6)$$

Where  $\Omega_a, \Omega_c, \Omega_d, \Omega_j, \Omega_i$  are the number of possible configurations for the  $a, c, d, j, i$  respectively. Which were calculated in the  $2 \times 2 \times 2$  supercell of the disordered model, as follows:

$$\Omega_x = \binom{n_x}{N_x} \quad (8.7)$$

where  $\Omega_x$  is the number of configurations for site  $x$ ,  $N_x$  the total number of available  $x$  sites and  $n_x$  is the number of occupied  $x$  sites. As described in our strategy for modeling the disordered structure,  $N_x = 16, 16, 32, 64, 64$  for the  $a, c, d, j, i$  respectively and  $n_x = 9, 11, 16, 24, 4$  for the  $a, c, d, j, i$ .

Since most of the disordered structures falls in the energy  $[-4.7 - -4.6]$  eV/formula unit, as shown in Fig. [8.9]. The static lattice energy was approximated by taking the average of the energies of the 100 disordered structures shown in Fig. [8.8]. The calculated Helmholtz free energy per formula unit for the 100 disordered configurations of  $\text{Li}_4\text{PS}_4\text{I}$  and the sum of its decomposition products, the  $\gamma\text{-Li}_3\text{PS}_4$  and  $\text{LiI}$ , over a temperature range from 0 K to 800 K is shown in Fig. [8.10]. The Figure shows that the free energy for the disordered  $\text{Li}_4\text{PS}_4\text{I}$  equals the free energy for the decomposition products at 350 K and it becomes even lower than the free energy beyond

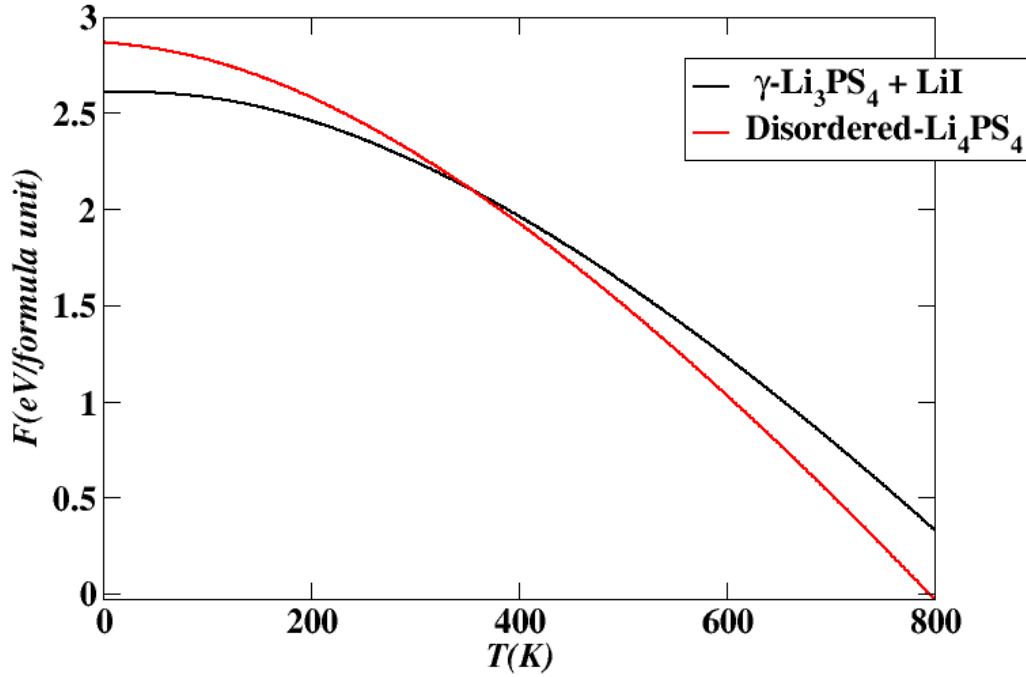


Figure 8.10: Comparison of the Helmholtz free energies per formula unit as a function of temperature for the 100 disordered structures of  $\text{Li}_4\text{PS}_4\text{I}$  and the sum of contributions of  $\gamma\text{-Li}_3\text{PS}_4$  and  $\text{LiI}$

this temperature. Which suggest that the disordered  $\text{Li}_4\text{PS}_4\text{I}$  is stable even at low temperature.

Our structural and stability analysis of  $\text{Li}_4\text{PS}_4\text{I}$ , has so far failed to find a stable ordered ground state structure, but has shown that configurational entropy is likely to play an important role in stabilizing the disordered phase of the material at room temperature.

## 8.5 $\text{Li}_4\text{PS}_4\text{I}$ Interface with metallic Li

The third task of the simulations, is to investigate the stability of the material with metallic Li. Several surfaces of  $\text{Li}_4\text{PS}_4\text{I}$  modeled by the  $Pnm2_1$  structure were investigated for their interface with metallic Li, including the (100) surface, (001) surface, and the (110) surface. The (100) and (001) surfaces have equal numbers of LiI groups within their model supercells. The (110) surface is more interesting since it has more LiI groups at its surface and therefore its study helps to analyze the effect of LiI on the stability of this material. Interfaces of these three surfaces with metallic Li were investigated. In each case, the supercell contained 5 layers of  $\text{Li}_4\text{PS}_4\text{I}$  and several layers of metallic Li. In order to obtain a qualitative measure of the interface stability, the partial densities of states were calculated for each of these interfaces, distinguishing the contributions from the bulk of the material, for the interface, and for the metallic Li layers. The interfaces simulations and the partial density of states analysis shows a reactivity of this material with metallic Li, as we observe S-P bonds breaking at the interface, and a  $\text{Li}_2\text{S}$  layer forming at the interface. However, the reactivity is limited to the atoms at the interface since the bulk of the material is relatively unchanged by the metallic Li layers. One interesting observation is that the (110) surface has fewer bonds breaking than (100) and (001) surfaces due to the presence of extra LiI at this surface. The interface simulations show that this material is reactive with metallic Li. However, we believe it is less reactive than its analogue  $\text{Li}_3\text{PS}_4$ . We observe fewer P-S bonds breaking for  $\text{Li}_4\text{PS}_4\text{I}/\text{Li}$  than for  $\text{Li}_3\text{PS}_4/\text{Li}$ , which suggests that LiI increases the stability of this material with metallic Li.

## 8.6 Molecular Dynamics simulation of $\text{Li}_4\text{PS}_4\text{I}$

Molecular dynamics simulation were performed for several ordered and disordered structure models of  $\text{Li}_4\text{PS}_4\text{I}$ . The MD simulations were performed with the microcanonical ensemble (NVE) using temperatures between 300 K to 800 K. The total time of the simulation was about (13-18) ps, and time step (dt) used in the simulation is 2 fs. The site occupancy factor (SOF) was calculated over time and the temperatures of the MD simulation, the SOF analysis shows that all the atoms in the structure have fractional occupancy with ( $\text{SOF} < 1$ ) and to be consistent with the experimentally reported SOF. In order to understand the Li migration of the atoms in this material, the Li mobility was visualized with a ball and stick model of the crystal with superposed Li positions at 136 time steps at intervals of 0.05 ps at 600 K temperature. The visualization shows a three dimensional migration pathways along the x,y and z directions for the Li ion in the crystal. In order to analyse the probability of these pathways, we have separated the mean square displacement of the Li to x,y and z components over the time of the simulation, the x and y components was found to be equal and the z-component was found to be much larger than the x and y components, which indicates that the z-axis is a more favorable path for Li diffusion. The diffusion coefficient was calculated from the mean square displacement of the Li atoms over the temperature of the MD simulations, and the activation energy was calculated from the diffusion coefficient. The calculated activation energy was found to be much lower than the experimentally measured value which indicates that  $\text{Li}_4\text{PS}_4\text{I}$  might be a true superionic conductor with higher conductivity than the experimental measurement.

# Chapter 9

## Topological Doping Effects in 2D Chalcogenide Thermoelectrics

### 9.1 Abstract

Two-dimensional, topological systems as seen in numerous chalcogenides, can present novel opportunities in heterogeneous conduction that are just beginning to be unlocked. In this work, a phase coherent, metal dopant is added to reactive edges of the low-dimensional  $\text{Bi}_2\text{Te}_3$  system. This results in an atomic heterojunction interface and a facile charge exchange in a region of the platelet that is proximal to its known topological states. Temperature dependent conductivity suggests that local band bending across the interface acts as a pre-energy filter for carrier injection. As a result, an evident decoupling between the electrical conductivity and Seebeck coefficient is observed, leading to surprisingly high power factors (PF). Specifically, a fivefold/eightfold increase in thermoelectric PF is seen over pure  $\text{Bi}_2\text{Te}_3$  platelets with the addition of Ag/Cu respectively, with the correlate being the barrier height at the platelets edge. First-principles calculations show that the electronics of the semiconductor-metal interfaces are quite different for edge and facial configurations,

suggesting that the site of metal dopant plays an important role in the enhanced thermoelectric performance.

## 9.2 Computational Methods

The computational methods used in this work are based on density functional theory (DFT) ,implemented by the projected augmented wave (PAW) projector functions were generated by the ATOMPAW formalism. The PAW basis and code and used in QUANTUM ESPRESSO package. Visualizations of the crystal structures were constructed using the XCrySDEN, VESTA software packages.

The exchange correlation function is approximated using the local-density approximation (LDA). The choice of LDA functional was made based on previous investigations of similar materials which showed that the simulations are in good agreement with experiment, especially the fractional lattice parameters, the vibrational frequencies, and heats of formation. The simulated magnitudes of the lattice parameters, when systematically scaled by a factor of 1.03, are also in good agreement with experiment.

The partial densities of states (PDOS) were calculated as described in previous work, 14, 16 using weighting factors based on the charge within the augmentation spheres of each atom with radii  $rc^{Bi} = 2.9$ ,  $rc^{Te} = 2.4$ , and  $rc^{Ag} = 2.5$  in bohr units. The reported partial densities of states curves  $N_a(E)$  were averaged over the atomic sites of each type  $a$ . The calculations were well converged with plane wave expansions of the wave function including  $|k + G|^2 \leq 64$  bohr<sup>-2</sup>. The Brillouin zone integrals were evaluated by using uniform sampling volumes of 0.001 bohr<sup>-3</sup> or smaller.

### 9.3 My Contribution

This experimental part of this work was mainly done by Dr. Chaochao Dun and I did the theoretical work. This work was accepted for publication, the full text of the paper can be found in the link (<http://iopscience.iop.org/article/10.1088/2053-1583/aad01c>). Dr. Dun asked me to contribute to this work by performing first-principles simulation of the  $\text{Bi}_2\text{Te}_3$  semiconductor with Ag metal. I performed all the first-principles interface simulations between the  $\text{Bi}_2\text{Te}_3$  and Ag metal, in order to explore the difference between the edge and facial configurations in the semiconductor-metal interface.

First-principles calculations based on Density Functional Theory (DFT) were performed to better understand the geometry of  $\text{Bi}_2\text{Te}_3$  and Ag interface. Several configurations including lateral and facial metal-semiconductor heterojunctions were investigated (Fig. [9.2]), corresponding to (111) surface of face centered cubic (fcc) Ag combined with facial (0001) and lateral (1230) surfaces of  $\text{Bi}_2\text{Te}_3$ . Different Ag to  $\text{Bi}_2\text{Te}_3$  ratios were also considered. The configuration given in Fig. [9.1(a)] has a stoichiometry of  $\text{Ag}_{27}(\text{Bi}_2\text{Te}_3)_8$  with a lateral Ag (111)/  $\text{Bi}_2\text{Te}_3$  (1230) interface. The corresponding partial density of states (PDOS) plots are given in Fig. [9.1(b)], together with bulk fcc Ag,  $\text{Ag}_2\text{Te}$  (monoclinic) and  $\text{Bi}_2\text{Te}_3$ . Details of the computational methods are described in the supplementary information documents, including the calculated lattice constant.

First of all, first-principles simulations based on our model found a metal-stable structure. PDOS of the interior region of the heterojunction resembles that of pure  $\text{Bi}_2\text{Te}_3$ . Theoretically, we expected an unaffected PDOS in the interior region compared with that of bulk  $\text{Bi}_2\text{Te}_3$ . However, in the supercell, there is a minimum in the densities in the energy range of the band gap due to the finite size effects of

the model, especially the thin layer of  $\text{Bi}_2\text{Te}_3$ . Secondly, the PDOS of the interface region of  $\text{Ag}_{27}(\text{Bi}_2\text{Te}_3)_8$  resembles that of pure  $\text{Ag}_2\text{Te}$ , indicating the charge transfer between Ag and Te in this region. This agrees well with experimental results that show the formation of a slight  $\text{Ag}_2\text{Te}$  layer between Ag and  $\text{Bi}_2\text{Te}_3$  from HRTEM and XRD studies, and is consistent with the increased electrical conductivity. Due to the processing procedures we used, Bi sites near Ag included in the present model are not present in the experiment. Consequently, the PDOS contributions of Bi in the interface region may not be realistic.

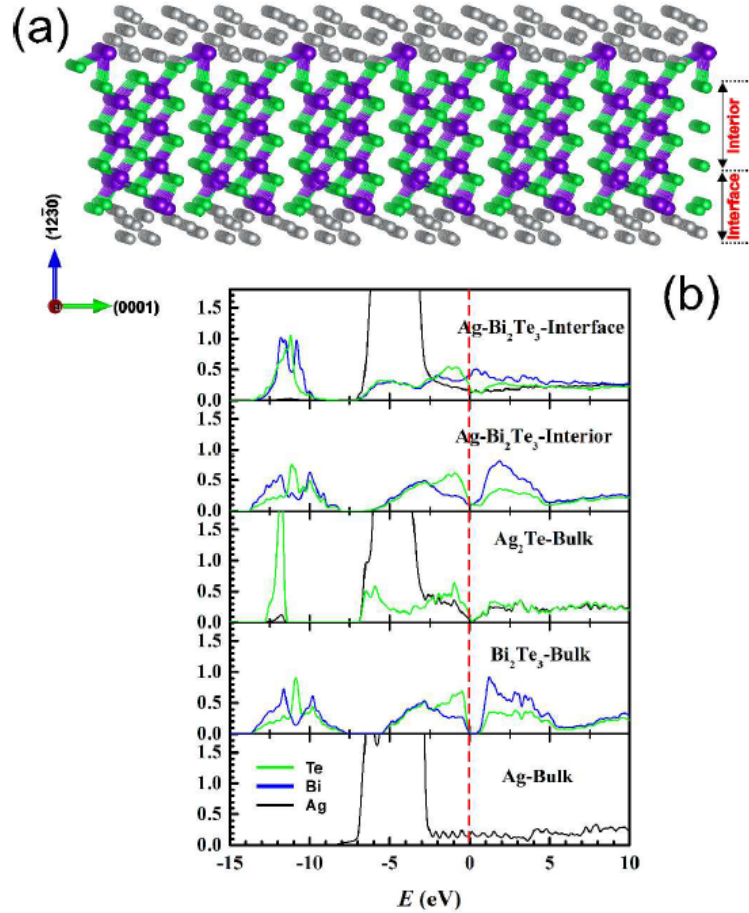


Figure 9.1: (a) Structural diagram of supercell for the lateral Ag (111)/ $\text{Bi}_2\text{Te}_3$  (1230) interface after relaxation, with Ag, Te and Bi atoms represent by silver, green and purple balls, respectively. (b) The corresponding PDOS plots based on the first principle calculations of the interface and interior region of Ag/ $\text{Bi}_2\text{Te}_3$ , bulk Ag,  $\text{Ag}_2\text{Te}$  and  $\text{Bi}_2\text{Te}_3$ . The zero of energy in the plot indicates the Fermi level.



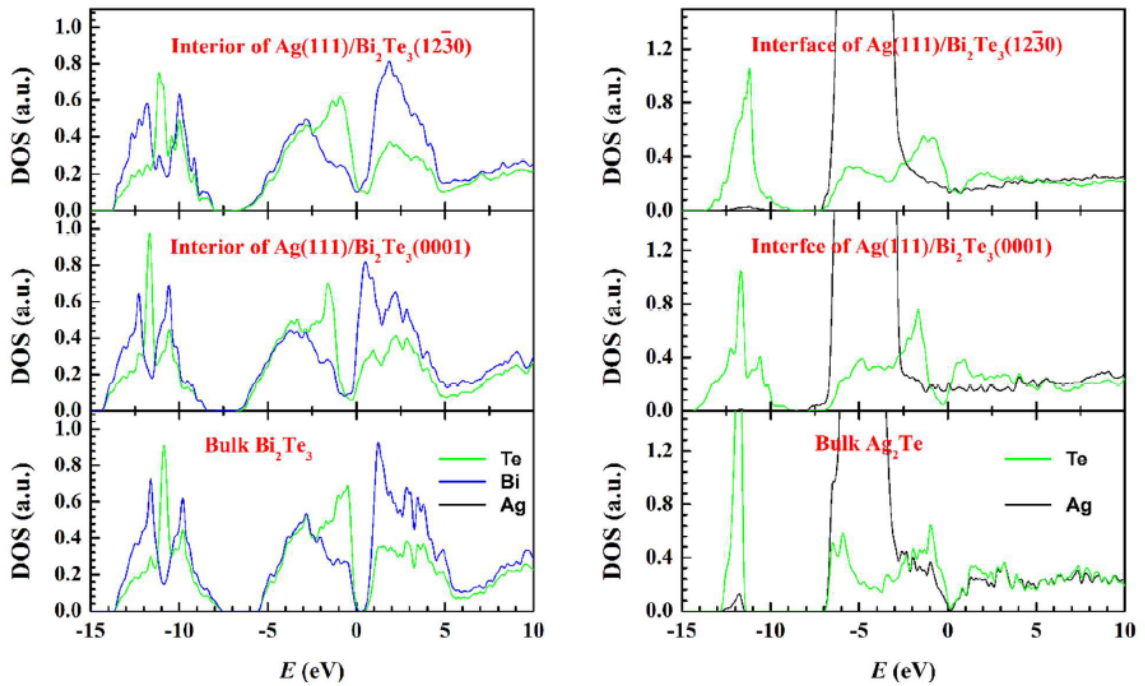


Figure 9.2: PDOS plots based on the first-principles calculations of Ag/Bi<sub>2</sub>Te<sub>3</sub> interfaces, with different number of Ag atoms. Both (111)/(1230) lateral and (111)/(0001) facial interfaces are shown, together with bulk PDOS of Ag, Ag<sub>2</sub>Te and Bi<sub>2</sub>Te<sub>3</sub>. The zero of energy in the plot indicates the Fermi level.

# Chapter 10

## Summary and Conclusions

In this thesis, we have given an overview about the importance of rechargeable batteries in resolving the energy problem in the modern world. We have explained in detail the basic operations of batteries and why Li-ion batteries are the most popular for most applications. We gave a detail overview about the operation and the components of Li-ion batteries and we have explained the problems facing the development of these batteries, in terms of the instability of liquid electrolyte materials. We have explained how inorganic solid electrolyte materials can solve the instability issues of liquid electrolyte materials, and the need of improvement of the Li ionic conductivity of these electrolytes in order to serve as good alternatives to liquid electrolytes. We gave an overview about a recently developed inorganic solid electrolyte with promising ionic conductivity and we motivated the usage of computational research to improve these electrolytes. We have introduced first-principles (*ab initio*) methods as a powerful computational tool in understanding materials properties. We have explained the details of these methods and we have explained how these methods can be used to model materials properties.

We have successfully applied first principles (*ab initio*) methods, to understand

the structure, Li ion migration, and the stability of recently developed promising inorganic solid electrolyte materials. The structure and the Li ion migration of the alloys system [44],  $\text{Li}_{3+x}\text{As}_{1-x}\text{Ge}_x\text{S}_4$ , was studied using first-principles methods. The structure of the pure  $\text{Li}_3\text{AsS}_4$  was found to be characterized by the  $Pmn2_1$  space group. We are very confident of this structure based on the simulated heat of formation and X-ray diffraction patterns. Based on a modification of the  $\text{Li}_3\text{AsS}_4$ , two plausible structures of the  $x = 1/3$  alloy and the  $x = 1/4$  alloy were simulated. The diffusion mechanisms in the  $Pmn2_1$  structure of the  $\text{Li}_3\text{AsS}_4$  and the alloys, was found to be dominated by the interstitial mechanism along the **c** axis and the kick-out mechanism along the **b** axis. Our analysis finds that the effect of Ge in enhancing the conductivity of alloy systems, is to lower the formation energy and to adjust position of interstitials to lower the migration energy of the pure  $\text{Li}_3\text{AsS}_4$ .

The  $\text{Li}_4\text{SnS}_4$ , which was reported by MacNeil [50] and the Kaib [53] groups was investigated along with its Se analogue. The MacNeil structure was identified to be the ground state structure,  $\text{Li}_4\text{SnS}_4^0$  and  $\text{Li}_4\text{SnSe}_4^0$ , and the Kaib structure was identified to be the metastable state structure,  $\text{Li}_4\text{SnS}_4^*$  and  $\text{Li}_4\text{SnSe}_4^*$ . The Li ion migration was studied for the structures using the NEB method and molecular dynamics, the NEB analysis found the dominant diffusion mechanism to be the interstitialcy mechanism along the **b** and **c** axes. For this mechanism the lowest migration energy was found to be 0.2 eV for the  $\text{Li}_4\text{SnS}_4^0$  and  $\text{Li}_4\text{SnSe}_4^0$  and was found to have a much lower value of 0.07 eV in  $\text{Li}_4\text{SnS}_4^*$  and  $\text{Li}_4\text{SnSe}_4^*$  indicating better conduction properties. The formation energy for vacancy-interstitial pairs was found to be much lower in meta-stable state structures than the ground state structure indicating a disordered nature of the meta-stable state structures. MD simulations show a 3 dimensional migration pathways in these materials. They also show that the meta-stable state structures tend to be disordered at low temperature while the ground state structures remains ordered,

which is consistent with experimental observations. The MD simulation shows that the meta-stable state structures have higher Li ion conductivity than the ground state structures which is consistent with the NEB results.

First principles simulations were used to investigate the electrolyte properties of two recently reported nitrogen rich crystalline LiPON electrolyte materials, the  $\text{Li}_{14}\text{P}_2\text{O}_3\text{N}_6$  [54] and  $\text{Li}_7\text{PN}_4$  [55, 56]. The simulation results were compared to the analogous electrolyte  $\gamma\text{-Li}_3\text{PO}_4$  in order to explore the effect of N on the stability and the conductivity of the materials. The simulations suggest that these materials are very promising solid electrolytes due to their ideal interface with metallic Li and their promising activation energy. One interesting result of the simulations is that the dominant diffusion mechanism for the nitrogen rich materials was found to be the vacancy mechanism in comparison to the interstitialcy mechanism in the oxygen rich  $\gamma\text{-Li}_3\text{PO}_4$ .

# Appendix A

## Computational Study of Li Ion Electrolytes Composed of $\text{Li}_3\text{AsS}_4$ Alloyed with $\text{Li}_4\text{GeS}_4$

Reproduced from the Journal of Electrochemical Society, volume 163, issue 9, pages A2079–A2088, 2016. With a permission from Elsevier.



## Computational Study of Li Ion Electrolytes Composed of $\text{Li}_3\text{AsS}_4$ Alloyed with $\text{Li}_4\text{GeS}_4$

Ahmad Al-Qawasmeh and N. A. W. Holzwarth<sup>\*,z</sup>

Department of Physics, Wake Forest University, Winston-Salem, North Carolina 27109-7507, USA

First principles computational techniques are used to study properties of promising Li ion electrolytes, recently developed at Oak Ridge National Laboratory, based on alloys having the composition  $\text{Li}_{3+x}\text{As}_{1-x}\text{Ge}_x\text{S}_4$ . The crystal structure of pure  $\text{Li}_3\text{AsS}_4$  is found to be characterized by the  $Pmn2_1$  space group. Based on modifications of this structure, reasonable models of the  $x = 1/4$  and  $x = 1/3$  alloys are found to be in good agreement with the experimental X-ray diffraction patterns and to be consistent with the measured trends in Li ion conduction. As a consequence of their  $Pmn2_1$ -based structures, interstitial and interstitialcy mechanisms are found to be important for the Li ion conduction processes in these systems.

© The Author(s) 2016. Published by ECS. This is an open access article distributed under the terms of the Creative Commons Attribution 4.0 License (CC BY, <http://creativecommons.org/licenses/by/4.0/>), which permits unrestricted reuse of the work in any medium, provided the original work is properly cited. [DOI: 10.1149/2.1131609jes] All rights reserved.

Manuscript submitted May 25, 2016; revised manuscript received July 12, 2016. Published July 27, 2016.

The development of stable solid electrolytes with high ionic conductivity provides a challenge for basic materials research<sup>1</sup> which has been identified as a key to improved battery technologies.<sup>2</sup> Recent experimental studies by Sahu et al.<sup>3</sup> explored new electrolyte compositions for Li ion electrolytes and found promising results based on alloys of  $\text{Li}_3\text{AsS}_4$  and  $\text{Li}_4\text{GeS}_4$ . Significantly higher ionic conductivity was found for the alloys  $\text{Li}_{3+x}\text{As}_{1-x}\text{Ge}_x\text{S}_4$  with compositions  $0 < x < 0.5$ , compared with the pure materials, especially for  $x = 1/3$ . In order to understand the reported experimental results in terms of the stability and ion conduction mechanisms in this system, we have computationally examined this alloy system using first principles methods.

The notion of improving ionic conductivity by preparing solid solutions of two compatible ionic crystalline materials has been discussed several times in the literature. For example, in a 1977 publication, Hu et al.<sup>4</sup> studied a series of compounds with compositions  $\text{Li}_{3+x}\text{P}_{1-x}\text{Si}_x\text{O}_4$ , finding the highest conductivities for  $x \approx 0.5$ . This system has been further examined by several other researchers, including a recent combined experimental and simulation study by Deng et al.<sup>5</sup> who analyzed the detailed structures of the solid solutions in addition to the ionic conductivity from impedance and nuclear magnetic resonance measurements. For this system, in the composition range  $0 \leq x \lesssim 0.5$ , the compounds are derived from the structure of  $\gamma\text{-Li}_3\text{PO}_4$ , having the space group  $Pnma$  (No. 62 as listed in the International Table of Crystallography<sup>6</sup>), with Si substituting for P. The simulation studies of this work suggest that the dominant Li ion migration mechanism for this system involves the correlated motions of interstitial and lattice Li ions in “interstitialcy” or “kick-out” processes.

Another related alloy system was recently investigated by Hori et al.<sup>7</sup> who determined the phase diagram of  $\text{Li}_{3+x}\text{P}_{1-x}\text{Ge}_x\text{S}_4$ . These authors find that for very small values of  $x$  ( $0 \leq x \leq 0.02$ ), the system takes the  $Pmn2_1$  (No. 31) structure of  $\gamma\text{-Li}_3\text{PS}_4$ , but for  $0.02 \leq x < 0.2$  the system takes the  $Pnma$  (No. 62) structure of  $\beta\text{-Li}_3\text{PS}_4$ . The alloy system having the  $\beta\text{-Li}_3\text{PS}_4$  structure was found to have a room temperature ion conductivity of  $10^{-3}$  S/cm for  $x = 0.2$ .<sup>8</sup> For larger values of  $x$  the system includes the so-called superionic conducting phase<sup>9</sup> for  $x = 1/3$  which is usually written as  $\text{Li}_{10}\text{GeP}_2\text{S}_{12}$  (LGPS). The LGPS structure is found for values of  $0.2 < x < 0.6$ , while for  $x > 0.6$  the system takes the  $Pnma$  structure of  $\text{Li}_4\text{GeS}_4$ . From the temperature dependence of the phase diagram, the authors argue that these structures are stabilized by entropy which is effected by the distribution of differently sized building blocks of  $\text{PS}_4$  and  $\text{GeS}_4$  ions. The LGPS system has been shown<sup>9,10</sup> to have a room temperature Li ion conductivity of  $10^{-2}$  S/cm.

The importance of the lattice structure in determining the ionic conductivity of these electrolytes was recently shown by Liu et al.<sup>11</sup> who developed a novel preparation method which stabilizes the  $\beta\text{-Li}_3\text{PS}_4$  structure at room temperature and increases the ionic conductivity by a factor of 100 to  $10^{-4}$  S/cm. Other preparation methods have found<sup>8,12</sup> that pure  $\beta\text{-Li}_3\text{PS}_4$  is not stable at room temperature, but its high temperature Li ion conductivity extrapolated to room temperature is approximately  $10^{-6}$  S/cm.

For the  $\text{Li}_{3+x}\text{As}_{1-x}\text{Ge}_x\text{S}_4$  alloy system studied by Sahu et al.,<sup>3</sup> which is the subject the present computational study, the X-ray experimental results suggest that the structure remains that of the  $\text{Li}_3\text{AsS}_4$  lattice throughout the composition range  $0 \leq x \leq 0.5$ . While a more detailed analysis of the X-ray patterns may reveal some structural variations, we based our simulations on the assumption that Ge substitutes for As in the  $\text{Li}_3\text{AsS}_4$  structure. The first task of the simulations is to determine the  $\text{Li}_3\text{AsS}_4$  structure itself. Secondly, the likely Ge substitutions and their corresponding placements of the extra Li sites must be determined. Once plausible structures for the alloy are determined, the ion migration mechanisms can be investigated for each structure.

### Computational Methods

The computational methods used in this work are based on density functional theory (DFT),<sup>13,14</sup> using the projected augmented wave (PAW)<sup>15</sup> formalism. The PAW basis and projector functions were generated by the ATOMPAW<sup>16</sup> code and used in QUANTUM ESPRESSO<sup>17</sup> package. Visualizations were constructed using the XCrySDEN,<sup>18,19</sup> VESTA<sup>20</sup> software packages.

The exchange correlation function is approximated using the local-density approximation (LDA).<sup>21</sup> The choice of LDA functional was made based on previous investigations<sup>22-30</sup> of similar materials which showed that provided that the lattice constants are scaled by a correction factor or 1.02, the simulations are in good agreement with experiment, especially lattice vibrational frequencies and heats of formation.

In this work, the heat of formation  $\Delta H_f$  reported here is determined at 0 degrees K as estimated from the total electronic energy of the material per formula unit minus the energies of the elemental constituents in their standard states as defined by the CRC Handbook.<sup>31</sup> For example, the heat of formation for the alloy can be approximated from the zero temperature total energy results according to

$$\Delta H_f = E[\text{Li}_{3+x}\text{As}_{1-x}\text{Ge}_x\text{S}_4] - (3+x)E_{\text{std}}(\text{Li}) - (1-x)E_{\text{std}}[\text{As}] - xE_{\text{std}}[\text{Ge}] - 4E_{\text{std}}[\text{S}], \quad [1]$$

where  $E_{\text{std}}$  corresponds to the total energies of Li in the bcc structure, As in the  $R\bar{3}m$  structure, Ge in the diamond structure, and S in the  $Fddd$  ( $\alpha - S_8$ ) structure, respectively. Also of interest is the decomposition energy ( $\Delta H_D$ ) for an alloy which can also be estimated from

\*Electrochemical Society Member.

<sup>z</sup>E-mail: natalie@wfu.edu

the zero temperature total energy results according to:

$$\Delta H_D = E[\text{Li}_{3+x}\text{As}_{1-x}\text{Ge}_x\text{S}_4] - (1-x)E[\text{Li}_3\text{AsS}_4] - xE[\text{Li}_4\text{GeS}_4]. \quad [2]$$

With this sign convention, a negative value for  $\Delta H_D$  implies that the alloy is stable with respect to decomposition into the pure materials. These energy estimates neglect the effects of finite temperature and pressure which van de Walle and Ceder<sup>32</sup> estimate to contribute  $10^{-2}$  eV/atom at room temperature for most materials.

For analyzing the heats of formation and other perfect crystal properties, calculations were performed with plane wave expansions of the wave function including  $|\mathbf{k} + \mathbf{G}|^2 \leq 64 \text{ bohr}^{-2}$  and with a Brillouin-zone sampling grid density of at least  $10^{-3} \text{ bohr}^{-3}/\mathbf{k}$  point. The partial densities of states were calculated as described in previous work,<sup>26,29</sup> using weighting factors based on the charge within the augmentation spheres of each atom with radii  $r_c^{\text{Li}} = 1.6$ ,  $r_c^{\text{As}} = 2.3$ ,  $r_c^{\text{Ge}} = 2.1$ , and  $r_c^{\text{S}} = 1.7$  in bohr units. The reported partial densities of states curves ( $N^a(E)$ ) were averaged over the atomic sites of each type  $a$ .

Li vacancies and interstitials were modeled in supercell containing 16, 16, and 24 formula units for simulating pure  $\text{Li}_3\text{AsS}_4$ , the alloy  $\text{Li}_{1/3/4}\text{As}_{3/4}\text{Ge}_{1/4}\text{S}_4$ , and the alloy  $\text{Li}_{10/3}\text{As}_{2/3}\text{Ge}_{1/3}\text{S}_4$ , respectively. For the case of  $\text{Li}_{10/3}\text{As}_{2/3}\text{Ge}_{1/3}\text{S}_4$ , the plane wave cut off was reduced to  $49 \text{ bohr}^{-2}$ . The estimated error for the relative energies computed with the reduced plane wave cutoff is less than 0.02 eV. These supercells were used to estimate the minimum energy path for Li ion migration using the “nudged elastic band” (NEB) method<sup>33–35</sup> as programmed in the QUANTUM ESPRESSO package, using 5 images between each metastable configuration. In modeling charged defects (Li ion vacancies or interstitials), the system was assumed to remain electrically insulating and a uniform background charge was added in order to evaluate the electrostatic interactions. For each minimum energy path, the migration energy,  $E_m$  was determined as the energy difference between the lowest and highest energy of the path. The “formation energies”  $E_f$  for producing neutral defects in the form of vacancy-interstitial pairs were calculated for the same supercells. These energies are related to the experimentally measured ionic conductivity through an Arrhenius relationship of the form

$$\sigma = \frac{A}{T} e^{-E_A/kT}, \quad [3]$$

where  $A$  denotes a constant,  $T$  denotes the temperature in Kelvin,  $k$  denotes the Boltzmann constant, and  $E_A$  denotes the activation energy for ion migration. The activation energy is related to the migration and formation energies according to<sup>36</sup>

$$E_m + \frac{1}{2}E_f \geq E_A \geq E_m. \quad [4]$$

In Eq. 4 the upper limit of  $E_A$  applies to the “intrinsic” case when ion migration must be preceded by the creation of a pair of vacancy and interstitial ions by thermal activation. The lower limit applies to the “extrinsic” case when a population of vacancy or interstitial ions is available so that the conduction depends only the thermal activation due to the migration energy barriers characterized by  $E_m$ . In principle, the energy of charged defects should be corrected for finite size errors by using one of several methods reported in the literature.<sup>37,38</sup> This was not done in the present work, although we expect that the finite size errors for energy difference such as  $E_m$  benefit from error cancellation.

## Results

**Structures of the pure materials.**—To the best of our knowledge, the crystal structure of  $\text{Li}_3\text{AsS}_4$  has not been analyzed, although its X-ray diffraction pattern is reported by Sahu et al.<sup>3</sup> It is reasonable to assume that  $\text{Li}_3\text{AsS}_4$  has structural properties similar to those of  $\text{Li}_3\text{PS}_4$ , which has been well studied.<sup>12,26,39–42</sup> As mentioned in the introduction,  $\text{Li}_3\text{PS}_4$  is known to have the low temperature structure,  $\gamma\text{-Li}_3\text{PS}_4$ , characterized by the space group  $Pmn2_1$  (No. 31). At temperatures between 200 and 300 degrees C, a transition to the

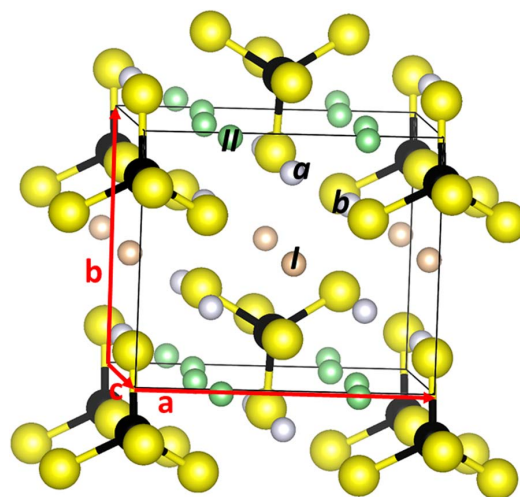
**Table I.** Heats of formation (in eV), as defined in Eq. 1, for  $\text{Li}_3\text{AsS}_4$  and  $\text{Li}_3\text{PS}_4$  in four different model structures.

Structure	$\text{Li}_3\text{AsS}_4$ $\Delta H_f$ (eV)	$\text{Li}_3\text{PS}_4$ $\Delta H_f$ (eV)
$\gamma\text{-Li}_3\text{PS}_4$ ( $Pmn2_1$ )	−7.17	−8.37
$\gamma\text{-Li}_3\text{PO}_4$ ( $Pnma$ )	−6.95	−8.18
$\beta\text{-Li}_3\text{PS}_4\text{-}b$ ( $Pnma$ )	−7.00	−8.28
$\beta\text{-Li}_3\text{PS}_4\text{-}c$ ( $Pnma$ )	−7.03	−8.25

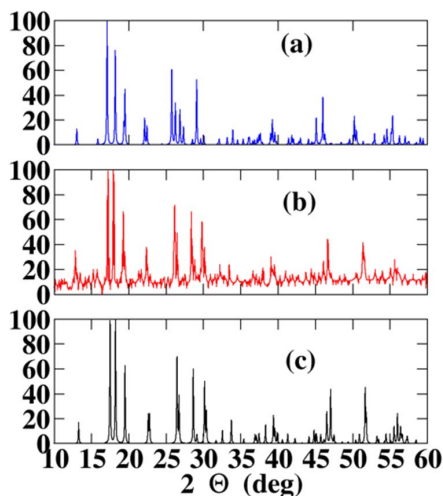
$\beta\text{-Li}_3\text{PS}_4$  structure has been reported,<sup>12,41</sup> which is characterized by the space group  $Pnma$  (No. 62) with fractional occupancy of some of the Li sites. The  $\beta\text{-Li}_3\text{PS}_4$  structure can be stabilized at room temperature and has been shown to have higher Li ion conductivity than the  $\gamma$  phase.<sup>40</sup> In previous work, we simulated the ideal crystalline structures of four models of  $\text{Li}_3\text{PS}_4$  based on the ordered structures of  $Pmn2_1$   $\gamma\text{-Li}_3\text{PS}_4$ ,  $Pnma$   $\gamma\text{-Li}_3\text{PO}_4$ , and two idealizations of disordered  $Pnma$   $\beta\text{-Li}_3\text{PS}_4$ .<sup>26</sup> The idealizations of disordered  $Pnma$   $\beta\text{-Li}_3\text{PS}_4$  were labeled  $\beta\text{-Li}_3\text{PS}_4\text{-}b$  and  $\beta\text{-Li}_3\text{PS}_4\text{-}c$  representing models with 100% occupancy of the Li sites with Wyckoff labels  $b$  and  $c$ , respectively. More recently, Ganesh et al.<sup>39</sup> have shown that the disordered  $\beta\text{-Li}_3\text{PS}_4$  structure can be explained by using molecular dynamics (MD) simulations which show that the 70% occupancy of the  $b$  site and 30% occupancy of the  $c$  site correlates with the site analysis of the time averaged Li MD trajectories.

Table I lists the heats of formation ( $\Delta H_f$ ) calculated for four structural models structures of  $\text{Li}_3\text{AsS}_4$  and  $\text{Li}_3\text{PS}_4$ . The heat of formation results given in Table I, indicate that the ground state structure of  $\text{Li}_3\text{AsS}_4$  corresponds to the  $Pmn2_1$  ground state structure of  $\gamma\text{-Li}_3\text{PS}_4$ . The calculated lattice constants are  $a = 7.65 \text{ \AA}$ ,  $b = 6.54 \text{ \AA}$ ,  $c = 6.14 \text{ \AA}$ , which agrees well with experiment when scaled by the 1.02 LDA correction factor. A structural diagram of  $\text{Li}_3\text{AsS}_4$  in this structure is shown in Fig. 1. The calculated fractional coordinates are listed in Table AI in the Appendix.

In order to compare the simulation results with experiment, we generated the X-ray powder diffraction pattern with the help of the Mercury<sup>43</sup> software package and compared it with the experimental pattern, obtained by digitizing the published results,<sup>3</sup> as shown in Fig. 2. The simulated powder pattern is seen to be in good agreement with the experimental results. Also included in Fig. 2 is the



**Figure 1.** Ball and stick diagram of the unit cell of the  $Pmn2_1$  structure of  $\text{Li}_3\text{AsS}_4$ . The Li, As and S sites are displayed with gray, black, and yellow balls respectively. The labels  $a$  and  $b$  indicate examples of Li sites with those Wyckoff labels. Also indicated are the lowest energy interstitial sites for Li ions, labeled  $I$  and  $II$  and tinted orange and green respectively.



**Figure 2.** Comparison of X-ray powder diffraction patterns from simulations and experiment. Panel (b) shows the experimental data from Ref. 3, plotted from a digitized analysis of the published graph. Panels (c) and (a) show the powder diffraction patterns generated using Mercury<sup>43</sup> software from the simulation results of the  $Pmn2_1$   $\gamma$ - $\text{Li}_3\text{PS}_4$  and  $Pnma$   $\beta$ - $\text{Li}_3\text{PS}_4$ - $c$  structures, respectively. For both of the simulations, the 1.02 LDA scaling correction was applied.

simulated powder pattern for the so-called  $\beta$ - $\text{Li}_3\text{PS}_4$ - $c$  model structure of  $\text{Li}_3\text{AsS}_4$ , which has less favorable correspondence to the experimental pattern, consistent with its calculated total energy being 0.14 eV above that of the ground state configuration.

From the simulation results and from the reported X-ray diffraction experiments on  $\text{Li}_3\text{PS}_4$  and its alloys,<sup>44</sup> it is reasonable to assume that the  $Pmn2_1$  structure forms the basis of the structure throughout the composition range. That is, unlike  $\text{Li}_3\text{PS}_4$ , there is no evidence of multiple structural phases.

In anticipation of the analysis of Li ion migration in this material, it is useful to study the relative energies of vacancy and interstitial defects. The  $Pmn2_1$  structure of  $\text{Li}_3\text{AsS}_4$  has two geometrically distinct host lattice sites with Wyckoff labels  $a$  and  $b$  as indicated in Fig. 1. We found several metastable interstitial sites in the lattice; the lowest energy sites are labeled  $I$  (having a multiplicity of 2 in the conventional unit cell) and  $II$  (having a multiplicity of 4). These sites and their equivalents are shown in Fig. 1. The relative energies of vacancies in the 16 formula unit supercell are given in Table II. Interestingly, the relative energies and fractional coordinates of the vacancy and interstitial sites are calculated to be very similar for  $\text{Li}_3\text{AsS}_4$  and its  $\gamma$ - $\text{Li}_3\text{PS}_4$  analog.

The crystal structure of  $\text{Li}_4\text{GeS}_4$ , which has been studied by several groups,<sup>45–47</sup> has the  $Pnma$  (No. 62) space group. The calculated lattice

**Table II.** List of relative energies  $\Delta E$  (eV) for vacancy (Vac) and interstitial (Inter) Li sites in  $\text{Li}_3\text{AsS}_4$  compared with the corresponding defects in  $\gamma$ - $\text{Li}_3\text{PS}_4$  calculated for  $2 \times 2 \times 2$  supercell models. The zero energies are taken to be the  $b$  site for the vacancy defect and the  $I$  site for the interstitial defect. The “Position” entries indicate the fractional coordinates referenced to the conventional cell of the perfect lattice.

Type	Label	$\text{Li}_3\text{AsS}_4$		$\gamma$ - $\text{Li}_3\text{PS}_4$	
		Position	$\Delta E$	Position	$\Delta E$
Vac	$a$	(0.00, 0.85, 0.99)	0.07	(0.00, 0.82, 1.00)	0.05
Vac	$b$	(0.24, 0.32, 0.00)	0	(0.24, 0.32, 0.00)	0
Inter	$I$	(0.00, 0.49, 0.65)	0	(0.00, 0.48, 0.64)	0
Inter	$II$	(0.23, 0.00, 0.68)	0.09	(0.24, 0.00, 0.66)	0.00

constants are  $a = 13.83 \text{ \AA}$ ,  $b = 7.59 \text{ \AA}$ , and  $c = 6.00 \text{ \AA}$ , in good agreement with the literature results after scaling by 1.02 to correct for the systematic LDA error. The local configuration of the  $\text{GeS}_4$  tetrahedra of this structure are very similar to those of  $\text{AsS}_4$ , consistent with the formation of substitutional alloys.

**Structures of the alloys.**—In order to perform detailed first principles simulations of the alloy structures, it is necessary to find plausible ordered structures within computationally manageable supercells as described below. We also briefly investigated the question of whether the material produced in the experiment is likely to be an ordered structure such as found in our simulations, or more likely to be a disordered alloy with Ge replacing As randomly. In the X-ray power diffraction patterns, the ordered structures are characterized by site occupancy factors of 1, while disordered structures have fractional site occupancies representing incoherent averages of diffractions from all possible crystal configurations. Using the Mercury software<sup>43</sup> to generate simulated X-ray powder patterns, it is possible to adjust the occupancy factors to compare the patterns for the ordered structures with those generated for corresponding structures with random occupation of the Ge and As sites. The simulations show small differences in the X-ray patterns. While it is possible that future experiments could detect such differences, the reported experimental powder patterns<sup>3</sup> are in good agreement with the generated X-ray powder patterns of the ordered structures and nearly equally good agreement with the corresponding patterns generated for the disordered structures. This suggests that the structures discussed below are very plausible models, but not the only possibilities.

The search for optimal alloy structures was based on supercells of the  $\text{Li}_3\text{AsS}_4$  structure; four and six formula unit supercells were used for the  $x = 1/4$  and  $x = 1/3$  alloys respectively. For each supercell, all unique configurations of Ge substitutions were considered. For each Ge substitution an additional Li was added at a grid of likely positions. QUANTUM ESPRESSO<sup>17</sup> was used to optimize the structures of each of the initial configurations. For each alloy concentration considered, the optimized alloy model was found to have the lowest energy of the configurations considered by 0.2–0.3 eV.

In order to check for additional alloy models, we also sampled a few configurations from larger supercells with the help of symmetry analysis available from Site Occupancy Disorder (SOD) program of Grau-Crespo et al.<sup>48</sup> Although we failed to find alloy structures with lower energy, it is possible that a more exhaustive search may reveal additional possibilities. On the other hand, the alloy models that we did find, appear to make optimal use of the original  $\text{Li}_3\text{AsS}_4$  structure and its low energy interstitial sites, as explained in more detail below.

$3/4 \text{ Li}_3\text{AsS}_4 + 1/4 \text{ Li}_4\text{GeS}_4$ .—One of the alloys studied by Sahu et al.<sup>3</sup> is composed of  $\text{Li}_3\text{AsS}_4$  and  $\text{Li}_4\text{GeS}_4$  in the ratio 3:1, forming the compound  $\text{Li}_{13/4}\text{As}_{3/4}\text{Ge}_{1/4}\text{S}_4$ . The optimal model structure for this alloy is shown in Fig. 3a. It can be described in terms of a  $2 \times 1 \times 1$  supercell of the  $Pmn2_1$  structure of  $\text{Li}_3\text{AsS}_4$ , with Ge substituting for As in the  $x = 0$  plane and the associated extra Li located close by as indicated with the symbol “ $x$ ” in the figure. The  $x$  site Li of the alloy occupies a position close to interstitial site of type “ $I$ ” of the original  $\text{Li}_3\text{AsS}_4$  lattice. This structure is 0.15 eV lower in energy than the other configurations we investigated for this alloy. The optimized lattice constants of this structure are  $a = 15.20 \text{ \AA}$ ,  $b = 6.60 \text{ \AA}$ , and  $c = 6.13 \text{ \AA}$ , corresponding to a very slight contraction of the  $\text{Li}_3\text{AsS}_4$  host lattice along the  $a$  axis. The structure shown in Fig. 3a has the space group  $Pm$  (No. 6). The fractional coordinates of the unique atoms are listed in the Appendix in Table AII.

In anticipation of the analysis of Li ion migration in this material, we studied the relative energies of vacancy and interstitial defects. The  $Pm$  structure of the  $1/4$  alloy has 8 distinct Li sites and 6 distinct interstitial sites as shown in Fig. 3a. The corresponding relative vacancy and interstitial energies are listed in Table III. From the simulations based on 16 formula unit supercells, the  $x$  site Li ion has the lowest vacancy energy, defined as  $\Delta E = 0$ . The nearest neighbor



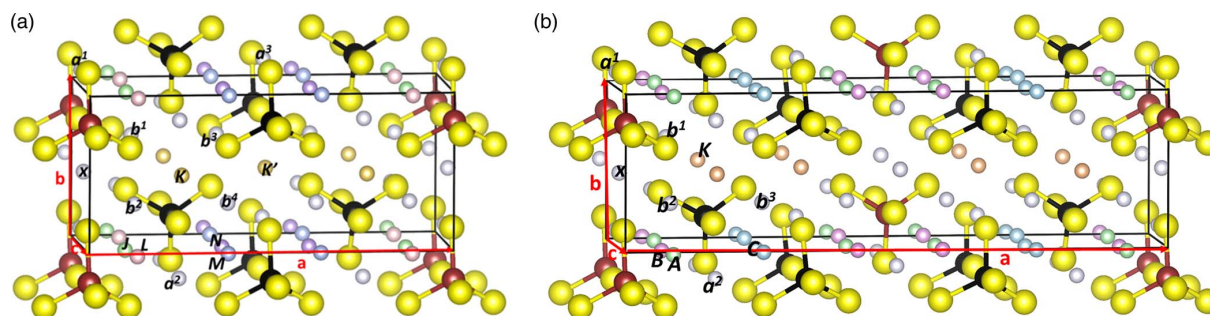


**Figure 3.** Ball and stick model of the optimized structures of the  $\text{Li}_{3+x}\text{As}_{1-x}\text{Ge}_x\text{S}_4$  alloys considered in this study. The Li, As, Ge, and S atomic sites are shown in gray, black, dark red, and yellow respectively. The labels  $a^i$  and  $b^i$  for  $i = 1, 2, \dots$  represent Li sites corresponding to the  $a$  and  $b$  Wyckoff labels of pure  $\text{Li}_3\text{AsS}_4$ , which are now modified in these alloys. The label  $x$  references the additional Li site introduced by the presence of Ge. Also shown are the low energy interstitial sites for Li ions. (a) Shows the alloy  $x = 1/4$  with interstitial sites indicated with green, pink, purple, blue, orange, and orange tint corresponding to the unique labels,  $J, L, M, N, K,$  and  $K'$ , respectively. (b) Shows the alloy  $x = 1/3$  with interstitial sites indicated with green, pink, blue, and orange tint corresponding to the unique labels  $A, B, C,$  and  $K$ , respectively.

Li vacancy sites,  $a^1, b^1,$  and  $b^2$ , are all unstable relative to the  $x$  site vacancy. These are listed in Table III with  $\Delta E = 0$  because their relaxed configuration is that of  $x$  site vacancy. The vacancy energies for Li ions further from the Ge site are more than 0.5 eV higher in energy. Accordingly, we expect that the population of vacancies on the  $a^2, a^3, b^3,$  and  $b^4$  sites to be substantial lower than the population of vacancies on the  $x$  sites. However, entropy effects<sup>32</sup> which reduce the free energies, increase the probability of forming these vacancies.

The interstitial energies of sites  $K$  and  $K'$ , both corresponding to the type  $I$  interstitial of the pure  $\text{Li}_3\text{AsS}_4$  lattice, are 0.06 eV higher in energy than the lowest energy  $J$  interstitial site, which is defined as  $\Delta E = 0$ . The four unique interstitial sites  $J, L, M,$  and  $N$  all correspond to the type  $II$  interstitials in pure  $\text{Li}_3\text{AsS}_4$ . The lowest energy  $J$  site is closest to the plane containing the substitutional Ge atoms, although because of its  $c$  axis placement, the interstitial  $L$  site interstitial is closer to its nearest Ge site, as noted in Table III.

$2/3 \text{Li}_3\text{AsS}_4 + 1/3 \text{Li}_4\text{GeS}_4$ .—Another alloy studied by Sahu et al.,<sup>3</sup> is composed of  $\text{Li}_3\text{AsS}_4$  and  $\text{Li}_4\text{GeS}_4$  in the ratio 2:1, forming the compound  $\text{Li}_{10/3}\text{As}_{2/3}\text{Ge}_{1/3}\text{S}_4$ . The optimal model structure

for this alloy is shown in Fig. 3b. It can be described in terms of a  $3 \times 1 \times 1$  supercell of pure  $\text{Li}_3\text{AsS}_4$ , with Ge substituting for As in planes perpendicular to the  $a$ -axis at the fractional coordinates  $x = 0$  and  $x = 1/2$ . The associated 2 extra Li sites are located close by as indicated with the symbols  $x$  in the figure. The  $x$  site Li's of the alloy occupy positions close to interstitial site of type “ $I$ ” of the original  $\text{Li}_3\text{AsS}_4$  lattice. This structure is 0.27 eV lower in energy than all the other configurations we investigated for this alloy. The lattice constants of this optimized structure are  $a = 22.77 \text{ \AA}, b = 6.60 \text{ \AA},$  and  $c = 6.14 \text{ \AA}$ , corresponding to a slight contraction of the  $\text{Li}_3\text{AsS}_4$  lattice along the  $a$  axis. This structure of the  $\text{Li}_{10/3}\text{As}_{2/3}\text{Ge}_{1/3}\text{S}_4$  alloy has the space group  $Pmn2_1$  (No. 31), as does the optimal structure of the  $\text{Li}_3\text{AsS}_4$  host lattice. The fractional coordinates of the unique atoms are listed in the Appendix in Table AIII.

In anticipation of the analysis of Li ion migration in this material, we studied the relative energies of vacancy and interstitial defects. The  $Pmn2_1$  structure of the  $1/3$  alloy has 6 distinct Li sites and 4 distinct interstitial sites as shown in Fig. 3b. The corresponding relative vacancy and interstitial energies are listed in Table IV. From the simulations based on 24 formula unit supercells, the  $x$  site Li ion has the lowest vacancy energy, defined as  $\Delta E = 0$ . As in the case of the  $1/4$  alloy, the nearest neighbor Li vacancy sites,  $a^1, b^1,$  and  $b^2$ , are all unstable relative to the  $x$  site vacancy. Vacancies at sites further from the Ge substitutions,  $a^2$  and  $b^3$  are approximately 0.5 eV

**Table III.** List of relative energies  $\Delta E$  (eV) for vacancy (Vac) and interstitial (Inter) Li sites in  $\text{Li}_{13/4}\text{As}_{3/4}\text{Ge}_{1/4}\text{S}_4$  based on 16 formula unit simulations. For each defect site, the column labeled “Ref” lists the equivalent site in the pure  $\text{Li}_3\text{AsS}_4$  structure. The column labeled “Proximity” indicates the distance of the defect to the nearest Ge (in  $\text{\AA}$ ). For the vacancy sites, the “\*” indicates that the vacancy is unstable with respect to neighboring  $x$  site vacancy (defined as the 0 energy). For the interstitial sites, the lowest energy interstitial energy ( $J$ ) was defined as zero.

Type	Label	Ref	Proximity ( $\text{\AA}$ )	$\Delta E$ (eV)
Vac	$a^{1*}$	$a$	3.6	0.00
Vac	$b^{1*}$	$b$	3.7	0.00
Vac	$a^2$	$a$	3.8	0.65
Vac	$b^{2*}$	$b$	3.8	0.01
Vac	$a^3$	$a$	8.5	0.61
Vac	$b^3$	$b$	6.5	0.56
Vac	$b^4$	$b$	6.6	0.54
Vac	$x$	$I$	3.0	0.00
Int	$K$	$I$	4.3	0.06
Int	$K'$	$I$	8.8	0.06
Int	$J$	$II$	2.9	0.00
Int	$L$	$II$	2.6	0.07
Int	$M$	$II$	5.8	0.12
Int	$N$	$II$	7.2	0.13

**Table IV.** List of relative energies  $\Delta E$  (eV) for vacancy (Vac) and interstitial (Inter) Li sites in  $\text{Li}_{10/3}\text{As}_{2/3}\text{Ge}_{1/3}\text{S}_4$  based on 24 formula unit simulations. For each defect, the column labeled “Ref” lists the equivalent site in the pure  $\text{Li}_3\text{AsS}_4$  structure. The column labeled “Proximity” indicates the distance of the defect to the closest Ge (in  $\text{\AA}$ ). For the vacancy sites, the “\*” indicates that the vacancy is unstable with respect to neighboring  $x$  site vacancy (defined as the 0 energy). For the interstitial sites, the lowest energy interstitial energy ( $B$ ) was defined as zero.

Type	Label	Ref	Proximity ( $\text{\AA}$ )	$\Delta E$ (eV)
Vac	$a^{1*}$	$a$	3.6	0.00
Vac	$b^{1*}$	$b$	3.7	0.00
Vac	$a^2$	$a$	3.8	0.59
Vac	$b^{2*}$	$b$	3.8	0.00
Vac	$b^3$	$b$	6.5	0.49
Vac	$x$	$I$	3.0	0.00
Int	$K$	$I$	4.3	0.07
Int	$A$	$II$	2.6	0.05
Int	$B$	$II$	2.9	0.00
Int	$C$	$II$	6.0	0.14

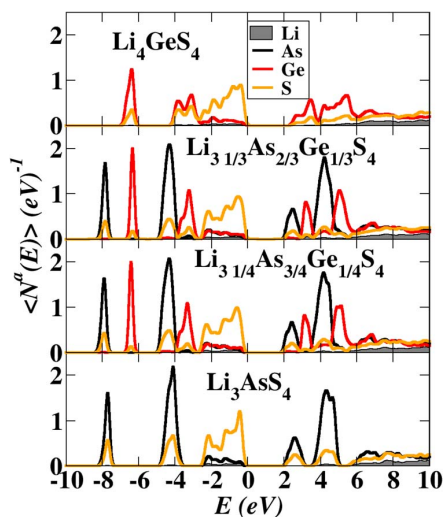


**Figure 4.** Partial densities of states plots for the pure materials  $\text{Li}_4\text{GeS}_4$  and  $\text{Li}_3\text{AsS}_4$  in their ground state structures and for the two alloys  $\text{Li}_{3+x}\text{As}_{1-x}\text{Ge}_x\text{S}_4$  with  $x = 1/4$  and  $x = 1/3$ , in their optimized structures.

**Table V.** Heats of formation ( $\Delta H_f$ ) and of decomposition ( $\Delta H_D$ ) (in eV/formula unit) for pure and alloy materials.

	$\Delta H_f$	$\Delta H_D$
$\text{Li}_3\text{AsS}_4$	-7.17	
$\text{Li}_4\text{GeS}_4$	-10.18	
$\text{Li}_{13/4}\text{As}_{3/4}\text{Ge}_{1/4}\text{S}_4$	-7.86	0.06
$\text{Li}_{10/3}\text{As}_{2/3}\text{Ge}_{1/3}\text{S}_4$	-8.09	0.06

or higher in energy. As in the case of the 1/4 alloy, we expect that entropy effects will enable the population of vacancies on these to be non negligible. The interstitial sites have relative energies similar to those of the 1/4 alloy. In this case, the lowest energy site is labeled *B*, defined as  $\Delta E = 0$ , and has the smallest distance from the plane containing the Ge substitutions.

**Densities of states and heats of formation.**—The partial density of states analysis provides qualitative information about the atomic contributions to the occupied and unoccupied states of the materials. Fig. 4 shows the results for the materials in this study. It is interesting that the two alloys with  $x = 1/4$  and  $x = 1/3$  show nearly identical densities of states. The valence band of these materials is primarily composed of the S 3*p* states, while the conduction bands are composed

of unoccupied As and Ge states, hybridized with S. In general the states associated with Ge lie above their corresponding As counter parts; the bandgap of the alloy is expected to be similar to that of  $\text{Li}_3\text{AsS}_4$ .

A more quantitative measure of density functional results is the heats of formation ( $\Delta H_f$ ) of the materials referenced to the elemental materials in their standard states determined from the total energies of the systems as described by Eq. 1. Also of interest is the decomposition energies ( $\Delta H_D$ ) for the alloys which can also be estimated from the zero temperature total energy results according to Eq. 2. Both of these energies are listed in Table V. The results show that  $\text{Li}_4\text{GeS}_4$  has the largest magnitude of  $\Delta H_f$  of the materials studied. Small positive values of  $\Delta H_D$  having the order of magnitude of the expected finite temperature and pressure corrections,<sup>32</sup> suggest that at equilibrium the alloys are marginally stable with respect to decomposition into the pure materials.

**Ion migration mechanisms.**—Using the NEB technique described in the Computational methods section, we examined several possible Li ion migration processes in  $\text{Li}_3\text{AsS}_4$  and in the  $\text{Li}_{3+x}\text{As}_{1-x}\text{Ge}_x\text{S}_4$  alloys. The results are summarized in Table VI and the details are described below.

**Ion Migration in pure  $\text{Li}_3\text{AsS}_4$ .**—For defect-free crystalline materials, the energy to form an interstitial-vacancy pair,  $E_f$  contributes to the activation energy for conductivity as described in Eq. 4. For pure  $\text{Li}_3\text{AsS}_4$ , we found the lowest formation energy for an interstitial-vacancy pair to be  $E_f = 0.86$  eV corresponding to a type *I* interstitial site and a nearby *b* vacancy site. The formation energy for a type *II* interstitial and nearby *b* vacancy is very similar. The corresponding interstitial-vacancy pair formation energy in  $\gamma\text{-Li}_3\text{PS}_4$  is  $E_f = 0.81$  eV due to a type *II* interstitial site being occupied by a nearby *b* vacancy site.<sup>26</sup>

Several Li ion vacancy migration paths in  $\text{Li}_3\text{AsS}_4$  were investigated according to the diagram shown in Fig. 5a with the resulting NEB energies shown in Fig. 5b. For comparison, the corresponding NEB energies for  $\gamma\text{-Li}_3\text{PS}_4$  are also shown in Fig. 5b. For these paths, the energies for Li vacancy migration in  $\text{Li}_3\text{AsS}_4$  are considerably higher than that of the thiophosphate. The migration energies  $E_m$  are determined as the maximum energy difference along the path which is  $E_m = 0.4$  eV for  $\text{Li}_3\text{AsS}_4$  and  $E_m = 0.3$  eV for  $\gamma\text{-Li}_3\text{PS}_4$ .

Because of the relatively large value of  $E_m$  for pure Li ion vacancy migration in  $\text{Li}_3\text{AsS}_4$ , we were motivated to investigate other diffusion mechanisms such as ion migration involving interstitial Li ion sites. Three different such paths were found as shown in Fig. 6. Two paths with net motion along the *b* axis are shown in Fig. 6a. The path indicated by red arrows  $II_1 \rightarrow I_1 \rightarrow II_4$  corresponds to pure interstitial migration. The path indicated by black arrows involves a kick-out process of the  $II_1$  interstitial ion displacing an “*a*” host lattice ion into the  $I_1$  interstitial position. Subsequently, the  $I_1$  interstitial Li ion displaces the “*b*” host lattice ion into the  $II_4$  interstitial position. The third path, with net motion along the *c* axis, is shown

**Table VI.** Summary of calculated optimal Li ion migration energies  $E_m$  and interstitial-vacancy pair formation energies  $E_f$ , compared with experimental activation energies  $E_A$  quoted or analyzed from Ref. 12 for  $\gamma\text{-Li}_3\text{PS}_4$  and from Ref. 3 for  $\text{Li}_{3+x}\text{As}_{1-x}\text{Ge}_x\text{S}_4$ . All energies are in eV units.

Material	Migration Path	Simulation			Experiment
		$E_m$	$E_f$	$E_m + \frac{1}{2}E_f$	
$\gamma\text{-Li}_3\text{PS}_4$	Vacancy along <i>a</i> axis	0.3	0.8	0.7	0.5
$\text{Li}_3\text{AsS}_4$	Vacancy along <i>a</i> or <i>c</i> axes	0.4	0.9	0.8	0.4
$\text{Li}_3\text{AsS}_4$	Interstitial along <i>c</i> axis	0.3	0.9	0.7	0.4
$\text{Li}_3\text{AsS}_4$	Interstitial along <i>b</i> axis	0.5	0.9	0.9	0.4
$\text{Li}_3\text{AsS}_4$	Kick-out along <i>b</i> axis	0.3	0.9	0.8	0.4
$\text{Li}_{13/4}\text{As}_{3/4}\text{Ge}_{1/4}\text{S}_4$	Kick-out along <i>b</i> axis	0.3	0.3	0.4	0.3
$\text{Li}_{13/4}\text{As}_{3/4}\text{Ge}_{1/4}\text{S}_4$	Interstitial along <i>c</i> axis	0.3	0.3	0.4	0.3
$\text{Li}_{10/3}\text{As}_{2/3}\text{Ge}_{1/3}\text{S}_4$	Kick-out along <i>b</i> axis	0.2	0.3	0.4	0.2
$\text{Li}_{10/3}\text{As}_{2/3}\text{Ge}_{1/3}\text{S}_4$	Interstitial along <i>c</i> axis	0.2	0.3	0.3	0.2

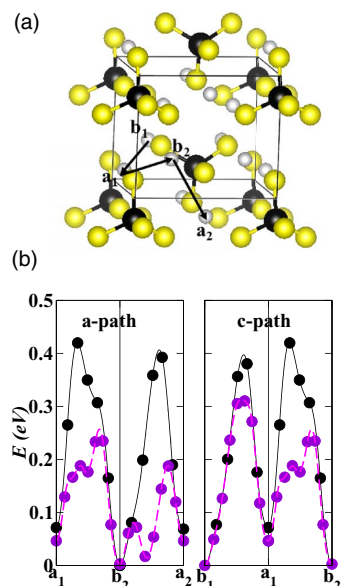


**Figure 5.** (a) Ball and stick model of  $\text{Li}_3\text{AsS}_4$  indicating Li ion vacancy migration pathways. (b) Corresponding minimum energy paths for Li ion vacancy migration along the  $a$  and  $c$  axes. In addition to the results for  $\text{Li}_3\text{AsS}_4$ , the corresponding NEB migration energies are also given for  $\gamma\text{-Li}_3\text{PS}_4$  as indicated with purple symbols and lines.

in Fig. 6b. This is a purely interstitial migration between neighboring  $II$  type interstitials between sites  $II_1 \rightarrow II_2 \rightarrow II_3$ . For this path, the NEB analysis shows a correlated motion of the host lattice Li ion at the neighboring “ $a$ ” site was found in partial kick-out like process. While this correlated motion contributes to the energetics of the process, it does not seem to directly contribute to ion migration. The corresponding minimum energy paths as determined from the NEB method are shown in Fig. 7. We see that for the paths along the  $b$  axis, the kick-out mechanism, with a migration energy  $E_m = 0.34$  eV, is more favorable than the pure interstitial mechanism with a migration energy  $E_m = 0.5$  eV, and also more favorable than the pure vacancy migration shown in Fig. 5. The pure interstitial migration path along the  $c$  axis has a migration energy  $E_m = 0.31$  eV, which is the most favorable of the paths considered for this material.

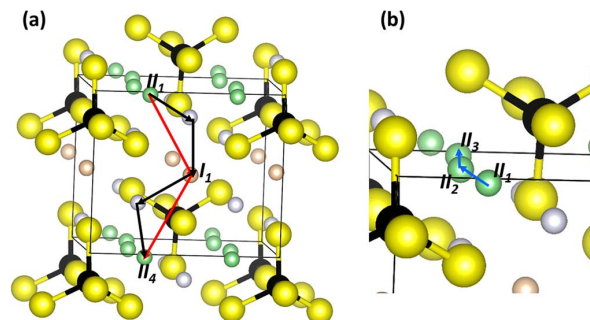


**Figure 6.** Ball and stick diagram of  $\text{Li}_3\text{AsS}_4$  using the same orientation and ball convention as Fig. 1. (a) Indicates a migration path with net motion along the  $b$  axis, the red arrows indicating the pure interstitial process and the black arrow indicating a related process including the “kick-out” of host lattice ions at each step. (b) Indicates a migration path with net motion along the  $c$  axis with a pure interstitial process.

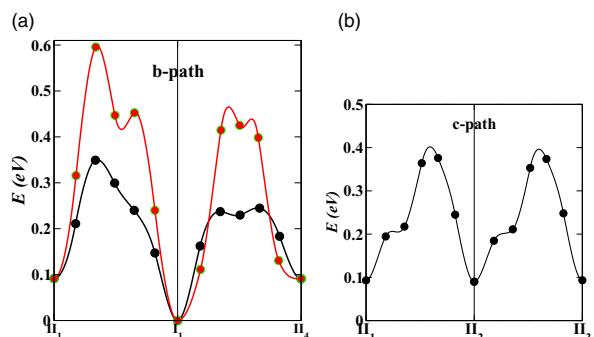


**Figure 7.** (a) Minimum energy paths as determined from the NEB method for the pure interstitial mechanism along the  $b$  axis (red curve) and for the kick-out mechanism (black curve) corresponding to the diagram in Fig. 6a. (b) Minimum energy path as determined by the NEB method for the pure interstitial mechanism along the  $c$  axis corresponding to the diagram in Fig. 6b.

*Ion migration in  $\text{Li}_{13/4}\text{As}_{3/4}\text{Ge}_{1/4}\text{S}_4$ .*—For an alloy, it is expected that the role of the interstitial-vacancy pair formation energy  $E_f$  in contributing to the activation energy as described by Eq. 4 is less important than it is in highly ordered crystals. However,  $E_f$  is a well-defined quantity within our ordered models for these alloys. For the  $\text{Li}_{13/4}\text{As}_{3/4}\text{Ge}_{1/4}\text{S}_4$  alloy, the lowest formation energy was found to be  $E_f = 0.27$  eV involving the  $J$  type interstitial and its neighboring “ $x$ ” site vacancy. This value of  $E_f$  is considerably smaller than that pure  $\text{Li}_3\text{AsS}_4$  and its mechanism is a consequence of the extra “ $x$ ” Li ions introduced by Ge.

For several reasons, it is reasonable to assume that interstitial and interstitial-vacancy ion migration mechanisms, and not pure vacancy mechanisms, are of main importance for ion migration in  $\text{Li}_{3+x}\text{As}_{1-x}\text{Ge}_x\text{S}_4$  alloys. Firstly, as discussed for pure  $\text{Li}_3\text{AsS}_4$ , these mechanisms have smaller migration energy barriers in the  $\text{Li}_3\text{AsS}_4$  lattice itself. Secondly, as discussed above, the  $x$  site Li can contribute to the interstitial population with a relatively small formation energy. Finally, as discussed in the structural analysis section, several potential Li ion vacancy sites in the vicinity of Ge (sites  $a^1$ ,  $b^1$ , and  $b^2$  shown in Fig. 3a) are found to be unstable relative to the  $x$  site vacancy, limiting the pure vacancy pathways available within this lattice.

As discussed above, for pure  $\text{Li}_3\text{AsS}_4$ , the most energetically favorable Li ion migration paths were found to be a kick-out mechanism along  $b$  axis and a pure interstitial mechanism along the  $c$  axis. In the  $\text{Li}_{13/4}\text{As}_{3/4}\text{Ge}_{1/4}\text{S}_4$  alloy, several variations of these paths occur; it is expected that their energy profiles will depend on the location of the paths relative to the planes of Ge substitution.

We studied three representative paths based on a kick-out mechanism with net migration along the  $b$  axis, as shown in Fig. 8a. The path  $L_1 \rightarrow b^2 \rightarrow K'_2 \rightarrow a^2 \rightarrow L_2$  has a migration energy of  $E_m = 0.28$  eV. It is geometrically equivalent to the path  $II_4 \rightarrow b \rightarrow I_1 \rightarrow a \rightarrow II_1$  with a migration energy of  $E_m = 0.34$  eV found in the pure  $\text{Li}_3\text{AsS}_4$  structure. A contributing factor to the decrease in  $E_m$  for this path in the alloy is the alignment of the interstitial energies of the  $L$  and  $K'$  sites due to their proximity to Ge as reported in Table III. A similar path within the  $1/4$  alloy is represented by the sequence  $N_1 \rightarrow a^3 \rightarrow K_1 \rightarrow b^3 \rightarrow N_2$  which is found to have a migration energy of  $E_m = 0.31$  eV, involving sites further from the Ge substitutions. We also considered the path represented with the sequence  $J_1 \rightarrow a^2 \rightarrow K'_1 \rightarrow b^2 \rightarrow J_2$ . As illustrated in Fig. 9a, the migration energy for this path,  $E_m = 0.52$  eV, is so large that this mechanism is unlikely to contribute to the diffusion process. While the geometry of this path is similar to the other two  $b$  axis kick-out mechanisms, the hop distances for the first and last steps of the process are  $0.2 \text{ \AA}$  longer. In addition, due to its proximity to the plane of Ge substitutions, the  $J$  interstitial site is the most stable of the interstitial

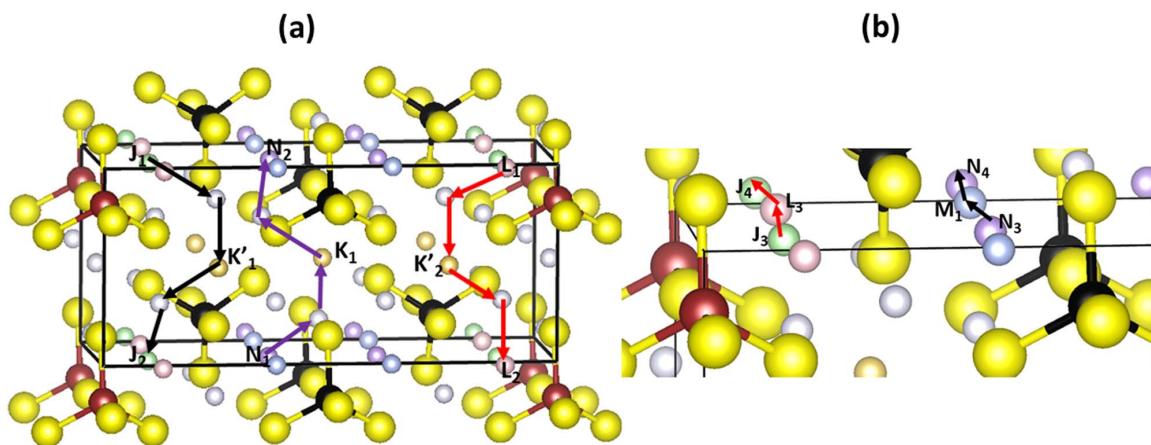


**Figure 8.** Ball and stick diagram of the  $\text{Li}_{13/4}\text{As}_{3/4}\text{Ge}_{1/4}\text{S}_4$  using the same orientation and ball convention as Fig. 3a. (a) Shows three distinct migration paths with net motion along the  $b$  axis, involving interstitial ions and the “kick-out” of host lattice ions at each step, indicated with black, purple, and red arrows. (b) Shows two distinct migration paths with net motion along the  $c$  axis with pure interstitial processes, indicated with red and black arrows.

sites as shown in Table III. Both of these factors may explain the high migration energy of this path.

For the pure interstitial migration, two different paths with a net migration along the  $c$  axis were considered as shown in Fig. 8b. The migration energy was determined from the NEB calculations, as presented in Fig. 9b. These paths are similar to that found in pure  $\text{Li}_3\text{AsS}_4$  where it involves the interstitial sites  $I1_1 \rightarrow I1_2 \rightarrow I1_3$ . For the path  $J_3 \rightarrow L_3 \rightarrow J_4$ , the first hop has a very low migration barrier apparently due to a correlated motion of the  $a^1$  lattice site in a partial “kick-out” like process. For the second hop of this path, there is apparently no correlated motion by the nearby host Li ion of type  $a^2$  and the overall migration barrier for this path is increased to  $E_m = 0.42$  eV. The path  $N_3 \rightarrow M_1 \rightarrow N_4$  involves the correlated motion of the nearby Li ion at a  $a^3$  site on both hops, resulting in the overall migration energy for this path of  $E_m = 0.29$  eV which is slightly lower than the corresponding migration energy of  $E_m = 0.31$  eV in pure  $\text{Li}_3\text{AsS}_4$ .

**Ion migration in  $\text{Li}_{10/3}\text{As}_{2/3}\text{Ge}_{1/3}\text{S}_4$ .**—For the  $\text{Li}_{10/3}\text{As}_{2/3}\text{Ge}_{1/3}\text{S}_4$  alloy, the lowest formation energy was found to be  $E_f = 0.27$  eV, involving the  $B$  type interstitial and its neighboring  $x$  site vacancy, geometrically and energetically similar to the  $1/4$  alloy.

For modeling  $b$  axis migration with the kick-out mechanism, three different paths were considered, as shown in Fig. 10a. The correspond-

ing minimum energy paths determined from NEB calculations are presented in Fig. 11a. The path sequence  $A_1 \rightarrow a^2 \rightarrow K_1 \rightarrow b^2 \rightarrow A_2$  has a migration energy of  $E_m = 0.23$  eV which is smaller than  $E_m = 0.28$  eV and  $E_m = 0.34$  eV for the corresponding migrations in the  $1/4$  alloy and pure  $\text{Li}_3\text{AsS}_4$ , respectively. The path sequence  $C_1 \rightarrow a^2 \rightarrow K_2 \rightarrow b^3 \rightarrow C_2$  has a migration energy of  $E_m = 0.30$  eV which very slightly smaller than  $E_m = 0.31$  eV and  $E_m = 0.34$  eV for the corresponding migrations in the  $1/4$  alloy and pure  $\text{Li}_3\text{AsS}_4$ , respectively. The third path considered in this study,  $B_1 \rightarrow a^2 \rightarrow K_3 \rightarrow b^2 \rightarrow A_3$ , has a relatively large migration barrier of  $E_m = 0.39$  eV. The first hop of this path involves the  $B$  type interstitial site which tends to cause larger migration barriers due to its stability, similar behavior of the  $J$  site in the  $1/4$  alloy. The second hop of this process is identical (within the calculational error) to the  $K_1 \rightarrow b^2 \rightarrow A_2$  sequence.

For the pure interstitial mechanism along the  $c$  axis, two paths were considered as shown in Fig. 10b with the corresponding NEB energy paths shown in Fig. 11b. The path  $A_1 \rightarrow B_2 \rightarrow A_4$  has a migration energy of  $E_m = 0.47$  eV. As in the case of the  $1/4$  alloy, the migration energy is large for this case due to the asymmetric correlated motion of nearby Li ions at inequivalent  $a$  sites. For the path  $C_1 \rightarrow C_2 \rightarrow C_3$  the migration energy is  $E_m = 0.2$  eV. As in the similar paths in the  $1/4$  alloy and the pure  $\text{Li}_3\text{AsS}_4$ , the migration involves the correlated partial kick-out of the neighboring Li ion at a  $a^2$  site. In

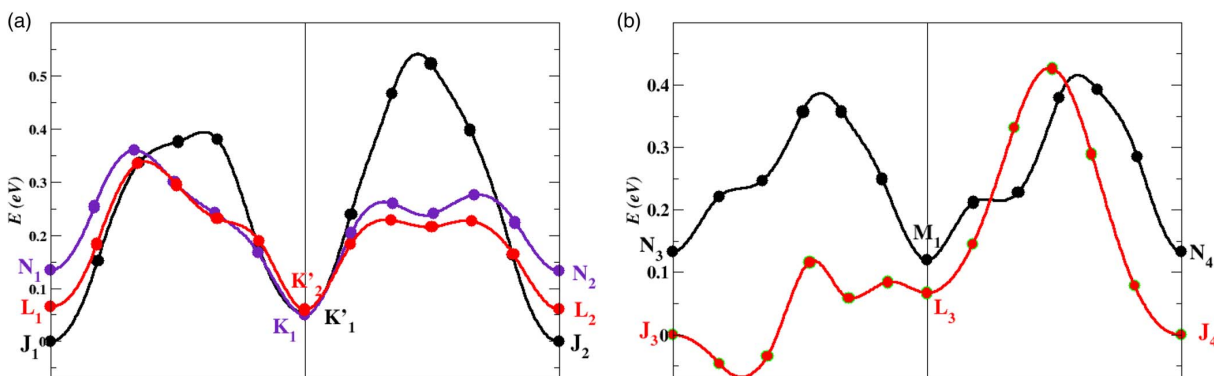


**Figure 9.** (a) Minimum energy paths as determined from the NEB method for the three distinct kick-out mechanism paths along the  $b$  axis shown in Fig. 8a. The line colors of the plot are consistent the arrows in the structural diagram. (b) Minimum energy paths as determined by the NEB method for the pure interstitial mechanism along the  $c$  axis corresponding to the diagram in Fig. 8b. The line colors of the plot are consistent the arrows in the structural diagram.

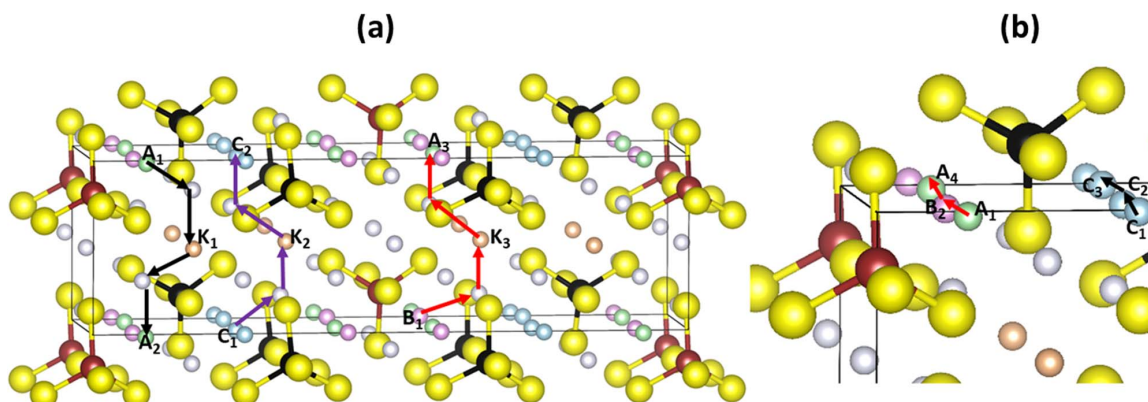


**Figure 10.** Ball and stick diagram of the  $\text{Li}_{10/3}\text{As}_{2/3}\text{Ge}_{1/3}\text{S}_4$  using the same orientation and ball convention as Fig. 3b. (a) Shows migration paths with net motion along the **b** axis, with a process including the “kick-out” of host lattice ions at each step, indicated with black, purple, and red arrows. (b) Shows migration paths with net motion along the **c** axis with a pure interstitial process, indicated with red and black arrows.

this case, the resulting process has the lowest migration energy in the study.

### Conclusions

As a result of this computational study, we are reasonably confident in our determination that pure  $\text{Li}_3\text{AsS}_4$  forms in the  $Pmn2_1$  crystal structure. Our first principles optimizations found this structure to have the lowest energy of those that we studied, and the results are in good agreement with the X-ray diffraction data reported by Sahu et al.,<sup>3</sup> as shown in Fig. 2.

The X-ray data of Sahu et al.<sup>3</sup> for the prepared materials with compositions  $\text{Li}_{3+x}\text{As}_{1-x}\text{Ge}_x\text{S}_4$  suggests that they are substitutional alloys based on the  $\text{Li}_3\text{AsS}_4$  structure. Our simulations assumed this to be the case, and the results are consistent. Despite the chemical similarities, the  $\text{Li}_{3+x}\text{As}_{1-x}\text{Ge}_x\text{S}_4$  alloy system based on substitutions into the  $Pmn2_1$  structure, is quite different from  $\text{Li}_{3+x}\text{P}_{1-x}\text{Ge}_x\text{S}_4$  which has been shown<sup>7</sup> to undergo several structural transitions within a similar composition range. Presumably, the size similarity of the  $\text{AsS}_4$  and  $\text{GeS}_4$  building blocks help stabilize the  $Pmn2_1$  structure.

We determined idealized models for the  $x = 1/4$  and  $x = 1/3$  alloys which turned out to be based on  $2 \times 1 \times 1$  and  $3 \times 1 \times 1$  supercells of  $\text{Li}_3\text{AsS}_4$ , respectively. The analysis shows how the  $Pmn2_1$  structure can accommodate efficient ionic transport with a combination of interstitial and host lattice sites. For  $\text{Li}_3\text{AsS}_4$  and the

two alloy models, the migration of interstitial Li ions along the **c** axis gives the smallest value of the migration energy  $E_m$ . The migration of interstitial Li ions along the **b** axis using a kick-out process also gives a small value for  $E_m$ . The summary of the calculated values for the migration energies  $E_m$  as well as the energy  $E_f$  to form vacancy-interstitial pairs are given in Table VI where they are compared with the experimentally determined activation energies  $E_A$ . In general, we find  $E_m \approx E_A$ , suggesting that the prepared materials correspond to the “extrinsic” case described by Eq. 4. The simulations generally show that an important effect of Ge is to adjust the energies of the participating interstitial and vacancy Li ion sites to reduce  $E_m$ . Another effect of Ge is to stabilize an extra Li ion in the lattice at what we called the “*x*” site. Undoubtedly, this extra Li contributes to population of mobile interstitial Li ions, although our models cannot explain the details of these processes. The results of our simulations are in general agreement with the trends presented by the experimental work of Sahu et al.<sup>3</sup> One question that has not yet been resolved is the suggestion that the concentration  $x = 1/3$  may be optimal. Our models show that the minimal values of the migration energies follow the trend  $E_m(x = 0) > E_m(x = 1/4) > E_m(x = 1/3)$ , suggesting that the substitutional Ge incrementally reduces the migration barrier and improves the ionic conductivity.

The  $\text{Li}_{3+x}\text{As}_{1-x}\text{Ge}_x\text{S}_4$  alloy system of Li ion conductors is the only system (that we know about) which is based on the  $Pmn2_1$  structure. Several related alloy systems, such as  $\text{Li}_{3+x}\text{P}_{1-x}\text{Si}_x\text{S}_4$

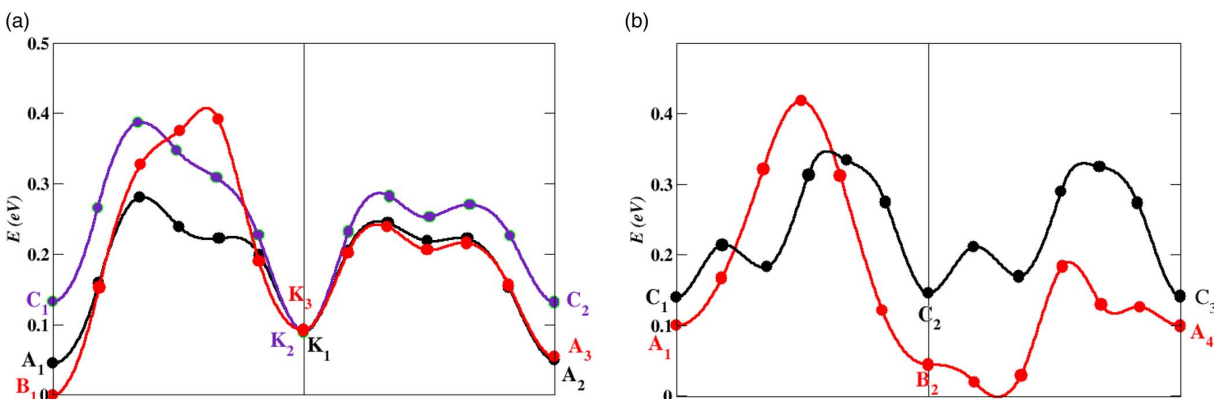


**Figure 11.** (a) Minimum energy paths as determined from the NEB method for the kick-out mechanism along the **b** axis corresponding to the diagram in Fig. 10a. The line colors correlate with the arrows in the structural diagram. (b) Minimum energy path as determined by the NEB method for the pure interstitial mechanism along the **c** axis corresponding to the diagram in Fig. 10b. The line colors correlate with the arrows in the structural diagram.

and  $\text{Li}_{3+x}\text{P}_{1-x}\text{Ge}_x\text{S}_4$ , transform into a  $Pnma$  structure or more complicated structures in order to achieve their improved Li ion conduction.<sup>5,7</sup>

### Acknowledgments

This work was supported by NSF grants DMR-1105485 and DMR-1507942. Computations were performed on the Wake Forest University DEAC cluster, a centrally managed resource with support provided in part by the University. Help from Chaochao Dun and Ching-Wan Yip with digitizing the experimental X-ray results is gratefully acknowledged.

### Appendix: Structural Details

This appendix lists the detailed structural parameters determined from the simulations. It is our experience that the fractional coordinates are generally in excellent agreement with experiment. The lattice constants, when scaled by a factor of 1.02 to compensate the systematic error of LDA, are also in excellent agreement with experiment. Table AI lists the fractional coordinates of  $\text{Li}_3\text{AsS}_4$  in comparison with the corresponding coordinates of  $\text{Li}_3\text{PS}_4$ , showing the close similarity. Tables AII and AIII list the fractional coordinates of our models of the 1/4 and 1/3 alloys.

**Table AI. Fractional coordinates of unique sites of the optimal structure of  $\text{Li}_3\text{AsS}_4$  having the  $Pmn2_1$  structure (with computed lattice constants  $a = 7.57 \text{ \AA}$ ,  $b = 6.54 \text{ \AA}$ ,  $c = 6.13 \text{ \AA}$ ) in comparison with the corresponding coordinates for  $\gamma\text{-Li}_3\text{PS}_4$  (with computed lattice constants  $a = 7.55 \text{ \AA}$ ,  $b = 6.45 \text{ \AA}$ ,  $c = 6.05 \text{ \AA}$ ). The “Site” column lists the site multiplicity in the unit cell and the Wyckoff label.**

Atom	Site	$\text{Li}_3\text{AsS}_4$ ( $x, y, z$ )	$\text{Li}_3\text{PS}_4$ ( $x, y, z$ )
Li	4b	(0.243, 0.319, -0.001)	(0.243, 0.317, 0.000)
Li	2a	(0.000, 0.152, 0.487)	(0.000, 0.150, 0.488)
As/P	2a	(0.000, 0.821, 1.000)	(0.000, 0.819, 0.999)
S	4b	(0.231, 0.666, 0.884)	(0.221, 0.670, 0.888)
S	2a	(0.000, 0.131, 0.879)	(0.000, 0.118, 0.886)
S	2a	(0.000, 0.813, 0.352)	(0.000, 0.811, 0.337)

**Table AII. Fractional coordinates of unique sites of the optimal structure of  $\text{Li}_{13/4}\text{As}_{3/4}\text{Ge}_{1/4}\text{S}_4$  (with computed lattice constants  $a = 15.20 \text{ \AA}$ ,  $b = 6.60 \text{ \AA}$ , and  $c = 6.13 \text{ \AA}$ ) The multiplicity of the site within the simulations cell and the Li labels as defined in Fig. 3a (rather than the labels of its  $Pm$  space group) are also listed.**

Atom	Mult.	Label	( $x, y, z$ )
Li	1	$a^1$	(0.000, 0.107, 0.510)
Li	2	$b^1$	(±0.138, 0.691, 0.514)
Li	2	$a^2$	(±0.247, 0.840, 0.026)
Li	2	$b^2$	(±0.122, 0.319, 0.994)
Li	1	$a^3$	(0.500, 0.164, 0.516)
Li	2	$b^3$	(±0.372, 0.692, 0.495)
Li	2	$b^4$	(±0.379, 0.318, 0.997)
Li	1	$x$	(0.000, 0.483, 0.341)
As	1		(0.500, 0.822, 0.998)
As	2		(±0.249, 0.186, 0.496)
Ge	1		(0.000, 0.818, 0.001)
S	1		(0.000, 0.135, 0.115)
S	1		(0.500, 0.127, 0.123)
S	1		(0.000, 0.782, 0.641)
S	1		(0.500, 0.825, 0.646)
S	2		(±0.116, 0.655, 0.131)
S	2		(±0.616, 0.664, 0.110)
S	2		(±0.129, 0.335, 0.607)
S	2		(±0.637, 0.350, 0.611)
S	2		(±0.254, 0.886, 0.634)
S	2		(±0.250, 0.179, 0.144)

**Table AIII. Fractional coordinates of unique sites of the optimal structure with space group  $Pmn2_1$  of  $\text{Li}_{10/3}\text{As}_{2/3}\text{Ge}_{1/3}\text{S}_4$  (with computed lattice constants  $a = 22.77 \text{ \AA}$ ,  $b = 6.60 \text{ \AA}$ , and  $c = 6.14 \text{ \AA}$ ) The multiplicity of the site within the simulations cell and Wyckoff label, as well as the Li labels as defined in Fig. 3b are also listed.**

Atom	Mult.	Label	( $x, y, z$ )
Li	2 $a$	$x$	(0.000, 0.474, 0.664)
Li	2 $a$	$a^1$	(0.000, 0.098, 0.496)
Li	4 $b$	$b^1$	(0.092, 0.683, 0.489)
Li	4 $b$	$a^2$	(0.167, 0.827, 0.972)
Li	4 $b$	$b^2$	(0.082, 0.311, 0.010)
Li	4 $b$	$b^3$	(0.251, 0.311, 0.002)
As	4 $b$		(0.335, 0.822, 0.003)
Ge	2 $a$		(0.000, 0.810, 0.002)
S	2 $a$		(0.000, 0.128, 0.890)
S	2 $a$		(0.000, 0.774, 0.361)
S	4 $b$		(0.740, 0.653, 0.884)
S	4 $b$		(0.078, 0.647, 0.871)
S	4 $b$		(0.415, 0.673, 0.897)
S	4 $b$		(0.669, 0.122, 0.865)
S	4 $b$		(0.833, 0.167, 0.853)

### References

1. Y. Wang, W. D. Richards, S. P. Ong, L. J. Miara, J. C. Kim, Y. Mo, and G. Ceder, *Nature Materials*, **14**, 1026 (2015).
2. J. Li, C. Ma, M. Chi, C. Liang, and N. J. Dudney, *Advanced Energy Materials*, **5**, 1041408 (2015).
3. G. Sahu, E. Rangasamy, J. Li, Y. Chen, K. An, N. Dudney, and C. Liang, *Journal of Materials Chemistry A*, **2**, 10396 (2014).
4. Y.-W. Hu, I. D. Raistrick, and R. A. Huggins, *Journal of the Electrochemical Society*, **124**, 1240 (1977).
5. H. Deng, P. Nie, H. Luo, Y. Zhang, J. Wang, and X. Zhang, *J. Mater. Chem. A*, **2**, 18256 (2014).
6. T. Hahn, ed., *International Tables for Crystallography, Volume A: Space-group symmetry, Fifth revised edition* (Kluwer, 2002) ISBN 0-7923-6590-9.
7. S. Hori, M. Kato, K. Suzuki, M. Hirayama, Y. Kato, and R. Kanno, *Journal of the American Ceramic Society*, **98**, 3352 (2015).
8. K. Homma, M. Yonemura, T. Kobayashi, M. Nagao, M. Hirayama, and R. Kanno, *Solid State Ionics*, **182**, 53 (2011).
9. N. Kamaya, K. Homma, Y. Yamakawa, M. Hirayama, R. Kanno, M. Yonemura, T. Kamiyama, Y. Kato, S. Hama, K. Kawamoto, and A. Mitsui, *Nature Materials*, **10**, 682 (2011).
10. R. Kanno and M. Murayama, *Journal of the Electrochemical Society*, **148**, A742 (2001).
11. Z. Liu, W. Fu, E. A. Payzant, X. Yu, Z. Wu, N. J. Dudney, J. Kiggans, K. Hong, A. J. Rondinone, and C. Liang, *Journal of the American Chemical Society*, **135**, 975 (2013).
12. M. Tachez, J.-P. Malugani, R. Mercier, and G. Robert, *Solid State Ionics*, **14**, 181 (1984).
13. P. Hohenberg and W. Kohn, *Physical Review*, **136**, B864 (1964).
14. W. Kohn and L. J. Sham, *Physical Review*, **140**, A1133 (1965).
15. P. E. Blöchl, *Phys. Rev. B*, **50**, 17953 (1994).
16. N. A. W. Holzwarth, A. R. Tackett, and G. E. Matthews, *Computer Physics Communications*, **135**, 329 (2001), available from the website <http://pwpaw.wfu.edu>.
17. P. Giannozzi, S. Baroni, N. Bonini, M. Calandra, R. Car, C. Cavazzoni, D. Ceresoli, G. L. Chiarotti, M. Cococcioni, I. Dabo, A. D. Corso, S. de Gironcoli, S. Fabris, G. Fratesi, R. Gebauer, U. Gerstmann, C. Gougousis, A. Kokalj, M. Lazzeri, L. Martin-Samos, N. Marzari, F. Mauri, R. Mazzarello, S. Paolini, A. Pasquarello, L. Paulatto, C. Sbraccia, S. Scandolo, G. Sclauzero, A. P. Seitsonen, A. Smogunov, P. Umari, and R. M. Wentzcovitch, *J. Phys.: Condens. Matter*, **21**, 394402 (2009), available from the website <http://www.quantum-espresso.org>.
18. A. Kokalj, *Journal of Molecular Graphics and Modelling*, **17**, 176 (1999), code available at the website <http://www.xcrysden.org>.
19. A. Kokalj, *Computational Materials Science*, **28**, 155 (2003).
20. K. Momma and F. Izumi, *Applied Crystallography*, **44**, 1272 (2011), code available from the website <http://jp-minerals.org/vesta/en/>.
21. J. P. Perdew and Y. Wang, *Phys. Rev. B*, **45**, 13244 (1992).
22. Y. A. Du and N. A. W. Holzwarth, *Phys. Rev. B*, **76**, 174302 (2007).
23. N. A. W. Holzwarth, N. D. Lepley, and Y. A. Du, *Journal of Power Sources*, **196**, 6870 (2011).
24. Y. A. Du and N. A. W. Holzwarth, *Phys. Rev. B*, **81**, 184106 (2010).
25. N. D. Lepley and N. A. W. Holzwarth, *Journal of the Electrochemical Society*, **159**, A538 (2012).
26. N. D. Lepley, N. A. W. Holzwarth, and Y. A. Du, *Phys. Rev. B*, **88**, 104103 (2013).

27. K. Senevirathne, C. S. Day, M. D. Gross, A. Lachgar, and N. A. W. Holzwarth, *Solid State Ionics*, **333**, 95 (2013).
28. N. D. Lepley and N. A. W. Holzwarth, *Phys. Rev. B*, **92**, 214201 (2015).
29. Z. D. Hood, C. Kates, M. Kirkham, S. Adhikari, C. Liang, and N. A. W. Holzwarth, *Solid State Ionics*, **284**, 61 (2015).
30. L. E. Rush Jr. and N. A. W. Holzwarth, *Solid State Ionics*, **286**, 45 (2016).
31. W. M. Haynes, ed., *CRC Handbook of Chemistry and Physics*, 92th Edition (CRC Press, Taylor & Francis Group, 2011) ISBN 978-1-4398-5511-9.
32. A. Van De Walle and G. Ceder, *Reviews of Modern Physics*, **74**, 11 (2002).
33. H. Jónsson, G. Mills, and K. W. Jacobsen, in *Classical and Quantum Dynamics in Condensed Phase Simulations*, edited by B. J. Berne, G. Ciccoliti, and D. F. Coker (World Scientific, Singapore, 1998) pp. 385–404.
34. G. Henkelman, B. P. Uberuaga, and H. Jónsson, *J. Chem. Phys.*, **113**, 9901 (2000).
35. G. Henkelman and H. Jónsson, *J. Chem. Phys.*, **113**, 9978 (2000).
36. A. R. West, *Basic Solid State Chemistry*, second edition (John Wiley & Sons, LTD, 1999).
37. G. Makov and M. C. Payne, *Physical Review B*, **51**, 4014 (1995).
38. C. Freysoldt, J. Neugebauer, and C. G. Van de Walle, *Physical Review Letters*, **102** (2009).
39. P. Ganesh, A. A. Lubimtsev, G. K. P. Dathar, J. Anchell, P. R. C. Kent, A. J. Rondinone, and B. G. Sumpter, *Bulletin of the American Physical Society*, **60** (2015), APS March Meeting 2015.
40. Z. Liu, W. Fu, E. A. Payzant, X. Yu, Z. Wu, N. J. Dudney, J. Kiggans, K. Hong, A. J. Rondinone, and C. Liang, *Journal of the American Chemical Society*, **135**, 975 (2013).
41. K. Homma, M. Yonemura, T. Kobayashi, M. Nago, M. Hirayama, and R. Kanno, *Solid State Ionics*, **182**, 53 (2011).
42. R. Mercier, J.-P. Malugani, B. Fahys, and G. Robert, *Acta Cryst.*, **B38**, 1887 (1982).
43. “Mercury 3.5.1”, (2014), developed and distributed by the Cambridge Crystallographic Data Centre <http://www.ccdc.cam.ac.uk/mercury/>.
44. G. Sahu, Z. Lin, J. Li, Z. Liu, N. Dudney, and C. Liang, *Energy Environ. Sci.*, **7**, 1053 (2014).
45. Y. Matsushita and M. G. Kanatzidis, *Z. Naturforsch.*, **53 b**, 23 (1998).
46. M. Murayama, R. Kanno, Y. Kawamoto, and T. Kamiyama, *Solid State Ionics*, **154–155**, 789 (2002).
47. J. H. MacNeil, D. M. Massi, J.-H. Zhang, K. A. Rosmus, C. D. Brunetta, T. A. Gentile, and J. A. Aitken, *Journal of Alloys and Compounds*, **586**, 736 (2014).
48. R. Grau-Crespo, S. Hamad, C. R. A. Catlow, and N. H. d. Leeuw, *Journal of Physics: Condensed Matter*, **19**, 256201 (2007).

## Appendix B

# $\text{Li}_4\text{SnS}_4$ and $\text{Li}_4\text{SnSe}_4$ : Simulations of Their Structure and Electrolyte Properties

Reproduced from the Journal of Electrochemical Society, volume 164, issue 1, pages  
A6386–A6394, 2017. With a permission from Elsevier.





FOCUS ISSUE OF SELECTED PAPERS FROM IMLB 2016 WITH INVITED PAPERS CELEBRATING 25 YEARS OF LITHIUM ION BATTERIES

## Li<sub>4</sub>SnS<sub>4</sub> and Li<sub>4</sub>SnSe<sub>4</sub>: Simulations of Their Structure and Electrolyte Properties

Ahmad Al-Qawasmeh, Jason Howard,\* and N. A. W. Holzwarth\*\*,\*z

Department of Physics, Wake Forest University, Winston-Salem, North Carolina 27109-7507, USA

Recent experimental literature reports the solid state electrolyte properties of Li<sub>4</sub>SnS<sub>4</sub> and Li<sub>4</sub>SnSe<sub>4</sub>, identifying interesting questions regarding their structural details and motivating our first principles simulations. Together with Li<sub>4</sub>GeS<sub>4</sub>, these materials are all characterized by the orthorhombic space group *Pnma* and are found to be isostructural. They have a ground state crystal structure (denoted Li<sub>4</sub>SnS<sub>4</sub><sup>0</sup>) having interstitial sites in void channels along the *c*-axis. They also have a meta-stable structure (denoted Li<sub>4</sub>SnS<sub>4</sub><sup>\*</sup>) which is formed by moving one fourth of the Li ions from their central sites to the interstitial positions, resulting in a 0.5 Å contraction of the *a* lattice parameter. Relative to their ground states, the meta-stable structures are found to have energies 0.25 eV, 0.02 eV, and 0.07 eV for Li<sub>4</sub>GeS<sub>4</sub><sup>\*</sup>, Li<sub>4</sub>SnS<sub>4</sub><sup>\*</sup>, and Li<sub>4</sub>SnSe<sub>4</sub><sup>\*</sup>, respectively. Consistent with these simulation results, the ground state forms for Li<sub>4</sub>GeS<sub>4</sub><sup>0</sup>, Li<sub>4</sub>SnS<sub>4</sub><sup>0</sup> and Li<sub>4</sub>SnSe<sub>4</sub><sup>0</sup> and the meta-stable form for Li<sub>4</sub>SnS<sub>4</sub><sup>\*</sup> have been reported in the experimental literature. In addition, simulations of Li ion migration in these materials are also investigated.

© The Author(s) 2017. Published by ECS. This is an open access article distributed under the terms of the Creative Commons Attribution 4.0 License (CC BY, <http://creativecommons.org/licenses/by/4.0/>), which permits unrestricted reuse of the work in any medium, provided the original work is properly cited. [DOI: 10.1149/2.0581701jes] All rights reserved.



Manuscript submitted September 29, 2016; revised manuscript received November 8, 2016. Published January 18, 2017. This was Paper 842 presented at the Chicago, Illinois, Meeting of the IMLB, June 19–24, 2016. This paper is part of the Focus Issue of Selected Papers from IMLB 2016 with Invited Papers Celebrating 25 Years of Lithium Ion Batteries.

Recently, there has been significant progress in developing stable solid electrolytes with high ionic conductivity,<sup>1</sup> which has been identified as a key to improving battery technologies.<sup>2</sup> Recent literature<sup>3–7</sup> reports the use of Li<sub>4</sub>SnS<sub>4</sub> and related materials as relatively stable solid electrolytes for use in all-solid-state Li batteries. Kaib, Haddadpour, et al.<sup>3</sup> and Kaib, Bron, et al.<sup>5</sup> synthesized Li<sub>4</sub>SnS<sub>4</sub> and Li<sub>4</sub>SnSe<sub>4</sub>, showing that pure materials could be obtained by removing water or methanol from solution based preparations, and comparing their structures and ionic conductivities. MacNeil et al.<sup>4</sup> used high temperature solid state techniques to synthesize Li<sub>4</sub>SnS<sub>4</sub> and made a detailed structural analysis to show it to be isostructural with Li<sub>4</sub>GeS<sub>4</sub>. Sahu et al.<sup>6</sup> showed that Li<sub>4</sub>SnS<sub>4</sub> and its alloys with Li<sub>3</sub>AsS<sub>4</sub> have reasonable ionic conductivity (10<sup>-5</sup>–10<sup>-4</sup> S/cm at room temperature) with comparatively more air-stability than other sulfide electrolytes. Park et al.<sup>7</sup> demonstrated favorable conductivity and stability properties of Li<sub>4</sub>SnS<sub>4</sub> and its alloys with LiI.

From this literature, some interesting questions arise regarding crystal structures and mechanisms for ion mobility. In order to address these questions, we use first principles methods to examine the ideal crystal forms and defect structures of Li<sub>4</sub>SnS<sub>4</sub> and the structurally and chemically related materials Li<sub>4</sub>GeS<sub>4</sub> and Li<sub>4</sub>SnSe<sub>4</sub>. For each of these materials, we identify two closely related structures – an ideal ground state structure and an ideal meta-stable structure. The simulations show that the meta-stable structural form is most accessible to Li<sub>4</sub>SnS<sub>4</sub> of the three materials studied. The simulations are extended to study mechanisms of Li ion migration in both Li<sub>4</sub>SnS<sub>4</sub> and Li<sub>4</sub>SnSe<sub>4</sub> and are related to the experimental results reported in the literature.

### Computational Methods

The computational methods used in this work are based on density functional theory (DFT),<sup>8,9</sup> using the projected augmented wave (PAW)<sup>10</sup> formalism. The PAW basis and projector functions were generated by the ATOMPAW<sup>11</sup> code and the crystalline materials were modeled using the QUANTUM ESPRESSO<sup>12</sup> and ABINIT<sup>13</sup> packages. Visualizations were constructed using the XCrySDEN,<sup>14,15</sup> and VESTA<sup>16</sup> software packages.

\*Electrochemical Society Student Member.

\*\*Electrochemical Society Member.

<sup>z</sup>E-mail: natalie@wfu.edu

The exchange correlation function is approximated using the local-density approximation (LDA).<sup>17</sup> The choice of LDA functional was made based on previous investigations<sup>18–20</sup> of similar materials which showed that, provided that the lattice constants are scaled by a correction factor of 1.02, the simulations are in good agreement with experiment, especially lattice vibrational frequencies and heats of formation. The partial densities of states were calculated as described in previous work<sup>20,21</sup> using weighting factors based on the charge within the augmentation spheres of each atom with radii  $r_c^{\text{Li}} = 1.6$ ,  $r_c^{\text{Sn}} = 2.3$ ,  $r_c^{\text{S}} = 1.7$ , and  $r_c^{\text{Se}} = 2.3$  in bohr units. The reported partial densities of states curves  $\langle N^a(E) \rangle$  were averaged over the atomic sites of each type *a*.

The calculations were well converged with plane wave expansions of the wave function including  $|\mathbf{k} + \mathbf{G}|^2 \leq 64$  bohr<sup>-2</sup>. Calculations for the conventional unit cells were performed using a Brillouin-zone sampling grid of  $4 \times 8 \times 8$ . Simulations of Li ion migration were performed at constant volume in supercells constructed from the optimized conventional cells extended by  $1 \times 2 \times 2$  and a Brillouin-zone sampling grid of  $2 \times 2 \times 2$ . In modeling charged defects (Li ion vacancies or interstitials), the system was assumed to remain electrically insulating and a uniform background charge was added in order to evaluate the electrostatic interactions. The minimum energy path for Li ion migration was estimated using the “nudged elastic band” (NEB) method<sup>22–24</sup> as programmed in the QUANTUM ESPRESSO package, using 5 images between each metastable configuration. For each minimum energy path, the migration energy,  $E_m$  was determined as the energy difference between the lowest and highest energy of the path. The “formation energies”  $E_f$  for producing neutral defects in the form of vacancy-interstitial pairs were calculated for the same supercells. The molecular dynamics simulations were performed at constant volume in neutral  $1 \times 2 \times 2$  supercells using further reduced convergence parameters, including a reduced plane wave expansion cutoff of  $|\mathbf{k} + \mathbf{G}|^2 \leq 49$  bohr<sup>-2</sup> and a Brillouin-zone sampling grid of  $1 \times 1 \times 1$ . The simulations were performed for a microcanonical ensemble with a time integration step of  $\Delta t = 3.6 \times 10^{-15}$  s for simulation temperatures less than 900 K. For simulation temperatures greater than 900 K, the time integration step was reduced to  $\Delta t = 2.4 \times 10^{-15}$  s. This resulted in total energy conservation within 0.1 eV throughout the simulation. The simulations were carried out for durations between 3–8 pico seconds. After an equilibration delay of approximately 0.1 ps, the temperature of the simulation was determined from the averaged kinetic energy of the ions. The

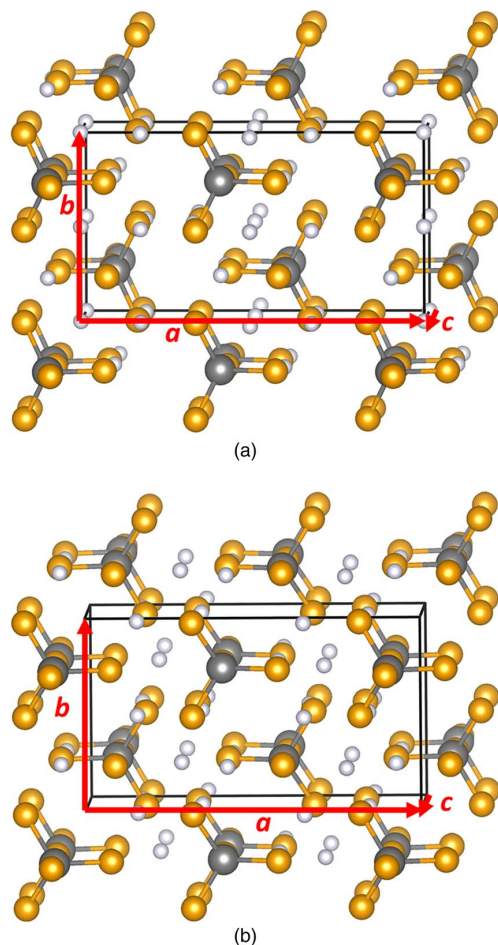


**Figure 1.** Ball and stick models of (a)  $\text{Li}_4\text{SnS}_4^0$  and (b)  $\text{Li}_4\text{SnS}_4^*$ . Li, Sn, and S are represented by light gray, dark gray, and orange balls respectively. The red arrows indicate the  $a$ ,  $b$ , and  $c$  lattice vectors.

simulated temperatures ranged between 550 K and 1000 K, well below the melting temperature of 1231 K reported by MacNeil et al.<sup>4</sup>

### Simulated Crystal Structures

There are two reported analyses of the crystal structure of  $\text{Li}_4\text{SnS}_4$ .<sup>3,4</sup> The two analyses agree that the structure is characterized by the space group  $Pnma$  (No. 62 in the International Table of Crystallography<sup>25</sup>), but differ slightly in the reported lattice constants and the fractional coordinates of one of the Li sites.<sup>4</sup> The structural analysis of MacNeil et al.<sup>4</sup> was measured at room temperature and is perfectly ordered. However, the structural analysis of Kaib, Haddadpour, et al.,<sup>3</sup> was measured at the temperatures in the range 100–193 K, and instead of the Li sites found by MacNeil et al. at the Wyckoff labeled  $4a$  positions, fractionally occupied  $8d$  Li sites are found.

We computationally investigated both structures, finding that the ordered structure analyzed by MacNeil et al.<sup>4</sup> to be the ground state structure which we denote as “ $\text{Li}_4\text{SnS}_4^0$ ”. Simulations of ordered approximations to the disordered structure of Kaib, Haddadpour, et al.<sup>3</sup> find a meta-stable structure which we denote as “ $\text{Li}_4\text{SnS}_4^*$ ” having an energy 0.02 eV/formula unit higher in energy than the ground state structure. Ball and stick drawings of the two structures are shown in Fig. 1. The corresponding calculated and measured lattice constants are listed in Table I and the calculated and measured fractional coordinates

**Table I.** Comparison of lattice parameters for  $\text{Li}_4\text{SnS}_4$  and related compounds in their ground state and meta-stable structures. Calculated parameters are scaled by factor of 1.02 to correct for systematic LDA error. Measured parameters are listed in parentheses. The relative energies  $E$  for the ground state and meta-stable structures are also listed in units of eV per formula unit.

	$\text{Li}_4\text{GeS}_4^0$	$\text{Li}_4\text{GeS}_4^*$
$a$ (Å)	14.01 (14.06) <sup>a</sup>	13.49
$b$ (Å)	7.74 ( 7.75) <sup>a</sup>	7.79
$c$ (Å)	6.12 ( 6.15) <sup>a</sup>	6.30
$E$ (eV/FU)	0.00	0.25
	$\text{Li}_4\text{SnS}_4^0$	$\text{Li}_4\text{SnS}_4^*$
$a$ (Å)	14.25 (14.31) <sup>a</sup>	13.81 (13.81) <sup>b</sup>
$b$ (Å)	7.86 ( 7.90) <sup>a</sup>	7.93 ( 7.96) <sup>b</sup>
$c$ (Å)	6.31 ( 6.33) <sup>a</sup>	6.41 ( 6.37) <sup>b</sup>
$E$ (eV/FU)	0.00	0.02
	$\text{Li}_4\text{SnSe}_4^0$	$\text{Li}_4\text{SnSe}_4^*$
$a$ (Å)	14.98 (14.93) <sup>c</sup>	14.48
$b$ (Å)	8.26 ( 8.22) <sup>c</sup>	8.38
$c$ (Å)	6.62 ( 6.60) <sup>c</sup>	6.86
$E$ (eV/FU)	0.00	0.07

<sup>a</sup>Ref. 4.

<sup>b</sup>Ref. 3.

<sup>c</sup>Ref. 5.

are listed in Table II. In addition to results for  $\text{Li}_4\text{SnS}_4$ , results for  $\text{Li}_4\text{GeS}_4$  and  $\text{Li}_4\text{SnSe}_4$  are also listed in these tables.

Interestingly, the main difference between the simulated structures of  $\text{Li}_4\text{SnS}_4^0$  and  $\text{Li}_4\text{SnS}_4^*$  is that four Li's per unit cell occupy different void regions between the  $\text{SnS}_4$  tetrahedra. In the  $\text{Li}_4\text{SnS}_4^0$  structure, the special Li ions occupy sites at the center and boundaries of the unit cell having multiplicity and Wyckoff label  $4a$ . In the  $\text{Li}_4\text{SnS}_4^*$  structure, the special Li ions instead occupy sites interior to the unit cell having multiplicity and Wyckoff label  $4c$ . In order to avoid confusion of this site with the other fully occupied  $4c$  Li site of these structures, we use the symbol  $c'$  to refer to this site. While the simulated fractional coordinates of the special Li ions for this  $4c'$  site do not agree with the two  $8d$  fractionally occupied coordinates found by Kaib, Haddadpour, et al.,<sup>3</sup> the optimized lattice constants are in excellent agreement, as shown in Table I. It is interesting to note that the lattice constants for these ideal structures are characterized by a contraction of the  $a$  lattice parameter by approximately 0.5 Å for the meta-stable structure relative to the ground state structure, while the changes to the other lattice parameters are in the neighborhood of 0.1 Å. This lattice contraction is energetically significant; the energy difference between  $\text{Li}_4\text{SnS}_4^*$  calculated with the lattice constants of  $\text{Li}_4\text{SnS}_4^0$  relative to  $\text{Li}_4\text{SnS}_4$  calculated with its optimized lattice constants is 0.03 eV/formula unit. We should also point out that the original X-ray analysis of Kaib, Haddadpour, et al.,<sup>3</sup> for the  $\text{Li}_4\text{SnS}_4^*$  structure was performed at low temperatures (100–193 K) while the X-ray analysis of MacNeil et al.<sup>4</sup> was performed at room temperature. It is our experience that lattice constants typically change with temperature by less than 0.1 Å, so that the lattice constant differences between the  $\text{Li}_4\text{SnS}_4^0$  and  $\text{Li}_4\text{SnS}_4^*$  structures should not be attributed to temperature alone. In addition, Sahu et al.<sup>6</sup> report room temperature X-ray analysis for  $\text{Li}_4\text{SnS}_4^*$  consistent with an expansion of the lattice by approximately 0.02 Å.

Because of its low atomic number, the X-ray signal for Li positions is notoriously small so that it is reasonable to ask whether the simulated  $\text{Li}_4\text{SnS}_4^*$  structure might be compatible with the structural data reported by Kaib, Haddadpour, et al.,<sup>3</sup> even if the site analysis differs. Using the Mercury software package,<sup>26</sup> with the structural data from experiment and simulations we compare the computed X-ray patterns for the structures of  $\text{Li}_4\text{SnS}_4^0$  and  $\text{Li}_4\text{SnS}_4^*$  in Fig. 2. We see that the patterns for  $\text{Li}_4\text{SnS}_4^0$  and  $\text{Li}_4\text{SnS}_4^*$  are distinguishable and that there

**Table II.** Comparison of fractional coordinates of unique atomic positions for  $\text{Li}_4\text{SnS}_4$  and related compounds in their ground state and meta-stable structures, using orientation and origin choice given in Ref. 4. The second column lists the site multiplicity and Wyckoff label. We use the notation  $c'$  to denote the special Li site which characterizes the meta-stable structures. Measured parameters are listed in square brackets when available.

Atom	Site	$\text{Li}_4\text{GeS}_4^0(x, y, z)$	$\text{Li}_4\text{GeS}_4^*(x, y, z)$
Li	4a	(0.000, 0.000, 0.000) [(0.000, 0.000, 0.000)] <sup>a</sup>	—
Li	4c'	—	(0.260, 0.250, -0.001)
Li	4c	(0.412, 0.250, 0.127) [(0.412, 0.250, 0.129)] <sup>a</sup>	(0.429, 0.250, 0.216)
Li	8d	(0.177, 0.000, 0.186) [(0.178, 0.000, 0.192)] <sup>a</sup>	(0.147, -0.023, 0.139)
Ge	4c	(0.089, 0.250, 0.645) [(0.089, 0.250, 0.649)] <sup>a</sup>	(0.097, 0.250, 0.620)
S	4c	(0.084, 0.250, 0.277) [(0.086, 0.250, 0.291)] <sup>a</sup>	(0.105, 0.250, 0.261)
S	8d	(0.158, 0.010, 0.780) [(0.157, 0.015, 0.779)] <sup>a</sup>	(0.177, 0.019, 0.761)
S	4c	(0.437, 0.250, 0.728) [(0.439, 0.250, 0.731)] <sup>a</sup>	(0.434, 0.250, 0.810)
Atom	Site	$\text{Li}_4\text{SnS}_4^0(x, y, z)$	$\text{Li}_4\text{SnS}_4^*(x, y, z)$
Li	4a	(0.000, 0.000, 0.000) [(0.000, 0.000, 0.000)] <sup>a</sup>	—
Li	4c'	—	(0.287, 0.250, 0.003) [- ] <sup>b</sup>
Li	4c	(0.410, 0.250, 0.124) [(0.409, 0.250, 0.126)] <sup>a</sup>	(0.429, 0.250, 0.359) [(0.430, 250, 0.338)] <sup>b</sup>
Li	8d	(0.176, 0.003, 0.178) [(0.178, 0.004, 0.179)] <sup>a</sup>	(0.158, -0.004, 0.149) [(0.160, 0.005, 0.154)] <sup>b</sup>
Sn	4c	(0.093, 0.250, 0.640) [(0.092, 0.250, 0.642)] <sup>a</sup>	(0.090, 0.250, 0.633) [(0.087, 0.250, 0.635)] <sup>b</sup>
S	4c	(0.080, 0.250, 0.255) [(0.083, 0.250, 0.267)] <sup>a</sup>	(0.092, 0.250, 0.256) [(0.091, 0.250, 0.263)] <sup>b</sup>
S	8d	(0.152, -0.005, 0.787) [(0.161, 0.001, 0.784)] <sup>a</sup>	(0.158, -0.004, 0.149) [(0.167, 0.007, 0.767)] <sup>b</sup>
S	4c	(0.430, 0.250, 0.732) [(0.432, 0.250, 0.766)] <sup>a</sup>	(0.423, 0.250, 0.748) [(0.424, 0.250, 0.736)] <sup>b</sup>
Atom	Site	$\text{Li}_4\text{SnSe}_4^0(x, y, z)$	$\text{Li}_4\text{SnSe}_4^*(x, y, z)$
Li	4a	(0.000, 0.000, 0.000) [(0.000, 0.000, 0.000)] <sup>c</sup>	—
Li	4c'	—	(0.282, 0.250, 0.002)
Li	4c	(0.413, 0.250, 0.118) [(0.412, 0.250, 0.106)] <sup>c</sup>	(0.428, 0.250, 0.358)
Li	8d	(0.175, 0.003, 0.178) [(0.178, 0.005, 0.180)] <sup>c</sup>	(0.157, -0.006, 0.147)
Sn	4c	(0.094, 0.250, 0.639) [(0.092, 0.250, 0.643)] <sup>c</sup>	(0.090, 0.250, 0.630)
Se	4c	(0.080, 0.250, 0.252) [(0.082, 0.250, 0.264)] <sup>c</sup>	(0.093, 0.250, 0.250)
Se	8d	(0.162, -0.008, 0.785) [(0.161, -0.002, 0.784)] <sup>c</sup>	(0.177, 0.005, 0.770)
Se	4c	(0.430, 0.250, 0.725) [(0.432, 0.250, 0.728)] <sup>c</sup>	(0.422, 0.250, 0.750)

<sup>a</sup>Ref. 4.

<sup>b</sup>Ref. 3, omitting fractionally occupied Li position.

<sup>c</sup>Ref. 5.

seems to be good agreement between our simulated structures and the corresponding X-ray results. While it would be better to compare the simulated diffraction patterns directly with the experimental data, the good agreement between the simulations and the fitted results from experiment shown in Fig. 2 is encouraging. It is interesting to note that two other groups<sup>6,7</sup> have recently reported preparations of  $\text{Li}_4\text{SnS}_4$  using relatively low temperature processing similar to that of Kaib, Haddadpour, et al.<sup>3</sup> Both of these studies report X-ray diffrac-

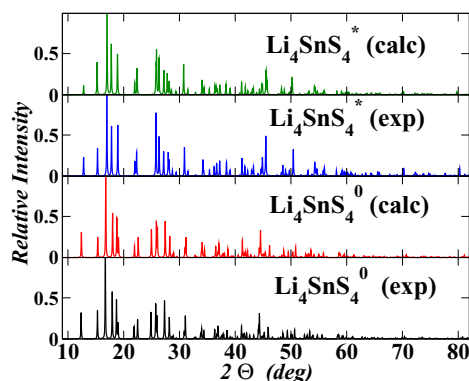


**Figure 2.** X-ray diffraction patterns generated by the Mercury software package<sup>26</sup> assuming an X-ray wavelength of  $\lambda = 1.54056 \text{ \AA}$ , comparing simulation (calc) and experimental (exp) results for the  $\text{Li}_4\text{SnS}_4^0$  and  $\text{Li}_4\text{SnS}_4^*$  structures. The structural parameters from experiment were taken from Ref. 4 for  $\text{Li}_4\text{SnS}_4^0$  and from Ref. 3 for  $\text{Li}_4\text{SnS}_4^*$ .

tion patterns, presumably measured at room temperature, which show strong similarity to the patterns for  $\text{Li}_4\text{SnS}_4^*$  shown in Fig. 2. Presumably, the ground state  $\text{Li}_4\text{SnS}_4^0$  structure is accessible using the higher temperature processes described by MacNeil et al.<sup>4</sup>

It is interesting to ask the question whether the structurally and chemically similar material  $\text{Li}_4\text{GeS}_4$  behaves in a similar way. The simulation results for the  $\text{Li}_4\text{GeS}_4^0$  and  $\text{Li}_4\text{GeS}_4^*$  structures are listed in Table I and in Table II together with available experimental values. The fractional coordinates are very similar to those of  $\text{Li}_4\text{SnS}_4$ . However, in this case, we would predict that the meta-stable  $\text{Li}_4\text{GeS}_4^*$  structure is less likely to form since its energy is predicted to be 0.25 eV/formula unit higher in energy than the ground state energy. The investigation was also extended to  $\text{Li}_4\text{SnSe}_4$  which was recently synthesized by Kaib, Bron, et al.<sup>5</sup> using relatively high temperature techniques. These authors find  $\text{Li}_4\text{SnSe}_4$  to take the “ground state”  $\text{Li}_4\text{SnSe}_4^0$  structure. Our simulations find that the meta-stable  $\text{Li}_4\text{SnSe}_4^*$  to have an energy of 0.07 eV/formula unit higher in energy than the ground state structure, suggesting that it is less likely than  $\text{Li}_4\text{SnS}_4^*$  to form at room temperature. The results are listed in Table I and in Table II.

### Electronic Structure Results

In order to gain a qualitative understanding of the electronic structure of the various forms of these materials, it is helpful to analyze the partial densities of states which are shown in Fig. 3. The partial density of states of  $\text{Li}_4\text{GeS}_4^0$  in its ground state structure was previously presented in Ref. 27. While, density functional theory is known to systematically underestimate the band gaps, the relative band gaps are usually well represented. For these materials,  $\text{Li}_4\text{GeS}_4$  has a computed bandgap of 2.1 eV, while the computed band gaps for  $\text{Li}_4\text{SnS}_4$  and  $\text{Li}_4\text{SnSe}_4$  are 2.2 eV and 1.6 eV respectively. For both of these

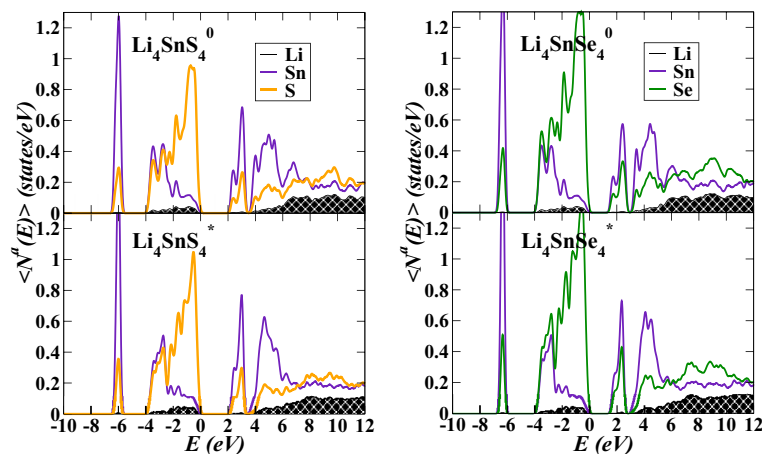


**Figure 3.** Partial densities of states for  $\text{Li}_4\text{SnS}_4^0$  and  $\text{Li}_4\text{SnS}_4^*$  (a) and  $\text{Li}_4\text{SnSe}_4^0$  and  $\text{Li}_4\text{SnSe}_4^*$  (b), separately indicating contributions from Li, Sn, S, and Se sites.

materials the upper part of the valence band is dominated by chalcogenide states while the conduction band is dominated by Sn 5s states forming a narrow band below the Sn 5p states. The results for  $\text{Li}_4\text{SnS}_4$  presented in Fig. 3 are consistent with the results previously reported by MacNeil et al.<sup>4</sup> The partial densities of states for the ground state and meta-stable structures have nearly indistinguishable partial density of states curves. The materials are clearly insulating with band gaps expected to be larger than 2 eV found in the present study due to the systematic gap underestimation known for LDA calculations.

Another result from the electronic structure calculations is the total energies which approximate the internal energies at zero temperature. These can be used to study the stability of the materials relative to various possible reactions such as those listed in Table III. If the effects of zero point motion and finite temperature are small, the results can be related to experimental enthalpies. The values listed in this table correspond to the ground state structures of  $\text{Li}_4\text{SnS}_4^0$ . Results for the meta-stable form of  $\text{Li}_4\text{SnS}_4^*$  can be determined by adding 0.02 eV or 0.07 eV for Ch=S or Ch=Se, respectively. Reaction 1 listed in Table III corresponds to the enthalpy of formation referenced to the standard states of the elements<sup>28</sup> including Li in the bcc structure, Sn in the diamond structure, S in the orthorhombic structure,<sup>29</sup> and Se in the trigonal structure.<sup>30</sup> Reaction 2 listed in Table III corresponds to decomposition into two binary materials.  $\text{Li}_2\text{S}$  and  $\text{Li}_2\text{Se}$  both form in the fluorite structure, while  $\text{SnS}_2$  and  $\text{SnSe}_2$  both form in the hexagonal  $\text{CdI}_2$  structure. Our simulations indicate that the two reactions have opposite sign, meaning that  $\text{Li}_4\text{SnS}_4$  is more stable than its binary products, while  $\text{Li}_4\text{SnSe}_4$  is less stable. Reaction 3 listed in Table III involves two new materials with the stoichiometry  $\text{Li}_2\text{SnCh}_3$ . Recently, Brant et al.<sup>31</sup> synthesized and characterized  $\text{Li}_2\text{SnS}_3$ , finding it to have a densely packed layered structure. The electronic structure results indicate that  $\text{Li}_2\text{SnS}_3$  together with excess  $\text{Li}_2\text{S}$  is more stable than  $\text{Li}_4\text{SnS}_4$ .  $\text{Li}_2\text{SnSe}_3$  was recently synthesized by Kaib, Bron, et al.<sup>5</sup>, characterized by one dimensional chains of  $\text{SnS}_4$  tetrahedra. The electronic structure results indicate that this material together with excess  $\text{Li}_2\text{Se}$  has about the same stability as  $\text{Li}_4\text{SnSe}_4$ .

**Table III.** Estimates of various reaction energies (in eV) for  $\text{Li}_4\text{SnCh}_4$  for the chalcogens Ch=S and Ch=Se based on total energy calculations. In each case the ground state structures of  $\text{Li}_4\text{SnCh}_4^0$  was assumed; the structures of the products are mentioned in the text of the manuscript.

Reaction	Ch=S	Ch=Se
1 $\text{Li}_4\text{SnCh}_4 \rightarrow 4\text{Li} + \text{Sn} + 4\text{Ch}$	-9.99	-8.94
2 $\text{Li}_4\text{SnCh}_4 \rightarrow 2\text{Li}_2\text{Ch} + \text{SnCh}_2$	-0.09	0.04
3 $\text{Li}_4\text{SnCh}_4 \rightarrow \text{Li}_2\text{Ch} + \text{Li}_2\text{SnCh}_3$	0.17	-0.01

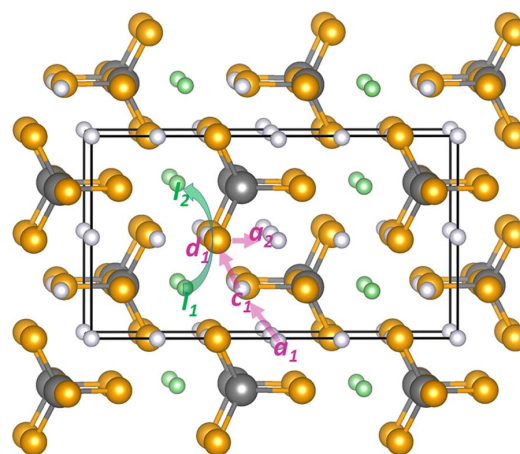


**Figure 4.** Ball and stick model of ground state structure of  $\text{Li}_4\text{SnS}_4^0$  and  $\text{Li}_4\text{SnSe}_4^0$  using the same ball convention and viewpoint as in Fig. 1(a). Distinct vacancy sites are indicated with their Wyckoff labels  $a_i$ ,  $c_i$ , and  $d_i$ . Interstitial sites are colored green and are labeled  $I_i$ . Possible vacancy and interstitialcy trajectories are indicated with transparent purple and green arrows respectively.

#### Defect Structures and Ion Migration Paths in $\text{Li}_4\text{SnS}_4^0$ , $\text{Li}_4\text{SnS}_4^*$ , $\text{Li}_4\text{SnSe}_4^0$ , and $\text{Li}_4\text{SnSe}_4^*$ .

Point defects were modeled at fixed volume in  $1 \times 2 \times 2$  supercells. For the ground state structure of  $\text{Li}_4\text{SnS}_4^0$  and  $\text{Li}_4\text{SnSe}_4^0$ , there are three distinct Li ion vacancy sites which can be uniquely labeled by the Wyckoff letters  $a_i$ ,  $c_i$ , and  $d_i$  as visualized in Fig. 4. The vacancy energies are listed in Table IV relative to the most stable vacancy at an  $a$  site.

Vacancy migration in  $\text{Li}_4\text{SnSe}_4^0$  was previously studied by Kaib, Bron, et al.<sup>5</sup> who showed that a sequence of hops of the vacancy between the sites  $a_1 \rightarrow c_1 \rightarrow d_1 \rightarrow a_2 \dots$  results in net ion motion

**Table IV.** Relative energies (in eV) of vacancies in the ground state structures of  $\text{Li}_4\text{SnS}_4^0$  and  $\text{Li}_4\text{SnSe}_4^0$  calculated in  $1 \times 2 \times 2$  supercells. The vacancy sites are indicated by their Wyckoff site labels with the zero energy chosen at the  $a$  site.

Vacancy label	$\text{Li}_4\text{SnS}_4^0$	$\text{Li}_4\text{SnSe}_4^0$
$a$	0.00	0.00
$c$	0.30	0.20
$d$	0.26	0.16

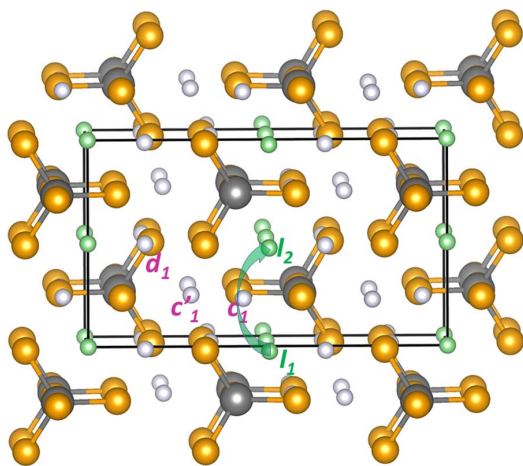


**Figure 5.** Ball and stick model of ground state structure of  $\text{Li}_4\text{SnS}_4^*$  and  $\text{Li}_4\text{SnSe}_4^*$  using the same ball convention and viewpoint as in Fig. 1(b). Distinct vacancy sites are indicated with their Wyckoff labels  $c'_1$ ,  $c_1$ , and  $d_1$ . Interstitial sites are colored green and are labeled  $I_1$ . Possible interstitial trajectories are indicated with transparent green arrows.

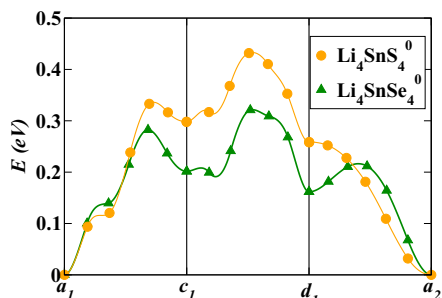


**Figure 6.** NEB calculated energy path diagram for Li ion vacancy migration in  $\text{Li}_4\text{SnS}_4^0$  and  $\text{Li}_4\text{SnSe}_4^0$ . The vacancy site labels correspond to the diagram in Fig. 4.

in the  $b$  and  $c$  directions in the crystal as illustrated in Fig. 4. The corresponding energies along this path as calculated using the NEB method are shown in Fig. 6 and tabulated in Table V. From Table V we see that the vacancy hopping distances  $d$  are slightly smaller and the path energies are somewhat larger for  $\text{Li}_4\text{SnS}_4^0$  compared with  $\text{Li}_4\text{SnSe}_4^0$ . The bottleneck of this process occurs during the  $c_1 \rightarrow d_1$  step, resulting in the estimated migration energies of  $E_m = 0.46$  eV and  $E_m = 0.32$  eV for  $\text{Li}_4\text{SnS}_4^0$  and  $\text{Li}_4\text{SnSe}_4^0$ , respectively. Another vacancy migration path for this involves vacancy hopping between the sites  $a \rightarrow c \rightarrow a \rightarrow c \dots$  resulting in net migration along the  $b$  axis. The estimated migration energy for this path is  $E_m = 0.33$  eV and  $E_m = 0.28$  eV for  $\text{Li}_4\text{SnS}_4^0$  and  $\text{Li}_4\text{SnSe}_4^0$ , respectively. We also investigated vacancy migration mechanisms along the  $a$  axis. The bottleneck for  $a$  axis vacancy migration involves hops between

**Table V.** NEB calculated migration energies ( $E_m$ ) and ideal distances ( $d$ ) for vacancy migration in  $\text{Li}_4\text{SnS}_4^0$  and  $\text{Li}_4\text{SnSe}_4^0$ . Migration energies are referenced to a vacancy at the  $a$  site.

	$\text{Li}_4\text{SnS}_4^0$		$\text{Li}_4\text{SnSe}_4^0$	
	$E_m$ (eV)	$d$ (Å)	$E_m$ (eV)	$d$ (Å)
$a \rightarrow c$	0.33	3.3	0.28	3.5
$c \rightarrow d$	0.46	3.6	0.32	3.8
$d \rightarrow a$	0.26	2.8	0.21	2.9

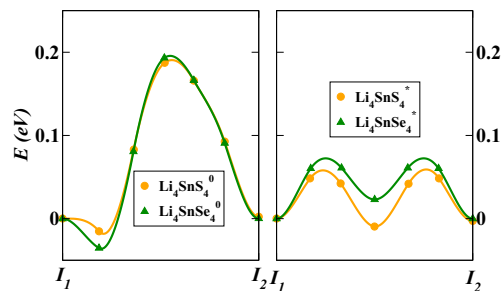


**Figure 7.** NEB calculated energy path diagram for Li ion migration with an interstitial mechanism as shown in Fig. 4 for  $\text{Li}_4\text{SnS}_4^*$  and  $\text{Li}_4\text{SnSe}_4^*$  and as shown in Fig. 5 for  $\text{Li}_4\text{SnS}_4^*$  and  $\text{Li}_4\text{SnSe}_4^*$ .

nearest neighbor  $d$  sites which raise the estimated migration energies substantially above the migration barriers along the  $b$  and  $c$  axes. In general there is good agreement between our calculated results for  $\text{Li}_4\text{SnSe}_4^0$  and the corresponding results of Kaib, Bron, et al.,<sup>5</sup> within a small discrepancy of 0.03 eV or less.

For the meta-stable structure of  $\text{Li}_4\text{SnS}_4^*$ , only the  $c'$  site vacancy is stable. Calculations initialized with vacancies on  $c$  or  $d$  sites relax to a vacancy on nearby  $c'$  site. For the meta-stable structure of  $\text{Li}_4\text{SnSe}_4^*$ , the story is slightly different. For that system, the  $c'$  site vacancy is again the most stable. Calculations initialized with vacancies on a  $c$  site relax to a vacancy on a nearby  $c'$  site. Calculations initialized with vacancies on a  $d$  site are meta-stable with considerable distortion, having an energy of 0.24 eV above the energy of the  $c'$  site vacancy. We did not investigate vacancy migration mechanisms in the meta-stable structures.

Another important mechanism for ion migration involves interstitial sites. For the ground state structures of  $\text{Li}_4\text{SnS}_4^0$  and  $\text{Li}_4\text{SnSe}_4^0$  there is one main interstitial site located in the void regions between  $\text{SnS}_4$  or  $\text{SnSe}_4$  tetrahedra as shown in Fig. 4 which happens to be the  $c'$  Li site of the meta-stable  $\text{Li}_4\text{SnS}_4^*$  and  $\text{Li}_4\text{SnSe}_4^*$  structures. Correspondingly, for the meta-stable structures of  $\text{Li}_4\text{SnS}_4^*$  and  $\text{Li}_4\text{SnSe}_4^*$  the one main interstitial site is located in the void regions which happens to be the  $a$  site of the ground state structures as shown in Fig. 5. For both structures, migration between these interstitial sites occurs most efficiently using an "interstitial" mechanism. An interstitial mechanism is one in which an interstitial ion moves into a host lattice site as that host lattice ion moves to an adjacent interstitial site. The resulting migration processes for  $\text{Li}_4\text{SnS}_4^0$  and  $\text{Li}_4\text{SnSe}_4^0$ , with an intermediate  $d$  host lattice site, and for  $\text{Li}_4\text{SnS}_4^*$  and  $\text{Li}_4\text{SnSe}_4^*$ , with an intermediate  $c$  host lattice site, are illustrated with the green arrows in Figs. 4 and 5 and the corresponding NEB energy paths are shown in Fig. 7.

From the energy path diagram shown in Fig. 7, it is evident that the interstitial mechanism results in the lowest migration barrier for all of the structures investigated and is predicted to dominate migration processes. For electrolytes in the so-called "intrinsic" regime, the NEB estimate of the activation energy  $E_A^{\text{NEB}}$  for conductivity is related to the migration energy  $E_m$  and the formation energy  $E_f$  to form a vacancy and interstitial pair according to

$$E_A^{\text{NEB}} = E_m + \frac{1}{2} E_f. \quad [1]$$

A summary of results including optimal calculated values of  $E_A^{\text{NEB}}$  from Eq. 1 and available experimental values are listed in Table VI. For the ground state structures of  $\text{Li}_4\text{SnS}_4^0$  and  $\text{Li}_4\text{SnSe}_4^0$  the calculated optimal values of  $E_f$  were obtained for vacancies on an  $a$  site moving to the nearest interstitial site  $Ic'$  which corresponds to the site we've called  $c'$  in the meta-stable structures. The calculated values of  $E_f$  are 0.27 eV and 0.36 eV for  $\text{Li}_4\text{SnS}_4^0$  and  $\text{Li}_4\text{SnSe}_4^0$ , respectively. The corresponding estimates of the activation energies  $E_A^{\text{NEB}}$  are 0.3 eV and 0.4 eV for  $\text{Li}_4\text{SnS}_4^0$  and  $\text{Li}_4\text{SnSe}_4^0$ , respectively. To the best of our

**Table VI.** Activation energies for ion migration for ground state and meta-stable state structures of  $\text{Li}_4\text{SnS}_4$  and  $\text{Li}_4\text{SnSe}_4$ . Calculated migration energies  $E_m$  were determined from NEB calculations of the interstitialcy mechanism shown in Fig. 7. Formation energies  $E_f$  for interstitial-vacancy pairs, calculated activation energies  $E_A^{\text{NEB}}$  based on Eq. 1 and literature values of the activation energy  $E_A^{\text{exp}}$  are also listed. For comparison, the calculated activation energies  $E_A^{\text{trace}}$  and their error estimates associated with the Arrhenius temperature dependence of the simulated “tracer” diffusion coefficients  $D^{\text{trace}}(T)$  are also listed here and will be discussed in the Molecular dynamics section.

	$E_m$ (eV)	$E_f$ (eV)	$E_A^{\text{NEB}}$ (eV)	$E_A^{\text{exp}}$ (eV)	$E_A^{\text{trace}}$ (eV)
$\text{Li}_4\text{SnS}_4^0$	0.19	0.27	0.3		$0.24 \pm 0.06$
$\text{Li}_4\text{SnS}_4^*$	0.06	0.15	0.1	0.41 <sup>a</sup>	$0.25 \pm 0.04$
$\text{Li}_4\text{SnSe}_4^0$	0.20	0.36	0.4	0.45 <sup>b</sup>	$0.23 \pm 0.1$
$\text{Li}_4\text{SnSe}_4^*$	0.07	0.15	0.1		$0.08 \pm 0.01$

<sup>a</sup>Ref. 3.

<sup>b</sup>Ref. 5.

knowledge, there are no published conductivity measurements for the  $\text{Li}_4\text{SnS}_4^0$  material, but  $\text{Li}_4\text{SnSe}_4^0$  has been well studied by Kaib, Bron, et al.<sup>5</sup> Our NEB calculated result for  $\text{Li}_4\text{SnSe}_4^0$  is in disagreement with the value of 0.6 eV calculated by Kaib, Bron, et al.,<sup>5</sup> but is in better agreement with the value of  $E_A = 0.45$  eV deduced from fitting the temperature dependence of the experimental conductivity measurements in the same study.

For the meta-stable structures of  $\text{Li}_4\text{SnS}_4^*$  and  $\text{Li}_4\text{SnSe}_4^*$ , the calculated optimal values of  $E_f$  were obtained for vacancies on an  $c'$  site moving to the nearest interstitial site  $Ia$  which corresponds to the  $a$  site in the ground state structures. The calculated values of  $E_f$  are 0.15 eV for both  $\text{Li}_4\text{SnS}_4^*$  and  $\text{Li}_4\text{SnSe}_4^*$ , resulting in estimates of the activation energies  $E_A^{\text{NEB}}$  of 0.1 eV for both materials. This result is not in agreement with the value of  $E_A = 0.41$  eV obtained from fitting the temperature dependence of the experimental conductivity measured by Kaib, Haddadpour, et al.<sup>3</sup>

### Molecular Dynamics Simulations

In studying the ion migration mechanisms for the  $\text{Li}_4\text{SnCh}_4^0$  and  $\text{Li}_4\text{SnCh}_4^*$  structures, we find the Li ion motions to be highly correlated presumably due to a complicated energy landscape. For example, in creating single defects in an otherwise perfect lattice, we found some of the configurations to be unstable. For example, in the  $\text{Li}_4\text{SnS}_4^0$  structure, a  $d$  site vacancy is unstable relative to a vacancy on the nearest  $a$  site Li. In the  $\text{Li}_4\text{SnS}_4^*$  structure a  $d$  site vacancy is unstable relative to a vacancy on the nearest  $c'$  site Li. The NEB analysis discussed in the previous section was unable to completely explain the conductivity results. In order to get additional information about the migration processes, we performed molecular dynamics simulations using the QUANTUM ESPRESSO<sup>12</sup> code. While the NEB method gives insight about the probability of individual hops of the migrating Li ions, molecular dynamics simulations provide information about the motions of the ensemble of ions within the simulation cell. As shown by Mo, Ong, and others,<sup>32-35</sup> one way to improve the configuration sampling of the simulations is to perform the simulations at elevated temperatures. The expectation (although unproven) is that the behaviors of the materials at room temperature can be estimated from the extrapolated simulation results.

Figure 8 shows a visualization of the Li mobility with a ball and stick model of the crystals with superposed Li positions at 136 time steps at intervals of 0.05 ps. It is apparent from these diagrams that at the relatively low simulation temperatures of  $T = 635$  K and  $T = 656$  K there is substantial motion of all of the Li ions. In addition to the vacancy and interstitialcy mechanisms studied by the NEB analysis as discussed above, several other pathways for Li ion motion are evident.

In order to better analyze the molecular dynamics simulations, it is convenient to define a site occupancy factor as a function of time  $s_i(t)$  where  $i$  denotes the site type. For the ground state structure, the sites were labeled according to their host site type ( $a$ ,  $c$ , or  $d$ ) or the interstitial site type ( $Ic'$ ). For the meta-stable state structure, the sites were labeled according to their host site type ( $c'$ ,  $c$ , or  $d$ ) or the interstitial site type ( $Ia$ ). The site label  $i$  was determined from the

closest Li position of the perfect lattice relative to the instantaneous position of each Li. For convenience, the site occupancy factors were normalized to unity at full occupancy and followed the sum rule:

$$\sum_i s_i(t) \frac{n_i}{N} = 1, \quad [2]$$

where  $n_i$  denotes the multiplicity of the site and  $N$  denotes the total number of Li sites. For the materials in this study,  $n_d/N = 2n_j/N$ , where  $j$  indexes the  $a$ ,  $c$ , or  $c'$  sites and  $d$  denotes the  $d$  site type. As shown in Fig. 9, the instantaneous site occupancy factors  $s_i(t)$  are very noisy and it is convenient to define a time averaged site occupancy parameter

$$\langle s_i \rangle_t \equiv \frac{1}{t} \int_0^t s_i(t') dt'. \quad [3]$$

As shown in Fig. 9,  $\langle s_i \rangle_t$  tends to an asymptotic value at long times.

It is interesting to study the asymptotic time averaged site occupancy factors  $\langle s_i \rangle_{t \rightarrow \infty} \equiv \langle s_i \rangle$  as a function of simulation temperatures for the four materials as shown in Fig. 10. These values were determined from the final time step of each simulation which was between 3 and 8 ps. The values of  $\langle s_i \rangle$  for  $\text{Li}_4\text{SnS}_4^0$  and  $\text{Li}_4\text{SnSe}_4^0$  structures show relative small values ( $< 0.5$ ) for the interstitial  $Ic'$  site and relative large values ( $> 0.75$ ) for the host lattice sites ( $a$ ,  $c$ , and  $d$ ), indicating a relatively well-ordered structure. On the other hand for the  $\text{Li}_4\text{SnS}_4^*$  and  $\text{Li}_4\text{SnSe}_4^*$  structures, the interstitial sites ( $Ia$ ) are substantially occupied ( $> 0.5$ ) throughout the temperature range, indicating relatively disordered structures.

It is possible to use molecular dynamics results in a more quantitative analysis of ionic conductivity following the approach implemented by Mo, Ong, and others.<sup>32-35</sup> For a molecular dynamics simulation at temperature  $T$  with resultant ion trajectories  $\{\mathbf{r}_i(t)\}$  as a function of time  $t$ , one can calculate the mean squared displacement and use Einstein's expression to determine the diffusion constant  $D_{\text{trace}}(T)$ :<sup>36</sup>

$$\left\langle \frac{1}{6N} \sum_{i=1}^N |\mathbf{r}_i(t) - \mathbf{r}_i(t_0)|^2 \right\rangle = D_{\text{trace}}(T)[t - t_0] + C. \quad [4]$$

Here the summation over  $i$  denotes the  $N$  Li ion positions  $\{\mathbf{r}_i(t)\}$  in the simulation cell and  $C$  denotes a constant. In order to improve the sampling of the simulation, the incremental distance is averaged over the initial times  $t_0$  as implied by the angular brackets in the expression. As pointed out by Murch,<sup>37-39</sup> the temperature dependent diffusion constant  $D_{\text{trace}}(T)$  calculated from the mean squared displacement in this way approximates the diffusion of tracked particles such that can experimentally realized in radioactive tracer experiments. Since diffusion takes place near equilibrium, it is reasonable to also assume that the diffusion coefficient has an Arrhenius temperature dependence<sup>40</sup>

$$D_{\text{trace}}(T) = D_{\text{trace}}(0) e^{-E_A^{\text{trace}}/kT}, \quad [5]$$

where  $D_{\text{trace}}(0)$  denotes the diffusion coefficient at 0 K,  $E_A^{\text{trace}}$  denotes the activation energy for diffusion, and  $k$  denotes the Boltzmann constant.

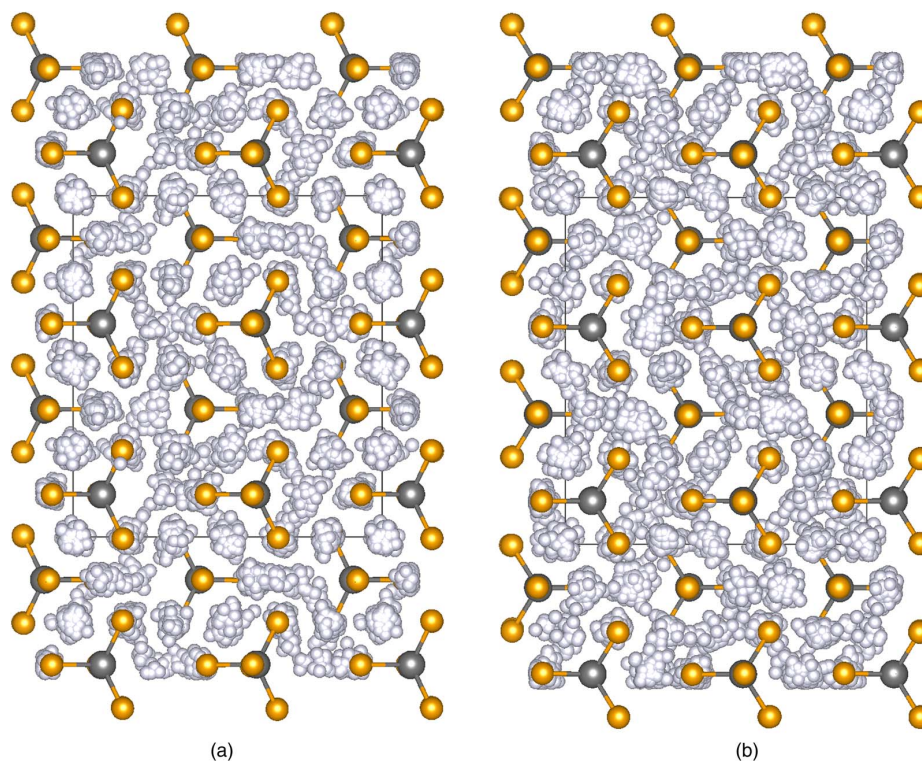


**Figure 8.** Ball and stick diagrams of molecular dynamics simulations for  $\text{Li}_4\text{SnS}_4^0$  at  $T = 635$  K (a) and  $\text{Li}_4\text{SnS}_4^*$  at  $T = 656$  K (b). Initial Sn and S positions are represented by gray and orange balls respectively. Li positions of the initial configuration and 136 subsequent positions at time intervals of 0.05 ps are indicated with gray balls. Simulations were performed using microcanonical ensembles (constant energy and volume) in  $1 \times 2 \times 2$  supercells. The viewpoint is a projection down the  $c$ -axis.

The temperature dependent direct-current ionic conductivity is related to  $D_{\text{trace}}(T)$  by the equation<sup>38</sup>

$$\sigma(T) = \frac{\rho q^2}{kT} \frac{D_{\text{trace}}(T)}{H}, \quad [6]$$

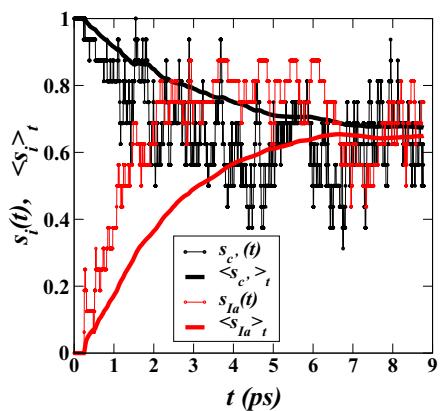


**Figure 9.** Instantaneous and time averaged site occupancy factors for molecular dynamics simulation of  $\text{Li}_4\text{SnS}_4^*$  at a temperature of  $T = 830$  K.

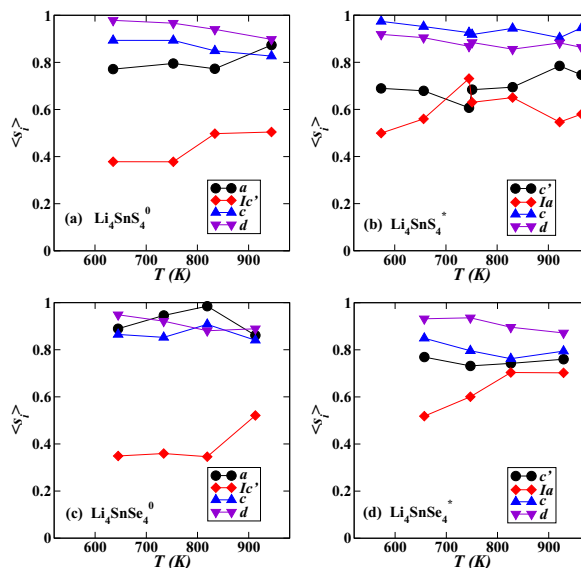


**Figure 10.** Asymptotic time averaged site occupancy factors ( $s_i$ ) for (a)  $\text{Li}_4\text{SnS}_4^0$ , (b)  $\text{Li}_4\text{SnS}_4^*$ , (c)  $\text{Li}_4\text{SnSe}_4^0$  and (d)  $\text{Li}_4\text{SnSe}_4^*$  evaluated at various simulation temperatures.

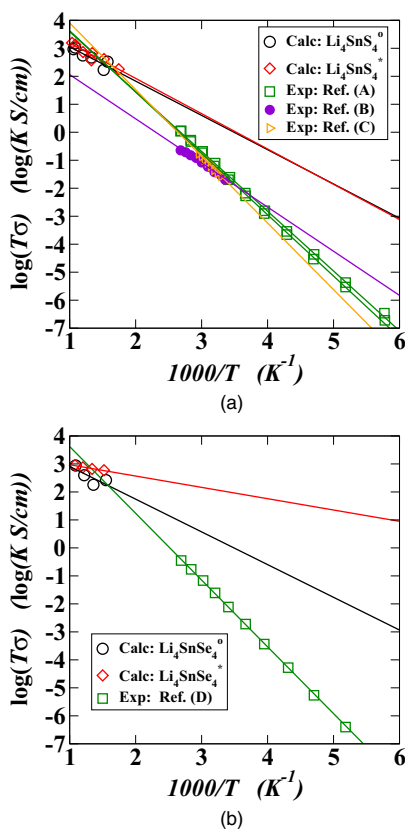


**Figure 11.** Plots of the ionic conductivity in terms of  $\log(T\sigma)$  of  $\text{Li}_4\text{SnS}_4$  (a) and  $\text{Li}_4\text{SnSe}_4$  (b). The calculated values were evaluated using Eq. 6 with  $H = 1$ . The experimental values for  $\text{Li}_4\text{SnS}_4^*$  were taken from Refs. 3 (A), 6 (B), and 7 (C), while experimental results for  $\text{Li}_4\text{SnSe}_4^0$  were taken from Ref. 5 (D). All of the experimental values were analyzed from the published graphs using digitizing software. The lines represent least squares fits to the calculated results or the digitized experimental values.

where  $\rho$  denotes the number of mobile ions (Li) per unit volume,  $q$  denotes the charge of each Li ion. The factor  $H$  is known as the Haven ratio<sup>41</sup> which takes into account so called correlation effects. For example, the conductivity due to an interstitialcy process which involves the concerted motion of interstitial and host ions as discussed above, is not well modeled by the mean squared displacements of independent ions. If the temperature dependence of the Haven ratio  $H$  were trivial, the activation energy for tracer diffusion  $E_A^{\text{trace}}$  would also approximate the activation energy of the conductivity according to Eq. (6). A simulation to estimate the Haven ratio<sup>42</sup> is beyond the scope of the present work. On the other hand, comparing a calculation of the conductivity using Eq. (6) assuming  $H = 1$ , with experiment, can provide information on the Haven ratios for these materials.

Figure 11 summarizes the simulation results in comparison with experimental conductivity measurements. The conductivity of  $\text{Li}_4\text{SnS}_4^*$  was measured by 3 independent groups,<sup>3,6,7</sup> showing very similar results. The small differences among the experimental conductivity results shown in Fig. 11a may be due to digitization errors. The digitized data from these experiments are consistent with the Arrhenius activation energy of  $E_A^{\text{exp}} = 0.4 \pm 0.1$  eV. The simulation results reported here should be regarded as preliminary, due to the relatively small number of configurations sampled. Previous work of this sort<sup>32-35</sup> was based on simulation times 10-100 times as long as our 3-8 ps simulations. For these reasons, the least squares fit lines

through the simulated results for  $\log(T\sigma)$  versus  $1000/T$  should be considered with large error bars.

Mindful of the limitations, it is nevertheless interesting to analyze the simulation results obtained in this study. Despite the differences in their site occupancies, the computed tracer diffusion behaviors of  $\text{Li}_4\text{SnS}_4^0$  and  $\text{Li}_4\text{SnS}_4^*$  shown in Fig. 11a were found to be similar. The magnitudes of the high temperature simulated conductivities is in the range of the extrapolated experimental conductivities. By fitting a straight line through the simulated conductivities, the deduced values of the tracer activation energies are  $E_A^{\text{trace}} = 0.24 \pm 0.06$  eV and  $0.25 \pm 0.04$  eV for  $\text{Li}_4\text{SnS}_4^0$  and  $\text{Li}_4\text{SnS}_4^*$  respectively as listed in Table VI. The reported errors of the activation energies are likely underestimates, since they include only errors due to the linear fit and not the additional sampling errors of the simulation. However, these errors suggest that the activation energies for Li ion diffusion in these materials may differ by as much as 0.1 eV. While the tracer diffusion result for  $\text{Li}_4\text{SnS}_4^0$  is consistent with the NEB result, the tracer diffusion result for  $\text{Li}_4\text{SnS}_4^*$  is not in agreement either with experiment or with the NEB estimate for the activation energies. For the selenide materials shown in Fig. 11b, the magnitudes of the high temperature simulated conductivities are again in the range of the extrapolated experimental conductivity. However, in contrast with sulfide materials, the deduced values of the tracer activation energies are distinct;  $E_A^{\text{trace}} = 0.23 \pm 0.1$  eV and  $0.08 \pm 0.01$  eV for  $\text{Li}_4\text{SnSe}_4^0$  and  $\text{Li}_4\text{SnSe}_4^*$  respectively as listed in Table VI. The activation energy for tracer diffusion in  $\text{Li}_4\text{SnSe}_4^0$  is smaller than both the values obtained from experimental conductivity measurements and from the NEB calculations. However, the computed  $E_A^{\text{trace}}$  value for  $\text{Li}_4\text{SnSe}_4^*$  happens to agree well with the NEB estimate of the activation energy  $E_A^{\text{NEB}}$  which was based on an idealized interstitialcy mechanism. In future work, the molecular dynamics simulations could be improved by reducing the sampling errors in terms of the finite size effects, increasing the simulation times, and considering multiple initial configurations. Additionally, it may be important to go beyond the constant volume simulations and to include the effects of lattice expansion. For example, in the  $\text{Li}_4\text{SnS}_4$  system, the lattice contraction accounts for an energy gain of 0.03 eV/formula unit. One can guess that the constant volume simulations might bias the systems to result in distinct configurations at high temperature. Perhaps more realistic representations of the volumetric variations with temperature could be used to investigate possible transitions between the structural forms. In addition to these possible numerical improvements, some of the discrepancies of the measured and simulated conductivities come from the Haven ratio which is expected to be non-trivial for these materials due to the importance of the interstitialcy mechanism.

## Conclusions

Our simulations identify ideal ground state structures for  $\text{Li}_4\text{GeS}_4^0$ ,  $\text{Li}_4\text{SnS}_4^0$ , and  $\text{Li}_4\text{SnSe}_4^0$  and ideal meta-stable structures  $\text{Li}_4\text{GeS}_4^*$ ,  $\text{Li}_4\text{SnS}_4^*$ , and  $\text{Li}_4\text{SnSe}_4^*$ . The meta-stable structures differ from the ground state configurations by the removal of the  $a$  site Li's to the so-called  $c'$  sites and the contraction of the  $a$  axis lattice parameter by approximately 0.5 Å. The ground state structures have been experimentally reported for  $\text{Li}_4\text{GeS}_4^0$ ,  $\text{Li}_4\text{SnS}_4^0$ , and  $\text{Li}_4\text{SnSe}_4^0$  in References 4, 4, and 5, respectively. Our ideal meta-stable structure is consistent with the structure of  $\text{Li}_4\text{SnS}_4^*$  reported by Reference 3 and corroborated by References 6 and 7.

Based on these ideal structures, Li ion migration processes were computationally examined for  $\text{Li}_4\text{SnS}_4^0$ ,  $\text{Li}_4\text{SnS}_4^*$ ,  $\text{Li}_4\text{SnSe}_4^0$ , and  $\text{Li}_4\text{SnSe}_4^*$ . Considering simple defects and NEB analysis, we find interstitialcy mechanisms in all of these materials to provide efficient motion of the Li ions primarily along the  $b$  and  $c$  lattice directions. The small "formation energy" involved with moving a Li ion from a host lattice site into an interstitial site resulting in an interstitial-vacancy pair,  $E_f = 0.15$  eV for both  $\text{Li}_4\text{SnS}_4^*$  and  $\text{Li}_4\text{SnSe}_4^*$  implies that these structures are likely to be disordered at relatively low temperatures as suggested by the original analysis of Kaib, Haddadpour, et al.<sup>3</sup> The



simulations indicate that the corresponding formation energy is larger for the ground state structures, where  $E_f = 0.27$  eV for  $\text{Li}_4\text{SnS}_4^0$  and  $E_f = 0.36$  eV for  $\text{Li}_4\text{SnSe}_4^0$ , suggesting that these structures are likely to remain ordered at relatively low temperatures. At the present time, experimental measurements of the activation energy for ion conductivity are available only for  $\text{Li}_4\text{SnSe}_4^0$  and  $\text{Li}_4\text{SnS}_4^0$ . As shown in Table VI, the NEB estimate of  $E_A^{\text{NEB}}$  for  $\text{Li}_4\text{SnSe}_4^0$  is in reasonable agreement with experiment assuming an interstitialcy mechanism. On the other hand, the NEB estimate of  $E_A^{\text{NEB}}$  for  $\text{Li}_4\text{SnS}_4^0$  is not in good agreement with experiment, presumably because significant contributions from more complicated configurations than the pure interstitialcy mechanism are important of ion migration in this case. Molecular dynamics simulations performed at temperatures of  $T = 600\text{K}$  and higher indicate that there is significant motion of all of the Li ions including appreciable occupancy of the interstitial sites for all of the structures. Plots of the site occupancy parameters from the molecular dynamics simulations shown in Fig. 10 are consistent with the notion that the ground state structures remain more ordered for a larger temperature range than do the meta-stable structures. Sequences of the molecular dynamics steps identify the interstitialcy mechanism as well as more complicated motions which contribute to the Li ion mobility. While these molecular dynamics studies, provide interesting insight into the properties of these materials, further work is needed to reconcile the calculated tracer diffusion simulations to quantitative estimates of the ion conductivity as shown in Fig. 11. In principle if the numerical accuracy and physical approximations could be improved, it would be reasonable to attribute the difference between the tracer diffusion simulations and the conductivity measurements to the Haven ratio. However, the error bars of the present work are too large to make this connection at the present time.

The simulations suggest that both  $\text{Li}_4\text{SnS}_4$  and  $\text{Li}_4\text{SnSe}_4$  have two ideal phases. The current literature suggests that the ground state structure is accessible by higher temperature processing while the meta-stable structure is formed at lower temperatures. For  $\text{Li}_4\text{SnS}_4^0$ , MacNeil et al.<sup>4</sup> report their highest synthesis temperature as 1023 K, while for  $\text{Li}_4\text{SnS}_4^*$ , Sahu et al.<sup>6</sup> report the highest synthesis temperature as 723 K. Understanding how to control the physical realization of these two phases, and possibly observing the phase transition might be of interest for future investigations.

### Acknowledgment

This work was supported by NSF grant DMR-1507942. Computations were performed on the Wake Forest University DEAC cluster, a centrally managed resource with support provided in part by the University. Helpful discussions with Jennifer A. Aitken from Duquesne University, Joseph H. MacNeil from Chatham University, Larry E. Rush, Jr. from Wake Forest University, and Kanchan Sarkar and Renata Wentzcovitch from the University of Minnesota are gratefully acknowledged.

### References

1. Y. Wang, W. D. Richards, S. P. Ong, L. J. Miara, J. C. Kim, Y. Mo, and G. Ceder, *Nature Materials*, **14**, 1026 (2015).
2. J. Li, C. Ma, M. Chi, C. Liang, and N. J. Dudney, *Advanced Energy Materials*, **5**, 1401408 (2015).
3. T. Kaib, S. Haddadpour, M. Kapitein, P. Bron, C. Schrder, H. Eckert, B. Roling, and S. Dehnen, *Chemistry of Materials*, **24**, 2211 (2012).
4. J. H. MacNeil, D. M. Massi, J.-H. Zhang, K. A. Rosmus, C. D. Brunetta, T. A. Gentile, and J. A. Aitken, *Journal of Alloys and Compounds* (2013).
5. T. Kaib, P. Bron, S. Haddadpour, L. Mayrhofer, L. Pastewka, T. T. Jrv, M. Moseler, B. Roling, and S. Dehnen, *Chemistry of Materials*, **25**, 2961 (2013).
6. G. Sahu, Z. Lin, J. Li, Z. Liu, N. Dudney, and C. Liang, *Energy Environ. Sci.*, **7**, 1053 (2014).
7. K. H. Park, D. Y. Oh, Y. E. Choi, Y. J. Nam, L. Han, J.-Y. Kim, H. Xin, F. Lin, S. M. Oh, and Y. S. Jung, *Advanced Materials*, **28**, 1874 (2016).
8. P. Hohenberg and W. Kohn, *Physical Review*, **136**, B864 (1964).
9. W. Kohn and L. J. Sham, *Physical Review*, **140**, A1133 (1965).
10. P. E. Blöchl, *Phys. Rev. B*, **50**, 17953 (1994).
11. N. A. W. Holzwarth, A. R. Tackett, and G. E. Matthews, *Computer Physics Communications*, **135**, 329 (2001), available from the website <http://pwpaw.wfu.edu>.
12. P. Giannozzi, S. Baroni, N. Bonini, M. Calandra, R. Car, C. Cavazzoni, D. Ceresoli, G. L. Chiarotti, M. Cococcioni, I. Dabo, A. D. Corso, S. de Gironcoli, S. Fabris, G. Fratesi, R. Gebauer, U. Gerstmann, C. Gougousis, A. Kokalj, M. Lazzeri, L. Martin-Samos, N. Marzari, F. Mauri, R. Mazzerello, S. Paolini, A. Pasquarello, L. Paulatto, C. Sbraccia, S. Scandolo, G. Sclauzero, A. P. Seitsonen, A. Smogunov, P. Umari, and R. M. Wentzcovitch, *J. Phys.: Condens. Matter*, **21**, 394402 (19pp) (2009), available from the website <http://www.quantum-espresso.org>.
13. X. Gonze, B. Amadon, P. M. Anglade, J. M. Beuken, F. Bottin, P. Boulanger, F. Bruneval, D. Caliste, R. Caracas, M. Cote, T. Deutsch, L. Genovese, P. Ghosez, M. Giantomassi, S. Goedecker, D. R. Hamann, P. Hermet, F. Jollet, G. Jomard, S. Leroux, M. Mancini, S. Mazevet, M. J. T. Oliveira, G. Onida, Y. Pouillon, T. Rangel, G. M. Rignanese, D. Sangalli, R. Shaltaf, M. Torrent, M. J. Verstraete, G. Zerah, and J. W. Zwanziger, *Computer Physics Communications*, **180**, 2582 (2009), code is available at the website <http://www.abinit.org>.
14. A. Kokalj, *Journal of Molecular Graphics and Modelling*, **17**, 176 (1999), code available at the website <http://www.xcrysden.org>.
15. A. Kokalj, *Computational Materials Science*, **28**, 155 (2003).
16. K. Momma and F. Izumi, *Applied Crystallography*, **44**, 1272 (2011), code available from the website <http://fp-minerals.org/vesta/en/>.
17. J. P. Perdew and Y. Wang, *Phys. Rev. B*, **45**, 13244 (1992).
18. Y. A. Du and N. A. W. Holzwarth, *Phys. Rev. B*, **76**, 174302 (14 pp) (2007).
19. Y. A. Du and N. A. W. Holzwarth, *Phys. Rev. B*, **81**, 184106 (15pp) (2010).
20. Z. D. Hood, C. Kates, M. Kirkham, S. Adhikari, C. Liang, and N. A. W. Holzwarth, *Solid State Ionics*, **284**, 61 (2015).
21. N. D. Lepley, N. A. W. Holzwarth, and Y. A. Du, *Phys. Rev. B*, **88**, 104103 (11 pp) (2013).
22. H. Jónsson, G. Mills, and K. W. Jacobsen, in *Classical and Quantum Dynamics in Condensed Phase Simulations*, edited by B. J. Berne, G. Cicciotti, and D. F. Coker (World Scientific, Singapore, 1998) pp. 385.
23. G. Henkelman, B. P. Uberuaga, and H. Jónsson, *J. Chem. Phys.*, **113**, 9901 (2000).
24. G. Henkelman and H. Jónsson, *J. Chem. Phys.*, **113**, 9978 (2000).
25. T. Hahn, ed., *International Tables for Crystallography, Volume A: Space-group symmetry, Fifth revised edition* (Kluwer, 2002) ISBN 0-7923-6590-9. The symmetry labels used in this work are all based on this reference.
26. "Mercury 3.5.1", (2014), developed and distributed by the Cambridge Crystallographic Data Centre <http://www.ccdc.cam.ac.uk/mercury/>.
27. A. Al-Qawasmeh and N. A. W. Holzwarth, *Journal of The Electrochemical Society*, **163**, A2079 (2016).
28. D. R. Lide, ed., *CRC Handbook of Chemistry and Physics, 90th Edition* (CRC Press, Taylor & Francis Group, 2009) ISBN 13: 978-1-4200-9084-0.
29. S. J. Rettig and J. Trotter, *Acta Cryst. C*, **43**, 2260 (1987).
30. R. Keller, W. B. Holzapfel, and H. Schulz, *Physical Review B*, **16**, 4404 (1977).
31. J. A. Brant, D. M. Massi, N. A. W. Holzwarth, J. H. MacNeil, A. P. Douvalis, T. Bakas, S. W. Martin, M. D. Gross, and J. A. Aitken, *Chemistry of Materials*, **27**, 189 (2015).
32. Y. Mo, S. P. Ong, and G. Ceder, *Chemistry of Materials*, **24**, 15 (2012).
33. S. P. Ong, Y. Mo, W. D. Richards, L. Miara, H. S. Lee, and G. Ceder, *Energy & Environmental Science*, **6**, 148 (2013).
34. Z. Zhu, I.-H. Chu, Z. Deng, and S. P. Ong, *Chemistry of Materials*, **27**, 8318 (2015).
35. Y. Deng, C. Eames, J.-N. Chotard, F. Lalre, V. Seznec, S. Emge, O. Pecher, C. P. Grey, C. Masquelier, and M. S. Islam, *Journal of the American Chemical Society*, **137**, 9136 (2015).
36. J. M. Haile, *Molecular Dynamics Simulations* (John Wiley & Sons, Inc., 1992).
37. G. E. Murch, *Philosophical Magazine A*, **45**, 685 (1982).
38. G. E. Murch, *Solid State Ionics*, **7**, 177 (1982).
39. G. E. Murch, *J. Phys. Chem. Solids*, **46**, 53 (1985).
40. J. Maier, *Physical Chemistry of Ionic Materials* (John Wiley & Sons, Ltd., 2004).
41. K. Compaan and Y. Haven, *Trans. Faraday Soc.*, **54**, 1498 (1958).
42. B. J. Morgan and P. A. Madden, *Physical Review Letters*, **112** (2014).

## Appendix C

**$\text{Li}_{14}\text{P}_2\text{O}_3\text{N}_6$  and  $\text{Li}_7\text{PN}_4$ :**

**Computational study of two  
nitrogen rich crystalline LiPON  
electrolyte materials**

Reproduced from the Journal of Power Sources, volume 364, pages 410–419, 2017.

With a permission from Elsevier.



# Li<sub>14</sub>P<sub>2</sub>O<sub>3</sub>N<sub>6</sub> and Li<sub>7</sub>PN<sub>4</sub>: Computational study of two nitrogen rich crystalline LiPON electrolyte materials



Ahmad Al-Qawasmeh, N.A.W. Holzwarth\*

Department of Physics, Wake Forest University, Winston-Salem, NC 27109-7507, USA

## HIGHLIGHTS

- First principles simulations of Li<sub>14</sub>P<sub>2</sub>O<sub>3</sub>N<sub>6</sub> and Li<sub>7</sub>PN<sub>4</sub> electrolytes.
- Simulations predict stable electrolyte/Li interfaces for both materials.
- Predict Li ion migration activation energies comparable to other good electrolytes.

## ARTICLE INFO

### Article history:

Received 20 June 2017  
Received in revised form  
26 July 2017  
Accepted 7 August 2017

### Keywords:

Solid electrolytes  
Li ion batteries  
First principles calculations

## ABSTRACT

Two lithium oxonitridophosphate materials are computationally examined and found to be promising solid electrolytes for possible use in all solid-state batteries having metallic Li anodes – Li<sub>14</sub>P<sub>2</sub>O<sub>3</sub>N<sub>6</sub> and Li<sub>7</sub>PN<sub>4</sub>. The first principles simulations are in good agreement with the structural analyses reported in the literature for these materials and the computed total energies indicate that both materials are stable with respect to decomposition into binary and ternary products. The computational results suggest that both materials are likely to form metastable interfaces with Li metal. The simulations also find both materials to have Li ion migration activation energies comparable or smaller than those of related Li ion electrolyte materials. Specifically, for Li<sub>7</sub>PN<sub>4</sub>, the experimentally measured activation energy can be explained by the migration of a Li ion vacancy stabilized by a small number of O<sup>2-</sup> ions substituting for N<sup>3-</sup> ions. For Li<sub>14</sub>P<sub>2</sub>O<sub>3</sub>N<sub>6</sub>, the activation energy for Li ion migration has not yet been experimentally measured, but simulations predict it to be smaller than that measured for Li<sub>7</sub>PN<sub>4</sub>.

© 2017 Elsevier B.V. All rights reserved.

## 1. Introduction

Twenty-five years after the pioneering work at Oak Ridge National Laboratory on LiPON solid electrolytes [1–9], new crystalline lithium oxonitridophosphate materials continue to be discovered. While the technologically viable LiPON electrolyte is disordered [1], studies of compositionally related crystalline materials has provided valuable insight. LiPON materials have the stoichiometry Li<sub>x</sub>PO<sub>y</sub>N<sub>z</sub> with  $x = 2y + 3z - 5$ . The building blocks of these materials are the PO<sub>u</sub>N<sub>4-u</sub> tetrahedra which are often formed into dimers, trimers, infinite chains, or more complicated interconnections [10–12]. Recently, Baumann and Schnick [13] found an interesting new crystalline LiPON which has the stoichiometry Li<sub>14</sub>P<sub>2</sub>O<sub>3</sub>N<sub>6</sub>, formed with a trigonal arrangement of isolated tetrahedral (PON<sub>3</sub>)<sup>6-</sup> ions and stabilized by isolated O<sup>2-</sup> ions. A

related electrolyte, having the stoichiometry of Li<sub>7</sub>PN<sub>4</sub> and based on a cubic arrangement of isolated tetrahedral (PN<sub>4</sub>)<sup>7-</sup> ions, was previously synthesized and characterized by Schnick and Luecke [14,15]. These are two examples of nitrogen rich LiPON materials constructed from isolated oxonitridophosphate tetrahedra. In the present work, we report the results of our computational study of the bulk and interface structures and Li ion migration properties of both Li<sub>14</sub>P<sub>2</sub>O<sub>3</sub>N<sub>6</sub> and Li<sub>7</sub>PN<sub>4</sub>. Results are compared with analogous studies of Li<sub>3</sub>PO<sub>4</sub> [16–21].

## 2. Computational methods

The computational methods used in this work are based on density functional theory (DFT) [22,23], implemented by the projected augmented wave (PAW) [24] formalism. The PAW basis and projector functions were generated by the ATOMPAW [25] code and used in the QUANTUM ESPRESSO [26] package. Visualizations of the crystal structures were constructed using the XCrySDEN [27,28],

\* Corresponding author.

E-mail address: [natalie@wfu.edu](mailto:natalie@wfu.edu) (N.A.W. Holzwarth).

VESTA [29] software packages.

The exchange correlation function is approximated using the local-density approximation (LDA) [30]. The choice of LDA functional was based on previous investigations [10,11,17,19,20,31] of similar materials which showed that the simulations are in good agreement with experiment, especially the fractional lattice parameters, the vibrational frequencies, and heats of formation. The simulated magnitudes of the lattice parameters, when systematically scaled by a factor of 1.02, are also in good agreement with experiment.

The calculations were well converged with plane wave expansions of the wave function including  $|\mathbf{k} + \mathbf{G}| \leq 64$  bohr<sup>-2</sup>. The Brillouin zone integrals were evaluated volumes of 0.006 bohr<sup>-3</sup> or smaller. Convergence tests showed that increasing the sampling volumes by a factor of 8 changed the total energy by less than 0.001 eV for 100 atom supercells.

The partial densities of states were calculated as described in previous work [20,32], using weighting factors determined from the charge within the augmentation spheres of each atom with radii  $r_c^{\text{Li}} = 1.6$ ,  $r_c^{\text{P}} = 1.7$ ,  $r_c^{\text{O}} = 1.2$ , and  $r_c^{\text{N}} = 1.2$  in bohr units. The reported partial densities of states curves  $\langle N^a(E) \rangle$  represent results averaged over the atomic sites of each type  $a$ . The Gaussian width used to evaluate the density of states was 0.01 eV.

Simulation of Li ion migration were performed at constant volume in supercells constructed from the optimized conventional cells. In modeling charged defects (Li ion vacancies or interstitials), the system was assumed to remain electrically insulating and a uniform background charge was added in order to evaluate the electrostatic interactions. The minimum energy path for Li ion migration was estimated using the “nudged elastic band” (NEB) method [33–35] as programmed in the QUANTUM ESPRESSO package, using 5 images between each metastable configuration. For each minimum energy path, the migration energy,  $E_m$  was determined as the energy difference between the lowest and highest energy of the path. The “formation energies”  $E_f$  for producing neutral defects in the form of vacancy-interstitial pairs were calculated within the same supercells. These energies are related to the experimentally measured ionic conductivity through an Arrhenius relationship of the form

$$\sigma = \frac{C}{T} e^{-E_A/KT}, \quad (1)$$

where  $C$  denotes a constant,  $T$  denotes the temperature in Kelvin,  $k$  denotes the Boltzmann constant, and  $E_A$  denotes the activation energy for ion migration. The activation energy  $E_A$  is related to the migration and formation energies according to [36].

$$E_m \leq E_A \leq E_m + \frac{1}{2}E_f. \quad (2)$$

In Eq. (2) the upper limit of  $E_A$  applies to the “intrinsic” case when ion migration is initiated by the creation of a pair of vacancy and interstitial ions with energy  $E_f$  by thermal activation in addition to the migration barrier  $E_m$ . The lower limit applies to the “extrinsic” case when a population of vacancy or interstitial ions is available in the sample so that the conduction depends only on the thermal activation due to the migration energy barriers characterized by  $E_m$ . Experimentally, sample preparation conditions presumably control the intrinsic versus extrinsic behaviors of the activation energy  $E_A$ . The static calculations cannot estimate the prefactor  $C$ , but calculations of  $E_m$  and  $E_f$  can provide the expected range of activation energies  $E_A$  according to Eq. (2).

Another important attribute of solid electrolytes is their interface properties, particularly their interfaces with metallic Li. These were modeled in supercells containing alternating slabs of

electrolyte and Li metal. The supercells were constrained to the optimized lattice parameters of the bulk electrolyte in the directions parallel to the interface, while the lattice parameter along the interface normal direction was allowed to vary in order to minimize the energy of the simulation cell. This procedure finds many metastable configurations of the interface. For some of the simulations we made a more quantitative assessment of the interface stability, following the approach of Lepley et al. [21] who defined a quasi-intensive interface energy between materials  $a$  and  $b$  as

$$\gamma_{ab}(\Omega) = \frac{E(\Omega, A, n_a, n_b) - n_a E_a - n_b E_b}{2A}. \quad (3)$$

Here  $E(\Omega, A, n_a, n_b)$  is the optimized total energy of the supercell containing the interface with  $n_a$  and  $n_b$  formula units of materials  $a$  and  $b$ .  $E_a$  and  $E_b$  denote the bulk energy per unit cell of materials  $a$  and  $b$ .  $\Omega$  represents the particular configuration of the system.  $A$  denotes the area normal to the surface; because of the periodic boundary conditions, each supercell necessarily has two equal area interfaces. For our case, material  $a$  represents the electrolyte –  $\text{Li}_{14}\text{P}_2\text{O}_3\text{N}_6$  or  $\text{Li}_7\text{PN}_4$  – and material  $b$  represents metallic Li. In order to assess the strain introduced by the periodic boundary conditions, the supercells are prepared with fixed  $n_a$  with the ideal lattice constants of the electrolyte, and a series of calculations are performed with similar configurations but varying numbers  $n_b$  of metallic Li atoms. The set of calculations can then be fit to an equation which varies linearly with  $n_b$  in the form

$$\gamma_{ab}(\Omega, n_b) = \gamma_{ab}^{\text{lim}}(\Omega) + n_b \sigma(\Omega). \quad (4)$$

Here  $\sigma(\Omega)$  represents the strain of the metallic Li in the configuration  $\Omega$  and  $\gamma_{ab}^{\text{lim}}(\Omega)$  represents the surface energy extrapolated to zero strain. For these systems, it is also interesting to reference the interface of the electrolyte with vacuum, for which Eq. (3) can be used with  $n_b=0$ .

### 3. Computational results

#### 3.1. $\text{Li}_{14}\text{P}_2\text{O}_3\text{N}_6$

##### 3.1.1. Structure of bulk $\text{Li}_{14}\text{P}_2\text{O}_3\text{N}_6$

Baumann and Schnick [13] reported the synthesis of  $\text{Li}_{14}\text{P}_2\text{O}_3\text{N}_6$  by heating powders of  $\text{PO}(\text{NH}_2)_3$  and  $\text{LiNH}_2$  in a sealed silica glass ampoule for 24 h at a temperature of 550 deg. C. The resulting crystals were analyzed to have a trigonal structure characterized by the space group  $P\bar{3}$  (No. 147 as listed in the International Table of Crystallography) [37]. Fig. 1 shows a ball and stick diagram of the structure from two different perspectives and Table 1 lists the calculated lattice parameters compared with experimental results. The scale factor of 1.02, used to correct the systematic LDA error on the magnitudes of the lattice constants, puts the simulated lattice constants within 0.1 Å of the experimental results. The simulated fractional coordinates for the P, O, and N sites are all within 0.01 of the experimental results. For the Li sites, the simulated fractional coordinates differ from the experimental values by a larger amount (0.06 or less). It is our experience [38] that it is common to find that X-ray analysis is less sensitive to the Li positions than to the positions of the other elements in the crystal which have larger X-ray cross sections due to their larger atomic numbers  $Z$ .

Simulations show that the trigonal symmetry is stabilized by the isolated  $\text{O}^{2-}$  ions located at  $1b$  sites and the corresponding  $\text{Li}^+$  ions located at  $2c$  sites. In addition to its trigonal symmetry, the crystal structure features an interesting arrangement of pairs of  $\text{PON}_3$  tetrahedra, forming  $c$ -axis planes of alternating  $\text{O}^{2-}$  and  $\text{N}^{3-}$  ions.

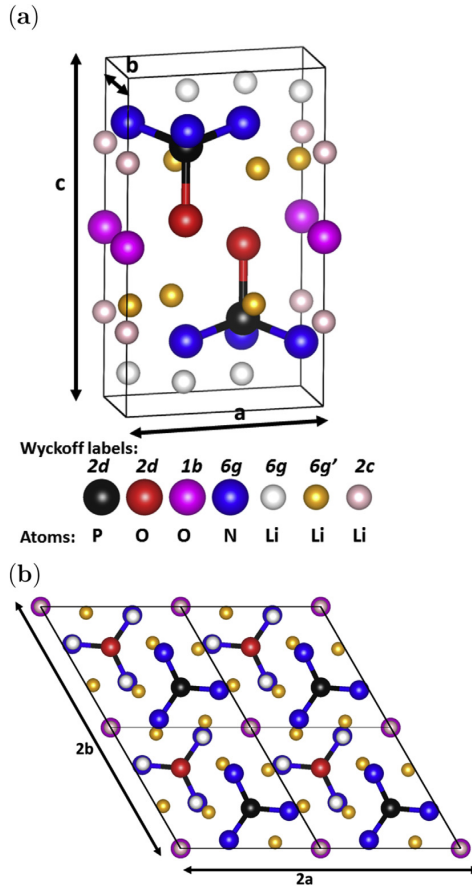


**Fig. 1.** (a) Ball and stick diagram of the  $P\bar{3}$  structure of a unit cell of  $\text{Li}_{14}\text{P}_2\text{O}_3\text{N}_6$ , viewing the  $c$ -axis along the vertical direction, using the indicated ball conventions to distinguish the inequivalent sites, labeled according to their Wyckoff letters. (b) Projection of 4 unit cells of  $\text{Li}_{14}\text{P}_2\text{O}_3\text{N}_6$  perpendicular to the  $c$  axis to show the trigonal symmetry.

**Table 1**

Optimized lattice parameters and fractional atomic positions of  $\text{Li}_{14}\text{P}_2\text{O}_3\text{N}_6$  having the space group  $P\bar{3}$  (#147) compared with experimental results reported in Ref. [13]. The simulated lattice parameters are multiplied by 1.02 factor to compensate for the underestimation of distances in the LDA approximation.

		Lattice constants (Å)	
		Simulation (this work)	Experiment (Ref. [13])
a		5.66	5.69
c		7.99	8.09
		Fractional coordinates	
		Simulation (this work)	Experiment (Ref. [13])
Atom	Site	(x, y, z)	(x, y, z)
Li	6g	(0.08, 0.70, 0.91)	(0.05, 0.64, 0.91)
Li	6g'	(0.35, 0.30, 0.41)	(0.29, 0.29, 0.41)
Li	2c	(0, 0, 0.75)	(0, 0, 0.77)
P	2d	( $\frac{1}{3}$ , $\frac{2}{3}$ , 0.23)	( $\frac{1}{3}$ , $\frac{2}{3}$ , 0.24)
O	2d	( $\frac{1}{3}$ , $\frac{2}{3}$ , 0.45)	( $\frac{1}{3}$ , $\frac{2}{3}$ , 0.45)
O	1b	(0, 0, $\frac{1}{2}$ )	(0, 0, $\frac{1}{2}$ )
N	6g	(0.07, 0.69, 0.17)	(0.06, 0.69, 0.17)

The arrangement of the isolated oxonitridophosphate tetrahedra is quite different from other crystalline LiPON materials of this type such as  $\text{Li}_7\text{PN}_4$  [14,15] and  $\beta$ - and  $\gamma$ - $\text{Li}_3\text{PO}_4$  which was studied previously [18,39].

It is interesting to compare the electronic structure of  $\text{Li}_{14}\text{P}_2\text{O}_3\text{N}_6$  with other oxonitridophosphates composed of isolated tetrahedra and related materials. The corresponding partial densities of states are given in Fig. 2. The valence band states are characterized by the  $2p$  states of O and N together with bonding combinations the P  $3s$  and  $3p$  states while the conduction bands are characterized by the corresponding antibonding states. The N  $2p$  states dominate the top of the valence band for  $\text{Li}_{14}\text{P}_2\text{O}_3\text{N}_6$ . The O  $2p$  contributions to  $\text{Li}_{14}\text{P}_2\text{O}_3\text{N}_6$  are of two types. The occupied states associated with P-O bonds contribute to the bottom of the valence band, while the non-bonded O  $2p$  states contribute to the middle of the valence band. Knowing that LDA calculations typically underestimate band gaps, we can safely conclude that the four materials are good insulators, having band gaps larger than 3 eV.

Related to the electronic structure is the stability of the compounds relative to decomposition. In order to thoroughly study the stability of this system, it would be helpful to construct a phase diagram such as achieved for  $\text{LiFePO}_4$  by Ong et al. [40]. While this is beyond the purview of the present study, some information about the stability can be determined by considering the energies of some possible chemical reactions. These can be roughly estimated from the calculated total energies, assuming that vibrational energies including zero point energies can be neglected. For example, we considered the following possible decomposition reaction.

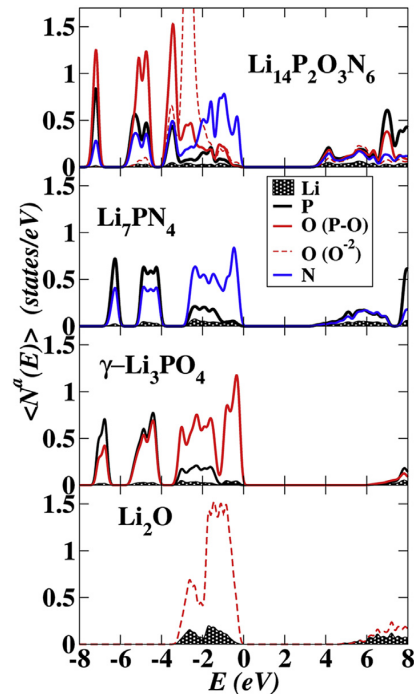
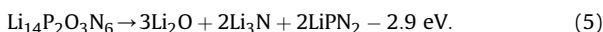
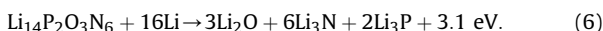


**Fig. 2.** Partial density of states plot for the LiPON materials  $\text{Li}_{14}\text{P}_2\text{O}_3\text{N}_6$  and  $\text{Li}_7\text{PN}_4$  in comparison with  $\gamma$ - $\text{Li}_3\text{PO}_4$  and  $\text{Li}_2\text{O}$ . Oxygen contributions from isolated  $\text{O}^{2-}$  ions and from oxygens associated with P-O bonds are distinguished with dashed and full red lines, respectively. In each plot,  $E = 0$  is aligned at the top of the valence band. (For interpretation of the references to colour in this figure legend, the reader is referred to the web version of this article.)



The negative energy on the right side of the equation indicates that  $\text{Li}_{14}\text{P}_2\text{O}_3\text{N}_6$  is stable with respect to decomposition into these binary and ternary products. In anticipation of the study of interfaces of this electrolyte with Li metal, we also considered the energy associated with reaction with Li metal as follows.



This reaction is exothermic, suggesting that under equilibrium conditions the interfaces would react with Li metal. However the exothermic energy is considerably smaller than 13.3 eV estimated for the analogous reaction of  $\text{Li}_3\text{PO}_4$  and Li metal [21].

### 3.1.2. Li ion migration mechanisms in $\text{Li}_{14}\text{P}_2\text{O}_3\text{N}_6$

Li ion migration in  $\text{Li}_{14}\text{P}_2\text{O}_3\text{N}_6$  was investigated using supercells based on  $2 \times 2 \times 1$  multiples of the unit cell. The energies of point defects were estimated from constant volume optimization of each structure containing a Li ion vacancy or interstitial and compensating uniform charge density within the supercell. Table 2 summarizes the 3 inequivalent vacancy energies relative to the  $g'$  site vacancy and 2 inequivalent interstitial energies relative to the  $I$  site interstitial. The placements of these defect sites are illustrated in Fig. 3(a) and (c) in an orthorhombic construction of the hexagonal unit cell.

In order to study likely migration pathways, using the NEB method [33–35], we considered a range of near neighbor hops between defect sites as summarized in Table 3. In this table, the distances  $d$  between defect sites are estimated from the perfect crystal configurations. The results show that  $\Delta E$ , the calculated energy variation within each trajectory between pairs of metastable configurations, is sensitive both to the distance  $d$  and to the local environment of the trajectory.

Considering Li ion vacancy migration, the large range of the relative energies of the unique vacancy configurations listed in Table 2 suggests that the energetically favorable vacancy migration processes are confined to hops between vacancies on equivalent sites. Table 3 lists the unique hops likely to contribute to Li ion migration in this material. These include several migration pathways between vacancies on  $g'$  sites and several pathways between vacancies on  $g$  sites. Geometric considerations suggest that  $c$  site vacancies are less likely to be involved in effective Li ion migration processes. The corresponding energy path diagrams are given in Fig. 3(b) for the vacancy mechanisms and in Fig. 3(d) for mechanisms actively involving interstitial sites.

The visualization of the trajectories shown in Fig. 3(a) shows that the vacancy migration processes involving sites of type  $g'$  take

**Table 2**

Distinct vacancy and interstitial Li ion sites within the unit cell of  $\text{Li}_{14}\text{P}_2\text{O}_3\text{N}_6$  and their relative energies estimated from  $2 \times 2 \times 1$  supercell optimizations. The reference energies were chosen as the  $g'$  site for the vacancy defects and the  $I$  site for the interstitial defects.

Vacancies	
Multiplicity and Wyckoff Label	Relative Energy (eV)
$4g'$	0.00
$4g$	0.95
$2c$	0.41
Interstitials	
Fractional Coordinates	Relative Energy (eV)
$I = (\frac{1}{3}, \frac{2}{3}, 0.73)$ ( $2d$ )	0.00
$II = (0, 0, 0)$ ( $1a$ )	0.22

place near planes of the crystal that include oxygen ions. The path  $g'_1 \rightarrow g'_2 \rightarrow g'_3 \rightarrow g'_4 \rightarrow g'_5$  is characterized by two unique hops. The hop  $g'_1 \rightarrow g'_2$  has a relatively low energy variation of  $\Delta E = 0.3$  eV, while the hop  $g'_2 \rightarrow g'_3$  has a more complicated trajectory with a net energy variation of  $\Delta E = 0.4$  eV. Examination of details of the trajectory shows that substantial rearrangement of the neighboring ions in the vicinity of a metastable interstitial configuration. The rearrangement lowers the energy of the configuration below that of the pure  $g'$  vacancy and thus increases the overall migration energy for the trajectory to  $E_m = 0.4$  eV. The path  $g'_6 \rightarrow g'_7 \rightarrow g'_8 \rightarrow g'_9 \rightarrow g'_{10}$  is characterized by one unique hop  $g'_6 \rightarrow g'_7$  which is identical to the hop  $g'_1 \rightarrow g'_2$  having an energy variation of  $\Delta E = 0.3$  eV resulting in the net migration barrier of  $E_m = 0.3$  eV which is the lowest migration barrier found for this material in this study.

Vacancy migration processes involving sites of type  $g$  take place near planes of the crystal that include nitrogen ions. The path  $g_6 \rightarrow g_7 \rightarrow g_8 \rightarrow g_9$  involves motion along the hexagonal  $a$  axis with two unique hops. The hop  $g_6 \rightarrow g_7$  has an energy variation of  $\Delta E = 0.3$  eV and the longer distance hop  $g_7 \rightarrow g_8$  has an energy variation of  $\Delta E = 1.6$  eV, resulting in the net migration barrier of  $E_m = 1.6$  eV for this path. The path  $g_1 \rightarrow g_2 \rightarrow g_3 \rightarrow g_4 \rightarrow g_5$  also involves net motion along the hexagonal  $a$  axis with two unique hops. The hop  $g_1 \rightarrow g_2$  is identical to the hop  $g_6 \rightarrow g_7$ , while the hop  $g_2 \rightarrow g_3$  has a component along the  $c$  axis having an energy variation of  $\Delta E = 0.6$  eV. The overall path which has a net motion along the hexagonal  $a$  axis in alternating proximity to two nearby nitrogen planes of the crystal, has a net migration energy of  $E_m = 0.6$  eV.

Li ion migration mechanisms involving interstitial sites were also considered as visualized in Fig. 3(c). A pure interstitial path was found in the proximity to two neighboring nitrogen planes, involving interstitial Li ions hopping 3.2 Å between type  $I$  and  $II$  sites. This path requires the Li ion to migrate through a region containing significant numbers of host lattice Li ions of type  $g$ . The simulations find significant distortion of the host lattice ions and the resulting energy variation along the path is very large –  $\Delta E > 2$  eV, suggesting that the pure interstitial mechanism is unlikely to contribute to the migration processes. On the other hand, a related kickout process, involving the same interstitial sites in concerted motion with nearby  $g$  site host lattice Li ions, as illustrated in Fig. 3(c), was found to have an energy variation of  $\Delta E = 0.6$  eV as shown in the energy path diagram of Fig. 3(d).

In order for Li ion migration to occur within a well-ordered crystalline material, it is necessary to take into account the “formation” energy  $E_f$  of vacancy-interstitial pairs of defects. The possible values of  $E_f$  for this material were estimated by optimizing defect pair geometries within the supercell, spanning the possibilities with interstitials of each type ( $I$  and  $II$ ) and near-neighbor vacancies of the types  $g'$ ,  $g$ , and  $c$ . For the pairs  $I$ - $c$  and  $II$ - $c$ , the formation energy was found to be relatively large –  $E_f \approx 1.0$  eV. For the pairs  $I$ - $g$  and  $II$ - $g$ , the formation energy was found to be very large –  $E_f > 1.6$  eV. However, for the pairs of type  $I$ - $g'$ , some smaller formation energies were found, with the minimum value of  $E_f = 0.3$  eV, involving nearest neighbor  $I$  and  $g'$  sites. Formation energies of type  $II$ - $g'$  were found to be  $E_f > 1.0$  eV.

From the analysis of  $E_m$  and  $E_f$  for this material, vacancy mechanism of diffusion near the oxygen planes with  $g'$  sites was found to be the most favorable with a migration energy  $E_m = 0.3$  eV and the minimum formation energy for this material was found to be  $E_f = 0.3$  eV. From these results the simulated activation energy can be estimated from Eq. (2) to be  $0.3 \leq E_A \leq 0.4$  eV.

### 3.1.3. $\text{Li}_{14}\text{P}_2\text{O}_3\text{N}_6/\text{Li}$ interfaces

From the structure of  $\text{Li}_{14}\text{P}_2\text{O}_3\text{N}_6$  shown in Fig. 1, a likely cleavage seems to be normal to the  $c$  axis between two planes

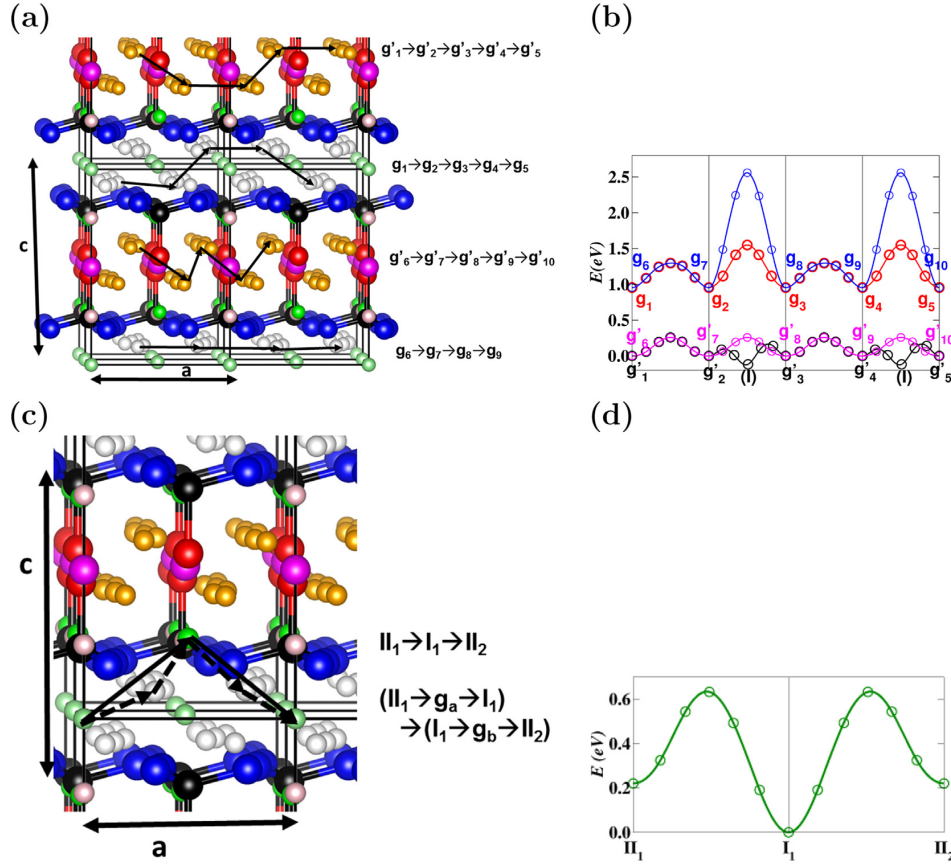


**Fig. 3.** Panels (a) and (c) show ball and stick models of several supercells of  $\text{Li}_{14}\text{P}_2\text{O}_3\text{N}_6$  using the same ball conventions as in Fig. 1 with the addition of type I and II interstitial sites shown in bright and pale green, respectively. The **a** and **c** axes are indicated in the diagrams while the third axis of the diagram is perpendicular to the other two, specifically constructed in the  $\mathbf{a} + 2\mathbf{b}$  direction. Panels (b) and (d) show energy path diagrams from NEB simulations of Li ion migration between metastable vacancy or interstitial configurations indicated by the vertical lines. Panel (a) shows 4 possible vacancy migration paths and panel (b) shows the corresponding energy path diagram, choosing the zero of energy at the  $g'$  vacancy configuration. Panel (c) shows possible interstitial (full arrows) and kickout (dashed arrows) mechanisms for Li ion migration and panel (d) shows the corresponding energy path diagram, choosing the zero of energy at the I interstitial configuration. (For interpretation of the references to colour in this figure legend, the reader is referred to the web version of this article.)

**Table 3**

Summary of Li ion migration steps in  $\text{Li}_{14}\text{P}_2\text{O}_3\text{N}_6$  using site labels are given in Figs. 3 (a) and (c). The hop distance  $d$  is based on ideal lattices before defect optimization. The energy range within each hop is given as  $\Delta E$ .

Type	Sites	$d$ (Å)	$\Delta E$ (eV)
Vacancy	$g'_1 \rightarrow g'_2, g'_6 \rightarrow g'_7$	2.3	0.3
Vacancy	$g'_2 \rightarrow g'_3$	2.6	0.4
Vacancy	$g_1 \rightarrow g_2, g_6 \rightarrow g_7$	2.6	0.3
Vacancy	$g_2 \rightarrow g_3$	2.4	0.6
Vacancy	$g_7 \rightarrow g_8$	3.3	1.6
Interstitial	$II_1 \rightarrow I_1$	3.2	>2.0
Kickout	$II_1 \rightarrow g_a \rightarrow I_1$	2.0 + 2.0	0.6

containing N. Using Eq. (3) with  $n_b = 0$ , we find  $\gamma(\text{Li}_{14}\text{P}_2\text{O}_3\text{N}_6[\mathbf{c}]/\text{vac}) = 0.07 \text{ eV}/\text{\AA}^2$ . The result is insensitive to the number of electrolyte layers; converging within 0.001  $\text{eV}/\text{\AA}^2$  even for a single layer. All other vacuum cleavages for this material were found to have a larger surface energy by at least 50%. The surface energy for this system is similar to that of  $\gamma\text{-Li}_3\text{PO}_4$ , which was reported by Lepley et al. [21] to be 0.04  $\text{eV}/\text{\AA}^2$  and 0.07  $\text{eV}/\text{\AA}^2$  for surface normals along the **a** and **b** axes, respectively.

We prepared two series of configurations of interfaces of  $\text{Li}_{14}\text{P}_2\text{O}_3\text{N}_6[\mathbf{c}]$  with Li as shown in Fig. 4(a) and (b) and the corresponding plots of the surface energy versus the number of metallic lithium atoms  $n_b$  are evaluated according to Eq. (4) as plotted in Fig. 4(c). Interface configurations  $\Omega_1$  and  $\Omega_2$  have approximately the same density of the Li atoms per unit volume 0.05–0.06 atoms/ $\text{\AA}^3$ , close to the density of bulk Li. The estimated strains of the two configurations are  $\sigma(\Omega_1) = 0.0004 \text{ eV}/\text{\AA}^2$  and  $\sigma(\Omega_2) = 0.0014 \text{ eV}/\text{\AA}^2$ , consistent with the notion that the more regular structure of configuration  $\Omega_1$  produces smaller strain. The strain corrected interface energy,  $\gamma_{ab}^{\text{lim}}$ , for the two configurations is found to be approximately 0.05  $\text{eV}/\text{\AA}^2$ . This value is similar to the corresponding values of 0.03–0.04  $\text{eV}/\text{\AA}^2$  reported by Lepley et al. [21] for interfaces of  $\beta$ - or  $\gamma$ - $\text{Li}_3\text{PO}_4$  with Li metal.

The partial densities of states for the interface 4(a) with  $n_b = 36$  are shown in Fig. 4(d). Even though the supercell contains only one formula unit of the electrolyte, the partial densities of states for the interior of the electrolyte is very similar to that of the bulk structure of  $\text{Li}_{14}\text{P}_2\text{O}_3\text{N}_6$  shown in Fig. 2. The metallic Li states are physically separated from the electrolyte, but energetically overlap with the top of the  $\text{Li}_{14}\text{P}_2\text{O}_3\text{N}_6$  valence band by approximately 1 eV. The

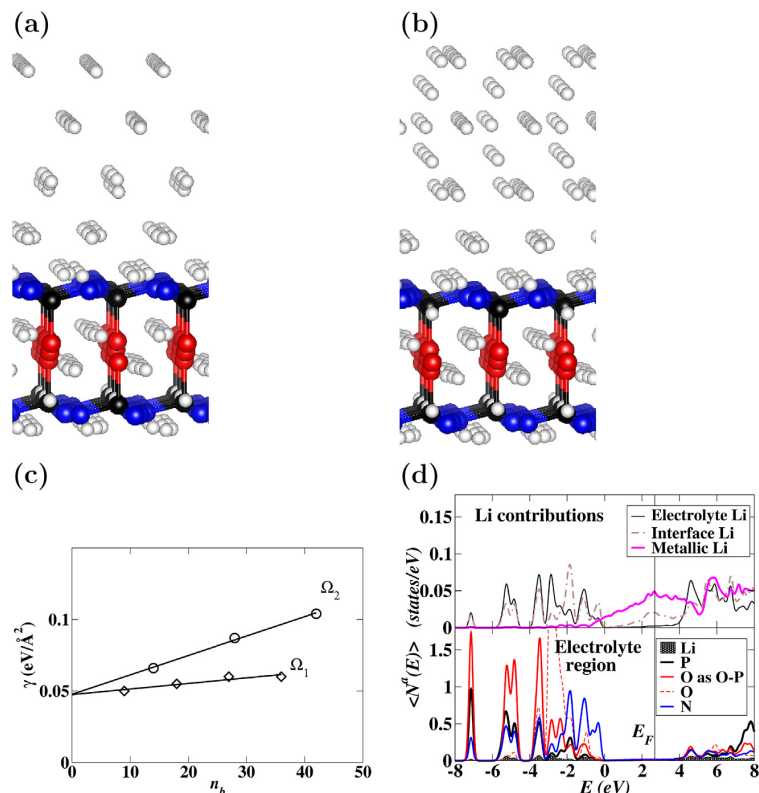


**Fig. 4.** Ball and stick models of interfaces of  $\text{Li}_{14}\text{P}_2\text{O}_3\text{N}_6[\text{c}]/\text{Li}$  from viewpoints similar to that given in Fig. 3 using simplified ball conventions with light gray, black, red, and blue balls representing Li, P, O, and N sites, respectively. Li configurations  $\Omega_1$  and  $\Omega_2$  are shown in panels (a) and (b), respectively. Panel (c) plots the interface energy for the two configurations as a function of  $n_b$  Li metal atoms, evaluated according to Eq. (4). Panel (d) presents the partial densities of states of configuration  $\Omega_1$  with 36 metallic Li atoms in the supercell. The zero of energy for the  $\langle N^i(E) \rangle$  plots is taken as the top of the valence band of the bulk electrolyte. The bottom portion of the plot shows the five contributions to partial densities of states from the interior of the electrolyte in the supercell, while the upper portion compares the partial densities of states of the three types of Li using an expanded intensity scale. (For interpretation of the references to colour in this figure legend, the reader is referred to the web version of this article.)

partial densities of states associated with the Li ions at the interface of the electrolyte and the metallic Li, show that they have more electronic charge than the  $\text{Li}^+$  ions in the interior of the electrolyte. The “Electrolyte Li” curve in the top portion of the plot 4(d) is the same as the “Li” curve in lower portion of the plot representing ionic Li within the interior of the electrolyte. Also shown in the top portion of the plot 4(d) are the “Interface Li” contributions corresponding to Li sites nearest the electrolyte and the “Metallic Li” contributions corresponding to the interior of the metallic Li region of the supercell.

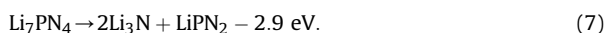
### 3.2. $\text{Li}_7\text{PN}_4$

#### 3.2.1. Structure of the bulk $\text{Li}_7\text{PN}_4$

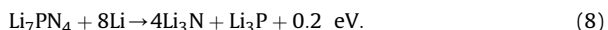
$\text{Li}_7\text{PN}_4$  was synthesized by Schnick and Luecke [14,15] by sealing  $\text{Li}_3\text{N}$  and  $\text{P}_3\text{N}_5$  under a nitrogen atmosphere in a quartz tube and heating to 620 deg C for one hour. The resulting crystals were analyzed to have a cubic structure with the space group  $P\bar{4}3n$  (No. 218) with 8 formula units (96 atoms) in each unit cell. A ball and stick diagram of the unit cell is shown in Fig. 5. Table 4 lists the lattice parameters from the simulation in comparison with the experimental results. The comparison is quite good. The LDA corrected simulated lattice constants agree with experiment within 0.02 Å, and the fractional coordinates including the Li sites agree within 0.01.

The partial densities of states for  $\text{Li}_7\text{PN}_4$  was shown in Fig. 2 in comparison with the related materials of this study. The similarity of the electronic structure with  $\text{Li}_3\text{PO}_4$  is evident from these plots, while  $\text{Li}_7\text{PN}_4$  has a smaller valence band width and a smaller gap between the conduction and valence bands compared with  $\text{Li}_3\text{PO}_4$ .

With a view toward considering a limited study of the stability of this system, from the electronic structure results, we can consider the following decomposition reaction:



The negative energy on the right side of the equation indicates that  $\text{Li}_7\text{PN}_4$  is stable with respect to decomposition into these binary and ternary products. We can also consider interaction with metallic Li.

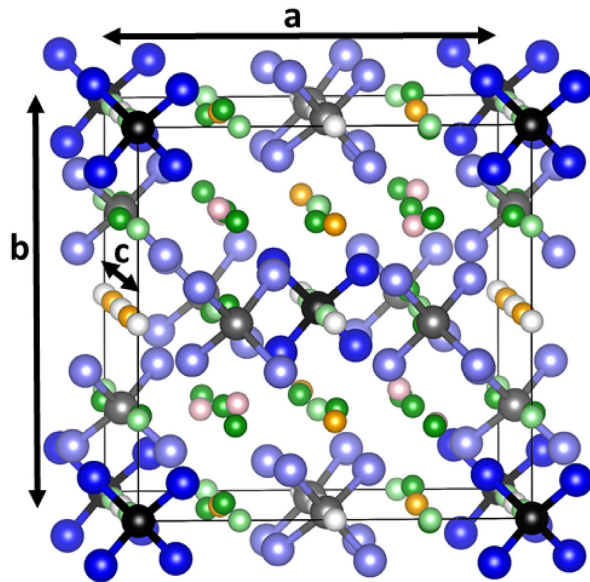


This reaction is exothermic suggesting that under equilibrium conditions the interfaces would react with Li metal. However the exothermic energy in this case is very small compared with the corresponding reaction energies of other LiPON electrolytes as discussed above.

#### 3.2.2. Li ion migration mechanisms in $\text{Li}_7\text{PN}_4$

We also considered Li ion migration mechanisms in  $\text{Li}_7\text{PN}_4$ . The





Wyckoff labels:

6c 2a 24i 8e 6b 6d 8e 24i 12f



Atoms: P P N N Li Li Li Li Li

Fig. 5. Ball and stick diagram of the  $P43n$  structure of a unit cell of  $\text{Li}_7\text{PN}_4$ , using the indicated ball conventions to distinguish the inequivalent sites; labeled with their Wyckoff letters. The axes **a**, **b** and **c** are equivalent.

Table 4

Optimized lattice parameters and fractional atomic positions of  $\text{Li}_7\text{PN}_4$  having the space group  $P43n$  (# 218) compared with experimental results reported in Ref. [14]. The simulated lattice parameters are multiplied by 1.02 factor to compensate for the underestimation of distances of LDA approximation.

		Lattice constant (Å)	
		Simulation (this work)	Experiment (Ref. [14])
<b>a</b>		9.34	9.36
		Fractional coordinates	
		Simulation (this work)	Experiment (Ref. [14])
Atom	Site	(x,y,z)	(x,y,z)
Li	6b	$(0, \frac{1}{2}, \frac{1}{2})$	$(0, \frac{1}{2}, \frac{1}{2})$
Li	6d	$(\frac{1}{4}, 0, \frac{1}{2})$	$(\frac{1}{4}, 0, \frac{1}{2})$
Li	8e	(0.23, 0.23, 0.23)	(0.22, 0.22, 0.22)
Li	12f	(0.26, 0, 0)	(0.26, 0, 0)
Li	24i	(0.25, 0.24, 0.98)	(0.25, 0.24, 0.97)
P	6c	$(\frac{1}{2}, 0, \frac{1}{4})$	$(\frac{1}{2}, 0, \frac{1}{4})$
P	2a	(0, 0, 0)	(0, 0, 0)
N	24i	(0.35, 0.39, 0.10)	(0.35, 0.38, 0.10)
N	8e	(0.10, 0.10, 0.10)	(0.10, 0.10, 0.10)

simulations were performed using the unit cell since it is quite large, containing 96 atoms. Vacancies were simulated by removing one  $\text{Li}^+$  ion and adding a compensating uniform charge of  $+e$  within the simulation cell. There are five distinct vacancy sites and the corresponding relative vacancy energies are given in Table 5. Interstitials were simulated by adding one  $\text{Li}^+$  ion and adding a

Table 5

Distinct vacancy and interstitial Li ion sites in  $\text{Li}_7\text{PN}_4$  and their relative energies. The *f* vacancy site is chosen as the reference for the vacancy sites, and the *l* interstitial type is chosen as the reference for the interstitial sites.

Vacancies	
Multiplicity and Wyckoff Label	Relative Energy (eV)
6b	0.15
6d	0.25
8e	0.00
12f	0.00
24i	0.10
Interstitials	
Fractional Coordinates	Relative Energy (eV)
<i>l</i> =(0.36, 0.85, 0.38) (24i)	0.00
<i>l</i> =(0.36, 0.36, 0.36) (8e)	0.32

compensating uniform charge of  $-e$  within the simulation cell. Two distinct low energy interstitial sites were found and these are also listed in Table 5, including their Wyckoff site label.

For simulating Li ion vacancy migration, it was determined that the paths with the shortest hops are along one of the equivalent crystallographic axes. For example, in Fig. 5, three distinct paths along the *c*-axis can be visualized. The corresponding energies along the migration path as computed with the NEB approach are illustrated in Fig. 6(a). From these diagrams, it is apparent that the path  $i \rightarrow e \rightarrow i \rightarrow e \rightarrow i$  has the smallest migration energy with  $E_m = 0.3$  eV. The simulations also show that the smallest “formation” energy for an interstitial-vacancy pair  $E_f = 1.9$  eV, corresponding to a type *l* interstitial paired with a all types of nearby vacancies within 5 Å distance from the interstitial. From these results, the simulated activation energy from Eq. (2) can be estimated to be  $0.3 \leq E_A \leq 1.3$  eV. On the other hand, the experimental

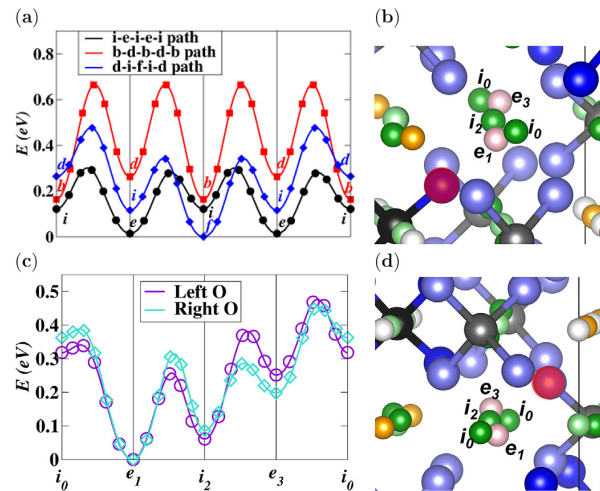
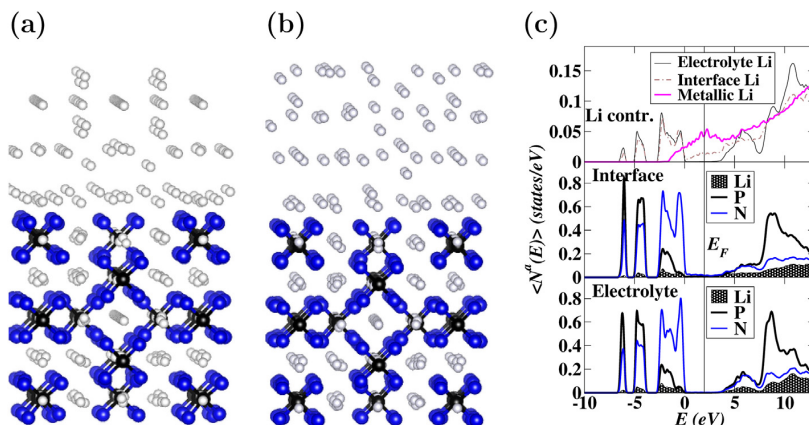


Fig. 6. (a) Energy path diagram for Li ion vacancy migration in  $\text{Li}_7\text{PN}_4$ , showing three distinct trajectories between metastable vacancy configurations indicated with the vertical lines and corresponding to the indicated Wyckoff labels; the zero of energy is taken as a Li ion vacancy at a *f* site. (c) Energy path diagram for Li ion vacancy migration in  $\text{Li}_7\text{PN}_4$  in the vicinity of an O ion substituting for N; the zero of energy is taken to be the lowest energy of the path (at the  $e_1$  site Li ion vacancy). Panels (b) and (d) show sections of the unit cell of  $\text{Li}_7\text{PN}_4$  as shown in Fig. 5 in the vicinity of Li sites  $i \rightarrow e \dots$ . These sections each have a substituted O ion represented by a red ball on the “left” and “right” sides of the path in panels (b) and (d), respectively. (For interpretation of the references to colour in this figure legend, the reader is referred to the web version of this article.)



**Fig. 7.** Panels (a) and (b) show ball and stick models of  $\text{Li}_7\text{PN}_4$  interfaced with metallic Li in two distinct configurations. The ball conventions have been simplified so that light gray, black, and blue balls represent Li, P, and N sites, respectively. Panel (c) shows partial densities of states corresponding to configuration (b), with separate  $\langle N^q(E) \rangle$  contributions for the interior of the electrolyte, the interface region, and the contributions from the three types of Li sites using an expanded intensity scale. The zero of energy for the plots is taken as the top of the valence band of the bulk electrolyte. (For interpretation of the references to colour in this figure legend, the reader is referred to the web version of this article.)

impedance measurements find the activation energy for ionic conductivity to be  $E_A = 0.48$  eV [15], suggesting that the experimental samples have a significant source of Li ion vacancies besides those available from thermal activation.

We reasoned that a possible source of Li ion vacancies in the experimental samples might be due to the presence of O ions replacing a small number N ions within the crystal. Since  $\text{O}^{2-}$  ions can be compensated with 2  $\text{Li}^+$  ions while  $\text{N}^{3-}$  can be compensated with 3  $\text{Li}^+$  ions, a O ion substitution stabilizes a Li ion vacancy. There are two inequivalent N sites leading to two inequivalent O ion substitutions. Fig. 6(b) illustrates the “Left O” geometry in which the substituted N site has Wyckoff label *e* and Fig. 6(d) illustrates the “Right O” geometry in which the substituted N site has Wyckoff label *i*. The corresponding NEB diagrams for Li ion migration along the nearby  $i \rightarrow e \rightarrow i \rightarrow e \rightarrow i$  paths are shown in Fig. 6(c). The energy diagram plots for the two substitution models are very similar (but not identical) and show that the presence of an O ion substitution does increase the migration energy barriers to  $E_m \approx 0.5$  eV. Since the activation energy for conductivity in the presence of a native population of vacancies is  $E_A = E_m$ , the simulations support the notion that experimental samples of  $\text{Li}_7\text{PN}_4$  may have O ion defects which stabilize Li ion vacancies and which increase the ionic conductivity.

In addition, we have investigated several possible Li ion interstitial mechanisms using the *I* and *II* type interstitial sites listed in Table 5. However, no direct hop or kickout paths were identified, based on geometric considerations.

### 3.2.3. $\text{Li}_7\text{PN}_4/\text{Li}$ interfaces

A plausible cleavage plane for forming a surface of  $\text{Li}_7\text{PN}_4$  is normal to a cube axis and exposes the smallest number of voids between  $\text{PN}_4$  groups as shown in Fig. 7. We studied this (100) surface with a variety of Li configurations. The relaxed structures of two these interfaces is shown in Fig. 7. The structure shown in Fig. 7(a) is a highly symmetric structure, while the structure shown in Fig. 7(b) is less symmetric, but has an energy of 6.1 eV lower in the 192 atom simulation cell. The interface energy for configuration 7(b) (not corrected for strain) was found to be  $0.04$  eV/ $\text{\AA}^2$ , a value similar to other  $\text{LiPON}/\text{Li}$  interfaces discussed above. The partial density of states for structure 7(b) is shown in Fig. 7(c). The corresponding partial densities of states for structure 7(a) is

qualitatively similar, differing mostly in the partial densities of states contributions from metallic Li. The partial densities of states results shown in Fig. 7(c) indicates that this  $\text{Li}_7\text{PN}_4/\text{Li}$  system has the properties of an ideal interface. It is structurally metastable and the Fermi level of the system falls well within the band gap of the interior portion of the electrolyte so that it is expected that the system will be electrically insulating. It is interesting to note that  $\langle N^q(E) \rangle$  curves corresponding to the interface region involving the P, N, and Li ions closest to the interface boundary, show small contributions within the band gap of bulk electrolyte, as shown in the middle panel of Fig. 7(c). The  $\langle N^q(E) \rangle$  contribution for metallic Li shown in the top of Fig. 7(c) has the typical shape of that of a free-electron metal.

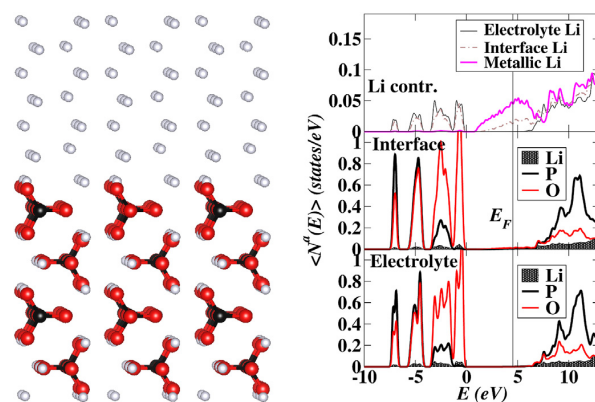


**Fig. 8.** Panel (a) shows ball and stick diagram of idealized  $\gamma\text{-Li}_3\text{PO}_4/\text{Li}$  with the surface normal oriented along the  $\mathbf{b}$  axis shown in the vertical direction and the  $\mathbf{a}$  axis of the electrolyte shown in the horizontal direction. The ball conventions are light gray, black, and red, representing Li, P, and O sites, respectively. Panel (b) shows the corresponding Partial densities of states plots for this interface, with separate  $\langle N^q(E) \rangle$  contributions for the interior of the electrolyte, the interface region, and the contributions from the three types of Li sites using an expanded intensity scale. The zero of energy for the plots is taken as the top of the valence band of the bulk electrolyte. (For interpretation of the references to colour in this figure legend, the reader is referred to the web version of this article.)

**Table 6**  
Comparison of calculated and measured activation energies. All energies are given in eV units.

Material	Mechanism	Simulation			Experiment
		$E_f$	$E_m$	$E_m + \frac{1}{2}E_f$	$E_A$
Li <sub>14</sub> P <sub>2</sub> O <sub>3</sub> N <sub>6</sub>	Vacancy	0.3	0.3	0.4	0.48 <sup>a</sup>
Li <sub>14</sub> P <sub>2</sub> O <sub>3</sub> N <sub>6</sub>	Kickout	0.3	0.6	0.8	
Li <sub>7</sub> PN <sub>4</sub>	Vacancy	1.9	0.3	1.3	
Li <sub>7</sub> PN <sub>4</sub> with O	Vacancy	—	0.5	—	
β-Li <sub>3</sub> PO <sub>4</sub>	Kickout	2.1 <sup>b</sup>	0.4 <sup>b</sup>	1.5 <sup>b</sup>	
γ-Li <sub>3</sub> PO <sub>4</sub>	Kickout	1.7 <sup>b</sup>	0.3 <sup>b</sup>	1.2 <sup>b</sup>	

<sup>a</sup> Ref. [15].

<sup>b</sup> Ref. [17].

<sup>c</sup> Ref. [42].

#### 4. Summary and conclusions

The results of the reported simulations suggest that both nitrogen rich crystalline lithium oxonitridophosphate materials of this study – Li<sub>14</sub>P<sub>2</sub>O<sub>3</sub>N<sub>6</sub> and Li<sub>7</sub>PN<sub>4</sub> – show promising properties as solid electrolytes for Li ion batteries, possibly for use with Li metal anodes.

Simulations of idealized interfaces constructed for Li<sub>14</sub>P<sub>2</sub>O<sub>3</sub>N<sub>6</sub>/Li and Li<sub>7</sub>PN<sub>4</sub>/Li are structurally metastable and electrically insulating. In both of these cases, the partial densities of states associated with the interfaces show small effects in their electronic structures, while the partial densities of states associated with the interior of the electrolytes are identical to their bulk values. The partial densities of states associated with the metallic Li layers show that the Fermi level of the system lies well within the band gap of the interior layers of the electrolyte. An analogous study of idealized interfaces for γ-Li<sub>3</sub>PO<sub>4</sub>[b]/Li previously studied by Lepley et al. [21] is shown in Fig. 8(a) and (b). Here we see that the partial densities of states in the interface are somewhat less effected than in the case of the nitrogen rich electrolytes, while the partial densities of states associated with the interior of the electrolytes are identical to their bulk values. The partial densities of states associated with the metallic Li layers show that the Fermi level of the system lies well within the band gap of the interior layers of the electrolyte. Interestingly, the bottom of the metallic Li band in γ-Li<sub>3</sub>PO<sub>4</sub>[b]/Li lies above the top of the valence band of the electrolyte, while for the nitrogen-rich materials, the bottom of the metallic Li band lies approximately 1 eV below the top of the valence band of the electrolyte. While the total energy results for these LiPON electrolytes suggest exothermic reactions with Li under equilibrium conditions such as shown in Eqs. (6) and (8), these simulations show that LiPON/Li interfaces are likely to be practically stable as has been shown in experimental demonstrations [41].

The simulations also suggest that the activation energies for Li ion migration in the nitrogen rich electrolytes are also quite promising. Table 6 summarizes the simulation estimates of Li ion activation energies with experiment and with previous results for other isolated oxonitridophosphate materials. Here we see that the most efficient predicted activation energy for Li ion migration in Li<sub>14</sub>P<sub>2</sub>O<sub>3</sub>N<sub>6</sub> is 0.3–0.4 eV for a pure vacancy mechanism involving g' site Li ions. The predicted activation energy for Li ion migration in Li<sub>14</sub>P<sub>2</sub>O<sub>3</sub>N<sub>6</sub> is lower than the experimentally measured values for Li<sub>7</sub>PN<sub>4</sub> [15] and for γ-Li<sub>3</sub>PO<sub>4</sub> [42] as well as the  $E_A = 0.6$  eV values measured for typical amorphous LiPON films [3]. The predicted activation energy of  $E_A = 0.5$  eV for Li ion migration in Li<sub>7</sub>PN<sub>4</sub> with Li ion vacancies, stabilized by O<sup>2-</sup> ions substituting for N<sup>3-</sup>, is close to that reported in experimental conductivity measurements for Li<sub>7</sub>PN<sub>4</sub> [15]. It is also interesting to note that while for these nitrogen rich crystalline electrolytes, Li ion migration is dominated by vacancy mechanisms, while for Li<sub>3</sub>PO<sub>4</sub> it was found that kickout

mechanisms provide the most efficient ion migration processes [17]. While the simulations represent many competing factors which contribute to these results, it is perhaps reasonable to suggest a more general trend from the fact that each N<sup>3-</sup> ion is associated with three Li ions while each O<sup>2-</sup> ion is associated with two Li ions. It is therefore reasonable to expect that Li ion migration in structures with greater numbers of occupied Li sites are likely to occur via vacancy mechanisms while structures with smaller numbers of occupied Li sites are likely to occur via mechanisms having more active involvement of the interstitial sites.

#### Acknowledgements

This work was supported by NSF grant DMR-1507942. Computations were performed on the Wake Forest University DEAC cluster, a centrally managed resource with support provided in part by the University. We would also like to thank Dr. Nicholas Lepley for the use of his unpublished simulations of a γ-Li<sub>3</sub>PO<sub>4</sub>/Li interface.

#### References

- [1] N.J. Dudney, Thin film micro-batteries, *Interface* 17 (3) (2008) 44–48 (3).
- [2] J.B. Bates, N.J. Dudney, B. Neudecker, A. Ueda, C.D. Evans, Thin-film lithium and lithium-ion batteries, *Solid State Ionics* 135 (2000) 33–45.
- [3] X. Yu, J.B. Bates, J.G.E. Jellison, F.X. Hart, A stable thin-film lithium electrolyte: lithium phosphorus oxynitride, *J. Electrochem. Soc.* 144 (1997) 524–532.
- [4] B. Wang, B.C. Chakoumakos, B.C. Sales, B.S. Kwak, J.B. Bates, Synthesis, crystal structure, and ionic conductivity of a polycrystalline lithium phosphorus oxynitride with the γ-Li<sub>3</sub>PO<sub>4</sub> structure, *J. Solid State Chem.* 115 (1995) 313–323.
- [5] J.B. Bates, N.J. Dudney, D.C. Lubben, G.R. Gruzalski, B.S. Kwak, X. Yu, R.A. Zuhr, Thin-film rechargeable lithium batteries, *J. Power Sources* 54 (1995) 58–62.
- [6] B. Wang, B.S. Kwak, B.C. Sales, J.B. Bates, Ionic conductivities and structure of lithium phosphorus oxynitride glasses, *J. Non-Crystalline Solids* 183 (1995) 297–306.
- [7] J.B. Bates, G.R. Gruzalski, N.J. Dudney, C.F. Luck, X. Yu, Rechargeable thin-film lithium batteries, *Solid State Ionics* 70–71 (1994) 619–628.
- [8] J.B. Bates, N.J. Dudney, G.R. Gruzalski, R.A. Zuhr, A. Choudhury, D.F. Luck, J.D. Robertson, Fabrication and characterization of amorphous lithium electrolyte thin films and rechargeable thin-film batteries, *J. Power Sources* 43–44 (1993) 103–110.
- [9] J.B. Bates, N.J. Dudney, G.R. Gruzalski, R.A. Zuhr, A. Choudhury, D.F. Luck, J.D. Robertson, Electrical properties of amorphous lithium electrolyte thin films, *Solid State Ionics* 53–56 (1992) 647–654.
- [10] Y.A. Du, N.A.W. Holzwarth, First-principles study of LiPON and related solid electrolytes, *Phys. Rev. B* 81 (2010) 184106 (15pp).
- [11] K. Senevirathne, C.S. Day, M.D. Gross, A. Lachgar, N.A.W. Holzwarth, A new crystalline LiPON electrolyte: synthesis, properties, and electronic structure, *Solid State Ionics* 333 (2013) 95–101.
- [12] E.-M. Bertschler, C. Dietrich, J. Janek, W. Schnick, Li<sub>18</sub>P<sub>6</sub>N<sub>16</sub> - a lithium nitridophosphate with unprecedented tricyclic [P<sub>6</sub>N<sub>16</sub>]<sub>18-</sub> ions, *Chem. A Eur. J.* 23 (2017) 2185–2191.
- [13] D. Baumann, W. Schnick, Li<sub>14</sub>(PON<sub>3</sub>)<sub>2</sub>O - a non-condensed oxonitridophosphate oxide, *Eur. J. Inorg. Chem.* 2015 (4) (2015) 617–621.
- [14] W. Schnick, J. Luecke, Synthesis and crystal structure of lithium phosphorus nitride Li<sub>7</sub>PN<sub>4</sub>: the first compound containing isolated PN<sub>4</sub> tetrahedra, *J. Solid State Chem.* 37 (1990) 101–106.
- [15] W. Schnick, J. Luecke, Lithium ion conductivity of LiPN<sub>2</sub> and Li<sub>7</sub>PN<sub>4</sub>, *Solid State Ionics* 38 (1990) 271–273.

- [16] Y.A. Du, N.A.W. Holzwarth, Li ion diffusion mechanisms in the crystalline electrolyte  $\gamma$ - $\text{Li}_3\text{PO}_4$ , *J. Electrochem. Soc.* 154 (2007) A999–A1004.
- [17] Y.A. Du, N.A.W. Holzwarth, Mechanisms of  $\text{Li}^+$  diffusion in crystalline  $\text{Li}_3\text{PO}_4$  electrolytes from first principles, *Phys. Rev. B* 76 (2007) 174302 (14 pp).
- [18] Y.A. Du, N.A.W. Holzwarth, Effects of O vacancies and N or Si substitutions on  $\text{Li}^+$  migration in  $\text{Li}_3\text{PO}_4$  electrolytes from first principles, *Phys. Rev. B* 78 (2008) 174301.
- [19] N.A.W. Holzwarth, N.D. Lepley, Y.A. Du, Computer modeling of lithium phosphate and thiophosphate electrolyte materials, *J. Power Sources* 196 (2011) 6870–6876.
- [20] N.D. Lepley, N.A.W. Holzwarth, Y.A. Du, Structures,  $\text{Li}^+$  mobilities, and interfacial properties of solid electrolytes  $\text{Li}_3\text{PS}_4$  and  $\text{Li}_3\text{PO}_4$  from first principles, *Phys. Rev. B* 88 (2013) 104103 (11 pp).
- [21] N.D. Lepley, N.A.W. Holzwarth, Modeling interfaces between solids: application to Li battery materials, *Phys. Rev. B* 92 (2015) 214201.
- [22] P. Hohenberg, W. Kohn, Inhomogeneous electron gas, *Phys. Rev.* 136 (1964) B864–B871.
- [23] W. Kohn, L.J. Sham, Self-consistent equations including exchange and correlation effects, *Phys. Rev.* 140 (1965) A1133–A1138.
- [24] P.E. Blöchl, Projector augmented-wave method, *Phys. Rev. B* 50 (1994) 17953–17979.
- [25] N.A.W. Holzwarth, A.R. Tackett, G.E. Matthews, A Projector Augmented Wave (PAW) code for electronic structure calculations, Part I: *atomPAW* for generating atom-centered functions, *Comput. Phys. Commun.* 135 (2001) 329–347 available from the website <http://pwpaw.wfu.edu>.
- [26] P. Giannozzi, S. Baroni, N. Bonini, M. Calandra, R. Car, C. Cavazzoni, D. Ceresoli, G.L. Chiarotti, M. Cococcioni, I. Dabo, A.D. Corso, S. de Gironcoli, S. Fabris, G. Fratesi, R. Gebauer, U. Gerstmann, C. Gougousis, A. Kokalj, M. Lazzeri, L. Martin-Samos, N. Marzari, F. Mauri, R. Mazzarello, S. Paolini, A. Pasquarello, L. Paulatto, C. Sbraccia, S. Scandolo, G. Sclauzero, A.P. Seitsonen, A. Smogunov, P. Umari, R.M. Wentzcovitch, Quantum espresso: a modular and open-source software project for quantum simulations of materials, *J. Phys. Condens. Matter* 21 (39) (2009) 394402 (19pp), available from the website, <http://www.quantum-espresso.org>.
- [27] A. Kokalj, XCrySDen— an new program for displaying crystalline structures and densities, *J. Mol. Graph. Model.* 17 (1999) 176–179 code available at the website, <http://www.xcrysden.org>.
- [28] A. Kokalj, Computer graphics and graphical user interfaces as tools in simulations of matter at the atomic scale, *Comput. Mater. Sci.* 28 (2003) 155–168.
- [29] K. Momma, F. Izumi, Vesta 3 for three-dimensional visualization of crystal, volumetric, and morphology data, *Appl. Crystallogr.* 44 (2011) 1272–1276 code available from the website, <http://jp-minerals.org/vesta/en/>.
- [30] J.P. Perdew, Y. Wang, Accurate and simple analytic representation of the electron-gas correlation energy, *Phys. Rev. B* 45 (1992) 13244–13249.
- [31] N.D. Lepley, N.A.W. Holzwarth, Computer modeling of crystalline electrolytes – lithium thiophosphates and phosphates, *J. Electrochem. Soc.* 159 (2012) A538–A547.
- [32] Z.D. Hood, C. Kates, M. Kirkham, S. Adhikari, C. Liang, N.A.W. Holzwarth, Structural and electrolyte properties of  $\text{Li}_4\text{P}_2\text{S}_6$ , *Solid State Ionics* 284 (2015) 61–70.
- [33] H. Jónsson, G. Mills, K.W. Jacobsen, Nudged elastic band method for finding minimum energy paths of transitions, in: B.J. Berne, G. Ciccotti, D.F. Coker (Eds.), *Classical and Quantum Dynamics in Condensed Phase Simulations*, World Scientific, Singapore, 1998, pp. 385–404.
- [34] G. Henkelman, B.P. Uberuaga, H. Jónsson, A climbing image nudged elastic band method for finding saddle points and minimum energy paths, *J. Chem. Phys.* 113 (2000) 9901–9904.
- [35] G. Henkelman, H. Jónsson, Improved tangent estimate in the nudged elastic band method for finding minimum energy paths and saddle points, *J. Chem. Phys.* 113 (2000) 9978–9985.
- [36] A.R. West, *Basic Solid State Chemistry*, second ed., John Wiley & Sons, LTD, 1999.
- [37] T. Hahn (Ed.), *International Tables for Crystallography, Volume a: Space-group Symmetry, Fifth Revised Edition*, Kluwer, 2002. ISBN 0-7923-6590-9. The symmetry labels used in this work are all based on this reference.
- [38] A. Al-Qawasmeh, J. Howard, N.A.W. Holzwarth,  $\text{Li}_4\text{SnS}_4$  and  $\text{Li}_4\text{SnSe}_4$ : simulations of their structure and electrolyte properties, *J. Electrochem. Soc.* 164 (2017) A6386–A6394.
- [39] Y.A. Du, N.A.W. Holzwarth, Li ion migration in  $\text{Li}_3\text{PO}_4$  electrolytes: effects of O vacancies and N substitutions, *ECS Trans.* 13 (2008) 75–82.
- [40] S.P. Ong, L. Wang, B. Kang, G. Ceder,  $\text{LiFePO}_2$  phase diagram from first principles calculations, *Chem. Mater.* 20 (5) (2008) 1798–1807.
- [41] J. Li, C. Ma, M. Chi, C. Liang, N.J. Dudney, Solid electrolyte: the key for high-voltage lithium batteries, *Adv. Energy Mater.* 5 (4) (2015) 1401408.
- [42] A.K. Ivanov-Shitz, V.V. Kireev, O.K. Mel'nikov, L.N. Demainets, Growth and ionic conductivity of  $\gamma$ - $\text{Li}_3\text{PO}_4$ , *Crystallogr. Rep.* 46 (2001) 864–867.

# Appendix D

## Atomics Units

Atomic units is a system of natural units which is especially convenient for atomic physics calculations. There are two different kinds of atomic units, Hartree atomic units and Rydberg atomic units, which differ in the choice of the unit of mass and charge. In this thesis we used Hartree atomic units, which define the physical constants as follows:

- The unit of mass is the mass of an electron  $m_e$ .
- The unit of charge is the magnitude of the charge of an electron  $e$ .
- The unit of length is the Bohr radius ( $a_0$ ), which is given by:

$$a_0 = \frac{4\pi\epsilon_0\hbar^2}{m_e e^2} \quad (\text{D.1})$$

- According to this definition in atomic units, the energy in atomic units will be given in Ha which stands for Hartree, which is defined as follows:

$$1Ha = \frac{e^2}{4\pi\epsilon_0 a_0} \quad (\text{D.2})$$

# Bibliography

- [1] Y. S. Meng and M. E. Arroyo-de Dompablo, *First principles computational materials design for energy storage materials in lithium ion batteries*, Energy & Environmental Science **2**, 589 (2009).
- [2] D. Linden and T. B. Reddy, *Handbook of Batteries*, (McGraw Hill, 2001).
- [3] J. B. Goodenough and Y. Kim, *Challenges for rechargeable Li batteries*, Chemistry of Materials **22**, 587 (2010).
- [4] N. Lepley, *First Principles Investigations of solid-solid Interfaces in Lithium Battery Materials*, Ph.D. thesis, Wake Forest University (2015).
- [5] W. M. Haynes, ed., *CRC Handbook of Chemistry and Physics, 92th Edition*, (CRC Press, Taylor & Francis Group, 2011).
- [6] M. S. Whittingham, *Electrical energy storage and intercalation chemistry*, Science **192**, 1126 (1976).
- [7] Y. Y. Kamaya N, Homma K, *A lithium superionic conductor*, Nature Materials **10**, 682 (2011).
- [8] N. J. Dudney, J. B. Bates, and B. J. Neudecker, *Thin-film materials for solid-state rechargeable batteries*, in *Encyclopedia of Materials: Science and Technology*, pp. 9302–9306, (Pergamon2008), iSBN-13:978-0-08-043152-9, ISB-10:0-08-043152-6.

- [9] J. B. Bates, N. J. Dudney, B. Neudecker, A. Ueda, and C. D. Evans, *Thin-film lithium and lithium-ion batteries*, Solid State Ionics **135**, 33 (2000).
- [10] X. Yu, J. B. Bates, J. G. E. Jellison, and F. X. Hart, *A stable thin-film lithium electrolyte: Lithium phosphorus oxynitride* **144**, 524 (1997).
- [11] B. Wang, B. C. Chakoumakos, B. C. Sales, B. S. Kwak, and J. B. Bates, *Synthesis, crystal structure, and ionic conductivity of a polycrystalline lithium phosphorus oxynitride with the  $\gamma$ - $\text{Li}_3\text{PO}_4$  structure*, Journal of Solid State Chemistry **115**, 313 (1995).
- [12] J. B. Bates, N. J. Dudney, D. C. Lubben, G. R. Gruzalski, B. S. Kwak, X. Yu, and R. A. Zuhr, *Thin-film rechargeable lithium batteries*, Journal of Power Sources **54**, 58 (1995).
- [13] B. Wang, B. S. Kwak, B. C. Sales, and J. B. Bates, *Ionic conductivities and structure of lithium phosphorus oxynitride glasses*, Journal of Non-Crystalline Solids **183**, 297 (1995).
- [14] J. B. Bates, G. R. Gruzalski, N. J. Dudney, C. F. Luck, and X. Yu, *Rechargeable thin-film lithium batteries* **70–71**, 619 (1994).
- [15] J. B. Bates, N. J. Dudney, G. R. Gruzalski, R. A. Zuhr, A. Choudhury, D. F. Luck, and J. D. Robertson, *Fabrication and characterization of amorphous lithium electrolyte thin films and rechargeable thin-film batteries*, Journal of Power Sources **43–44**, 103 (1993).
- [16] J. B. Bates, N. J. Dudney, G. R. Gruzalski, R. A. Zuhr, A. Choudhury, D. F. Luck, and J. D. Robertson, *Electrical properties of amorphous lithium electrolyte thin films*, Solid State Ionics **53–56**, 647 (1992).

- [17] F. Giustino, *Materials Modeling Using Density Functional Theory*, (Oxford University Press, 2014).
- [18] M. Born and K. Huang, *Dynamical Theory of Crystal Lattices*, (Oxford at the Clarendon Press, 1954).
- [19] E. Fermi, *Un metodo statistico per la determinazione di alcune proprieta dell'atome*, Rend. Accad. Naz. Lincei **6**, 602 (1927).
- [20] L. H. Thomas, *The calculation of atomic fields*, Proc. Cambridge Phil. Roy. Soc **23**, 542548 (1927).
- [21] P. Hohenberg and W. Kohn, *Inhomogeneous electron gas*, Physical Review B **136**, B864 (1964).
- [22] W. Kohn and L. J. Sham, *Self-consistent equations including exchange and correlation effects*, Physical Review B **140**, A1133 (1965).
- [23] J. P. Perdew and Y. Wang, *Accurate and simple analytic representation of the electron-gas correlation energy*, Physical Review B **45**, 13244 (1992).
- [24] R. O. Jones and O. Gunnarsson, *The density functional formalism, its applications and prospects*, Reviews of Modern Physics **61**, 689 (1989).
- [25] J. P. Perdew, K. Burke, and M. Ernzerhof, *Generalized gradient approximation made simple*, Physical Review Letters **78**, 1396 (1997).
- [26] A. García, C. Elsässer, J. Zhu, S. G. Louie, and M. L. Cohen, *Use of gradient-corrected functionals in total-energy calculations for solids*, Physical Review B **46**, 9829 (1992).
- [27] A. Zupan, P. Blaha, K. Schwarz, and J. P. Perdew, *Pressure-induced transitions in solid Si, SiO<sub>2</sub>, and Fe: Performance of local-spin-density and generalized-gradient-approximation density functionals*, Physical Review B **58**, 11266 (1998).



- [28] Y. A. Du and N. A. W. Holzwarth, *First-principles study of LiPON and related solid electrolytes*, Physical Review B **81**, 184106 (15pp) (2010).
- [29] Y. A. Du and N. A. W. Holzwarth, *Mechanisms of  $\text{Li}^+$  diffusion in crystalline  $\text{Li}_3\text{PO}_4$  electrolytes from first principles*, Physical Review B **76**, 174302 (14 pp) (2007).
- [30] J. C. Phillips and L. Kleinman, *New method for calculating wave functions in crystals and molecules*, Physical Review B **116**, 287 (1959).
- [31] M. C. Payne, M. P. Teter, D. C. Allan, T. A. Arias, and J. D. Joannopoulos, *Iterative minimization techniques for ab initio total-energy calculations: molecular dynamics and conjugate gradients*, Reviews of Modern Physics **64**, 1045 (1992).
- [32] P. E. Blöchl, *Projector augmented-wave method*, Physical Review B **50**, 17953 (1994).
- [33] D. Vanderbilt, *Soft self-consistent pseudopotentials in a generalized eigenvalue formalism*, Physical Review B **41**, 7892 (1990).
- [34] P. Giannozzi, S. Baroni, N. Bonini, M. Calandra, R. Car, C. Cavazzoni, D. Ceresoli, G. L. Chiarotti, M. Cococcioni, I. Dabo, A. D. Corso, S. de Gironcoli, S. Fabris, G. Fratesi, R. Gebauer, U. Gerstmann, C. Gougoussis, A. Kokalj, M. Lazzeri, L. Martin-Samos, N. Marzari, F. Mauri, R. Mazzarello, S. Paolini, A. Pasquarello, L. Paulatto, C. Sbraccia, S. Scandolo, G. Sclauzero, A. P. Seitsonen, A. Smogunov, P. Umari, and R. M. Wentzcovitch, *Quantum espresso: a modular and open-source software project for quantum simulations of materials*, Journal of Physics: Condensed Matter **21**, 394402 (19pp) (2009).
- [35] X. Gonze, F. Jollet, F. Abreu Araujo, D. Adams, B. Amadon, T. Applencourt, C. Audouze, J.-M. Beuken, J. Bieder, A. Bokhanchuk, E. Bousquet, F. Bruneval,

- D. Caliste, M. Ct, F. Dahm, F. Da Pieve, M. Delaveau, M. Di Gennaro, B. Dorado, C. Espejo, G. Geneste, L. Genovese, A. Gerossier, M. Giantomassi, Y. Gillet, D. Hamann, L. He, G. Jomard, J. Laffamme Janssen, S. Le Roux, A. Levitt, A. Lherbier, F. Liu, I. Lukaevi, A. Martin, C. Martins, M. Oliveira, S. Ponc, Y. Pouillon, T. Rangel, G.-M. Rignanese, A. Romero, B. Rousseau, O. Rubel, A. Shukri, M. Stankovski, M. Torrent, M. Van Setten, B. Van Troeye, M. Verstraete, D. Waroquiers, J. Wiktor, B. Xu, A. Zhou, and J. Zwanziger, *Recent developments in the ABINIT software package*, Comput. Phys. Commun. **205**, 106 (2016), ISSN 0010-4655.
- [36] A. Kokalj, *XCrySDen— an new program for displaying crystalline structures and densities*, Journal of Molecular Graphics and Modelling **17**, 176 (1999).
- [37] R. P. Feynman, *Forces in molecules*, Physical Review B **56**, 340 (1939).
- [38] C. A. Wert, *Diffusion coefficient of C in  $\alpha$ -iron*, Physical Review B **79**, 601 (1950).
- [39] G. H. Vineyard, *Frequency factors and isotope effects in solid state rate processes*, Journal of Physics and Chemistry of Solids **3**, 121 (1957).
- [40] J. M. Haile, *Molecular Dynamics Simulations*, (John Wiley & Sons, Inc., 1992).
- [41] L. Verlet, *Computer "experiments" on Classical Fluids. i. Thermodynamical Properties of Lennard-Jones Molecules*, Physical Review B **159**, 98 (1967).
- [42] N. D. Lepley and N. A. W. Holzwarth, *Modeling interfaces between solids: Application to Li battery materials*, Physical Review B **92**, 214201 (2015).
- [43] N. A. W. Holzwarth, G. E. Matthews, R. B. Dunning, A. R. Tackett, and Y. Zeng, *Comparison of the projector augmented-wave, pseudopotential, and linearized*

- augmented-plane-wave formalisms for density-functional calculations of solids*, Physical Review B **55**, 2005 (1997).
- [44] G. Sahu, E. Rangasamy, J. Li, Y. Chen, K. An, N. Dudney, and C. Liang, *A high-conduction Ge substituted  $Li_3AsS_4$  solid electrolyte with exceptional low activation energy*, Journal of Materials Chemistry A **2**, 10396 (2014).
- [45] M. Tachez, J.-P. Malugani, R. Mercier, and G. Robert, *Ionic conductivity of and phase transition in lithium thiophosphate  $Li_3PS_4$* , Solid State Ionics **14**, 181 (1984).
- [46] N. D. Lepley, N. A. W. Holzwarth, and Y. A. Du, *Structures,  $Li^+$  mobilities, and interfacial properties of solid electrolytes  $Li_3PS_4$  and  $Li_3PO_4$  from first principles*, Physical Review B **88**, 104103 (2013).
- [47] Z. Liu, W. Fu, E. A. Payzant, X. Yu, Z. Wu, N. J. Dudney, J. Kiggans, K. Hong, A. J. Rondinone, and C. Liang, *Anomalous high ionic conductivity of nanoporous  $-Li_3PS_4$* , Journal of the American Chemical Society **135**, 975 (2013).
- [48] K. Homma, M. Yonemura, T. Kobayashi, M. Nagao, M. Hirayama, and R. Kanno, *Crystal structure and phase transitions of the lithium ionic conductor  $Li_3PS_4$* , Solid State Ionics **182**, 53 (2011), ISSN 01672738.
- [49] M. Murayama, R. Kanno, Y. Kawamoto, and T. Kamiyama, *Structure of the thio-lisicon,  $Li_4GeS_4$* , Solid State Ionics **154-155**, 789 (2002).
- [50] J. H. MacNeil, D. M. Massi, J.-H. Zhang, K. A. Rosmus, C. D. Brunetta, T. A. Gentile, and J. A. Aitken, *Synthesis, structure, physicochemical characterization and electronic structure of thio-lithium super ionic conductors,  $Li_4Ges_4$  and  $Li_4SnS_4$* , Journal of Alloys and Compounds **586**, 736 (2014).

- [51] R. Grau-Crespo, S. Hamad, C. R. A. Catlow, and N. H. de Leeuw, *Symmetry-adapted configurational modelling of fractional site occupancy in solids*, Journal of Physics: Condensed Matter **19**, 256201 (2007).
- [52] A. van de Walle and G. Ceder, *The effect of lattice vibrations on substitutional alloy thermodynamics*, Reviews of Modern Physics **74**, 11 (2002).
- [53] T. Kaib, S. Haddadpour, M. Kapitein, P. Bron, C. Schrder, H. Eckert, B. Roling, and S. Dehnen, *New lithium chalcogenidotetrelates, LiChT: Synthesis and characterization of the  $\text{Li}^+$ -conducting tetralithium ortho-sulfidostannate  $\text{Li}_4\text{SnS}_4$* , Chemistry of Materials **24**, 2211 (2012).
- [54] D. Baumann and W. Schnick,  *$\text{Li}_{14}(\text{PON}_3)_2\text{O}$  a non-condensed oxonitridophosphate oxide*, European Journal of Inorganic Chemistry **2015**, 617 (2015).
- [55] W. Schnick and J. Luecke, *Synthesis and crystal structure of lithium phosphorus nitride  $\text{Li}_7\text{PN}_4$ : The first compound containing isolated  $\text{PN}_4$ -tetrahedra*, Journal of Solid State Chemistry **87**, 101 (1990).
- [56] W. Schnick and J. Luecke, *Lithium ion conductivity of  $\text{LiPN}_2$  and  $\text{Li}_7\text{PN}_4$* , Solid State Ionics **38**, 271 (1990).
- [57] E. Rangasamy, Z. Liu, M. Gobet, K. Pilar, G. Sahu, W. Zhou, H. Wu, S. Greenbaum, and C. Liang, *An iodide-based  $\text{Li}_7\text{P}_2\text{S}_8\text{I}$  superionic conductor*, Journal of the American Chemical Society **137**, 1384 (2015), ISSN 0002-7863, 1520-5126.
- [58] S. J. Sedlmaier, S. Indris, C. Dietrich, M. Yavuz, C. Drger, F. von Seggern, H. Sommer, and J. Janek,  *$\text{Li}_4\text{PS}_4\text{I}$ : A  $\text{Li}^+$  superionic conductor synthesized by a solvent-based soft chemistry approach*, Chemistry of Materials **29**, 1830 (2017), ISSN 0897-4756, 1520-5002.

- [59] N. H. H. Phuc, E. Hirahara, K. Morikawa, H. Muto, and A. Matsuda, *One-pot liquid phase synthesis of  $(100-x)\text{Li}_3\text{PS}_{4-x}\text{LiI}$  solid electrolytes*, Journal of Power Sources **365**, 7 (2017), ISSN 03787753.
- [60] N. H. H. Phuc, T. Yamamoto, H. Muto, and A. Matsuda, *Fast synthesis of  $\text{Li}_2\text{S}-\text{P}_2\text{S}_5-\text{LiI}$  solid electrolyte precursors*, Inorg. Chem. Front. **4**, 1660 (2017), ISSN 2052-1553.
- [61] S. Sicolo, C. Kalcher, S. J. Sedlmaier, J. Janek, and K. Albe, *Diffusion mechanism in the superionic conductor  $\text{Li}_4\text{PS}_4\text{I}$  studied by first-principles calculations*, Solid State Ionics **319**, 83 (2018), ISSN 01672738.
- [62] J. Kang and B. Han, *First-principles characterization of the unknown crystal structure and ionic conductivity of  $\text{Li}_7\text{P}_2\text{S}_8\text{I}$  as a solid electrolyte for high-voltage Li ion batteries*, The Journal of Physical Chemistry Letters **7**, 2671 (2016), ISSN 1948-7185.
- [63] T. Hahn, ed., *International Tables for Crystallography, Volume A: Space-group symmetry, Fifth revised edition*, (Kluwer, 2002), ISBN 0-7923-6590-9. The symmetry labels used in this work are all based on this reference.
- [64] K. OSullivan, G. Chiarotti, and P. A. Madden, *Silver-ion disorder in  $\alpha\text{-AgI}$ : A computer simulation study*, Physical Review B **43**, 13536 (1991).
- [65] S.-T. Kong, H.-J. Deiseroth, C. Reiner, . Gn, E. Neumann, C. Ritter, and D. Zahn, *Lithium argyrodites with phosphorus and arsenic: Order and disorder of lithium atoms, crystal chemistry, and phase transitions*, Chemistry - A European Journal **16**, 2198 (2010), ISSN 09476539, 15213765.
- [66] K. Homma, M. Yonemura, M. Nagao, M. Hirayama, and R. Kanno, *Crystal structure of high-temperature phase of lithium ionic conductor,  $\text{Li}_3\text{PS}_4$* , J. Phys. Soc. Jpn. **79**, 90 (2010).

## Part III

# Curriculum Vitae

## Ahmad Al-Qawasmeh

Department of Physics  
Wake Forest University  
Winston Salem, NC, USA

Cell: 001-336 -749-0391  
Email: [alqaan13@wfu.edu](mailto:alqaan13@wfu.edu)

---

### EDUCATION:

Wake Forest University, USA	Ph.D.	2018	Physics
Yarmouk University, Jordan	M.S.	2011	Physics
Yarmouk University, Jordan	B.S.	2008	Physics

### ACADEMIC EXPERIENCE:

<b>Aug 2013 – May 2018</b>	<b>Research Assistant, Department of Physics, Wake Forest University, USA.</b> Advisors: Professor Natalie Holzwarth Research Topics: Computational Research on Solid Electrolytes in Lithium Batteries
<b>Aug 2012 – May 2013</b>	<b>Lecturer, Philadelphia University, Jordan</b> Topic: Teaching Undergraduate Engineering Classes
<b>Sep 2010 – May 2011</b>	<b>Teaching Assistant, Department of Physics, Yarmouk University, Jordan</b> Topic: Teaching Undergraduate Science Labs

### PUBLICATIONS:

1. **Ahmad Al-Qawasmeh**, N. A. W. Holzwarth  
*Li<sub>14</sub>P<sub>2</sub>O<sub>3</sub>N<sub>6</sub> and Li<sub>7</sub>PN<sub>4</sub>: Computational study of two nitrogen rich crystalline LiPON electrolyte materials, Journal of Power Sources, 2017*
2. **Ahmad Al-Qawasmeh**, Jason Howard, N. A. W. Holzwarth  
*Li<sub>4</sub>SnS<sub>4</sub> and Li<sub>4</sub>SnSe<sub>4</sub>: Simulations of Their Structure and Electrolyte Properties, Journal of The Electrochemical Society, 2017*

3. **Ahmad Al-Qawasmeh**, N. A. W. Holzwarth  
*Computational Study of Li Ion Electrolytes Composed of Li<sub>3</sub>AsS<sub>4</sub> Alloyed with Li<sub>4</sub>GeS<sub>4</sub>*,  
*Journal of The Electrochemical Society*, 2016
4. C. Dun, **Ahmad Al-Qawasmeh**, et al.  
Modulation Doping and Energy Filtering in Low-Dimensional, Chalcogenide  
Thermoelectrics, *Journal of Materials Chemistry A*, 2018, under review
5. **Ahmad Al-Qawasmeh**, N. A. W. Holzwarth  
Computational study of the structural and electrolyte properties of Li<sub>4</sub>PS<sub>4</sub>I  
and related materials, in preparation

#### ORAL AND POSTER PRESENTATIONS:

1. Computational Study of the Solid Electrolyte Li<sub>4</sub>PS<sub>4</sub>I and Related Materials  
**Talk presented by Ahmad Al-Qawasmeh at the March 2018 Meeting of the American Physical Society, March 6-9, 2018 in Los Angeles, CA, USA.**
2. Li<sub>14</sub>P<sub>2</sub>O<sub>3</sub>N<sub>6</sub> and Li<sub>7</sub>PN<sub>4</sub> : Computational study of two nitrogen rich crystalline LiPON  
**Poster contributed by Ahmad Al-Qawasmeh at the 29th Annual Workshop on Recent Developments in Electronic Structure Methods, June, 2017 at Princeton University**
3. Li<sub>14</sub>(PON)<sub>3</sub>2O: Computational study of a possible new electrolyte for Li ion batteries  
**Talk presented by Ahmad N. Al-Qawasmeh at the March 2017 Meeting of the American Physical Society, March 2017, New Orleans, USA.**
4. Computational study of Li ion electrolytes composed of Li<sub>3</sub>AsS<sub>4</sub> alloyed with Li<sub>4</sub>GeS<sub>4</sub>  
**Talk presented by Ahmad Al-Qawasmeh at the March 2016 Meeting of the American Physical Society, March 2016, Baltimore, USA.**
5. Ab initio Simulation of Idealized Solid Electrolytes in Lithium Batteries  
**Talk presented by Ahmad Al-Qawasmeh, October 2017, Department of Physics, Wake University, USA.**
6. Electronic Structure Theory  
**Talk presented by Ahmad Al-Qawasmeh, April 2016, Department of Physics, Wake F University, USA.**



## **GRADUATE CLASSES:**

Classical Mechanics, Phys 711, Wake Forest University, USA.  
Electromagnetism, Phys 712, Wake Forest University, USA.  
Quantum Mechanics I, Phys 741, Wake Forest University, USA.  
Quantum Mechanics II, Phys 742, Wake Forest University, USA.  
Statistical Mechanics, Phys 770, Wake Forest University, USA.  
Solid State Physics, Phys 752, Wake Forest University, USA.  
Group Theory, Phys 745, Wake Forest University, USA.  
Special Topics in Physics (Electron Imaging), Phys 691, Wake Forest University, USA.  
Condensed Matter Seminar, Phys 663, Wake Forest University, USA.  
Physics Seminar, Phys 601, Wake Forest University, USA.

## **COMPUTATIONAL SKILLS:**

### **Scientific Software:**

**Quantum Espresso & Abinit:** Ab initio Molecular Dynamics Simulation,  
Structural optimization, Defect Analysis, Phonons analysis,  
Thermodynamics Properties

**Lammps & Gulp:** Classical Molecular Dynamics Simulation, Structural Optimization,  
Classical Force Field Mapping to Ab initio Calculations.

### **Programming Languages: FORTRAN & C++ & Python**

**Computer Skills:** Microsoft Word/Excel/PowerPoint, OriginPro, Adobe Suite (Photoshop, Premiere), Spartan, Mercury and Diamond software for structural simulation, XRD analysis Software (TOPAS, EVA, GSAS, HighScore Plus), Digital Micrograph, Thermo Avantage XPS software package.

**REFERENCES:**

Professor Natalie Holzwarth  
Department of Physics  
Wake Forest University, USA  
[natalie@wfu.edu](mailto:natalie@wfu.edu)

Professor Martin Guthold  
Department of Physics  
Wake Forest University, USA  
[gutholdm@wfu.edu](mailto:gutholdm@wfu.edu)

Professor Paul Anderson  
Department of Physics  
Wake Forest University, USA  
[anderson@wfu.edu](mailto:anderson@wfu.edu)

Professor Anas Ababneh  
Department of Physics  
Yarmouk University, Jordan  
[ababneha@yu.edu.jo](mailto:ababneha@yu.edu.jo)